University of Nottingham
UK | CHINA | MALAYSIA

Analytical modelling and control of thermal energy and geometry in wire-fed laser cladding

By Jinyi Li

Supervisors

Dr. Haonan Li

Prof. Dragos Axinte

Dr. Zhirong Liao

Thesis submitted to the University of Nottingham
for the degree of Doctor of Philosophy

School of Aerospace, Faculty of Science & Engineering

November 2022

(This page is left blank)

Preface

This thesis is submitted for the degree of Doctor of Philosophy at the University of Nottingham. The research work is carried out under the supervision of Dr. Haonan Li in School of Aerospace, Prof. Dragos Axinte, and Dr. Zhirong Liao in the Department of Mechanical, Materials and Manufacturing Engineering.

It is certified that the work presented in this thesis is original. References to any work from the literature are clarified in the text.

This thesis is composed of the publications listed as follows:

Journal Article 1

J. Li, H.N. Li, Z. Liao, D. Axinte, Analytical modelling of full single-track profile in wire-fed laser cladding, Journal of Materials Processing Technology, 290 (2021), 116978-116991. (Impact factor: 5.55, JCR Q1 journal)

Journal Article 2

J. Li, H.N. Li, Z. Liao, D. Axinte, Overlapped wire-fed laser cladding on inclined surfaces: An analytical model considering gravity and a model application, Journal of Materials Processing Technology, 304 (2022), 117559-117575. (Impact factor: 5.55, JCR Q1 journal)

Acknowledgements

The completion of this thesis and related research works are attributed by the whole team of supervisors and colleagues. The platforms and visions they provide during the whole Ph.D. period are the key elements that I will remember deeply in my heart even after many years of graduation.

First of all, the research work is supported by Prof. Dragos Axinte who carefully supervises each step and checks originality, experiments, and modelling. His supervision experience and expertise have ensured many of his Ph.D. students, including myself in the near future. I feel lucky that there is such a standard that guides me to finish the tasks one by one. The project cannot be pushed forward without his constant encouragement and monitor.

Secondly, the contributions are enormous that come from Dr. Haonan Li, who is the lead supervisor when the thesis is being pushed on forward steps. The works are including the validation of the research work and the finalizing of the thesis structure, which I realize it takes a great part of time because it includes enormous workload on critical thinking of all the experimental and modelling results. More importantly, he is always so patient that points out the minute details or faults. Actually, other than the help on research work, I especially thank him for his persistence of considering me into the research team at the first beginning.

Thirdly, the ideas are also provided by Dr. Zhirong Liao throughout the project which is the vital factor of consolidating the project. He constantly brings some

breakthroughs during the research when there are many times that the work cannot be continued. I am very thankful about his great patience in this supervisor team.

Fourthly, the experiment works are assisted by the technician Mr. John Zhu who contributes a lot. Many of the lab works can not be finished without his constant check and support. There are many times when I have to interrupt his weekends and ask for guidance of the equipment. I am so grateful about his patience that I also think of him as one of my supervisors.

In the end, the special gratitude is given to my sister who continuously gives me spiritual support throughout my Ph.D. period. I must have brought her a lot of worry these years because of not being around. I am grateful of my passed away parents and hope they can see my success.

Abstract

Laser cladding is an additive manufacturing technology. By forming a stable track on the target surface, metal can be rapidly deposited on the substrate in large quantities. It is now widely used in parts repair and net shape additive manufacturing. With the increasing popularity of automation systems in the manufacturing industry, the demand for built-in prediction and control models is more and more obvious, so that robots can complete tasks without human intervention.

In this study, the full shape of the material deposition has been analytically modelled, including the bulge (the part above the surface) and the melt pool (the part below the surface). The modelling method is based on the capillary theory to calculate the interfacial tension at the interface between the bulge and the air, the melt pool and the substrate, so that the full profiles of the deposited material can be predicted under different process parameters (such as laser power, scanning speed and wire feeding speed). In addition, the single-track cladding model is extended to overlapping tracks on horizontal surfaces to accurately predict and control geometry. The remelting and bonding behaviours were also analysed to assess the integrity of the cladding. In addition, the model is extended to take into account the cladding behaviour on the inclined surface, which creates the possibility of repairing free-form parts.

The model is validated by experimenting with various process parameters and then making appropriate measurements (the geometric shape/size of the bulge is measured by coordinate measurement machine, and the surface integrity is

measured by optical microscope). The shape error of laser cladding between experiment and simulation of optimizing process parameters is acceptable and can be used in actual manufacturing. Since the model is time dependent, it can be easily implemented on any machine tool or manipulator. Using this model, the shape of the bulge and the weld pool can be precisely controlled by changing the laser scanning speed in a complex way.

This work is helpful to understand the material accumulation process in the wire-fed laser cladding process, and shows the analytical modelling method, which can be used to improve the current capability of this technology in part repair or net-shape additive manufacturing.

Contents

Abbreviations

AM	Additive Manufacturing
CAD	Computer-Aided Design
CAGR	Compound Annual Growth Rate
CAM	Computer-Aided Manufacturing
CO_2	Carbon Dioxide
CMM	Coordinate Measurement machine
CNC	Computer Numerical Control
CNT	Carbon Nanotube
DLD	Direct Laser Deposition
DDL	Direct Diode Laser
DED	Directed Energy Deposition
EDM	Electric Discharge Machining
FDM	Finite Difference Method
FE	Finite Element
GUI	Graphic User Interface
Nd:YAG	Neodymium-doped Yttrium Aluminium Garnet
SEM	Scanning Electron Microscope
TiC	Titanium Carbide
WC	Tungsten Carbide
WLC	Wire-fed Laser Cladding

Nomenclatures

A_C	constant of contact angle function
A_I	constant of interfacial tension function
A_L	constant of Lorentz function
B_C	constant of contact angle function
B_I	constant of interfacial tension function
B_L	constant of Lorentz function
c_m	coefficient of melt pool profile
c_1, c_2, c_3	horizontal position coefficients
C_{ab}	absorption coefficient $(1/m)$
C_p	specific heat capacity $(J/(kg * K))$
C_p^*	modified specific heat capacity $(J/(kg * K))$
d	depth of melt pool (m)
d_{RG}	Rayleigh range (m)
d_w	distance from waist (m)
dx	shifted distance (m)
D	dilution $(\%)$
e	eccentricity
F_{gx}	gravity x component (N)
F_γ	surface tension at corner (N)
$F_{\gamma x}$	surface tension x component (N)
$F_{\gamma z}$	surface tension z component (N)
g	gravity acceleration (m/s^2)
h	bulge height (m)
h_n	convection-radiation coefficient $(W/(m^2K))$
I	laser intensity $(J/(m^2 * s))$
I_0	initial laser intensity $(J/(m^2 * s))$
k	heat conductivity $(W/(m * K))$
k_B	Boltzmann constant (J/K)
k_c	constant for Eotvos rule $(J/(K * mol^{(2/3)}))$

L_b	half-length of retention drop (m)
L_f	latent heat of fusion (J/kg)
L_1, L_2, L_r	retention drop coefficient (m)
M^2	beam propagation factor
n	super Gaussian order
p	hydrostatic pressure (N/m^2)
P	laser power (W)
Q_l	laser energy (J)
r	radius of laser beam (m)
r_w	radius of laser beam waist (m)
r_1, r_2	radius of two arcs (m)
R_{atom}	atomic radius (m)
R_w	radius of wire (m)
R_0	curvature radius at the apex of melt pool (m)
s	curve length (m)
S	bulge area (m^2)
$S_{overlap}$	overlap area (m^2)
T_b	boiling point (K)
T_C	critical temperature (K)
$T^{in}_{x,y,z,t}$	temperature of interior cells (K)
T_m	melting point (K)
T_{aver}	average temperature (K)
T_R	reference temperature (K)
$T_{x,y,z,t}$	spatial transient temperature (K)
$T^w_{x,y,z,t}$	wall temperature (K)
T_∞	environment temperature (K)
v_f	wire feed rate (m/s)
v_s	scanning speed (m/s)
V	molar volume (L/mol)
w	width of melt pool (m)
x_a	position of advancing arc (m)

x_r position of receding arc (m)
x_t current horizontal position (m)
x_0 horizontal position (m)
z_a position of advancing arc (m)
z_{in} height at the intersection (m)
z_m applicate of depth of melt pool (m)
z_r position of receding arc (m)
z_0 vertical position (m)
Z_x first order derivate of z
Z_{xx} second order derivate of z

α inclined angle (rad)
β absorptivity
γ surface tension (N/m)
γ_{sl} solid-liquid interfacial tension (N/m)
Γ Gamma function
σ Fresnel reflectivity
Δd mesh cell dimension (m)
Δt increment of time (s)
ϵ emissivity
δ ratio of bulge width
δ_a ratio of advancing side
δ_r ratio of receding side
η attenuation rate
η_{OR} overlap ratio
η_{SR} stagger ratio
θ intrinsic angle (rad)
θ_a advancing angle(rad)
θ_b contact angle at boiling (rad)
θ_e extension of melt pool (rad)

θ_m	contact angle at melting (rad)
θ_r	receding angle (rad)
λ	laser wavelength (m)
λ_c	capillary length (m)
ρ_a	density of air (kg/m^3)
ρ_l	density of metal liquid (kg/m^3)
φ	curve angle of melt pool profile (rad)
Ω_{sm}	atomic volume (m^3)

List of Figures

List of Tables

Chapter 1

None.

Chapter 2

None.

Chapter 3

Chapter 4

Chapter 5

Chapter 6

Chapter 7

None.

(This page is left blank)

Chapter 1 Introduction

1.1 Background

1.1.1 Repair needs in the industry

Procurement is one-time event, while repairs will follow the lifetime of a machine. The service life of the machine is predictable: 20 years for the design of an automobile, 40 years for the design of a civil aircraft, and 100 years for the design of a bridge. However, their service life will include numerous repairs, especially those parts that bear critical conditions such as heavy stress, high speed and high temperature and lead to failure such as wear, deformation, and fracture. Turbines, engine blocks, compressors, pumps, valves, heat exchangers, crankshafts, moulds, hydraulic cylinders, gear boxes, rail tracks, and buckets are all on the repair list (see Figure 1.1). These components are of high value, either (i) large in size, high in material and manufacturing costs, or (ii) manufactured with ultra-high precision methods, far exceeding the value of material consumption. Once damaged, these components usually need to be repaired rather than replaced [1], and the quality of the final product must be ensured to meet the design requirements of materials, processes and assemblies during the use of the equipment.

(Source: a[2], b[3], c[4], d[5], e[6], f[7], g[8], h[9], i[10], j[11], k[12], l[13])

Figure 1.1 Components that are in repair process: (a) turbines, (b) engine blocks, (c) compressors, (d) pumps, (e) valves, (f) heat exchangers, (g) crankshafts, (h) moulds, (i) hydraulic cylinders, (j) gear boxes, (k) rail tracks, and (l) buckets.

The demand for repairing mechanical parts is very high according to the following market research reports. The global rotating equipment repair market is predicted to reach a market value of USD 25.9 billion between 2021 and 2031 and is anticipated to grow at a Compound Annual Growth Rate (CAGR) of 4.8% by value [14] (see Figure 1.2). The main potential factor driving the market is the growth of end use industries such as oil, natural gas and power generation. Therefore, continuous maintenance, renovation and component upgrading have become the key to maintaining the operation of the industrial chain. Another report is about the aerospace sector in the European Union. The total value of remanufacturing and repairing is estimated as EUR 12.4 billion, which is 10% of the total market value of the aerospace manufacturing sector in the European Union [15]. Opportunities in this field are an important part of the economy: the cost of repaired aerospace products is about half of the cost of newly manufactured products, which makes repairing the most cost-effective choice in the industry.

The damaged parts can be reversed from the view of engineer as long as there is a set of provisions regarding the repair and renovation. A national standard CB/T 3711-2013 [16] in China specifies the technical welding repairing requirements for marine diesel engine parts. This standard is applicable to welding repairs such as casting defects, bumps, cracks, wear, corrosion, and ablation of marine diesel engine parts. Another standard GB/T 29796-2013 [17] relates to laser repair general specifications for cladding layer surface quality, mechanical performance, metallurgical structure, hardness and non-destructive inspection. In the US, a standard PCC-2-2018 [18] provides methods, including

relevant design, fabrication, examination, and testing practices, for repair of equipment, pipelines and associated auxiliary equipment. Also for pipelines, a standard BS 8561:2013 [19] in the UK defines requirements for structural strength/integrity, joint capabilities, sealing properties, corrosion resistance, and end load restraint.

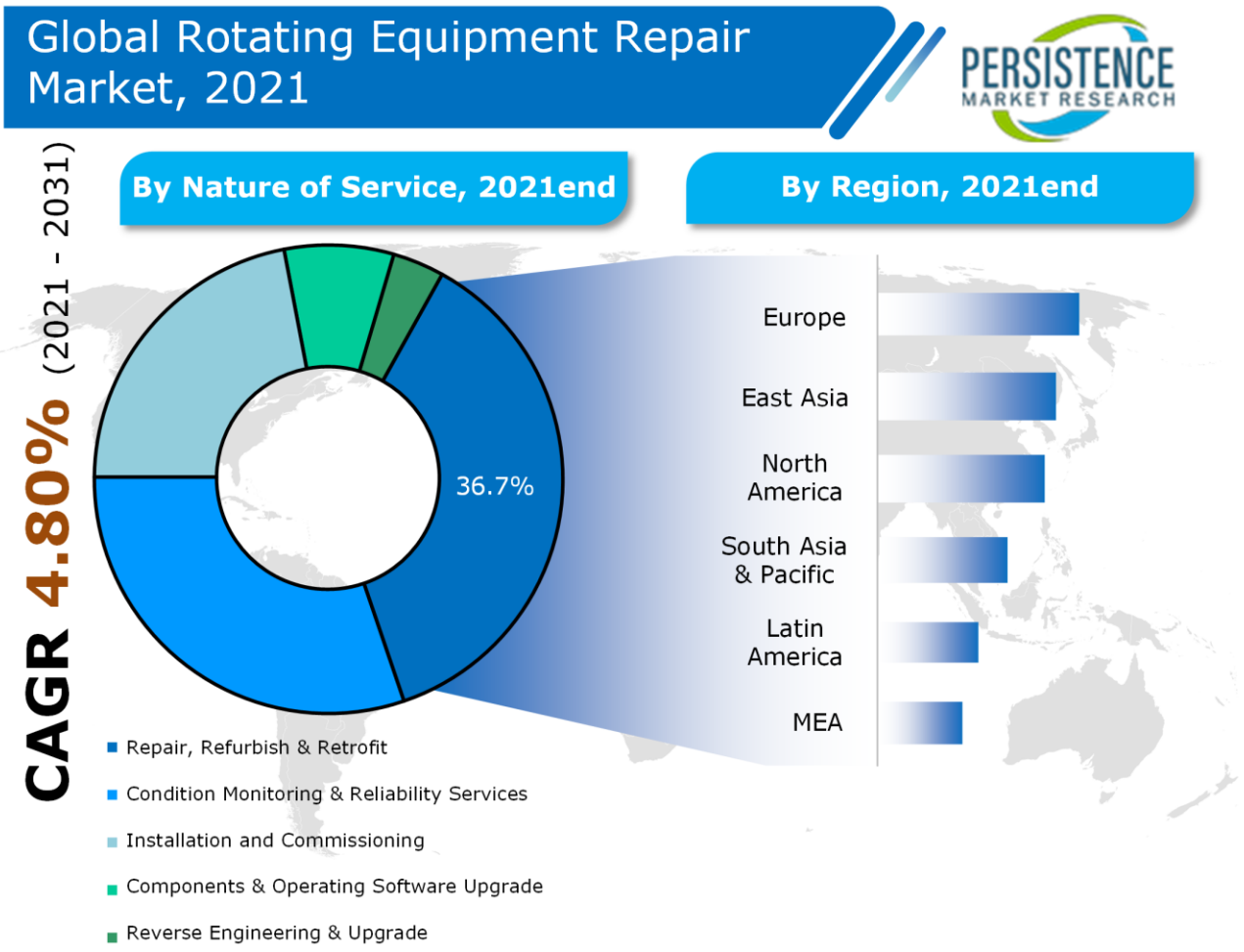

(Source: [14])

Figure 1.2 Global rotating equipment repair market.

The general procedure for repairing parts is to [20]: (i) machine the damaged or worn surface of the part; (ii) add filler material on the machined surface to build up the spare size; and (iii) post process including machining to original dimension

and heat treatment. Among the three steps, step ii is the key step to ensure the sustainability of repaired parts, hence the focus of this thesis.

1.1.2 Additive processes used in repair

The possible processes discussed in this section relate to material addition within a local spot.

Friction stir deposition is the additive process where filler rod is pressed on the substrate surface, rotated at high speed, melted by the friction heat, and eventually deposited on to the substrate [21] (see Figure 1.3a). The advantage is that no heat source is applied and there is no effect from the heat-affected zone. The drawback is that the boundary of bonding is not strictly controlled and there must be leftover material from the track boundary and filler rod.

Welding is a fabrication or sculptural process that joins materials, usually metals or thermoplastics, using a high-intensity heat source to melt the parts together allowing them to cool down, and causing fusion. An example of welding repair is to remove the damaged shell plate on the pressure vessel and replace it with an insert patch [22] (see Figure 1.3b). The advantage is the opportunity to reinforce the strength of the broken section by choosing a proper substitution. There is a limitation sometimes because the substitution that fits the cut-off section is not easy to find especially when it is in a complex shape, i.e. a tooth on a gear.

Powder bed fusion is a process where a heat source (e.g., laser or thermal print head) is used to consolidate material in a powder bed layer by layer, to form three-dimensional objects. One example is the repair of a gas turbine burner tip

inside a modified facility [23] (see Figure 1.3c). The advantage is the complexity and accuracy of the repaired component because of the small powder size and the small-sized focus of the heat source. The drawback is the relatively restricted application in the repair industry, because it can only be done on flat surface and in the specifically modified chamber.

Thermal spray is a coating process, including cold spray, plasma spray and high velocity oxygen fuel spray, in which melted (or heated) materials are sprayed onto a surface. One example is the repair case of a helicopter mast support via cold spray [24] (see Figure 1.3d). The advantage is the low heat input. The drawback is the relatively larger pore sizes and coarser microstructural texture than some competing technologies.

Direct energy deposition (DED) combines the material and energy delivery in one place at the same time to fuse and deposit one material over another one and generate a skin or layer. One example of direct energy deposition repair with laser heat source is the cladding on the top surface of a rail track [25] (see Figure 1.3e). Compared with thermal spray, the higher material deposition rate makes DED an ideal method for filling a hollow space or forming a measurable pad. DED is considered to be the most commonly used method in the repair process due to the flexibility in terms of additive material category and energy source type. The combination of material delivery rate and scanning speed is a convenient way to control the freeform geometry. Moreover, the heat source can be laser, arc, electron, plasma, or flammable gas. As a heat source, laser is attracting attention in the industry, and will be explained in the next section.

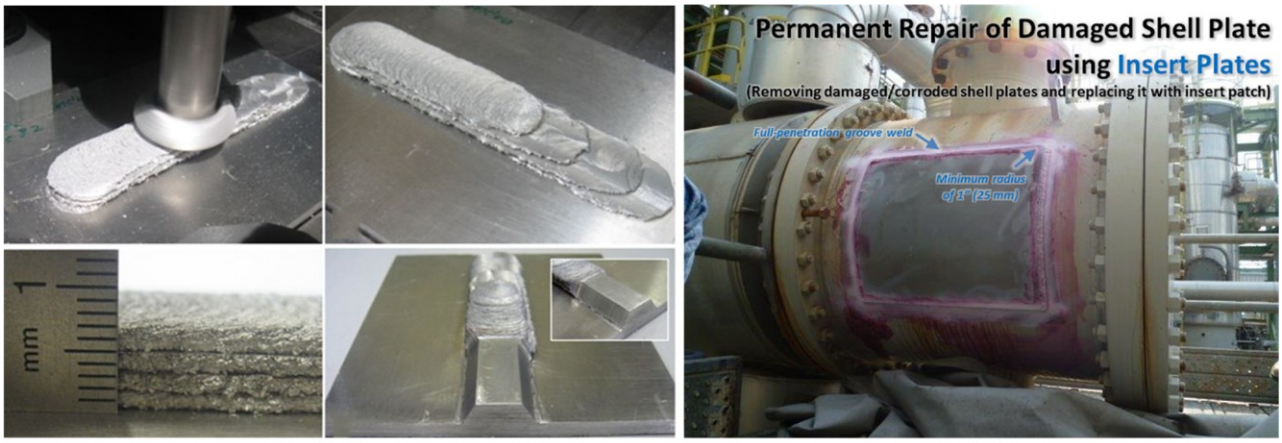

(a) (b)

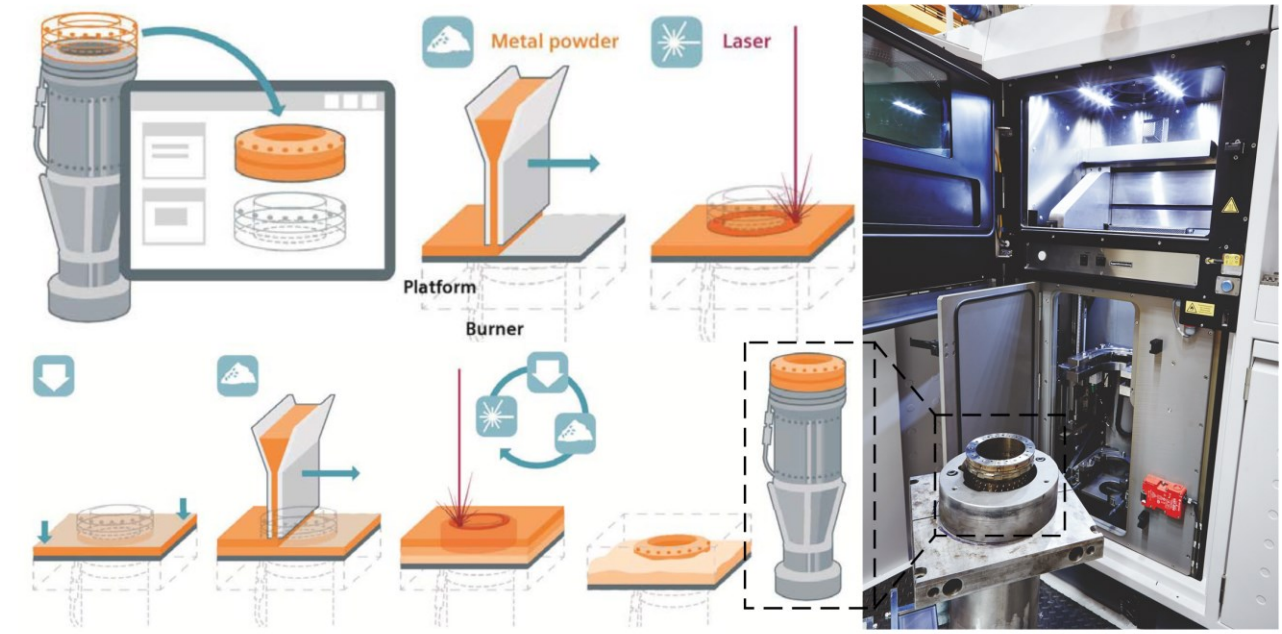

(c)

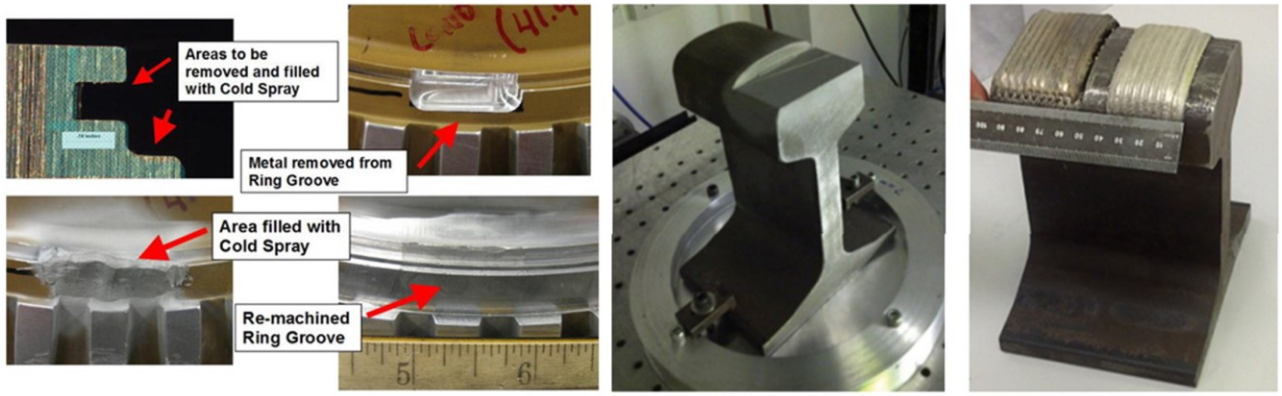

(d) (e)

(Source: a [21], b [22], c [23], d [24], e [25])

Figure 1.3 Repair examples with different processes: (a) build-up by friction stir deposition, (b) the example of welding repair by removing the damaged shell

plate and replacing it with insert patch, (c) powder bed fusion repair process for replacing top burner tip, (d) repair of helicopter aluminium mast support by cold spray, and (e) direct energy deposition repair with laser heat source on the top surface of rail track.

1.1.3 Laser cladding as a promising technology

Direct Laser Deposition (DLD), or Laser Cladding, is a process of melting metal material in a powder or wire feedstock using a laser, and consolidating it onto a substrate part. Laser, one form of energy source, is newly developed for material processing in the latest decade [26]. Its application in cladding repair is only in recent years, because its power is increasing, so it can melt metal. Today, the development of laser cladding continues and has diversified to meet three purposes: (i) equipment, (ii) materials and (iii) services.

The basic set of equipment for laser cladding includes: laser generator, manipulator, and material feeder. Auxiliary equipment includes: processing housing, power, electric control, console, cooling, and ventilation. According to the report on the global laser cladding equipment market by 2019, the market size has the potential to grow by USD 18.19 million over period from 2020 to 2024 [27].

The most widely used material in laser cladding includes: cobalt-, nickel-, and iron-based alloys, and carbides. According to the report on the global laser cladding material market until 2019 (USD 110 million), the global market size will reach USD 150 million by 2024 [28].

Based on application, the market is very vast including Mould and Die, Aircraft and Aerospace, Automotive, Energy, Construction and Agriculture. The laser cladding service market is growing at a moderate pace with substantial growth rates over the last few years (before 2019) and it is estimated that the market will grow significantly in the forecasted period i.e., 2020 to 2027 [29].

Advantages of applying laser cladding include [30]: (i) adaptability to a variety of materials, including metals, ceramics and even polymers; (ii) flexibility on freeform shapes generations; (iii) small size fusion area and limited heat affected zone; (iv) and high cooling rate to obtain superior microstructure.

1.1.4 Differences between powder-fed and wire-fed laser cladding

Powder was the early form of material stock used in laser cladding. Special precautions must be taken on the powder, powder shape, particle size distribution, surface condition, and humidity [31], to avoid any influences on cladding quality. Most importantly, it is generally considered that it is not environmentally friendly to supply powder through carrier gas, because a large amount of powder is ejected from the cladding area, resulting in system and environmental pollution.

In comparison with a powder-fed system, the wire-fed laser cladding (WLC) system possesses the unique advantages including 100% material utilization, high deposition efficiency, a strong metallurgical bond at the clad-substrate interface, minimal porosity, and inexpensive filler wires [32]. These advantages make WLC the usually first choice of laser cladding service suppliers since the technology has emerged.

1.2 Problem definition

The traditional laser cladding operation is challenged because the inevitable human factors will affect the cladding quality, even the operators with necessary training will be affected [33]. With the improvement of laser energy level, it is impossible to hold the laser head by hand. The operation of the laser head must depend on the automation system in a closed processing environment. In addition, the integration of laser cladding and automation systems meets the industry's demand for efficiency. This becomes an important step in the design of the control system, which requires mathematical modelling of the cladding process, which is the theme of this thesis. The complexity of the laser cladding process modelling lies in the following main challenges:

- The mathematical description of physics phenomena in laser cladding. The laser-metal interaction and heat transfer are the root causes of temperature changes. This temperature change leads to the geometric profile change of the deposition bulge and melt pool (see details in Chapter 4).
- The geometrical overlap interactions after repeated phases transformations. A common problem in any additive manufacturing is that components are formed by stacking tracks together. In this process, the material undergoes repeated phase transformations, including melting, solidification, and remelting. The merge of the original material and the new material forms a geometric overlapping profile (see details in Chapter 5).
- The multiple physical fields (including gravity and thermal fields) leading to the retention profiles of tracks on non-horizontal surface. The cladding on non-

horizontal surface is challenging, i.e. the cladding on a large-sized car body mould. The external force on the track at different tilt angles will lead to bulge and molten pool deformation (see details in Chapter 6).

1.3 Aims and objectives

For repair, both the bulge and melt pool are the predicted elements and the full shape profile is necessary in modelling process because there are multiple tracks overlapping to form the layer. The model proposed in this thesis is anticipated to adapt to the actual cladding conditions, with online controllability for industrial repair service. To achieve these aims, several objectives are listed as follows:

- Identify the knowledge gap that exists in the current area of WLC from the literature;
- Develop a research methodology that adapts to the challenges of WLC modelling;
- Fill the knowledge gap to some extent by using the results, discussions and conclusions that obtained in this study;
- Provide potential solutions for the applications of WLC.

The scope of this research is explained in detail as follows.

1.4 Scope of the study

This thesis focusses on the basic understanding of the process. The aim of this research is to investigate the precise energy and geometry prediction of laser

cladding, followed by exploring application cases on automation system (see Figure 1.4). The outline of each chapter is as follows:

Chapter 1, the current chapter, serves as a general introduction to the background of the repair industry. In particular this aims at briefly understanding the role of laser cladding among other possible repair methods, and its trends, possibilities, and developments. WLC is considered to be the more advanced technology and thus the main subject of this thesis. Several challenges in mathematical modelling in this process are identified. The mathematical model is aimed to develop with the application on the automation system.

Chapter 2 serves as a detailed literature review related to the field of study including the WLC (i) physics, (ii) outputs, and (iii) modelling. Research gaps are proposed in the end.

Chapter 3 introduces the methodology including (i) materials selection, (ii) equipment and techniques used throughout the research to conduct experiments, and (iii) modelling and analysis that are necessary to achieve the research aims.

Chapter 4 introduces the mathematical full single-track deposition shape modelling, including the bulge (the part above the surface) and the melt pool (the part below the surface). The fundamentals of laser cladding are transferred to the mathematical model which takes in the variable processing parameters (e.g., laser power, scanning speed and wire feed rate) and provides the related output

results (e.g., temperature field, bulge profile and melt pool profile). This provides the basis for the following Chapter 5 and Chapter 6.

Chapter 5 introduces the mathematical overlap deposition shape modelling, including (i) the two bulges overlap based on the experimental observations of remelting, (ii) the cladding layer on the horizontal flat surface with the overlap ratio (the tightness of tracks), and (iii) the second cladding layer on the as-clad layer with the stagger ratio (the location of tracks). Besides of the geometrical profiles, the metallurgy problems that induce error between model and experiment measurement are also verified. This provides the necessary geometrical and metallurgical analysis basis before introducing the next chapter.

Chapter 6 introduces the mathematical climbing deposition shape modelling, including the retention of one bulge on the inclined surface and climbing deposition on the inclined surface. The gravity that induces the deformations of bulge and melt pool is considered and put into the model. The model is qualified to do cladding work on the inclined surface with the controlled uniform layer thickness.

Chapter 7 serves as a summary and discussion of the research work, particularly outlining the outcomes of the thesis and the benefits for cutting edge industrial applications. It also includes recommendations for future work and follow-up studies.

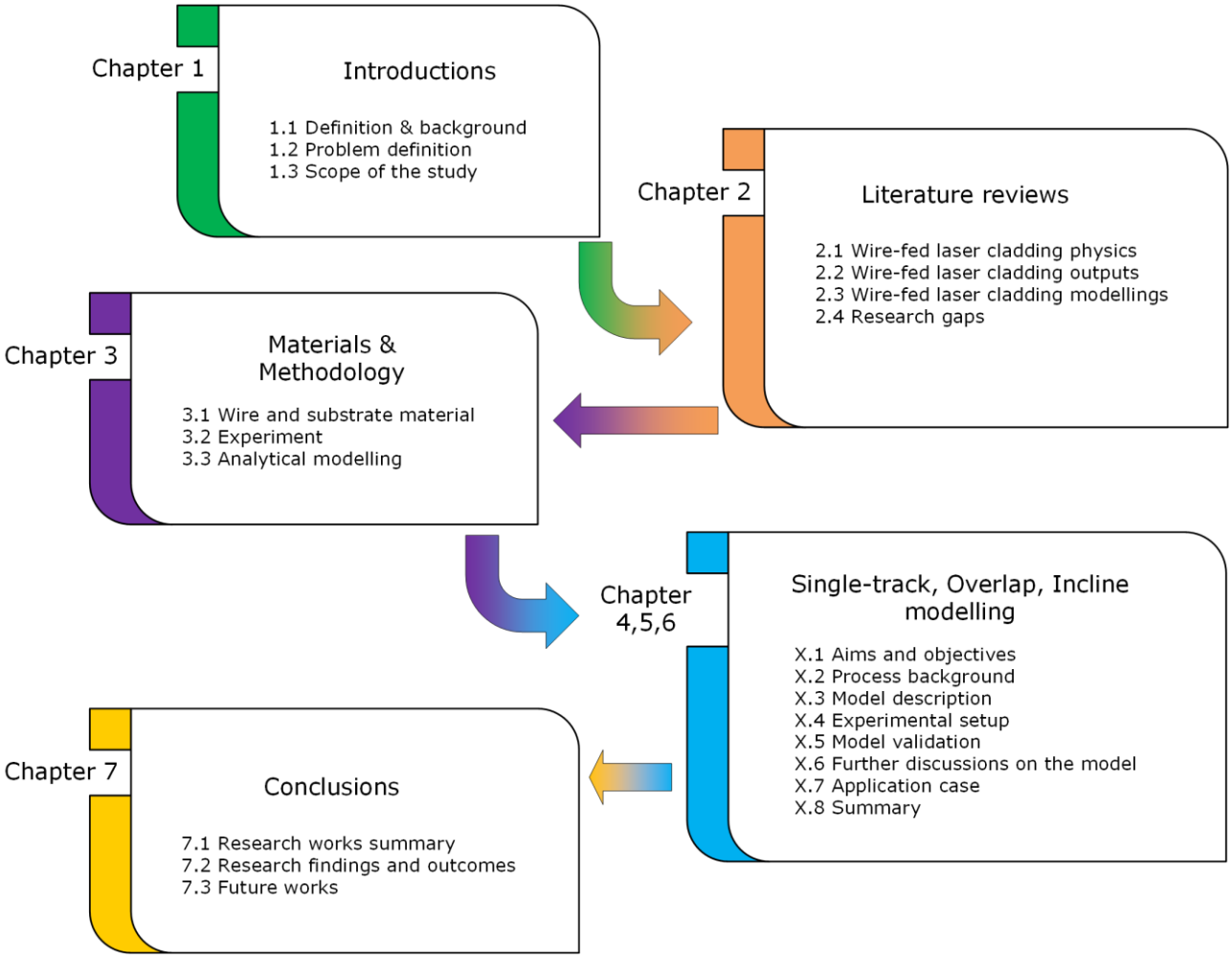

Figure 1.4 Scope of the study.

Chapter 2 Literature review

The basic process of WLC can be described with hardware compositions in the system including laser source, manipulator/robot for laser head, and wire feeding module (see Figure 2.1). The existing research of WLC falls on the categories shown in Figure 2.1, including the process physics (see Figure 2.1a), the outputs (see Figure 2.1b), and the modelling (see Figure 2.1c). Therefore, the following overview is carried out from the order of the above three aspects.

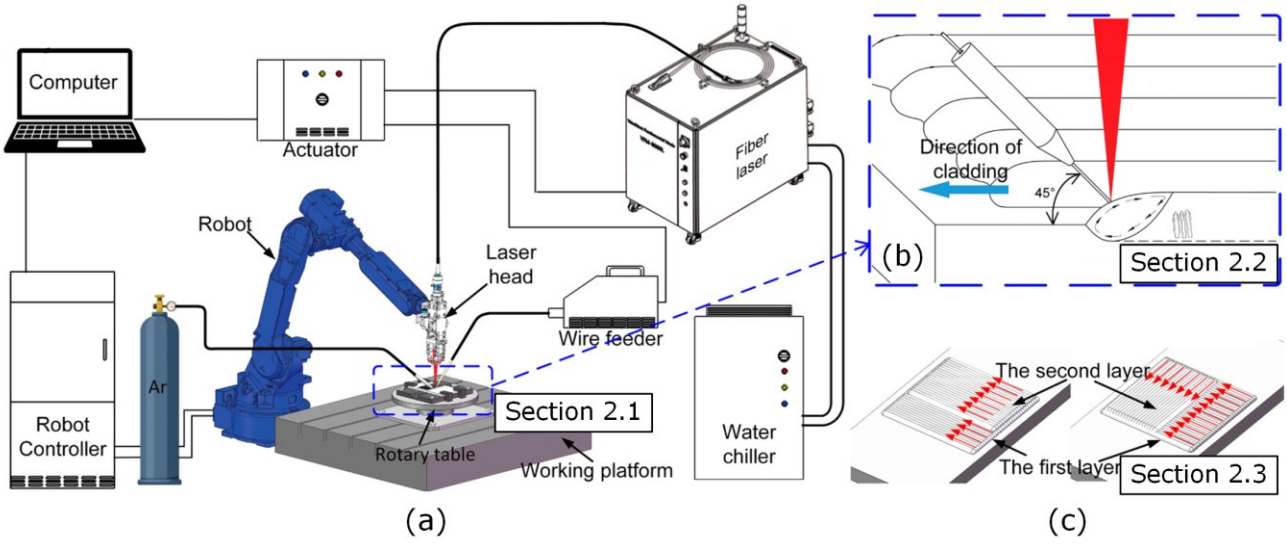

(Source: [34])

Figure 2.1 Schematic of wire-fed laser cladding system: (a) physics, (b) outputs, and (c) modelling.

2.1 Wire-fed laser cladding physics

WLC physics are the principles that are originated from experimental observations and inductions of the process. Understanding the physics of the process is the basis of any developments. Topics include the laser types for laser cladding, thermal behaviours, and temperature field in deposition zone.

2.1.1 Laser types for laser cladding

Laser types for laser cladding can be categorised in terms of energy gained methods and beam shapes.

The laser types for laser cladding based on energy gained method include: CO_2 laser, Nd:YAG crystal laser, diode laser, and fibre laser. The CO_2 laser produced a beam of infrared light with the principal wavelength bands centring on 9.4 and 10.6 μm which was the main absorbing range of non-metalic materials [35]. Nd:YAG lasers typically emitted light with a wavelength of 1064 nm, which showed better absorption for metals [36]. However, heat dissipation was always a problem for high power output although gain medium can be developed to large-aperture face-pumped thin-disk cooled by micro-channel cooler [37]. The choice of the semiconductor material of a diode laser determined the wavelength of the emitted beam, ranging from 0.2 to 1.6 μm [38]. However, a single diode laser had a limited output power of tens of watts due to the narrow luminous cavity area [39]. The energy gained from an optical fibre doped with rare-earth elements (i.e ytterbium [40]), with wavelength of 1.07 μm, can be beneficial for absorption by metal materials. A fibre laser with high brightness in particular had long focal length, small spot size, high beam quality and stable laser beam execution [41]. With the invention of double clad fiber and the continuous improvement of the performance of fiber devices, the output power of fiber laser had increased rapidly in recent years, including single-mode fiber laser power of 20 kW and multi-mode fiber laser power of 100 kW [42]. As the traditional

problems of fibre laser, Photodarkening-induced Loss [43], Stimulated Raman Scattering [44], and Transverse Mode Instability [45] were investigated, the laser output power can exceed the existing level.

Lasers are transformed into beam shapes based on application needs. To enhance the energy efficiency at the focus, the traditional Gaussian laser beam was transformed by a lens converter [46] to a uniform square beam [47] and a super-Gaussian laser beam which had a flat-top intensity distribution at the focus and evolved into traditional Gaussian intensity distribution as far away as the focus [48] (see Figure 2.2a). These types of laser beams can only be applied in laser cladding with wire fed from the side [49]. To break the cladding direction restriction of side fed wire, the traditional laser beam was also transformed by a pair of prisms to the hollow laser beam where wire was delivered inside the hollow space [50] (see Figure 2.2b). The beam can also be divided into three beams and targeted to the internal wire (see Figure 2.2c) [51]. The laser beams from a diode laser are in rectangular shapes of $2mm \times 7mm$ [52] and $2.5mm \times 5mm$ [53] due to the same energy gain method inside the diode. Six 200W laser diodes were positioned on a circle around the feeding lance which created a laser spot with an approximate diameter of 0.9 mm [54, 55]. Laser beam can also be transferred by a set of mirrors with holographic optical elements into any shape beneficial for melting wire and obtaining strong bonding with substrate [56].

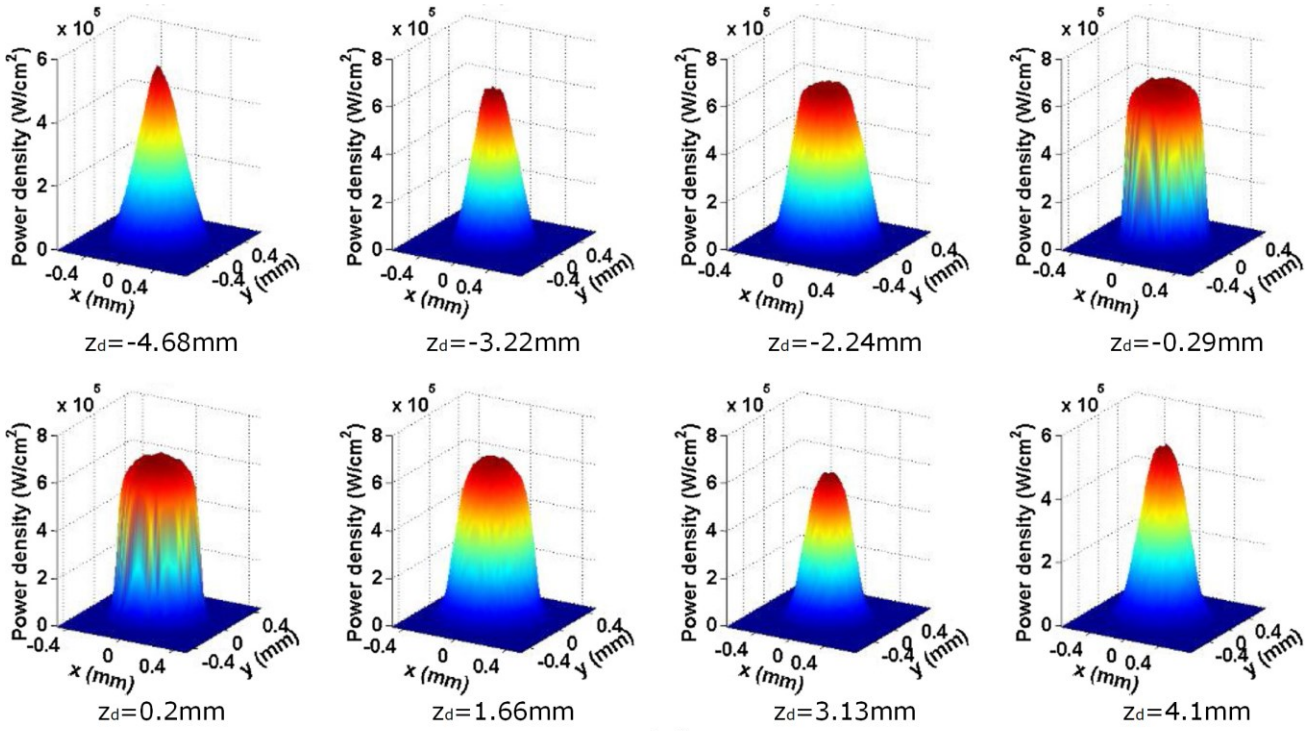

(a)

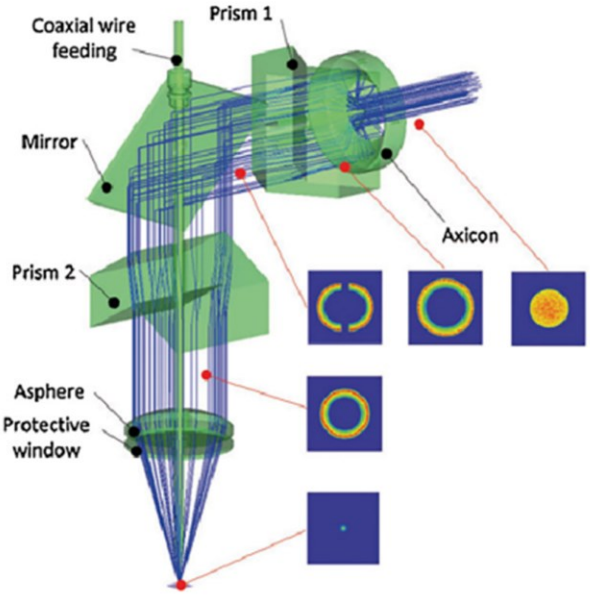

(b)

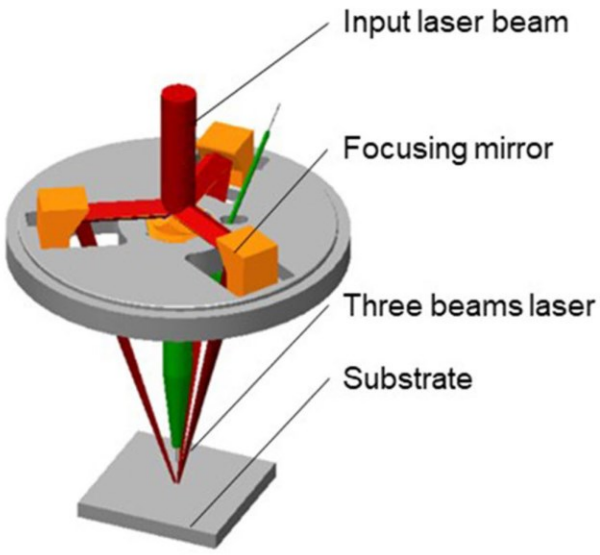

(c)

(Source: a [48], b [50], and c [51])

Figure 2.2 Three-dimensional Laser beam profiles diagrams: (a) the power density at cross-sections, (b) hollow beam profile, and (c) three beams targeted to the internal wire.

2.1.2 Thermal behaviours in deposition zone

Thermal behaviours in deposition zone include the melting of wire and melting of substrate material.

The laser heating is based on the same principle: the radiation of the laser, as a heat source, accelerates the vibrations of the atoms inside the radiated material, which leads to elevated temperatures. The distribution of laser radiation on wire and substrate surface leading to the thermal footprint were captured [57-59] (see Figure 2.3a). The delivery rate of the wire resulted in different process states, due to the balance with the energy input [57] (see Figure 2.3b). Single beads were deposited with a 316L wire on a similar substrate under optimized conditions using a 4 kW continuous wave fibre laser, and smooth dripping deposition appearance were observed [60]. The wire dripping, smooth wire transfer and wire stubbing of Inconel 625 single track deposition under different cladding conditions were studied using a 2 kW ytterbium doped fibre laser under different process parameters [61]. Processing characteristics, microstructural evolution and mechanical properties were also clarified [62] to fabricate Ni/WC composite. The 3.5 kW Nd: YAG laser and Ti- 6Al- 4V wire were used to produce single track, in which the process parameters such as laser power, scanning speed and wire feed rate were different [63]. Melted wire spatter was avoided by controlling the wire tip temperature (i.e. matching the wire feed speed and preheating current under certain laser power) in hot 5052 aluminum wire cladding [64].

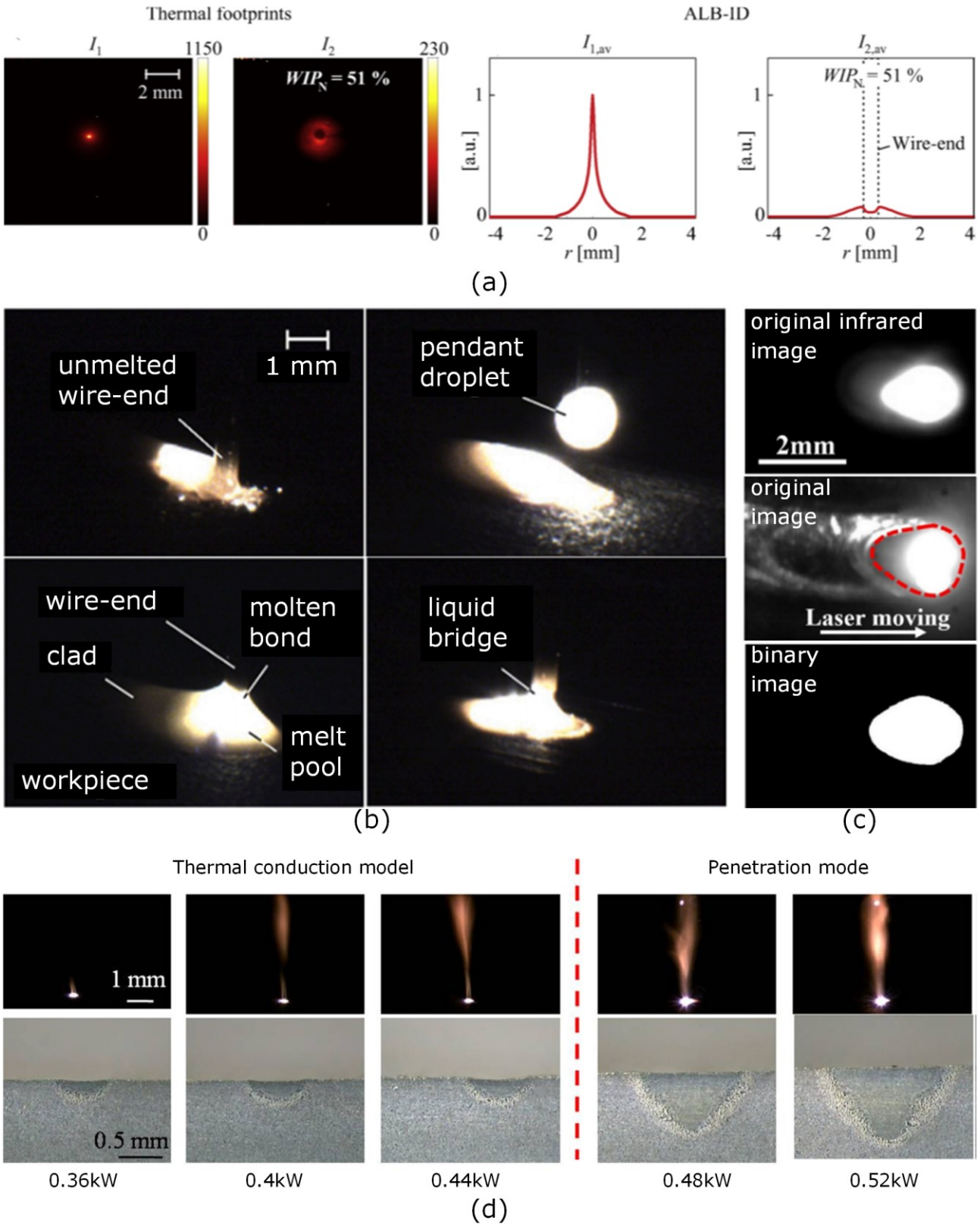

(Source: a and b [57], c [65], and d [66])

Figure 2.3 Thermal behaviours in deposition zone: (a) radiated footprint with wire intervene, (b) wire melting phenomena, (c) melt pool profile, and (d) melt pool depths at different laser powers.

The melt area profile was observed by the infrared and binary images [65] (see Figure 2.3c). Based on the laser power scale, the heating was divided into conduction mode and penetration mode where there was an obvious penetration depth increase from conduction to penetration [66] (see Figure 2.3d). The transition from conduction to penetration was characterised as the Fresnel absorptivity law which described the absorptivity change as melt pool depth increased [67]. The process development for wire-based laser metal deposition of a 5087 was conducted, with the finding of possibility to control the dilution within optimized parameter ranges [68].

2.1.3 Temperature field in deposition zone

Temperature field in deposition zone is very complex because of three dimensional heat transfer inside and around cladded workpiece.

After the wire was melted and deposited on the substrate, the thermal radiation was measured with a pyrometer (quantified as emissivity) that played the key role of bringing down the temperature in the deposition zone [69] (see Figure 2.4a). The development of temperature gradients, resulting cooling rates and thermal cycles for different laser beam irradiances was evaluated [70]. The typical temperature distribution around the moving laser rapidly reduced from the centre outwards [71] (see Figure 2.4b). In the time domain, the temperature fluctuated when the heat source was close to the selected spot on the workpiece [72] (see Figure 2.4c). Scanning strategies (regarding without cooling stage between layers and interlayer cooling through air forced convection) brought different results of base temperature after several layers were deposited [73].

Substrate induction heating, hot wire processes, and low power pulsed laser were combined to reduce temperature gradient and heat accumulation [74].

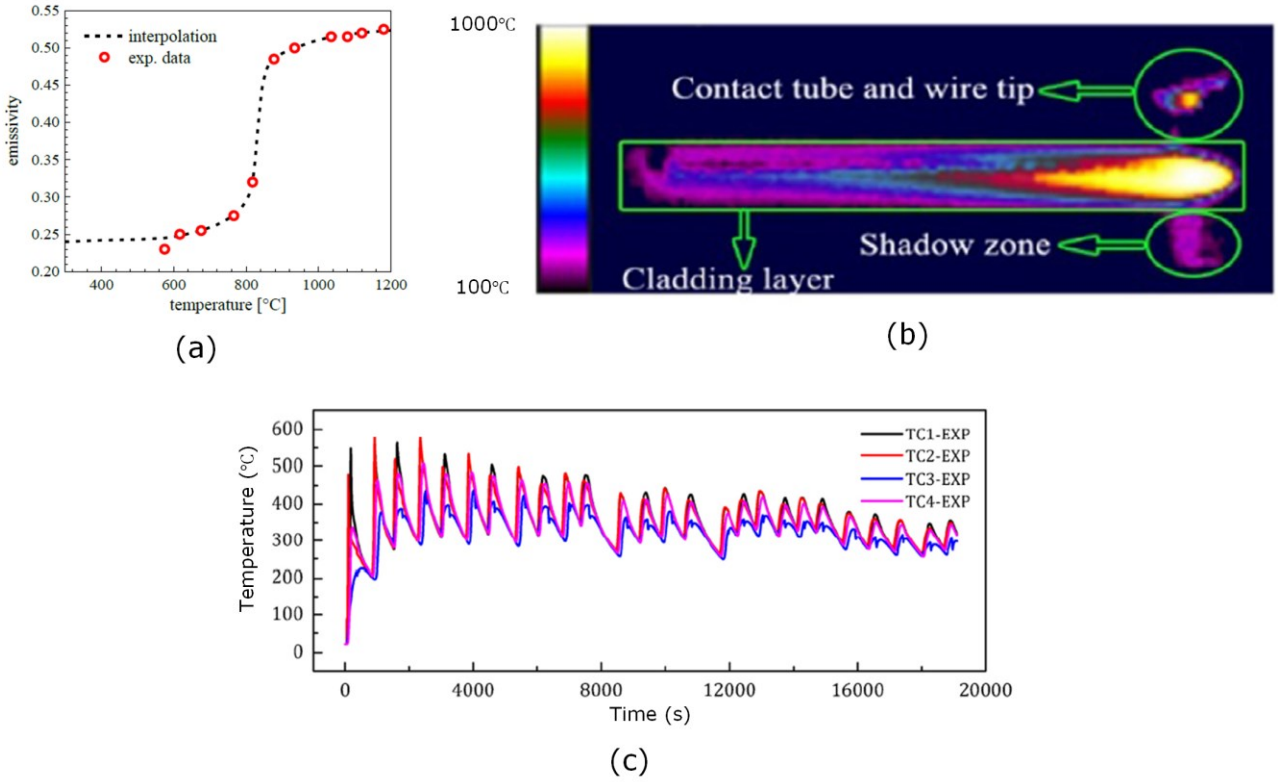

(Source: a [69], b [71], and c [72])

Figure 2.4 Temperature detection results: (a) thermal radiation as a key role of bringing down temperature, (b) thermal infrared image of cladding layer, and (c) temperature variation curves measured by thermocouples.

2.2 Wire-fed laser cladding outputs

Qualified WLC outputs include an intact clad geometry, with refined microstructures, and enough mechanical properties for service.

2.2.1 Clad geometry in deposition zone

As an additive process, clad geometry (shape, size) is the most important output in the WLC.

The different bulge profiles were experimentally observed based on energy density per wire deposition volume per unit track length [61] (see Figure 2.5a). The volume change, e.g., the shrinkage during solidification due to the new chemical element combination, is also one of the concerning effects on deposition shape [75]. For multiple track cladding, an operating window between the overlap ratio was determined based on experimental investigation to avoid lack of bonding between tracks and substrate surface, and protrusions between two tracks [76] (see Figure 2.5b). An experimental investigation was undertaken to characterize the differences in temperature and deformation histories using powder and wire [77]. In situ measurements showed that the selection of a powder feedstock resulted in higher temperatures and greater deformation.

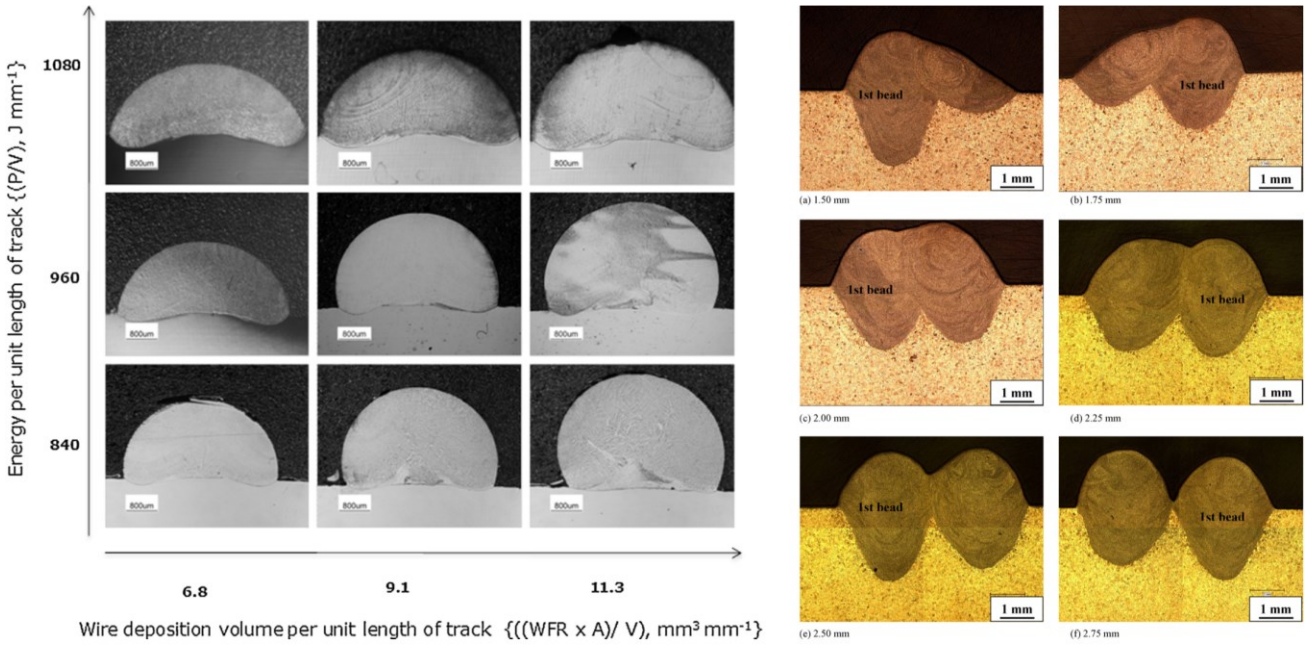

(a) (b)

(Source: a [61], b [76])

Figure 2.5 Clad geometry in WLC: (a) single track profile under the effect of laser power, wire feed rate, and scanning speed and (b) overlap profile under the effect of overlap ratio.

2.2.2 Microstructure in deposition zone

Microstructure is the essential topic determining the clad sustainability. The microstructures of (i) similar and (ii) dissimilar materials WLC are reviewed as follows.

The typical microstructures within the fusion zone of 316L wire laser cladding are the austenite matrix with eutectic, skeletal, or lathy ferrite according to the Fe-Cr-Ni contents and solidification temperature, in cellular or columnar forms according to the solidification rate and direction [60] (see Figure 2.6a and b). Within the same Fe-Cr-Ni system, the underwater 304 WLC showed lathy ferrite attributed to the higher cooling rate within the overlap region of tracks [78]. The typical microstructures within the fusion zone of Inconel 718 wire laser cladding are the austenite matrix with secondary and intermetallic phases according to the Ni-Nb-C contents and solidification temperature [79] (see Figure 2.6c and d). The typical microstructures within the fusion zone of Ti-6Al-4V wire laser cladding are the combinations (in size and arrangement) of hexagonal close packed phase α and body-centred cubic phase β according to Ti-Al contents and cooling rate, in laminar or equiaxed forms according to heat treatments [63] (see Figure 2.6e and f). Martensite was also observed indicating the cooling rate is fast in laser cladding [80]. Grains can also be refined by introducing the ultrasonic micro-forging treatment based on plastic deformation and ultrasonic vibration [81].

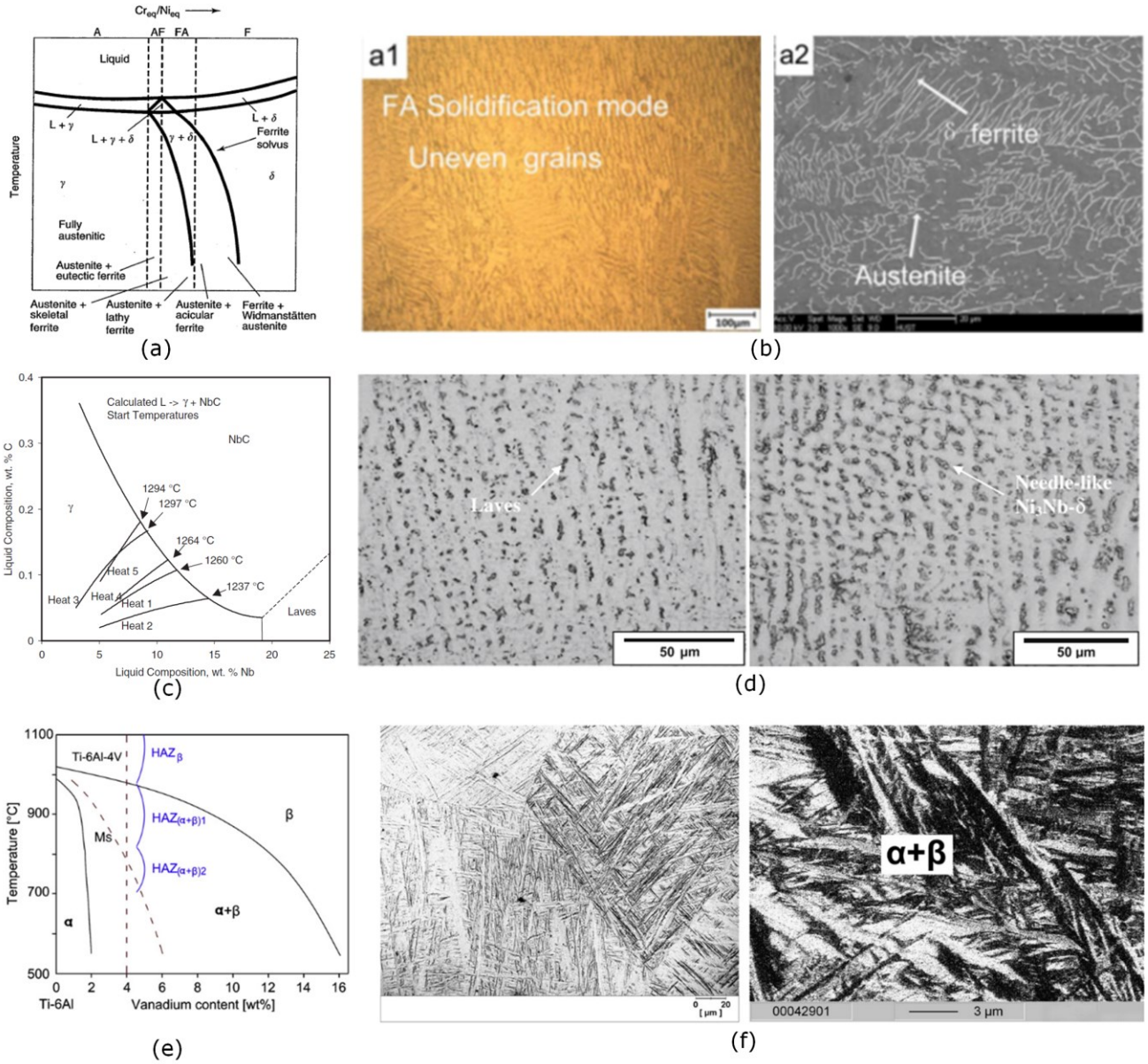

(Source: a [82], b [60], c [83], d [79], e and f [63])

Figure 2.6 Microstructures in different parts of wire-fed laser cladding layers: (a) phase diagram of 316L, (b) microstructures in 316L cladding case, (c) phase diagram of Inconel 718, (d) microstructures in Inconel 718 cladding case, (e) phase diagram of Ti-6Al-4V, and (f) microstructures in Ti-6Al-4V cladding case.

Stainless steel ER410NiMo wire was preheated and cladded on the surface of martensite precipitation hardening stainless steel FV520B by fiber laser, with the coarse lath martensite in the quenched area and the fine tempered martensite in the tempered area [84]. Inconel 625 wire was deposited on the surface of 316L

substrate by laser cladding where precipitated ferrite and laves were observed within the bonding area [85]. The microstructure morphology of Inconel 625 wire laser cladding on 316L substrate were compared between in parallel topology and in perpendicular topology, showing the effect of the cooling rate and heat dissipation of the melt pool on the size, shape and orientation of grains in the cladded tracks [34]. The NiTi wire cladded on 316 substrate with laser was capable of producing a much less defective cladding with homogeneous microstructure [86]. The refinement of the grain size was observed from each layer, top to bottom, of a thin-wall deposition of 316LSi on 304L due to the slightly higher content of silicon that improves the wetting behaviour of the metal during cladding [65]. The Inconel 625 wire was laser cladded on 316L substrate with reinforced TiC particles, producing the homogeneous distributed TiC particles, along with refined microstructures [87]. Inconel 625 wire was laser cladded on 316L with reinforced tungsten carbide (WC) and carbon nanotubes (CNTs), showing the main secondary compound of WC dissolution was W_2C, which was mainly distributed at grain boundaries [88].

2.2.3 Mechanical property in deposition zone

Mechanical properties of cladded structures are even more important than the clad geometry and microstructure. This is because mechanical properties determine the life span of service. Situations are divided in (i) similar and (ii) dissimilar materials cladding.

As for similar materials cladding, the added and parent materials are in the same material class. The heat treatment, that materials have experienced, led to the

characteristic mechanical properties, i.e. hardness, tensile strength, ductility, or corrosion resistance between clad and substrate (see Figure 2.7). Decreased microhardness was detected on the deposited layer of similar tool steel H13 wire and substrate [72]. Decreased corrosion resistance was resulted on the similar 304 wire laser cladding under water due to the high cooling rate [78]. In the cladding of 316L similar material, the harness was reduced, the tensile strength of the layered sample along the deposition direction was 89.5% of the substrate, and the value perpendicular to the deposition direction was greater than the tensile strength of the substrate [60]. Inconel 718 wire was cladded on the Inconel 718 substrate, where tensile strengths reach the standard of AMS 5596K and 5663M while ductility at room temperature was slightly lower than the standard [89]. The increase of microhardness was measured in the fusion zone in the Ti-6Al-4V alloy, and attributed to the non-diffusional martensitic transformation of the original α-β phases upon rapid cooling [90]. Hardness values were tested in the Ti-6Al-4V alloy deposits with wire-fed high power diode laser cladding, which tended to increase from the deposit, via the re-melted zone till to the heat affected zone, and then decrease again when the measurements were taken in the unaffected base material [52]. The static tensile and high cycle fatigue of as-clad Ti-6Al-4V alloy were compared after stress release and anneal treatments for space or aerospace applications [91].The aluminum 5052 wire was cladded by laser on the thin-wall aluminum 5052 tube with good metallurgical bonding, where average microhardness value gradually decreased as the laser power and shielding gas flow rate increased [92].

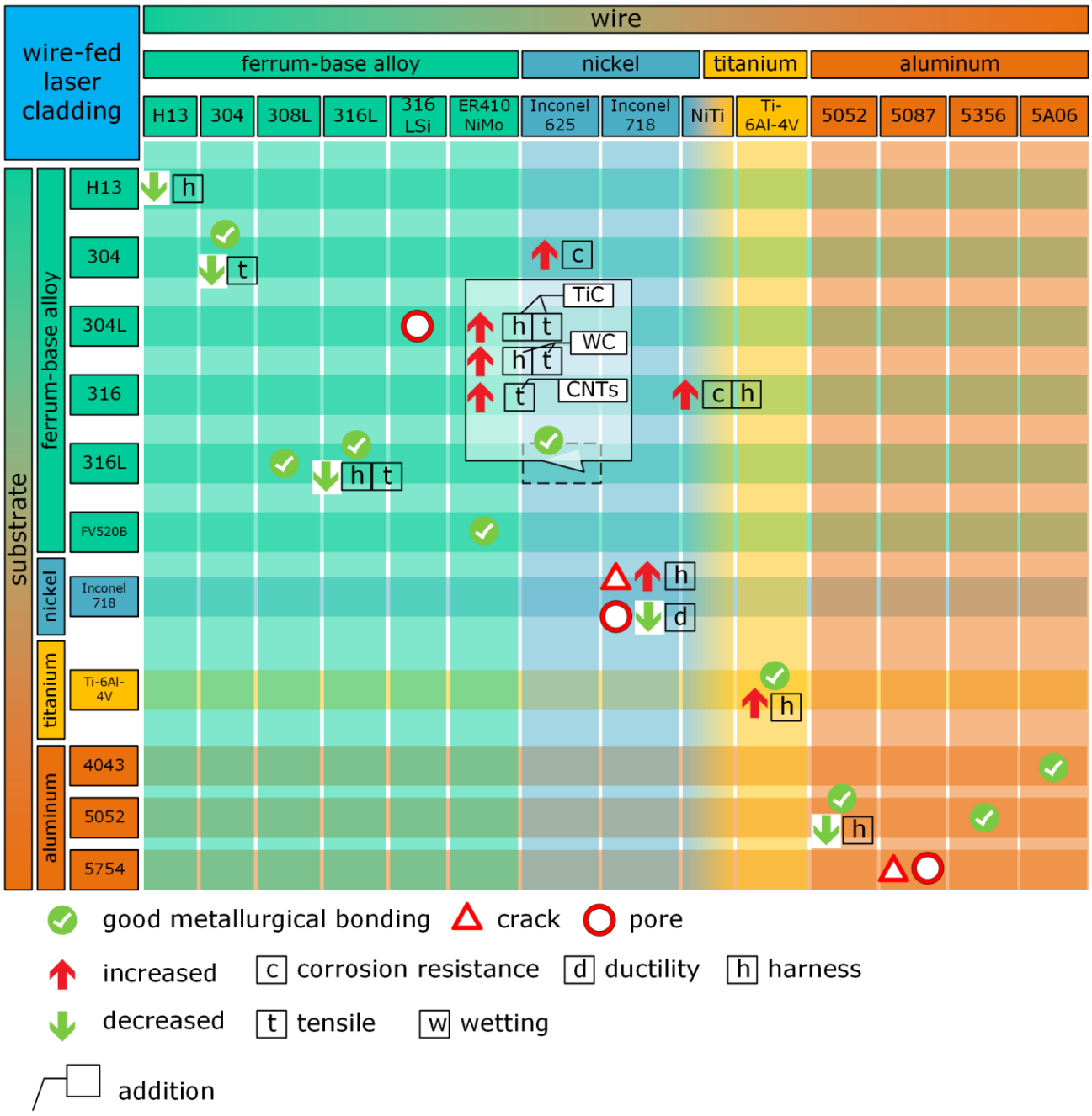

(Source: original)

Figure 2.7 Laser cladding ability of wire and substrate materials.

As for dissimilar materials cladding, the added and parent materials are mixed into new element compositions. The chemical stability of mixed materials and coexistence of mixed and parent materials are presented with possible defects, i.e., cracks, pores, or looseness, which eventually contributes to the mechanical

property (see Figure 2.7). The 308L wire was cladded on 316L substrate with good metallurgical bonding [93]. The ER410NiMo wire was cladded on FV520B substrate with good metallurgical bonding [84]. The electrochemical corrosion performance of Inconel 625 wire cladded layer on 304 substrate was investigated, showing corrosion thickness of only 0.1mm on the surface of 4mm thick cladded layer [94]. The Inconel 625 wire was cladded on 316L substrate with good metallurgical bonding [34, 85]. As the softening effect was normal in Inconel 625 wire deposits on 316L substrate, reinforced elements TiC particles [87] and WC particles [88] which improved the hardness were added during the cladding process. The 5087 aluminium alloy wire was cladded on the 5754 substrate to obtain the geometric shape, with the cracks and pores along the grain boundaries [68]. The 5356 wire was cladded on the 5052 under water with good metallurgical bonding [95]. The 5A06 wire was cladded by laser on the 4043 with good metallurgical bonding [96].

2.3 Wire-fed laser cladding modelling

The original explorations started from experiments as reviewed in Section 2.1 and 2.2. However, the experiments were limited by the methods used for observation, and some phenomena cannot be observed. Simulations were conducted based on the physical principles and contributed to the understanding of the process. Then theoretical modelling methods were proposed for the purpose of profile predictions.

2.3.1 Numerical modelling of cladding process

The difficulties in experimentally observing the details of the WLC process, such as the mass and heat transfer, especially at high temperature, drove the development of numerical studies. This was thanks to superior visualisation capability and rich process data.

Based on the thermal Finite Element (FE) simulation, the wire transfer behaviour was classified into three types (fusing, continuous and wire hit transfer) according to the melting position of the fed wire, determined by both the laser radiation and the melt pool conduction [97]. Based on a more comprehensive FE simulation (considering free surface tracking, material continuum, laser-material interactions, melting and solidification of the material, and mass addition) [98] (see Figure 2.8a and b), the Marangoni flow effect was induced by a non-uniform temperature distribution by the local laser beam heat source [99], where the melting material were transported from the centre to the periphery of the melt pool, resulting in a wider cladding formation. The mass transfer of chemical element, sulfur, also had effect on Marangoni flow [100]. Based on the Ginzburg Landau theory, a phase field model without tracking the position of the phase interface was established to solve: (i) conduction solid-liquid phase transition, and (ii) convection melting [101]. Based on thermo-mechanical FE simulations, the three-dimensional transient temperature field in the melt pool was obtained according to which the residual stress and distortion can be significantly minimised by reducing the layer thickness [102]. A computational framework for

thermal multi-phase flows was developed to address large density ratio between gas and condensed phases based on the FE method [103]. The material spattering under the intensive heat source was simulated which caused the inevitable material loss [104]. Pore formation mechanisms was studied [105]. Multiphysics approaches were also investigated by numerical simulation. A numerical model was coupled with electromagnetic and temperature fields in laser assisted UHF induction deposition to simulate (i) current density and temperature field [106], (ii) flow velocity field and material supply [107] and (iii) the application on high melting point metal with drop-on-demand deposition [108]. A computational fluid dynamic (CFD) transient model was developed for the understanding of gravity and pressure effects in WLC [109].

For multiple track cladding, numerical simulation of hot wire laser cladding was conducted to obtain the additive geometry with numerous analysis features including temperature, stress and strain fields, and the distortion [72, 110] (see Figure 2.8c to e). The solidification characteristics (including temperature gradient, solidification pattern, and cooling rate) were obtained based on a 3D FE model simulation of the thermal behaviors and microstructure evolution in multi-track laser cladding of Inconel 625 [111]. The temperature evolution, melt pool dimensions, and stress/strain fields during multi-track laser cladding were studied by proposing a 3D transient uncoupled thermo-elastic-plastic model [112].

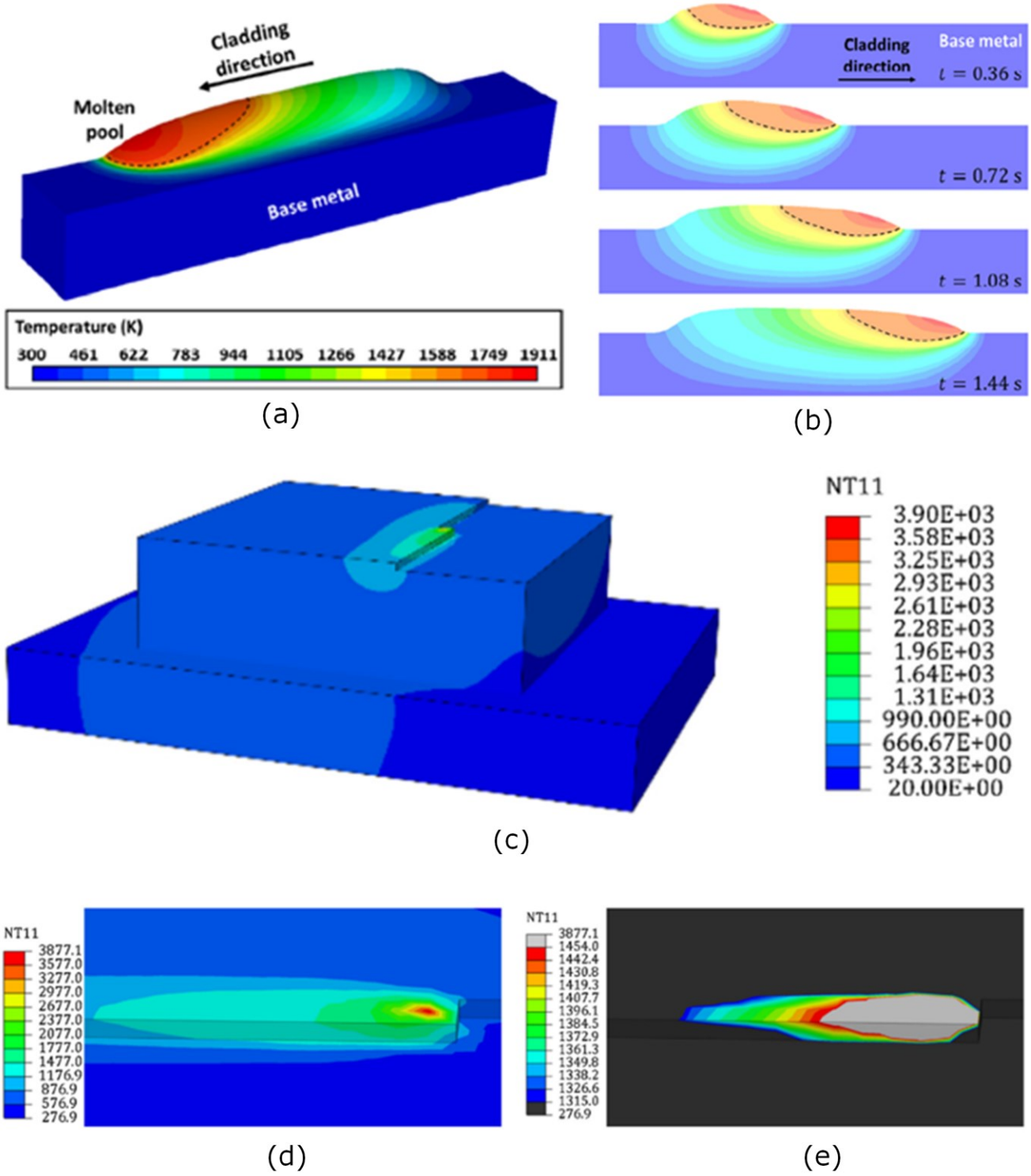

(Source: a and b [98], c to e [72])

Figure 2.8 Morphologies and temperature distributions FE simulation of single deposited track with wire: (a) axonometric view and (b) longitudinal cross-sectional views at various times; FE simulation of overlap cladding temperature field: (c) whole view, (d) temperature of ongoing track, and (e) melting zone profile.

2.3.2 Analytical modelling of cladding process

Despite the above efforts, large computation and unclear interrelationship between processing inputs and geometrical and thermal outputs limited the application of numerical studies, and analytical/theoretical methodologies were therefore proposed on some direct energy deposition processes that were related to WLC.

Based on the regression algorithm, the mathematical model was established to build the relation between the layer geometry characteristics (width, height and cross section area) and process parameters (laser power, scanning speed and wire feed rate) [113] (see Figure 2.9a and b). For multiple tracks cladding, the process development for wire-based laser metal deposition was conducted within optimized parameter ranges, giving the possibility to control the geometric shape, dilution, and aspect ratios of the deposited layers in a systematic way [68] (see Figure 2.9c to e).

The research of analytical modelling in WLC was limited. The related topic was also investigated here. An experimental study was carried out to determine the best model of track profile fitted with arc, parabola and cosine functions by comparing the actual and predicted track area of the three models [114]. In a model, phenomena such as recoil back pressure, surface tension inducing force, multiple reflection and angle dependent energy absorption of laser by melt pool wall were studied, showing that the trailing and deepening melt pool was wrapped around the unstable steam keyhole [115].

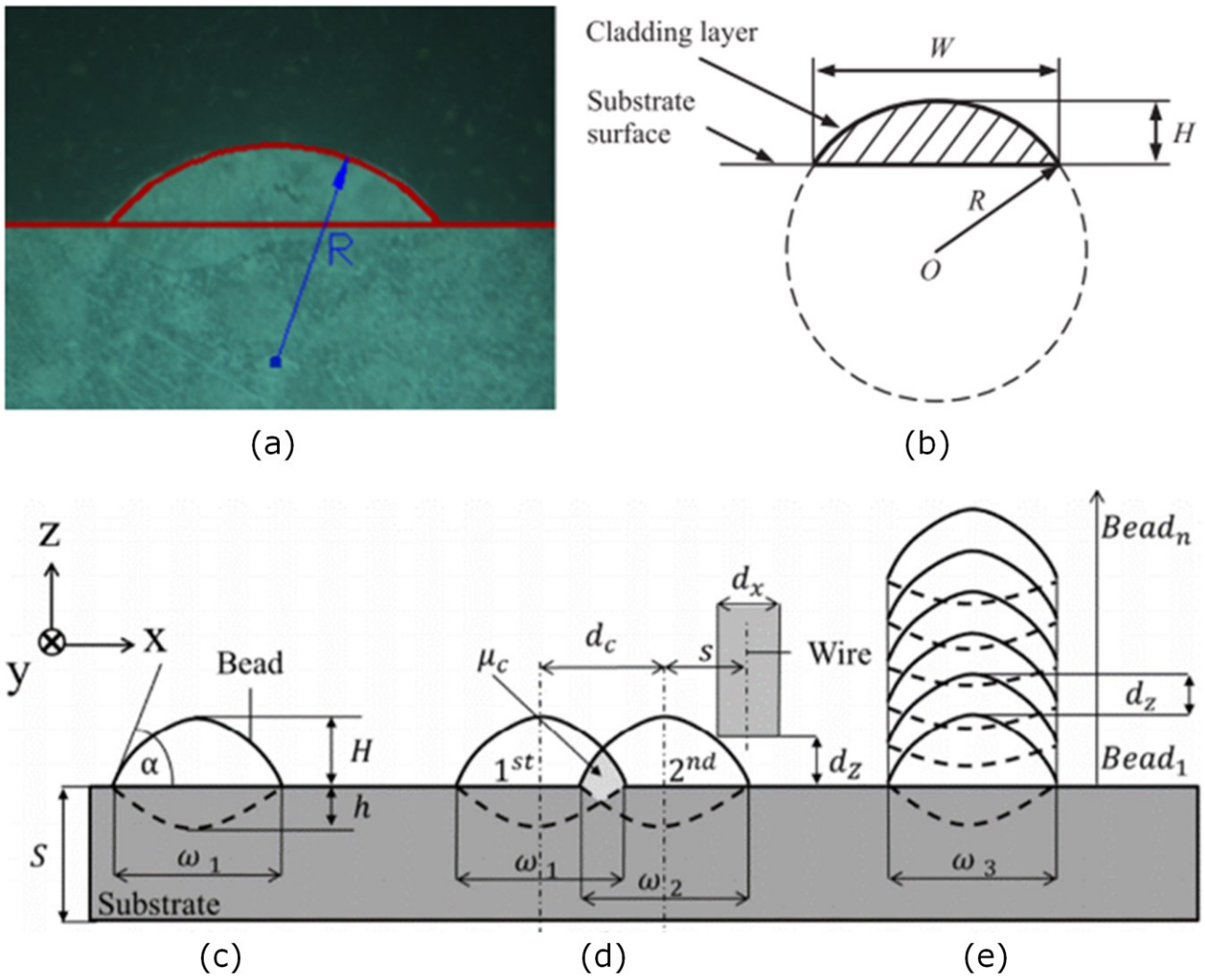

(Source: a and b [113], c to e [68])

Figure 2.9 Schematic of single cladding track: (a) experiment profile and (b) arc-shaped model profile; Schematic of the geometric parameters for bead morphologies after wire-based laser metal deposition for (c) single track; (d) multiple tracks next to each other, leading to a coating structure; alternately, (e) multiple layers on top of each other, resulting in a structure building process.

The effects of melt-pool geometrical parameters [116] and substrate crystallographic orientations [117] on crystal growth and microstructure development were studied through mathematical modelling. Based on a general and flexible analytical transformation model, combined with different

combinations of nucleation, growth and impact modes, the maximum value of solid state conversion rate for isothermal and isochronous transformation was evaluated [118]. The grain growth in a single-phase system with different anisotropic boundary energy was modelled using an improved Monte Carlo algorithm [119]. A model was developed which explained the β-phase to α-phase dissipation process caused by diffusion in bulk phase, lattice rearrangement and diffusion in interface area during solid/solid diffusion phase transition [120]. A grain refinement model for rapid solidification of undercooled single-phase solid solution alloys was developed, in which the combination of the dendrite fragmentation model and the overall solidification kinetics model allowed dendrite fragmentation to occur with the solidification process (e.g. during solidification in the mushy region) [121]. Assuming that the interface controls the growth mode, such as polycrystalline or allotropic transformation, an extended analytical model of non-isothermal solid state transformation was derived [122]. Based on the thermal stability of Sn-Ni peritectic alloy under external temperature gradient, the migration of solid/liquid interface and its position in the thermal stability process were analysed [123]. Through the analytical model of diffusion control, the simultaneous remelting/solidification of liquid particles moving from the interface of the mushy zone to the interface of the front/rear edge of the liquid particles was described [124]. The hard sphere theory derived from the first and second order approximation of isothermal compressibility was used to study the surface tension of some simple liquid metals, and the atomic transport properties of the same system, such as diffusion and shear viscosity, were also studied [125]. The dynamics of interfacial evolution of a particle in the binary alloy melt

affected by anisotropic surface tension was studied by means of the multiple variable analytical expansion method [126]. A theoretical method was described, in which the typical kinematic boundary conditions required by the Marangoni flow on the free surface was replaced by a class of "continuous" distribution functions with the homogeneous Neumann conditions, through which discontinuities or abrupt changes were not introduced into the model [127]. A detailed model was constructed to determine the full 3D melt pool and keyhole geometry by setting the appropriate energy and pressure balances which considered heat conduction, ablation losses and evaporation effects at the keyhole open surfaces, as well as the Fresnel and inverse Bremsstrahlung energy-absorption mechanisms [128]. The best estimation technique of tension and contact angle was developed, which was derived from the fourth order Runge-Kutta integral of the meridian curve and the best matching of discrete data representing the amplified droplet distribution [129]. A strategy was adopted to construct an objective function, which represented the error between the physical observation value and the theoretical Laplace curve, that was, the curve representing the solution of the capillary Laplace equation [130].

2.4 Summary and research gaps

Literatures on WLC are reviewed in this chapter, including the topics of: physics, outputs, and modelling (see Figure 2.10). Bullet points are the remarks in the literatures that are categorised in hierarchy. In general, the literatures cover the fundamentals of WLC.

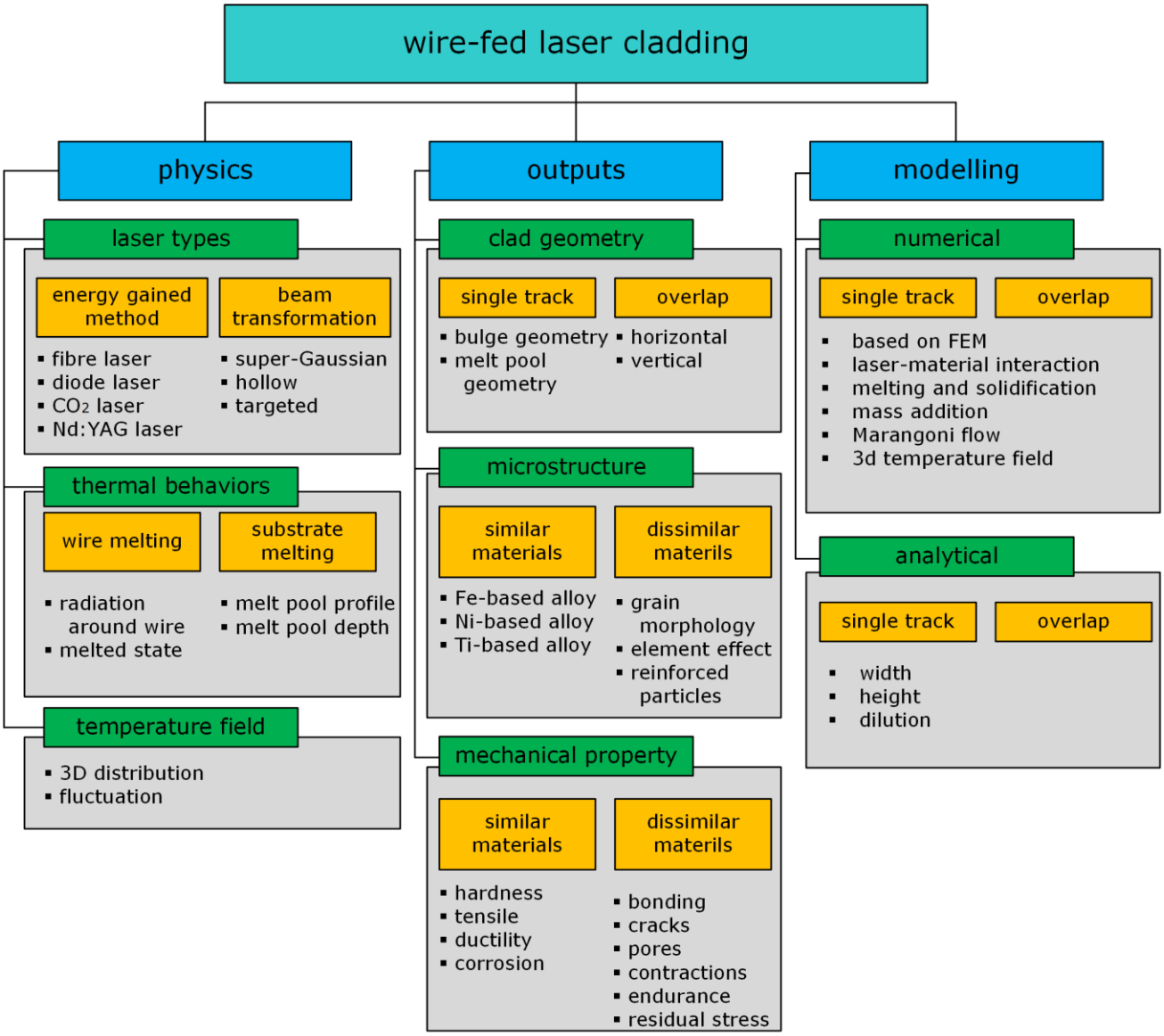

Figure 2.10 Summary of literatures.

Despite the availability of all the above efforts, the research gaps in relation to WLC still come from the following aspects:

- The WLC physics is in the initial explorational research status and there are few research concerning the optimized process. Although there are types of lasers can be used in WLC, no conclusion can be made about the most ideal

type. There is no clear indication of the optimized laser configuration effect on the thermal behaviors and temperature field.

- WLC outputs on non-horizontal surface is absent from the literatures. In most application cases, WLC are used on non-horizontal surface where gravity intervenes with the cladded material. Clad geometries, microstructure, and mechanical property are different when the material acts differently on non-horizontal surface.
- An analytical model of the full track profile in WLC, including both the bulge above the substrate surface and the melting pool below the surface, is absent from the literatures, which hinders the accurate prediction of the cladded surface and subsurface not only for the single-track but also when free-form surfaces are built from multiple overlapped tracks.

An analytical model allowing the prediction of a full track profile (including both bulge and melt pool) based on process parameters with the consideration of interfacial tension between different phases rightly fill the above gaps. The research methodology is introduced in the Chapter 3.

Chapter 3 Research methodology

This chapter illustrates the general steps towards the research aims while the details are unfolded in the following chapters. The methodology of this research is presented in three parts: (i) the wire and substrate material, (ii) the experiment, and (iii) the analytical modelling (see Figure 3.1).

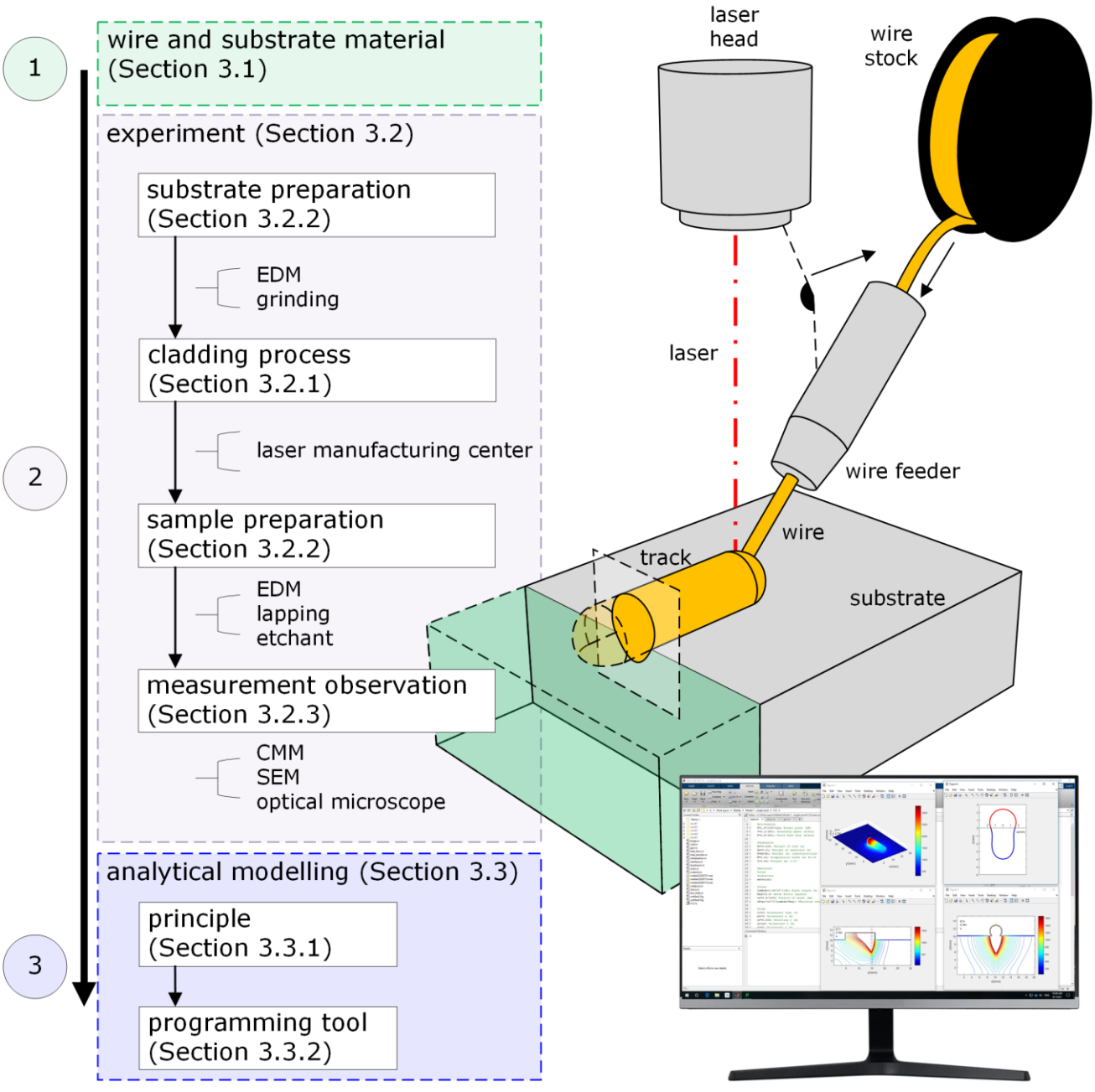

Figure 3.1 Research methodology and workflow.

3.1 Wire and substrate material

The material, among numerous types that are applicable in laser cladding, should be selected for wire and substrate. The thermal and metallurgical aspects of the material are analysed to give a preliminary material understanding before the experiment.

To emphasize the modelling process and the temperature change, similar material cladding is included in this research. Among the numerous materials, the employed wire (1.2mm in diameter, supplied by *CmCtw Ltd., Shanghai, China*) and substrate (20mm in thickness, supplied by *WUTAI Ltd., Taizhou, Jiangsu, China*) were both stainless steel 316L (see Table 3.1 and Table 3.2).

Table 3.1 Thermal properties of 316L for wire and substrate

Properties	Values	Units
C_p	500 [131]	$J/(kg*K)$
k	15 [131]	$W/(m*K)$
L_f	260000 [132]	J/kg
T_b	3086 [132]	K
T_m	1700 [132]	K
ρ	8000 [131]	kg/m^3

Table 3.2 Chemical compositions of 316L for wire and substrate

Element (wt.%)	C	Cr	Ni	Mo	Si	Mn	P	Cu	Fe
316L	0.014	18.74	11.82	2.67	0.56	1.55	0.03	0.17	Bal.

Thermal properties can also be obtained by a test [133]. The reasons for choosing 316L include:

(i) 316L is widely used as a workpiece material in industry due to its superior corrosion resistance [134];

(ii) 316L contains low carbon and is good for avoiding cladding decay [135];

(iii) most importantly, austenite dominates inside 316L before and after cladding, which is beneficial for determining microstructure transformation [136] contrast to the Ti-based alloy [137].

Figure 3.2 shows a phase diagram that will be used to explain the austenite stainless steel solidification [82]. Nickel is the element to promote the formation of austenite while Chromium is the element to inhibit the formation of austenite. Therefore, the combination of Nickel/Chromium is used to grade the austenite stainless steel. The region representing 316L based on content, Ni 11.0-14.0 wt% and Cr 17.0-20.0 wt%, is marked on Figure 3.2a. Figure 3.2b shows the combinations of austenite and ferrite that will exist at the end of solidification.

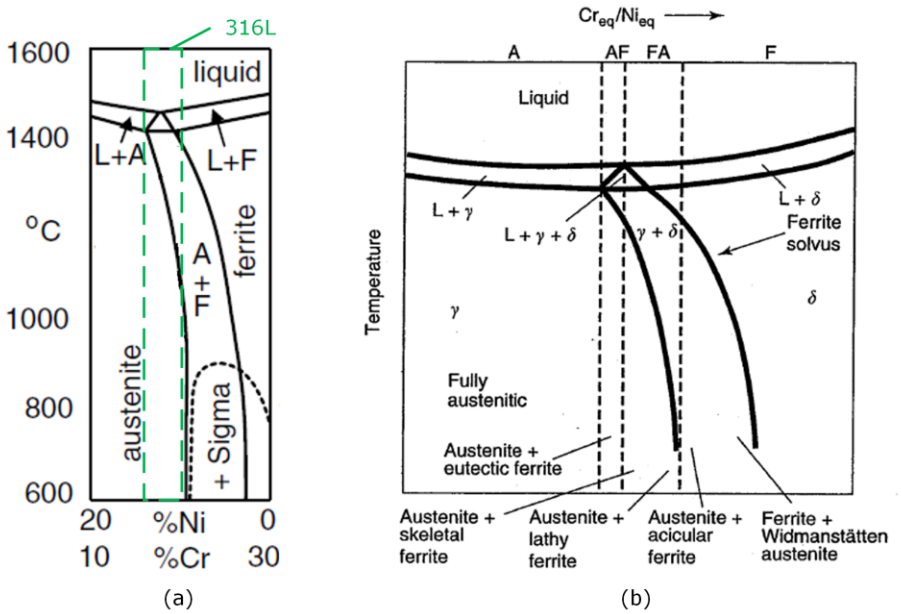

(Source: a and b [82])

Figure 3.2 Phase diagram to analyse solidification: (a) the phase diagram of austenite stainless steel and (b) the combination product of austenite and ferrite at the end of solidification.

Since the microstructure of austenite stainless steel has been systematically researched, the atlas is the most reliable tool to verify the microstructure inside stainless steel after solidification [82] (see Figure 3.3).

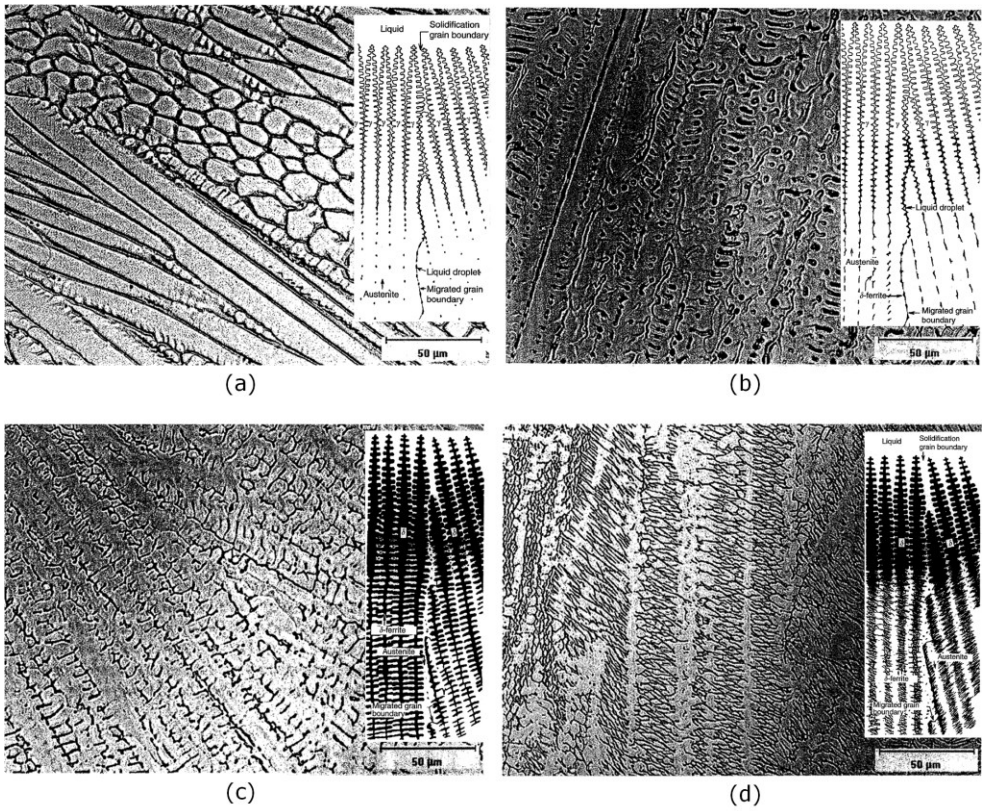

(Source: a and b [82])

Figure 3.3 Atlas of microstructure inside stainless steel after solidification: (a) full austenite from type A solidification, (b) austenite with eutectic ferrite from type AF solidification, (c) austenite with skeletal ferrite from type FA solidification, and (d) austenite with lathy ferrite from FA solidification.

In type A solidification, the substructures, cells, and dendrites, are apparent due to the segregation of alloying and the relatively low diffusivity of impurity elements at elevated temperature, which preserves the segregation profile that develops during solidification (see Figure 3.3a). AF type occurs if sufficient ferrite-promoting elements (primarily Cr and Mo) partition to the solidification subgrain

boundaries during solidification to promote the formation of ferrite as a terminal solidification product (see Figure 3.3b). FA type occurs when austenite forms via a peritectic-eutectic reaction and exists at the ferrite solidification boundaries at the end of solidification (see Figure 3.3c and d). F type will not be discussed because it is very rare in austenite stainless steel.

3.2 Experiment facilities and procedures

The laser cladding has a workflow in experiment including substrate preparation, cladding process, sample preparation and sample observation. In substrate preparation, Electronic Discharge Machining (EDM) and grinding will be used to shape the substrate. In the cladding process, the laser manufacturing centre is the workstation. In sample preparation, EDM is used to cut analysis samples while lapping pad and etchant are used to expose analysis surface. In the sample observation, a Coordinate Measurement Machine (CMM) is used to profile the cladding workpiece either before or after EDM cutting, while the Scanning Electron Microscope (SEM) and optical microscope are used to observe cross section surface. The facilities and settings are explained in the subsections.

3.2.1 Cladding process - Laser manufacturing centre

The cladding experiments are conducted in the laser manufacturing centre (HWF20, Hans Laser) (see Figure 3.4a) equipped with the laser generator (YLS-2000, IPG Photonics) (see Table 3.3). The processing module is mounted on the 3-axis linear feeding module with listed parameters (see Table 3.4). The processing zone is below the processing module.

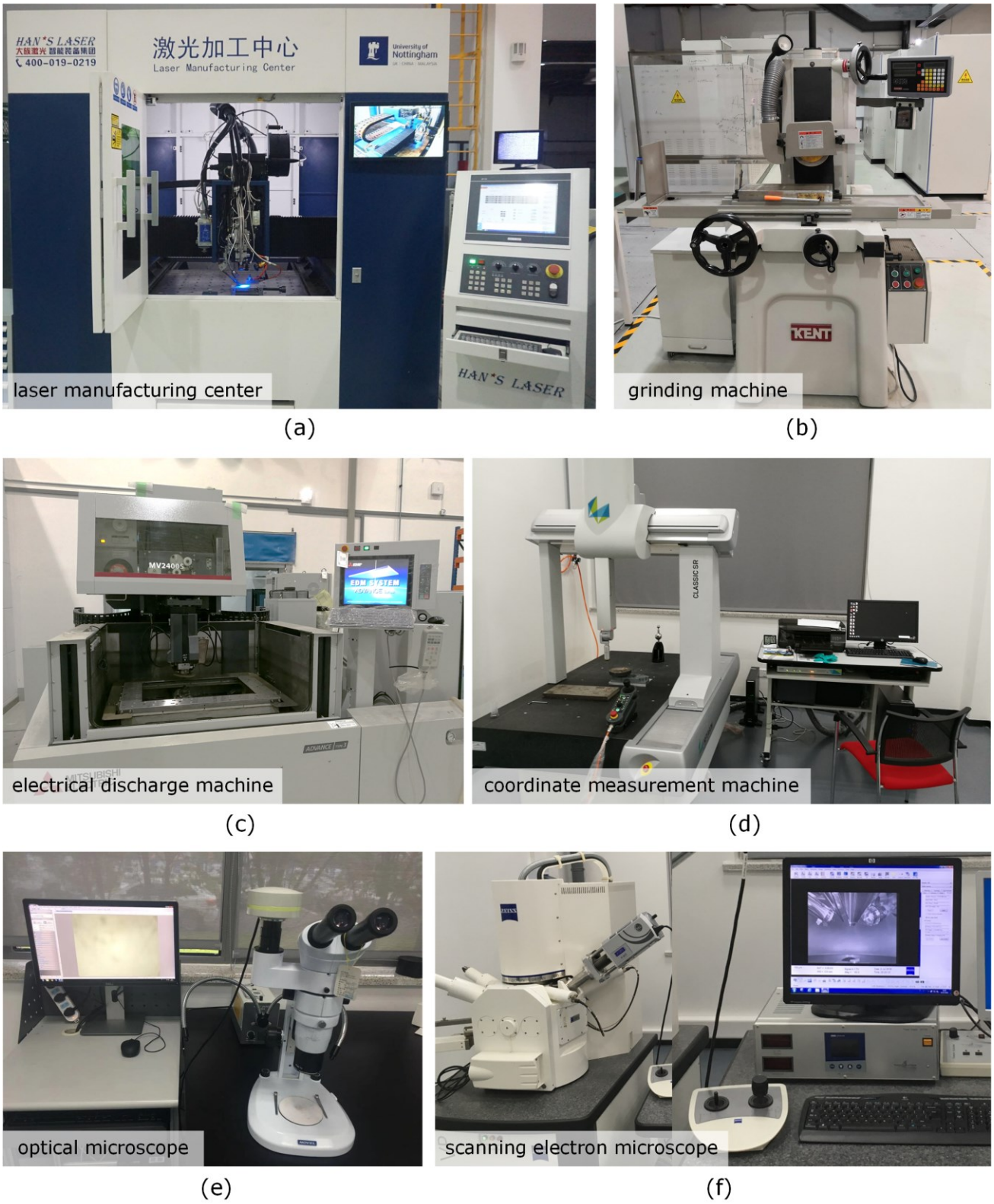

Figure 3.4 Facilities used in experiment: (a) laser manufacturing centre, (b) grinding machine, (c) electrical discharge machine, (d) coordinate measurement machine, (e) optical microscope, and (f) scanning electron microscope.

Before cladding, the basics of programming on the control panel is the input of laser power, scanning speed, and travel distance as a type of G-code. Wire feed rate is set by rotating knob on the service motor module. The height of laser head is adjusted manually on the control panel until the low voltage laser spot converges to minimum area. During cladding, the metal wire is melted by laser and deposited on the metal substrate when the G-code is run, and the protection gas N_2 is fed onto the workpiece with 20 L/min. Vacuum fume extraction ventilates air inside the housing to remove suspending vaporized particles which may impede the ongoing laser.

Table 3.3 Laser generator details

Item	Specifics
Laser Manufacturer	IPG Photonics
Description	Ytterbium CW Laser Systems
Model	YLS-2000
Operation mode	Continuous wave [138]
Max. power	2 kW
Wavelength	1070 nm
Laser spot diameter	0.4 mm

Table 3.4 Three-axis linear feeding module details

Item	Specifics
X-axis stroke	1000mm
Y-axis stroke	1000mm
Z-axis stroke	100mm
X/Y axis location accuracy	±0.02mm
X/Y/Z axis repeatability	±0.01mm
X/Y/Z axis max. running speed	30m/min
X/Y/Z axis max. acceleration	0.3m/s^2

3.2.2 Substrate and sample preparation

(i) Grinding machine

The raw substrate for deposition is relatively rough and covered with contaminants. To remove contaminations and obtain a flat surface, the substrate, size of $100mm \times 100mm \times 20mm$, is put on a flat grinding machine (KGS-618M, KENT) with a white corundum grinding wheel (P200 × 10 × 32WA 60L5V35) (see Figure 3.4b). Rotation speed is set as 2800 r/min. Workpiece is fed in with horizontal interval of 0.5mm each pass and vertical interval of 0.02mm for each layer.

(ii) Electronic discharge machining

Initial substrate or as-clad samples are cut using an EDM machine (MV2400S, MITSUBISHI ELECTRIC, see Figure 3.4c). Settings are as follows: discharge energy is set as E1021 (a mode code that specify energy and wire feed which are built in the operational system according to material type and thickness, where 1021 is the code suitable for a 316L plate with thickness of 20mm) and travel speed as 3.0mm/min. Wire diameter is 2.0 μm. Cutting zone range is X700mm, Y500mm, Z300mm.

(iii) Lapping

Before cladding, the substrate surface is put on a lapping pad with the abrasive size of #400 until the surface roughness Ra reached 1.6 μm to minimise the influence of any possible factors.

After cladding, the cross-section surface is put on the lapping pad with the abrasive size of #1200 and villus pad with 0.1 μm floating abrasive until the roughness Ra reaches 0.1 μm.

(iv) Etchant

Polished surface is dipped into etchant (CuSO4 $4g$, HCl $20mL$, water $20mL$) puddle for $20s$ and taken out to rinse clean followed by forced drying. After etched, the melt pool profile and microstructure features are exposed for observations.

3.2.3 Measurement and observation

(i) Coordinate measurement machine

As-clad samples are placed on the workbench of CMM (CLASSIC SR, HEXAGON METROLOGY, see Figure 3.4d) for morphology profiles. Settings are as follows: point density 30 per mm, scanning speed 2 mm/s, off set force 0.02 N, acceleration 5 mm/s^2. Measuring range in X1000mm, Y2000mm, Z1000mm with accuracy of 2 μm.

(ii) Optical microscope

The etched surface of as-clad samples is observed under an optical microscope (NSZ-810, NOVEL OPTICS, see Figure 3.4e). The magnitude includes 10X for an objective lens and 0.8X-8X for an ocular lens. The computer interface linked with the microscope is used to obtain digital images, put on dimension scales, and conduct various measurements. The digital images of track morphology are then used as the experimental profiles compared with the computation profiles from

the analytical modelling. The digital images of the etched surface are used to analyse the microstructure distribution. Observations were under magnification of 8X with scale accuracy of 0.5mm. To obtain statistical results, points on cross section profiles are extracted in radial direction with increment of 10 degrees. On each direction, average distances from original points to extracted points are calculated and all the average points form the statistical profile curve. Error bars are added vertical to statistical profile curve. For the cross section of a cladding layer that overshoots the view size of microscope, separate sections are captured individually followed by image merge. The error estimation method is adjusted to calculate the ratio of discrepancy area to experimental profile error.

(iii) Scanning electron microscope

The etched surface of as-clad samples, size of 10mm × 10mm × 5mm, is observed inside an SEM (Particle SCAN VP, ZEISS, see Figure 3.4f). The working voltage is set as 12kV with the magnification of 300X for the microstructural features. The digital images of the etched surface are used to analyse the microstructure distribution.

3.3 Analytical modelling

The analytical modelling includes the principle and programming tool. After the modelling and calculation, the calculation results are compared with the experiment results as a validation process which proves the model accuracy.

3.3.1 Principle of modelling

The analytical modelling is the process that takes in the processing input parameters (laser power, scanning speed and wire feed rate) and gives the output results (temperature field and geometrical profiles) using the mathematical equations that connect all of the physics parameters. The mathematical structure basically consists of (i) laser radiation and heat transfer, and (ii) the governing physics of geometrical profiles.

The laser intensity distribution can be obtained by scanning inside the laser radiation range point by point, providing the data for modelling. Based on the scanned results provided by Hans Laser, the laser intensity follows the super Gaussian distribution, which is an axisymmetric flat-top function at the focus location, and evolutes into a normal axisymmetric Gaussian function upwards and downwards of the propagation direction (see Figure 3.5). Some important parameters characterize the laser beam, including waist radius 0.397 mm, Rayleigh length 22.380mm, and propagation factor 20.9.

Heat transfers, including conduction, convection, and radiation, occur at the same time as laser radiation. The transfers can be calculated based on the finite difference method. The Finite Difference Method (FDM) is an approximate method for solving partial differential equations. It has been used to solve a wide range of problems, including linear and non-linear, time independent and dependent problems. After the calculation, the characteristic temperature at the melting zone can be obtained and then used to calculate the bulge and melt pool profiles.

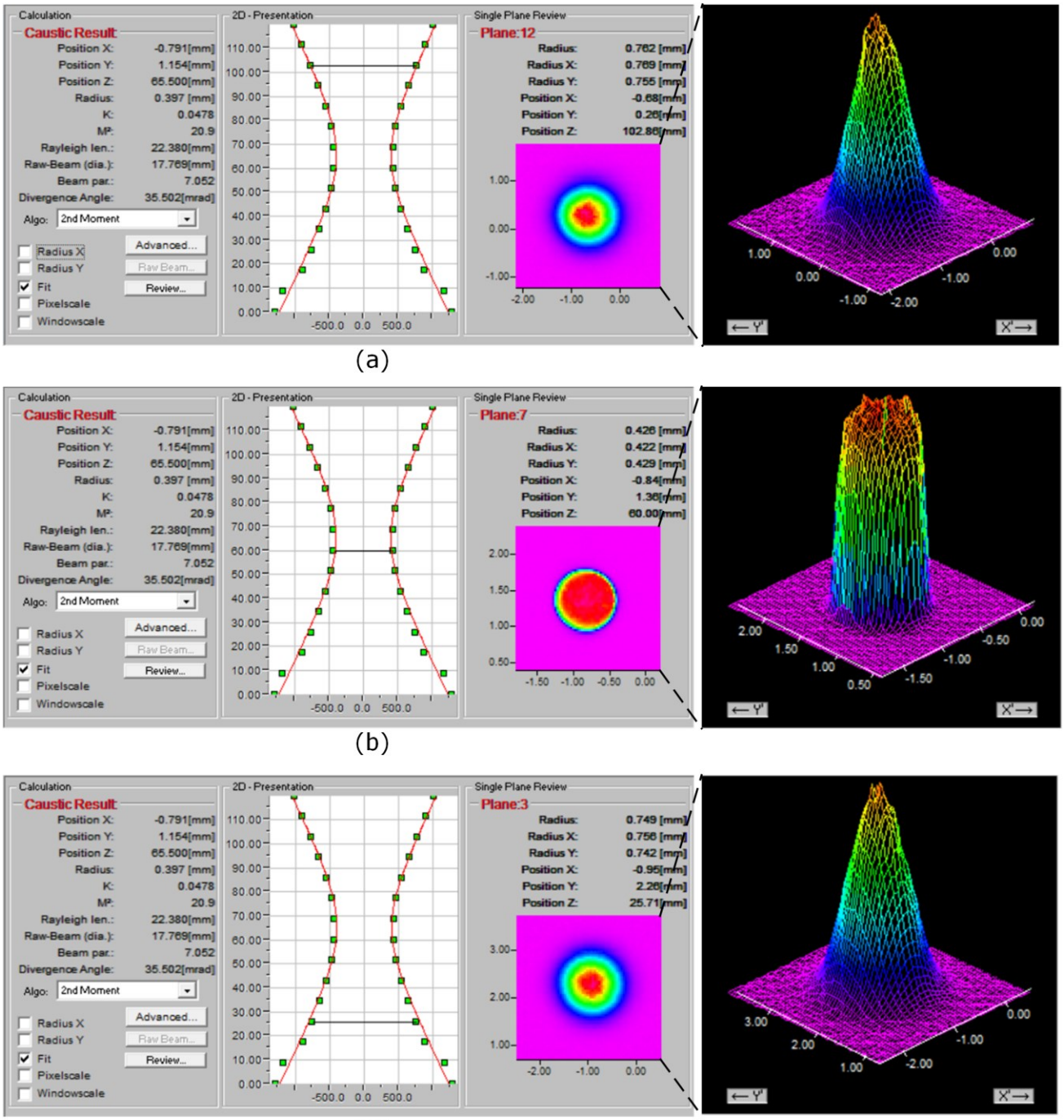

(Source: Hans Laser)

Figure 3.5 Laser intensity at cross sections along propagation path measured at 1kW laser power by Hans Laser: (a) cross section at 42.5mm above the focus, (b) cross section at the focus, and (c) cross section at 35mm below the focus.

There have been assumptions and guesses about the geometrical profiles of tracks (mostly about bulge, rarely about melt pool). The most reasonable profiles

come from the governing physics of interfacial tension. The surface tension on the sessile drop can be used to form the bulge shape (see Figure 3.6a). Since the temperature inside the melting zone has already been calculated, the characterized temperature can be used to determine the flatness of bulge. The tension on the pendant drop can be illustrated as interfacial tension between solid and liquid to form the melt pool shape (see Figure 3.6b). Since the depth of the melt pool can be obtained from the calculated temperature field, the melt pool profile is governed by interfacial tension (also determined by the characterized temperature) and can be plotted from the bottom to the substrate surface, intersecting with the bulge contact edge.

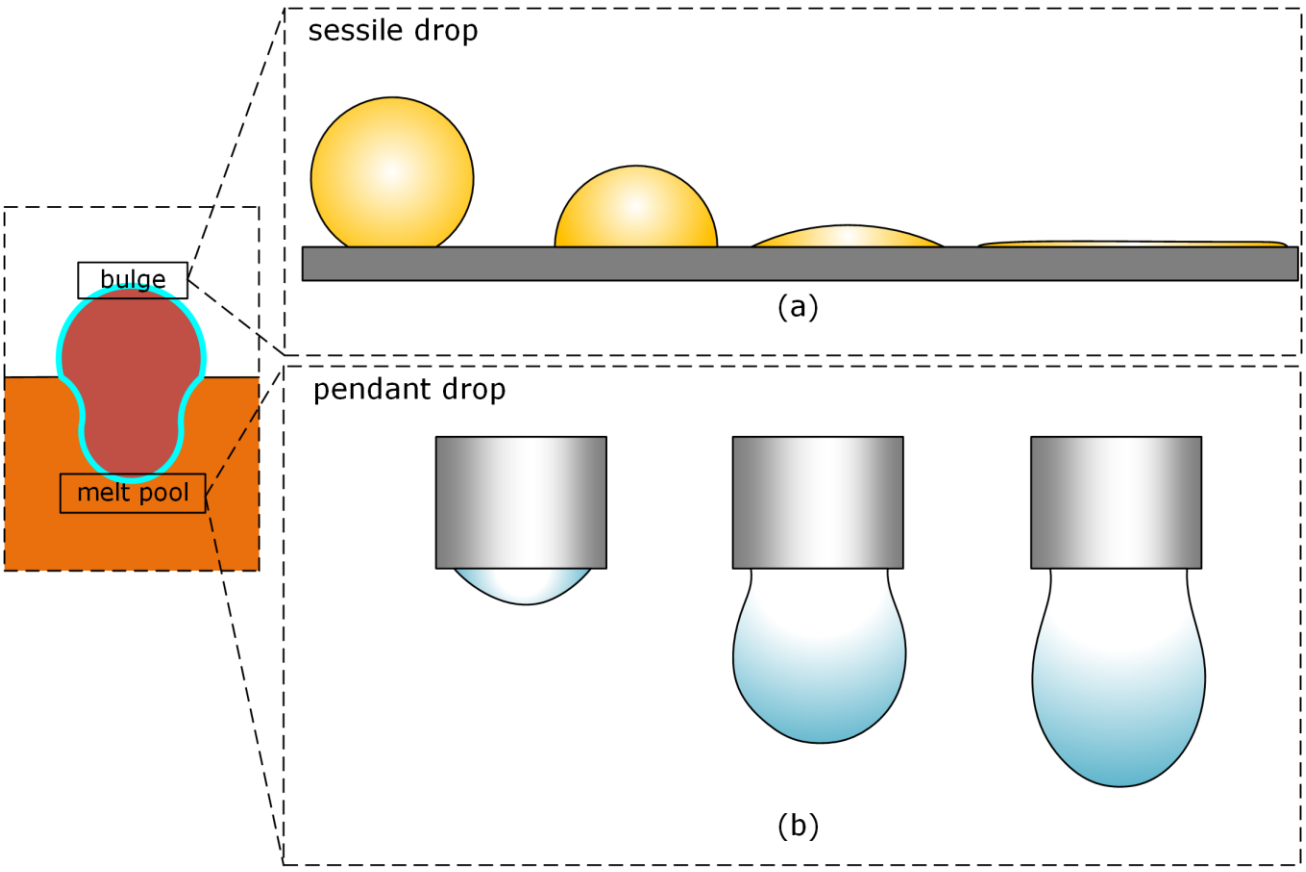

Figure 3.6 Schematic of governing physics in geometrical profiles modelling.

3.3.2 Programming tool for realising of model

MATLAB programming is used as a tool to run the code for the mathematical equations in order to run the model and predict the WLC temperature and geometrical profiles (see Figure 3.7). MATLAB, known as matrix laboratory, is a valuable matrix calculation tool which is efficient for making temperature field calculations using parallel computation. The codes are programmed in a set of text files as follows.

- Main – the file that defines the overall workflow of the WLC process and carries out the functions of the workflow including parameters, initialization, heating, heat transfer, temperature field, and geometrical profile.
  - Parameters - the function that sets up values for constant parameters including processing parameters, computation domain dimensions, material properties, and laser parameters.
  - Initialization - the function that sets up the initial status including bulge and melt pool geometry, calculation domain, laser, substrate, and clad addition.
  - Heating - the function that calculates the temperature of each cell radiated by the laser.
  - Heat transfer - the function that calculates the conduction, convection and radiation.
  - Temperature field - the function that sets up the cross sections of the temperature field and outputs the contours.
  - Geometrical profile - the function that plots the bulge and melt pool profiles.

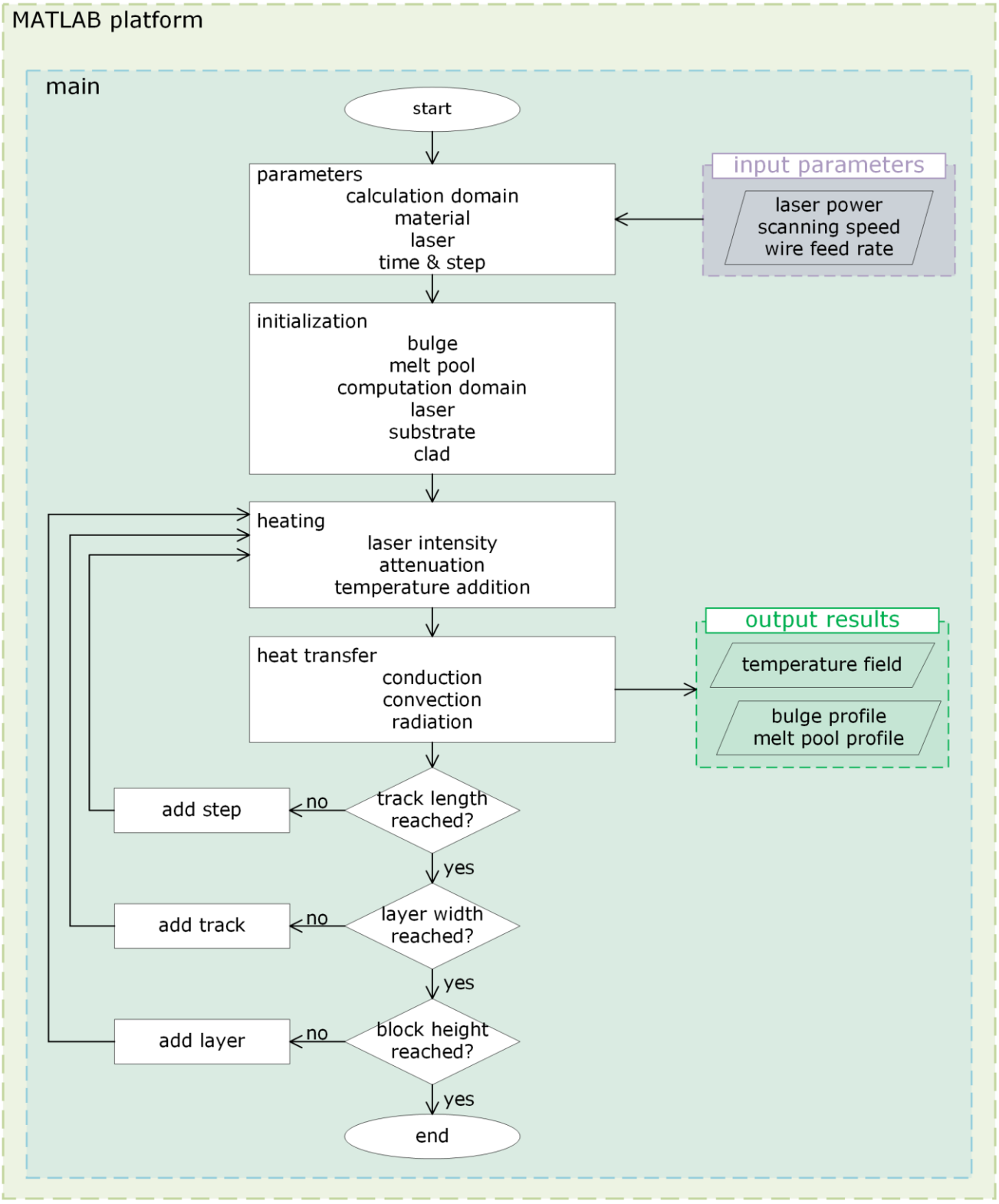

Figure 3.7 Programming structure on MATLAB platform.

(This page is left blank)

Chapter 4 Modelling of single-track wire-fed laser cladding on horizontal surface

4.1 Introduction

The aims and objective of this chapter are to model the profile and temperature field of the deposition zone in the single-track WLC on horizontal surface, which can be considered as the most basic event in this technology. The high temperature and intensive radiation determine the necessity of automation. It becomes the urgent need of helping manufacturing engineers to determine the *In-situ* path and parameters.

The model must be able to reflect the physics principle of the cladding profile during cladding process so that the needed cladding profile can be obtained. A full analytical model of the clad dimensions and shape was created based on the surface tension force of the liquid in the melt pool, and experimentally validated the model accuracy [139]. A developed model was proposed to predict not only the height and width of the deposited clad but also the insufficient metallurgical bonding in the deposited structure [140]. However, neither radiative nor conductive heat losses were considered in the above two models, and more importantly, that have been developed for the powder-fed laser cladding which is fundamentally different from WLC process by mass-radiation interaction. The physical and thermal behaviours in wire-fed welding were claimed similar to the ones in wire-fed cladding, and then the universal model was proposed to determine the solid–liquid interface in the molten pool based on heat conduction and the Marangoni flow [141]. Yet the solid–liquid interface of the model relied

on the type of heat source (i.e. micro-plasma transferred arc in the model), but not including laser which is different in many aspects (i.e. reflection, penetration and attenuation in laser). A theoretical model of laser welding was proposed considering the phenomena such as surface tension induced forces, laser beam reflection due to melt liquid surface, depth dependent laser energy absorption, temperature-dependent buoyancy effect and Marangoni force [115]. However, this model focused on fluid dynamics in the weld pool while not covering the prediction of the free surface, i.e. deposition shape, which is needed in WLC. Apart from the additive manufacturing, the subtractive manufacturing can also be a source for an analytical model. The evolution of the depth/height at any point on the surface can be described by the convolution of a radially-varying function which represented the steady state ablation footprint created by a pulsed laser scanned across the workpiece according to pulse separation distance (i.e. scanning speed) [142]. A model used to predict the eroded patches was presented that needed only few process parameters (e.g. pump pressure, scanning speed) and a simple calibration (i.e. to map the characteristics of the target materials) and enabled the prediction of the removed material for the tested condition with high accuracy (1.2%) [143]. A novel spatially and temporally (S&T) controlled laser heating model proposed, in which a large area can be heated up with a small laser spot by controlling the beam scanning, i.e., laser power, path and scanning speed [144]. An inverse modelling of time-dependent, algorithmic energy beam manufacturing processes control was proposed which was achieved through trial-and-error approaches in the past [145].

The structure of this chapter is: (i) the full shape of the material deposition on horizontal surface is analytically modelled, including bulge (the part above the surface) and melt pool (the part below the surface), (ii) validation by experiments for various process parameters followed by the appropriate measurements under optical microscope of the cross sections cutups, (iii) further discussions about the model, e.g. useful information from the model compared with other observations such as microstructure and hardness, and (iv) application cases with the model based on the encountered situations in repair.

4.2 Modelling background

In WLC process, a laser beam with high intensity energy radiates on a fed-in wire and static substrate while the laser beam and the wire move along the cladding direction. The wire material absorbs the energy, melts and forms a track of deposited material on the substrate (see Figure 4.1a).

Thus, the following aspects should be considered in the modelling:

- This process is a multiple inputs multi factors affecting single output problem. Inputs include laser power P, scanning speed v_s and wire feed rate v_f which cross influence with temperature, eventually influence the output track geometry (see Figure 4.1a).
- The laser intensity profile should also be considered in the modelling. The energy distribution in the laser beam follows an axisymmetric super Gaussian distribution which is a flat-top function at the waist (see Figure 4.1b A-A) and gradually evolves into a normal Gaussian function along the propagation

direction (see Figure 4.1b B-B and C-C). In addition, after the laser penetrates through material, the intensity attenuates as material absorbs energy and reflects a portion of energy out to the atmosphere.

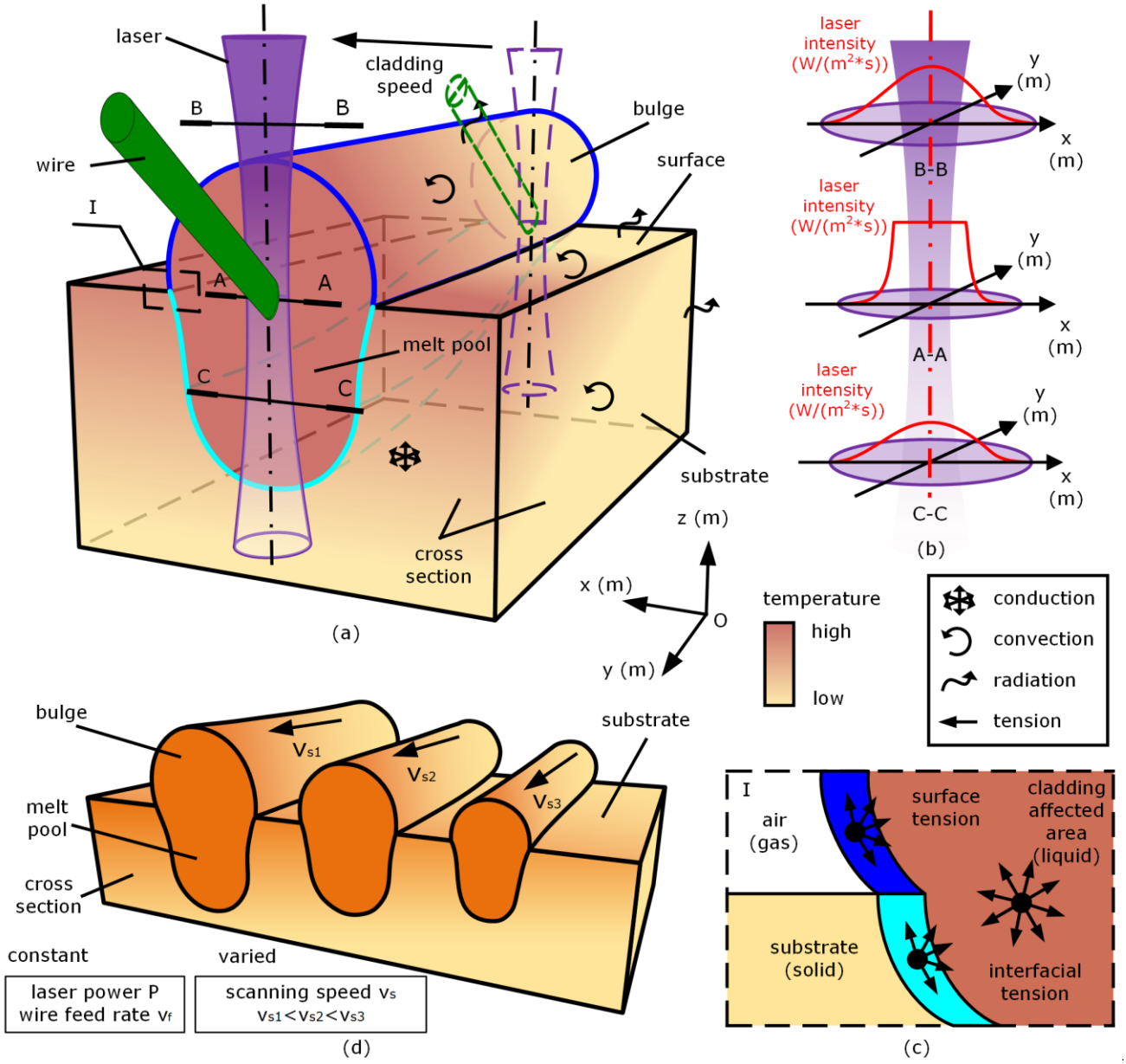

Figure 4.1 Principle of WLC process: (a) process schematics (bulge forms above the surface and melt pool forms below the surface), (b) laser intensity that follows the super Gaussian distribution, (c) interfacial tension between different states within the cladding affected area, and (d) the change of cladded track profile due to varied scanning speed ($v_{s1}<v_{s2}<v_{s3}$).

- The effect of interfacial tension should be considered in the modelling. The profiles of liquid bulge and melt pool are governed by temperature-dependent interfacial tension, i.e. gas-liquid tension between air and melt metal (see Figure 4.1c). When the temperature of melted bulge is low, the surface tension is large, resulting in the slight wetting to the substrate and the high bulge (see Figure 4.1c). As the laser inputs energy, the temperature of liquid bulge is rising and the surface tension decreases, resulting in the increased wetting to the substrate and the flattened bulge (see Figure 4.1c). The interfacial tension effect on melt pool profile is unique and significant. This is because the clad profile is determined by the liquid- stated melt metal whose behaviours are governed by the interfacial tension.
- The controlling strategy should be proposed to achieve freeform track surface. For industrial application, a control strategy of changing the processing parameters is feasible to produce the profile of cladded bulge and melt pool online. However, among these processing parameters, scanning speed is the most convenient way to be varied varying because it can be controlled online by any high-accuracy Computer Numerical Control (CNC) automation systems (e.g. via G code). Thus, the increase or decrease of scanning speed will lead to the change in size and shape of bulge and melt pool (see Figure 4.1d).

4.3 Model description

4.3.1 Modelling principle

The proposed model, in general, is based on the discretization of the full 3d computational field into cubic unit cells. The computation domain includes the

substrate part and the deposition zone with dimensions (see Figure 4.2a) and is cut into slices (see Figure 4.2b).

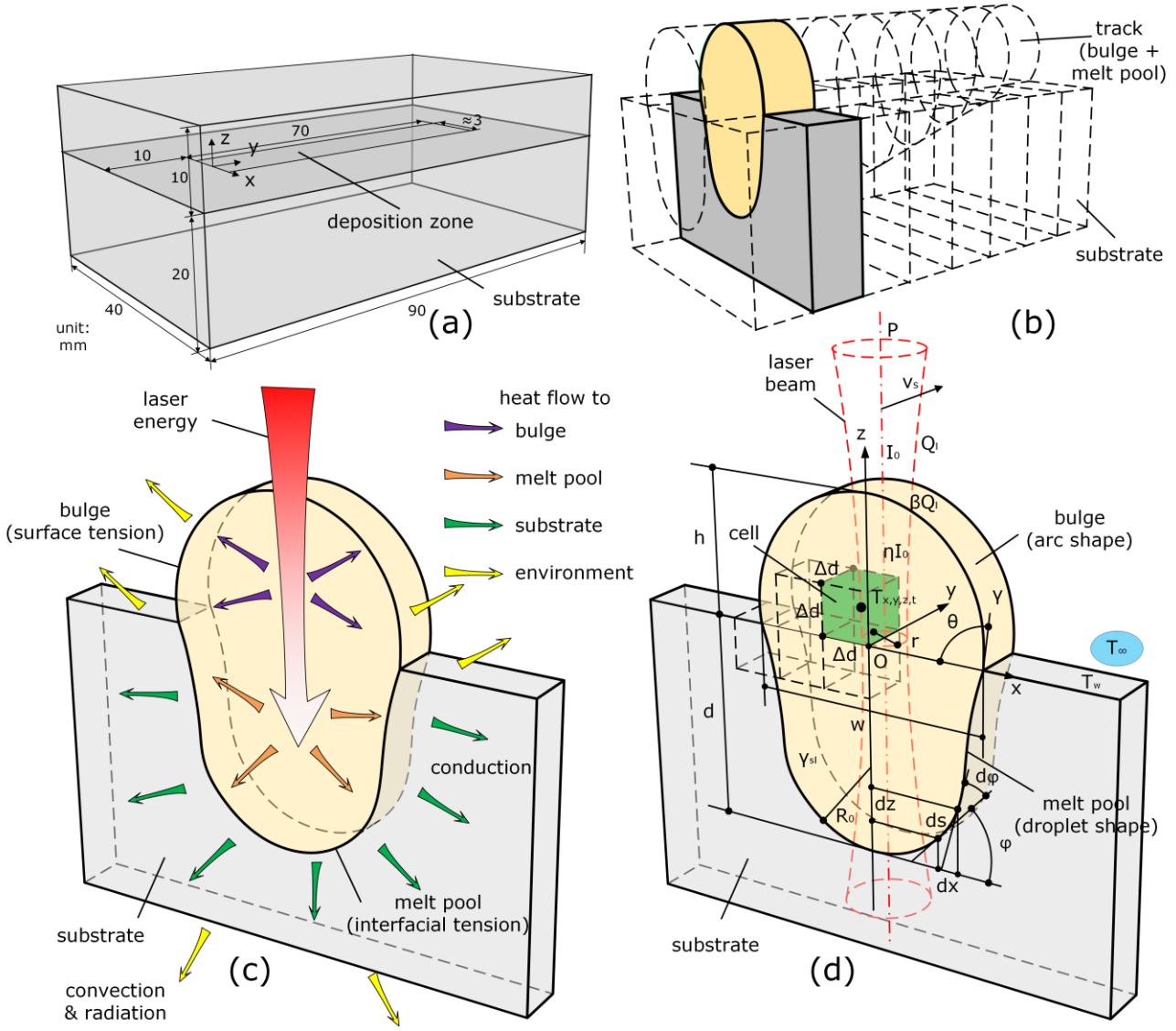

Figure 4.2 Schematics of theoretical modelling of the full shape of cladding affected area: (a) computation domain, (b) a slice of unit cells in the computation field, (c) heat flow from laser to the bulge and melt pool, and further to the solid substrate, and (d) the parameters in the modelling steps.

For each slice, the laser radiates through material and brings heat to the bulge and melt pool (see Figure 4.2c). Further, at the periphery of bulge, the heat is transferred to the atmosphere by convection and radiation [146]. Further, at the

periphery of melt pool, the heat is transferred to the substrate by conduction and eventually to the atmosphere by convection and radiation.

Based on above, the modelling principle is: (i) the temperature field dominated by laser energy is firstly solved (see Section 4.3.2), (ii) the bulge profile is calculated by the temperature-dependent surface tension between melted liquid and surrounding gas (see Section 4.3.3), (iii) melting point isotherm (a line on a 2D map that connects the points that have reached melting temperature at a given time) is calculated to roughly estimate the region of melt pool, especially the depth (see Section 4.3.4), and (iv) finally the melt pool outline is fitted.

4.3.2 Calculation of temperature field in the track and substrate

The temperature field is calculated for the purpose of estimating the shape of the bulge and of the melt pool. To obtain the full temperature field in WLC, the calculation domain is divided into cubic cells with the edge length Δd. Each cell position is denoted as (x, y, z) in the coordinate system (see Figure 4.2d) and has a varied temperature value T due to both the laser heating and the heat transfer.

The continuous temperature of a cell at time aspect can be expressed as a Taylor's series expansion. When time step is set sufficiently small, the second and higher order terms can be eliminated while the first derivative of temperature is remained. Based on the definition of heat capacity, the cell temperature due to instant laser heating, as a volumetric heating source [147], can be expressed as [148]

$$T'_{x,y,z,t} = T_{x,y,z,t} + \frac{Q_l}{\rho_l(\Delta d)^3 C_p^*}, \tag{4.1}$$

where $T_{\mathrm{x,y,z,t}}$ is the spatial transient temperature, ρ_l is the density of material, C_p^* is the modified specific heat capacity of material [149]. All thermal properties of material are assumed constants.

The temperature calculated by Equation (4.1) can be then updated by considering heat transfer behaviours including: (i) heat conduction from high to low temperature per unit time Δt as Equation (4.2) [150], also applied for the melt liquid assuming the fluid dynamics has negligible impact on temperature prediction because the melting zone is heated to the same level of temperature,

$$\rho C_p \frac{\partial T^{in}_{x,y,z,t+\Delta t}}{\partial t} = k\left(\frac{\partial^2 T'_{x,y,z,t}}{\partial^2 x} + \frac{\partial^2 T'_{x,y,z,t}}{\partial^2 y} + \frac{\partial^2 T'_{x,y,z,t}}{\partial^2 z}\right), \tag{4.2}$$

where k is the conductivity, and $T^{in}_{x,y,z,t+\Delta t}$ is the temperature of interior cells, and (ii) the convection and radiation transferring from workpiece to the environment as [149]

$$h_n\left(T^{w}_{x,y,z,t+\Delta t} - T_\infty\right) = -k\left(\nabla T'_{x,y,z,t} \cdot \boldsymbol{n}\right), \tag{4.3}$$

where $\nabla T'_{x,y,z,t}$ is the temperature gradient between boundary cell and interior cell, $\boldsymbol{n}$ is the normal vector of the surface, h_n is the combined convection-radiation coefficient, $T^{w}_{x,y,z,t+\Delta t}$ is the cell temperature at the boundary, and T_∞ is the temperature of environment.

Please note that the solutions of heat transfer in Equations (4.2)-(4.3) involve a numerical finite difference method proposed by Holman [150].

Equation (4.2) describes conduction inside material (see green cells in Figure 4.3), and is numerically solved with central differencing scheme by

$$T^{in}_{x,y,z,t+\Delta t} = \frac{k\Delta t}{\rho C_p(\Delta d)^2}\left(T'_{x-\Delta d,y,z,t} + T'_{x+\Delta d,y,z,t} + T'_{x,y-\Delta d,z,t} + T'_{x,y+\Delta d,z,t} + T'_{x,y,z-\Delta d,t} + T'_{x,y,z+\Delta d,t} - 6T'_{x,y,z,t}\right) + T'_{x,y,z,t}. \quad (4.4)$$

Equation (4.3) describes convection and radiation between material at the boundaries and the environment, and is calculated based on three different situations:

In Case (i), where one cell face is adjacent to environment in either x, y, or z direction (see blue cells in Figure 4.3), Equation (4.3) is numerically solved by

$$T^{w}_{x,y,z,t+\Delta t} = \frac{k\Delta t}{\rho C_p(\Delta d)^2}\left(\frac{2h_n\Delta d}{k}\left(T_\infty - T'_{x,y,z,t}\right) + 2T'_{x-\Delta d,y,z,t} + T'_{x,y-\Delta d,z,t} + T'_{x,y+\Delta d,z,t} + T'_{x,y,z-\Delta d,t} + T'_{x,y,z+\Delta d,t} - 6T'_{x,y,z,t}\right) + T'_{x,y,z,t}; \quad (4.5)$$

In Case (ii), where two cell faces are adjacent to environment in either $x-y$, $y-z$, or $x-z$ direction (see purple cells in Figure 4.3), Equation (4.3) is numerically solved by

$$T^{w}_{x,y,z,t+\Delta t} = \frac{2k\Delta t}{\rho C_p(\Delta d)^2}\left(\frac{2h_n\Delta d}{k}\left(T_\infty - T'_{x,y,z,t}\right) + T'_{x-\Delta d,y,z,t} + T'_{x,y-\Delta d,z,t} + T'_{x,y,z-\Delta d,t} + T'_{x,y,z+\Delta d,t} - 4T'_{x,y,z,t}\right) + T'_{x,y,z,t}; \quad (4.6)$$

In Case (iii), where three faces are adjacent to environment (see yellow cells in Figure 4.3), Equation (4.3) is numerically solved by

$$T^{w}_{x,y,z,t+\Delta t} = \frac{2k\Delta t}{\rho C_p(\Delta d)^2}\left(\frac{2h_n\Delta d}{k}\left(T_\infty - T'_{x,y,z,t}\right) + T'_{x-\Delta d,y,z,t} + T'_{x,y-\Delta d,z,t} + T'_{x,y,z-\Delta d,t} - 3T'_{x,y,z,t}\right) + T'_{x,y,z,t}. \tag{4.7}$$

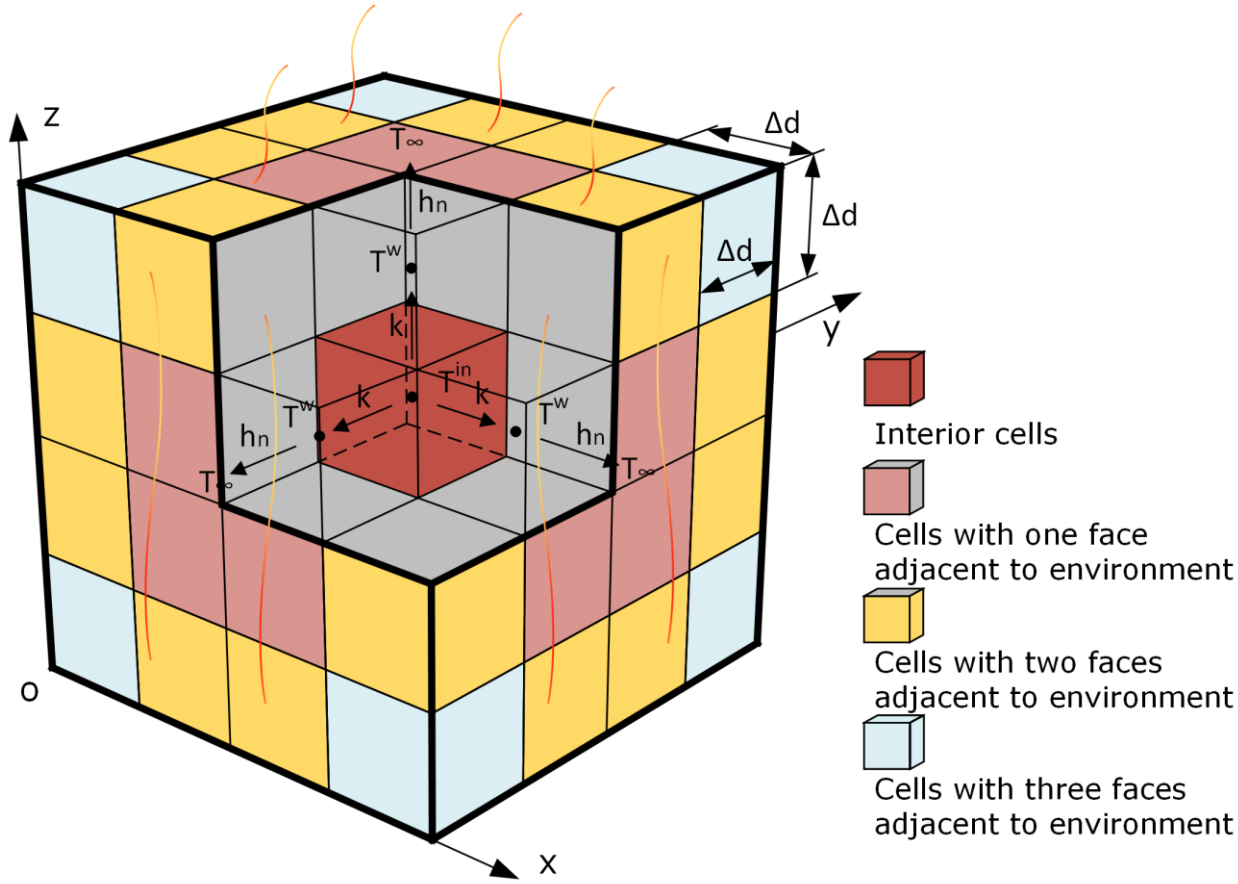

Figure 4.3 Schematic of finite difference method in numerical solution of heat transfer.

The laser energy Q_l in Equation (4.1) is calculated by the definition of energy absorbed by material in given area and time as follows [151]

$$Q_l = \beta(\Delta d)^2\Delta t\eta I, \tag{4.8}$$

where β is the laser absorptivity of material (0.3 for Ion-based alloy under wave length of $1\mu m$ [152]), Δt is the calculation time step, η is the attenuation function and I is the laser intensity defined by the energy in unit area and time. The

attenuation function η describes the remaining of the laser intensity I after absorbed by the material along the penetration path and can be written as [152]

$$\eta = exp\left[-C_{ab}\left(h(v_s, v_f) - z\right)\right], \tag{4.9}$$

where h is the height of bulge, C_{ab} is absorption coefficient [152] which is the material property that describes the extent of absorbing radiation (More descriptions in Section 4.5.1 Geometrical profiles model validation). Moreover, the processing parameters will be the factors of the energy absorption in such a way: (i) the scanning speed determines the dwell time, i.e. the accumulation of Equation (4.8) and (ii) the combination of scanning speed and wire feed rate determines the mass of material that absorbs the energy, i.e. the attenuation of Equation (4.9).

The laser intensity I in Equation (4.8) follows the super Gaussian distribution written as [48]

$$I = \frac{2^{1/n} nP}{\pi r^2 \Gamma(\frac{1}{n})} exp\left[-2\left(\frac{(x - x_l)^2 + (y - v_s t_i)^2}{r^2}\right)^n\right], \tag{4.10}$$

where P is the laser power, r is the radius of laser beam, n is the super Gaussian order and Γ is the Gamma function. Laser beam radius r is different at each cross section written as [48]

$$r = r_w \sqrt{1 + \left(\frac{d_w}{d_{RG}}\right)^2}, \tag{4.11}$$

$$d_{RG} = \frac{\pi r_w^2}{\lambda M^2}, \tag{4.12}$$

where r_w is the radius at waist, d_z is the distance from waist, d_{RG} is the Rayleigh Range, λ is laser wavelength, and M^2 is beam propagation factor. Super Gaussian order n is characterized using Lorentz function [48]

$$n = \frac{A_L}{B_L + d_w^2}, \tag{4.13}$$

where A_L and B_L are constants calibrated by laser measurement ($A_L = 5.53 * 10^{-4}$ and $B_L = 6.91 * 10^{-5}$). The Gamma function Γ is written as [153]

$$\Gamma(x) = \int_0^\infty e^{-t} t^{x-1} dt, \tag{4.14}$$

Along the propagation direction, only the possible useful section from 10mm above the waist to 20mm below the waist is extracted for laser model validation (see Figure 4.4a). Data are restored from the cross sections from A-A to D-D (see Figure 4.4b). As can be seen, the output laser energy intensity follows super Gaussian distribution, i.e. the intensity at the laser spot distributed in flat-top function (see Figure 4.4b A-A) while the intensity gradually evolves to normal Gaussian function as extending along z axis (see Figure 4.4b from B-B to D-D). Under the need of the model validation in laser intensity, calculation results from Equation (4.10) are put together with experiment results. The model precisely mimics the laser intensity distribution in reality.

Based on above, the temperature in each cell is calculated by heating effect of Equations (4.1-4.3).

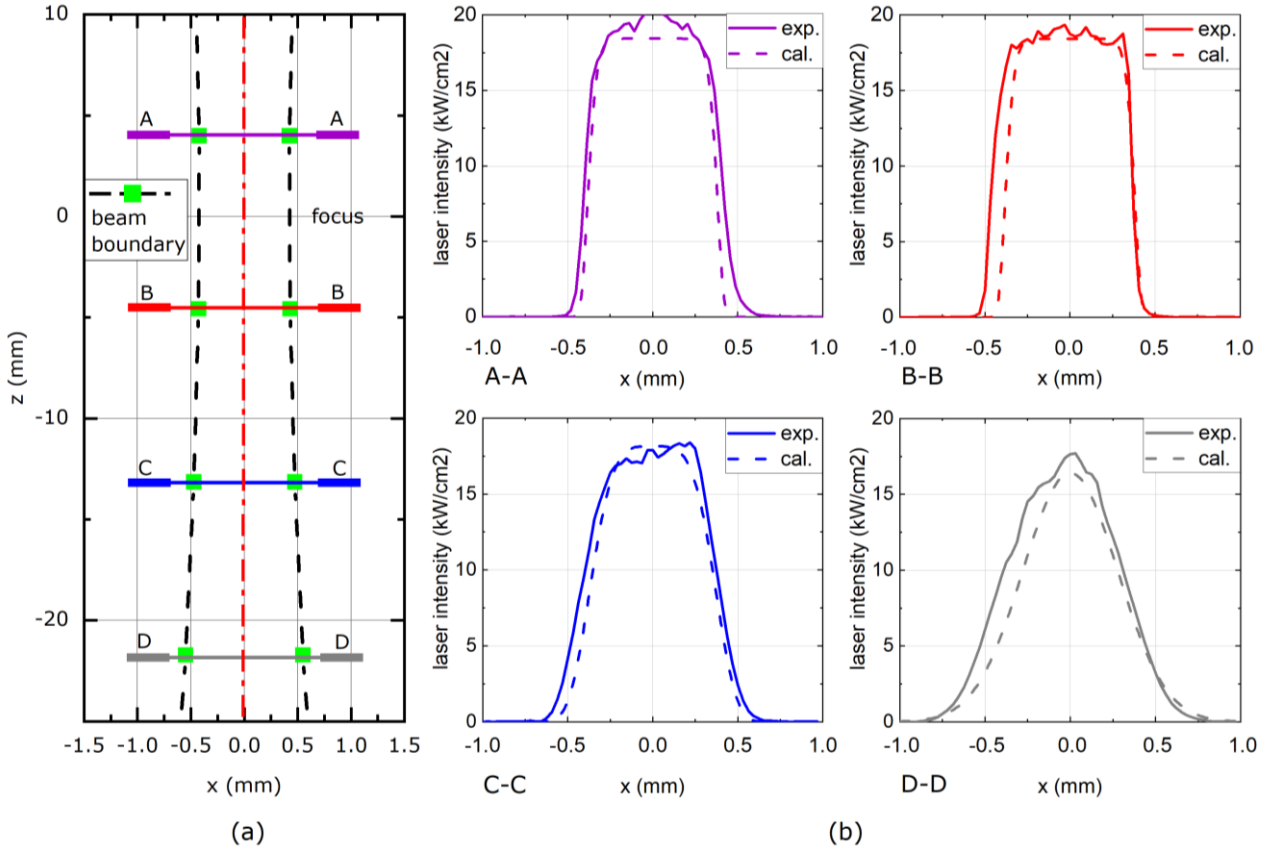

Figure 4.4 Laser intensity tested under power of 1 kW shown in aspects of: (a) the outline of the laser, (b) laser intensity at cross sections of A-A with flat-top profile and from B-B to D-D evolved to the normal Gaussian profile gradually.

4.3.3 Calculation of bulge profile

Based on the temperature field, the bulge profile can be calculated.

Based on the capillary theory [154], the capillary force counteracts the gravitational influence on fluid units for the liquid system within the capillary length $\lambda_c = \sqrt{\gamma/\rho g}$, where γ is the surface tension, ρ is the density of fluid and g is the gravity acceleration. According to the Laplace's equation [154], the curvature of the outer surface is constant. As a result, the bulge deposited on a horizontal surface forms the cross-section profile of arc whose edge intersects

the substrate with the contact angle θ. With the same contact angle θ, a series of arc in similarity are produced. To form the exact profile, the height h is selected as another determinant parameter. Based on the geometrical relation of the arc, the profile of bulge is written as

$$x^2 + \left(z + \frac{hcos\theta}{1-cos\theta}\right)^2 = \left(\frac{h}{1-cos\theta}\right)^2, \tag{4.15}$$

where $0° < \theta < 180°$.

Based on geometrical conversion of an arc, the height h is calculated as

$$h = \sqrt{\frac{S(1-cos\theta)^2}{\theta - \frac{1}{2}sin2\theta}}, \tag{4.16}$$

where θ is the contact angle and S is the cross-section area of the cladded bulge.

The cross-section area S in Equation (4.16) can be considered equal to the wire volume melt by laser energy per unit time and length as Equation (4.17). This means, if the laser energy is high enough to melt all fed-in wire, the cross-section area S should be fully melt material as $\frac{\pi R_w^2 v_f}{v_s}$, while if the laser energy is not enough, the cross-section area S should be partially melt material as $\frac{\beta P}{\rho v_s\left(L_f + C_p(T_m - T_{aver})\right)}$.

$$S = \min\left(\frac{\pi R_w^2 v_f}{v_s}, \frac{\beta P}{\rho v_s\left(L_f + C_p(T_m - T_{aver})\right)}\right), \tag{4.17}$$

where v_s is the scanning speed, v_f is the wire feed rate, R_w is the radius of wire, and T_{aver} is the average temperature at the cross section.

According to the Young's law [154], which describes the equilibrium of tensions at interface, the contact angle θ is related to the surface tension γ, i.e. the contact angle θ is the monotonic function of γ expressed as [155]

$$\cos\theta = A_C - B_C\gamma, \tag{4.18}$$

where the surface tension γ is dependent on temperature (More descriptions in Section 3.5.1 Geometrical profiles model validation). Please note Equation (4.18) was based on the assumptions including (i) the effect of melt pool wall of supporting bulge liquid is the same as the one of flat solid surface and (ii) the melt and deposited bulge does not solidify until contact angle reaches an equilibrium (More descriptions in Section 4.5 Geometrical profiles model validation).

According to the Eötvös rule, the surface tension γ is related to temperature written as [156]

$$\gamma V^{\frac{2}{3}} = k_c(T_C - T_R), \tag{4.19}$$

where V is the mole volume of material, k_c is the constant for Eötvös rule, T_C is the critical temperature of material (At the critical temperature the surface tension is zero) and T_R is one reference temperature ($V = 7.09 * 10^{-5}L/mol$, $k_c = 2.1 * 10^{-7}J/(K * mol\text{^}(2/3))$ and $T_C = 8500K$). The reference temperature T_R is the average temperature of melting zone at the current cross section because the Marangoni flow of melt liquid would lead to drastic heat exchange, and then uniformise the cross section temperature [157].

Based on above and making appropriate substitutions ((4.19)→(4.18)→(4.15) and (4.17)→(4.16)→(4.15)), the cross-section profile of bulge is obtained by Equation (4.15).

4.3.4 Calculation of melt pool profile

The calculation of melt pool profile, which, to the best knowledge of the authors, has not been reported before. The geometric profile of the melt pool has a stabilizing effect on the cladding layer, just like the root of the tooth has a stabilizing effect on the tooth, and the foundation has a stabilizing effect on the building. When it is necessary to model the structural sustainability of the workpiece after cladding, the predicted geometric profile of the melt pool will come to use. Therefore, the calculation of the melt pool profile is absolutely necessary.

Interfacial tension exists at the interface between any two different phases. There is a thin sticky layer between the melt pool and the substrate named mushy zone [158], can be assumed as a different phase of fluid. Hence, at the interface between the melt pool and the mushy zone, the melt pool profile is modelled by the analytical solution of the interfacial tension written as [159]

$$\frac{d\varphi}{ds} = \frac{\rho g c_m (z_m - z)}{\gamma_{sl}} - \frac{sin\varphi}{x} + \frac{2}{R_0}, \tag{4.20}$$

$$\frac{dx}{ds} = cos\varphi, \tag{4.21}$$

$$\frac{dz}{ds} = sin\varphi, \tag{4.22}$$

$$\varphi(0) = x(0) = 0, \qquad z(0) = z_m, \tag{4.23}$$

where z_m is the lowest point of melt pool obtained from temperature field, coefficient c_m is the modification factor to ensure the curve constructed by Equations (4.20)-(4.23) align with the curve of the bulge, γ_{sl} is interfacial tension and R_0 is the curvature radius at melt pool bottom. In addition, $\rho g(z_m - z)$ in Equation (4.20) measures the hydrostatic pressure difference from the melt pool bottom to the calculated point.

Under the same assumptions as Equations (4.20)-(4.23), the interfacial tension γ_{sl} in Equation (4.20) has been correlated to temperature with high accuracy written as [160]

$$\gamma_{sl} = \frac{k_B T_m}{\Omega_{sm}^{2/3}} \left(A_I + B_I \frac{T_R}{T_m} \right), \tag{4.24}$$

where T_m is the melting point, T_R is the reference temperature calculated from Equation (4.1) in Section 4.3.2, k_B is the Boltzmann constant, and Ω_{sm} is the atomic volume at the melting point ($A_I = 0.228$, $B_I = 0.3135$, $k_B = 1.38 * 10^{-23} J/K$ and $\Omega_{sm} = 1.15 * 10^{-25} m^3$).

Under the same assumptions as Equations (4.20)-(4.23), half width $w/2$ multiplied with the ratio δ based on numerous preliminary experimental observations, i.e.

$$R_0 = \delta w/2, \tag{4.25}$$

where δ can be determined by one trial and it is specific for each process setup (e.g. wire and substrate material type); hence, this can be considered as a part of a calibration procedure ($\delta = 0.8$). Based on above, the melt pool profile is obtained by Equations (4.20)-(4.23).

4.3.5 Flowchart of modelling

The flowchart of the full profile calculation is presented as Figure 4.5 to conclude the modelling steps. All the equations mentioned above are transferred into codes in MATLAB.

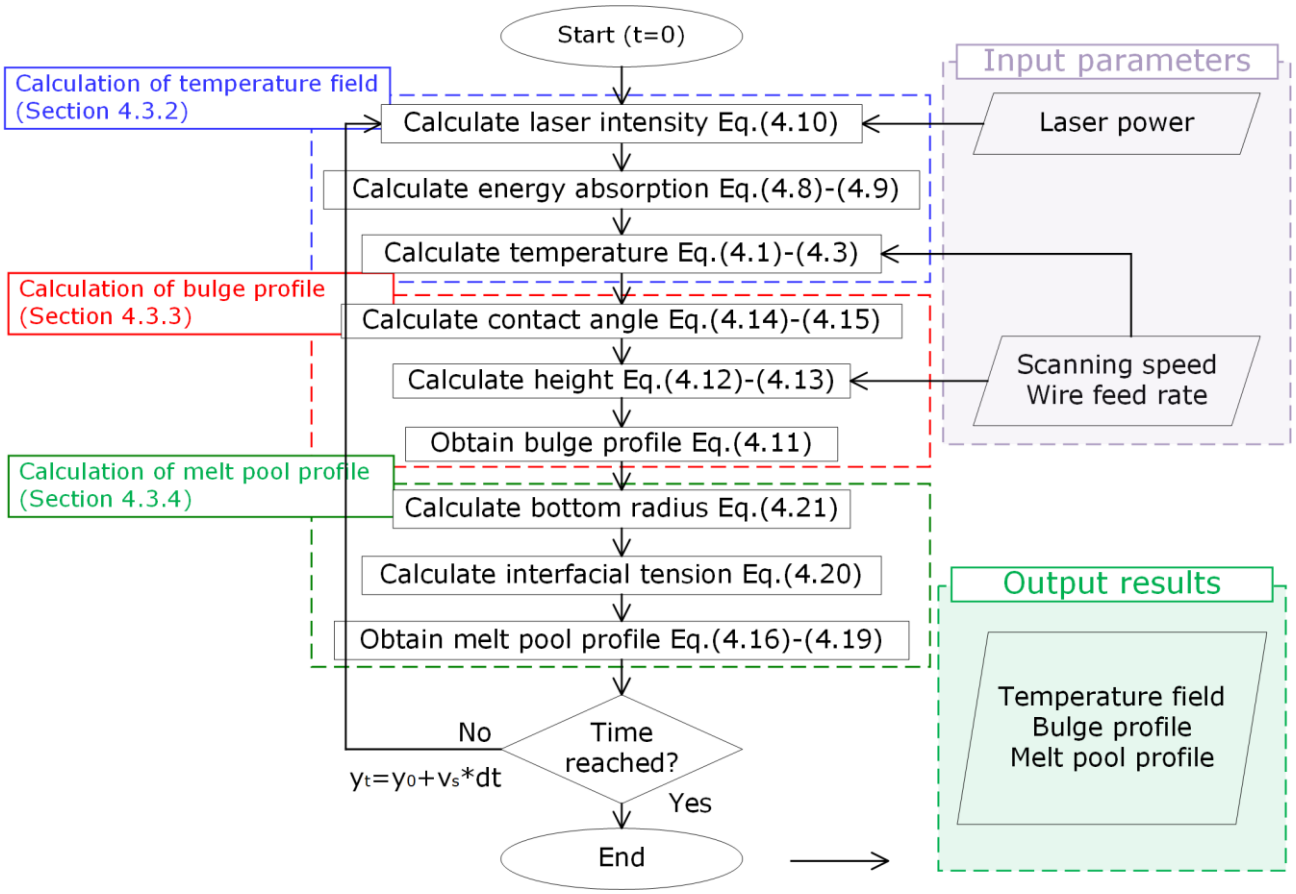

Figure 4.5 Flowchart of theoretical modelling to calculate the temperature field, the bulge profile and the melt pool profile by inputting processing parameters including the laser power, the scanning speed, and the wire feed rate.

4.4 Experimental setup

To validate the proposed model that predicts cladding affected area, a set of experiments were performed.

During cladding, the employed parameters for cladding experiments (see Table 4.1) were based on single-variable principle as it enabled robust evaluation of the model in relation to the described physics of the process (described in Section 4.3). To obtain a steady and smooth track, laser power ranged from 0.8kW to 2.0kW, scanning speed ranged from 0.175m/min to 0.22m/min and wire feed rate ranged from 0.3m/min to 0.9 m/min at the fed in angle of 45 degrees. Each track was kept 60mm in length to ensure reaching stable thermal status and also for the convenience of selecting the smooth section to cut samples for analysis. Two neighbouring tracks had the interval of 15mm and 15 minutes to avoid any thermal influence between the trials. N_2 protection gas kept feeding onto the cladding surface steadily (the above setup, see Figure 4.6).

Table 4.1 Track parameters for WLC experiments

Track	$P\ (kW)$	$v_s\ (m/min)$	$v_f\ (m/min)$
1	0.8	0.1	0.6
2	1.2	0.1	0.6
3	1.6	0.1	0.6
4	2.0	0.1	0.6
5	1.6	0.25	0.6
6	1.6	0.225	0.6
7	1.6	0.2	0.6
8	1.6	0.175	0.6
9	1.6	0.1	0.3
10	1.6	0.1	0.5
11	1.6	0.1	0.7
12	1.6	0.1	0.9

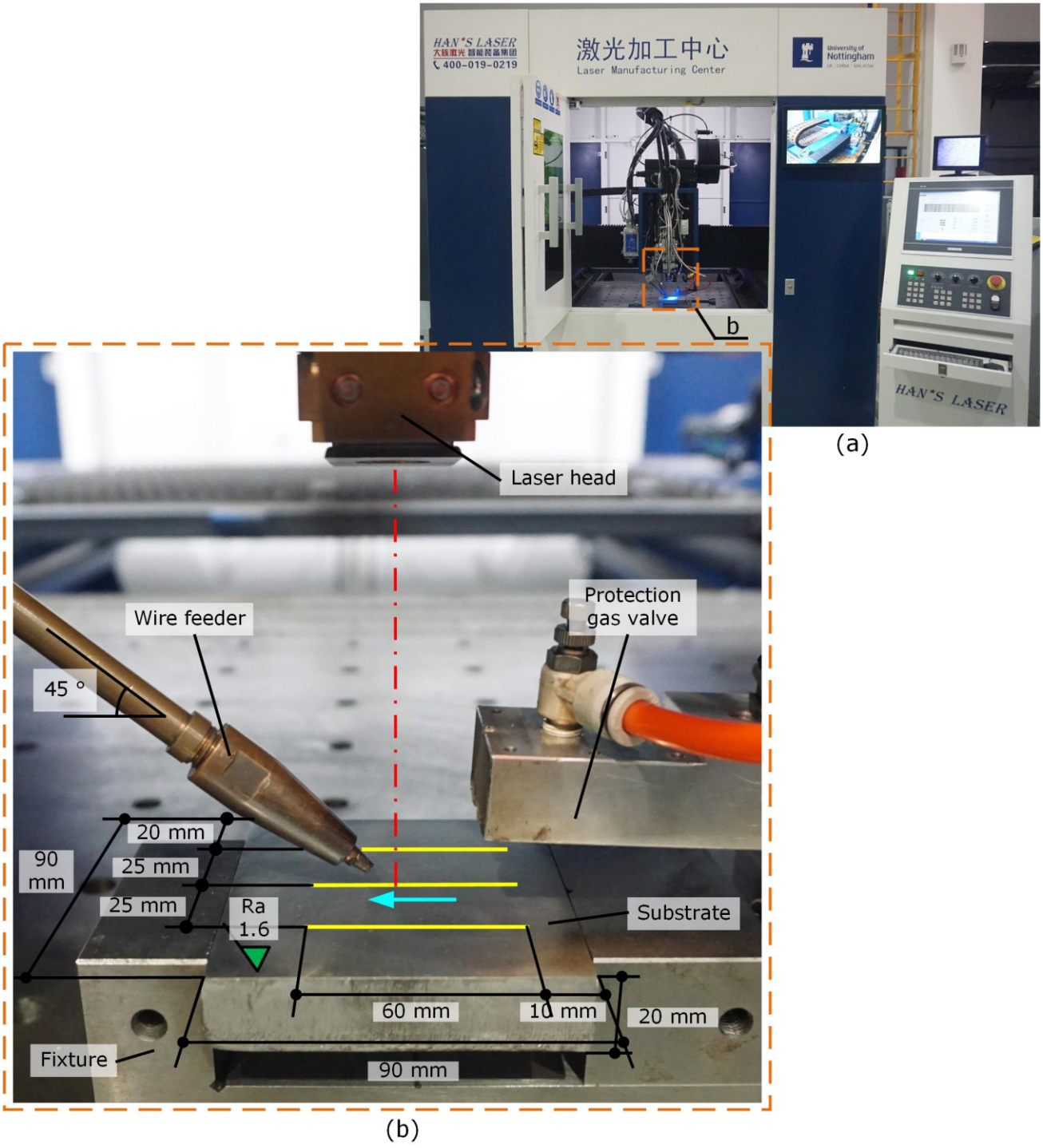

Figure 4.6 Illustration of experiment: (a) laser manufacturing centre and (b) cladding setup.

4.5 Model validation

Figure 4.7(a-d) shows that in general the calculated full track profile is close to the experimental ones when changing the laser power, where the maximum relative error is 15% at the melt pool. The alignment of measured and simulated profile depends on the laser position marking on the substrate before doing the cladding. The increase rate of melt pool depth when changing the laser power from 0.8kW to 1.2kW (see Figure 4.7a and b) is larger than from 1.2kW to 2.0kW (see Figure 4.7b to d). When the laser power is low, the contact angle of bulge metal is large because the temperature is low. As laser power is increased, the temperature and the contact angle of bulge metal reach a heat balance because larger portion of heat at high temperature than low temperature escapes from the bulge metal to the substrate metal through conduction Equation (4.2) and to the environment through convection and radiation Equation (4.3).

Figure 4.7(e-h) shows that in general the calculated full track profile is close to the experimental ones when the scanning speed is changed, where the maximum relative error is 19% at the bulge. The deviation of model may come from the assumption that some thermal properties of material are constants while they vary with temperature in actual condition. Some properties may increase while some others may decrease when varying scanning speed or wire feed rate. Moreover, the higher errors of bulge, compared to laser power group (a-d), can be explained with the energy density index Pv_s/v_f based on Equation (4.17). Higher energy density causes higher thermal expansion of melt material and forces material from melt pool to bulge. Yet the material in melt pool solidifies

earlier than bulge. Therefore, more material stays in bulge and then causes the larger cross section areas in experiment. Compared inside the scanning speed group (e-h), both the calculated and experimental results indicate the same tendency, i.e. when scanning speed decreases, the bulge cross-section areas increase accordingly due to the increase of material based on the Equation (4.17). The contact angles also increase with decrease of temperature based on Equations (4.18)-(4.19) due to the decrease of energy density.

Figure 4.7(i-l) shows that, in general, the calculated full track profile is close to the experimental ones when the wire feed rate is changed, where the maximum relative error is 25% at the melt pool and occurs mainly in the necking section of melt pool; this means the necking section (the transition section with smallest width between bulge and melt pool) is highly sensitive to any error because it is close to the centre of profile, i.e. reference distance is shorter than other sections, then the relative error is higher. Another explanation about the larger errors under different wire feed rate is also the energy density. High energy density has the same effect on (i-j) as in group (e-h) which has been explained. Low energy density affects the continuity and smoothness of track which are highly dependent on the balance of energy and material. When the bulge is not steady, the melt pool should be unsteady because the bulge affects the energy reaching the melt pool. It is suggested that the model works within the range of cladding steady track, which can be referred to the work of identifying steady range [61]. Compared inside the wire feed rate group (i-l), both the calculated and experimental results indicate the same tendency, i.e. when wire feed rate increases, the bulge cross-section areas increase accordingly due to the increase

of material based on the Equation (4.17). Because more material disperses the energy and then the temperature of the melt metal in the bulge decreases, the contact angles increase, which are exhibited by calculations and experiments. Moreover, the depth of melt pool tends to decrease in the experiments and the model reacts accordingly. It means that the increase of material does mitigate the extent of laser penetrating through material based on Equation (4.9).

Although the absorption coefficient C_{ab} in Equation (4.9) is the material property, it also changes when the surface geometry of melt pool bottom varies, referred to the phenomenon of conduction-to-penetration mode change [66, 161] due to laser entrapment [162]. Then $1/C_{ab}$ is called penetration coefficient. In conduction mode, the radiation hits the bottom of melt pool and reflects out to the atmosphere, then the penetration coefficient $1/C_{ab}$ is lower because the reflected energy does not continue to penetrate through material. In penetration mode, the radiation hits the bottom of melt pool but bounds around inside the melt pool, then the penetration coefficient $1/C_{ab}$ is higher because all the energy stays inside the material and are directed to deeper region. This mode change occurs in the model validation. Track 1 (see Figure 4.7a) is in the conduction mode while other tracks (see Figure 4.7b - i) experience from the conduction mode to the penetration mode. The transition factor is the ratio of half width and depth $w/2d$. At the beginning of cladding when $w/2d \geq 1$, penetration coefficient $1/C_{ab}$ is one value (calibrated by one trial, i.e. track 1), namely $1/C_{ab}(d_1)$, which is in conduction mode. When energy absorption is high enough leading to $w/2d < 1$, penetration coefficient $1/C_{ab}$ increases to another value (calibrated by one trial, i.e. track 2), namely $1/C_{ab}(d_2)$, which is in penetration mode.

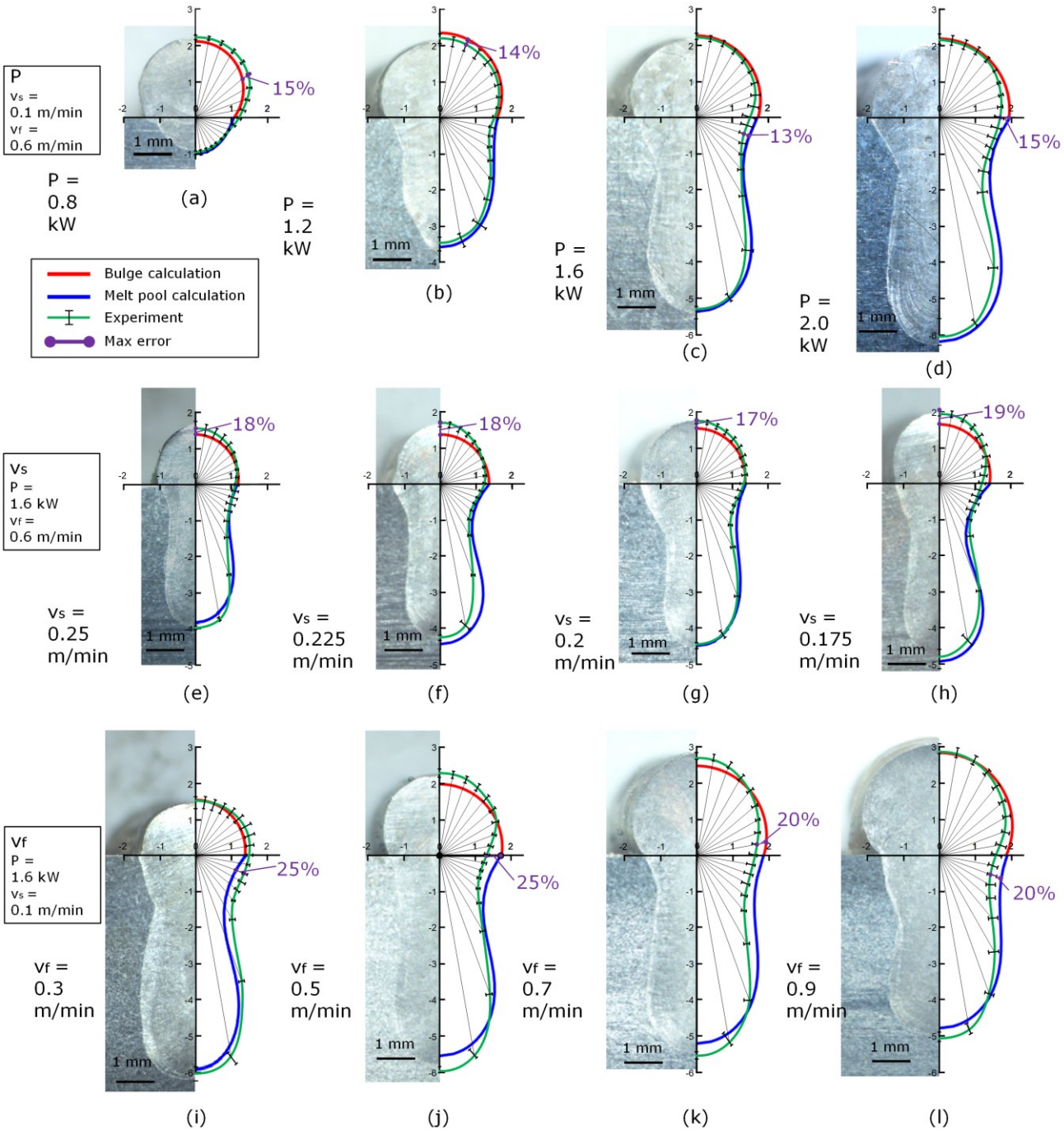

Figure 4.7 Cross sections of the cladding affected area for varying process parameters: laser power P (a) 0.8kW (b) 1.2kW (c) 1.6kW (d) 2.0kW at constant (v_s =0.1m/min and v_f =0.6m/min); scanning speed v_s (e) 0.25m/min (f) 0.225m/min (g) 0.2m/min (h) 0.175m/min at constant (P =1.6kW and v_f =0.6m/min); wire feed rate v_f (i) 0.3m/min (j) 0.5m/min (k) 0.7m/min (l) 0.9m/min at constant (P=1.6kW and v_s=0.1m/min).

The unknown variables A_C and B_C in Equation (4.18) are calibrated by two sets of the contact angle θ and the temperature T. One set is obtained by increasing laser power to observe boiling phenomenon, then the temperature T is the boiling point T_b. The other set is obtained by decreasing laser power to observe material being barely melted, then the temperature T is the melting point T_m. For both sets of temperature, the contact angles θ are measured by cutting and measuring from cross section, namely θ_b and θ_m. As a result,

$$A_C = \cos\theta_m + (\cos\theta_m - \cos\theta_b)\frac{T_c - T_m}{T_b + T_m}, \tag{4.26}$$

$$B_C = \frac{V^{\frac{2}{3}}(\cos\theta_m - \cos\theta_b)}{k_c(T_b + T_m)}, \tag{4.27}$$

where $A_C = 2.299$ and $B_C = 3.606$ under material properties in this thesis.

For the assumption of surface tension calculation in Equation (4.18), it can be proved by the schematic and experimental evidence as follows:

1 - As shown in Figure 4.8a, because the liquid is incompressible, the support of melt liquid in melt pool to bulge can be considered equivalent to the support of flat surface.

2 - As shown in Figure 4.8b, the melt track reaches equilibrium before solidification (see dash line marked on the monitor).

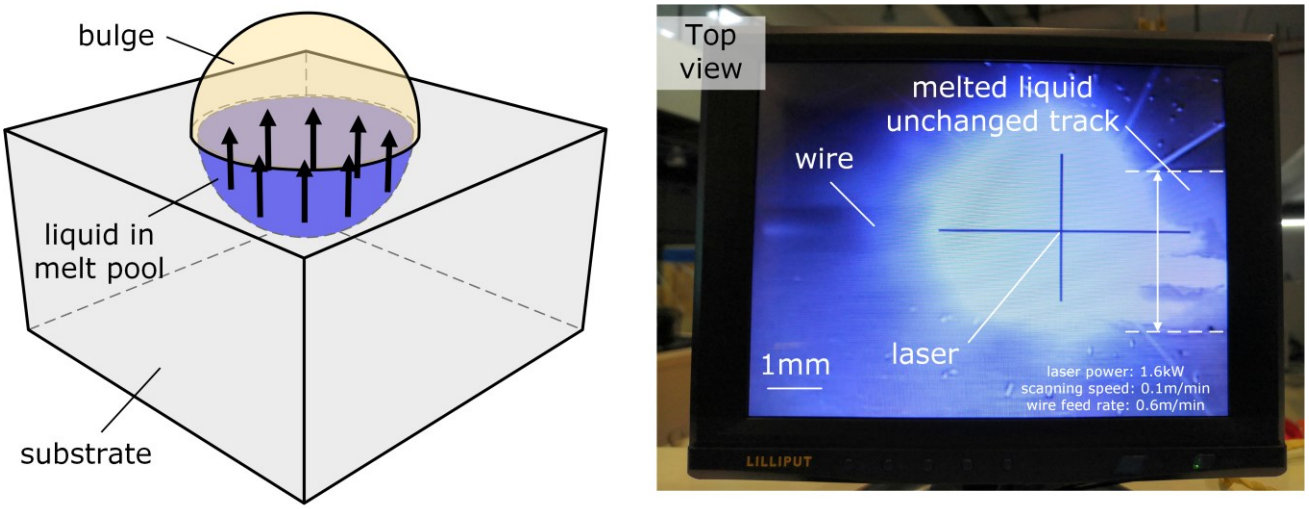

Figure 4.8 Schematic of (a) bulge supported by melt pool and (b) experimental image of track that has reached equilibrium before solidification.

The cell size Δd and time step Δt are important because they determine the calculation accuracy. Moreover, these two parameters do not affect calculation accuracy independently based on Equation (4.28) [150]: the time span cannot surpass the thermal conduction distance. Several runs of simulations proved that Δd with the value of 0.1 mm and Δt with the value of 0.1 ms can achieve a good balance between calculation accuracy and efficiency (see Figure 4.9a). Please note further reduced cell size Δd (even with the reduction ratio of 50%) can only lead to result difference of 0.18% but with highly increased computation effort by 1500% (see Figure 4.9b).

$$\Delta t \leq \frac{\rho C_p (\Delta d)^2}{4k}. \tag{4.28}$$

The model is validated by geometrical profiles. Yet more information can be found with the model.

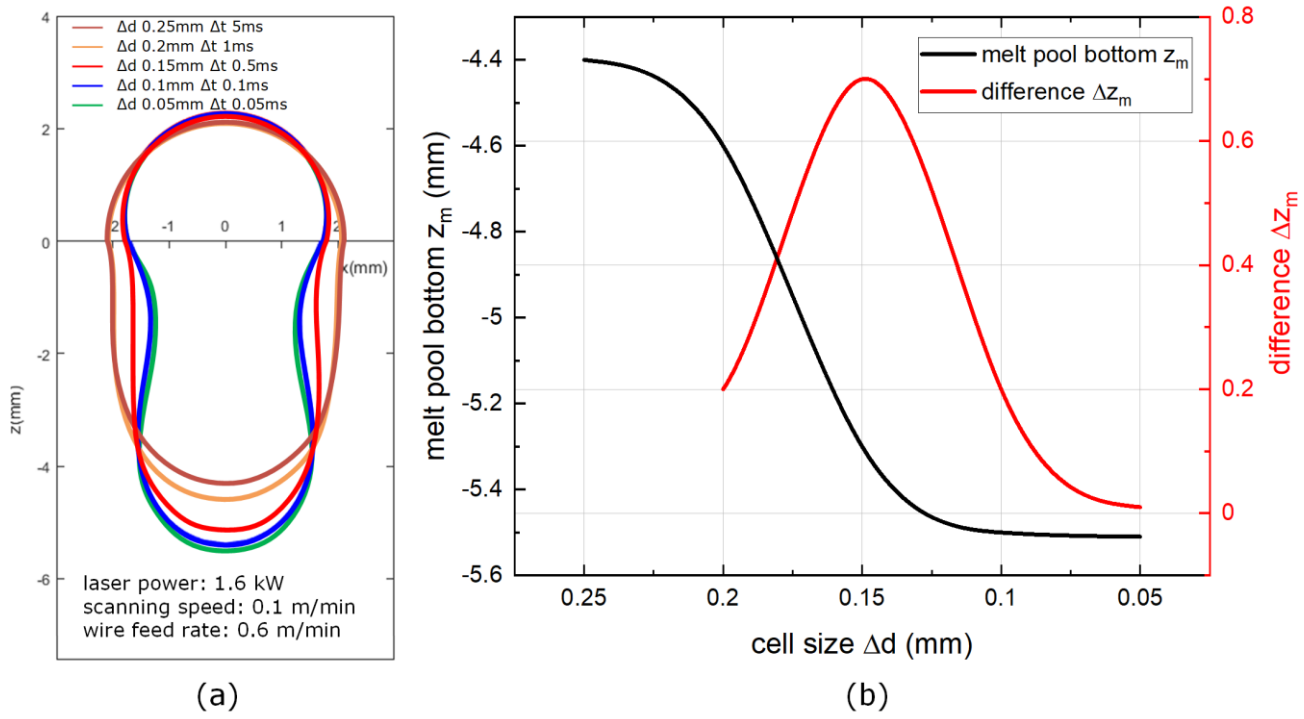

Figure 4.9 Sensitivity analysis and determinations of cell size Δd and time step Δt: (a) profile variation and (b) difference convergence.

4.6 Further discussions based on the model

Some metallurgical observations fit with the performance from the model when the solidification pattern is calculated with the model. The cooling rate (dT/dt) at the cell (x, y, z) at the time when it reaches melting point is plotted (see Figure 4.10a), where the points with the same cooling rate is classified in the same region although they solidify at different time. Then lowering the classification resolution will separate the overall cooling rate plot into several characteristic regions (see Figure 4.10b). The vast area above melt pool bottom is in relatively slower cooling rate. The faster cooling rate appears at the bottom of melt pool. Compared to microstructure in separate regions (see Figure 4.10c), the even temperature region owns the equiaxed grains, which are generated due to even

temperature (see Figure 4.10d and e) with the grains in the same size. The melt pool bottom region owns dendritic grains (see Figure 4.10f), which are generated due to fast cooling rate and large temperature gradient [163].

The microhardness also proves these observations. Figure 4.11a shows target points of hardness test which are selected according to the heat transfer path and probable cooling rate. Point A is the reference point at the substrate selected at a corner of the sample where heat affected zone won't reach. Point B is in the heat affected zone where heat is conducted from melt pool above. Point C collinear with base line is located where points surrounding it are waiting to cool down and heat conduction is highly dependent on temperature variation. Point D is cooled by conduction with substrate and point E is cooled by convection of protection gas above.

Figure 4.11b shows respective hardness values. From a preliminary observation, the hardness of all targets is higher than reference point, which means cladding universally brings hardening to substrate, contrast to some observation [164]. This hardening effect is most significant at point C where cooling rate is highest by conduction. Compared to point C, hardness at point B and D are lower due to the lower cooling rate by convection of protection gas and by heat transferred from melt pool respectively. Hardness at point D is most suspicious because it may be higher or lower than point C.

Till this moment, the potential of the model is proved in geometrical profiles and metallurgical aspects. To further approve the validated model, the cases for applications are presented next.

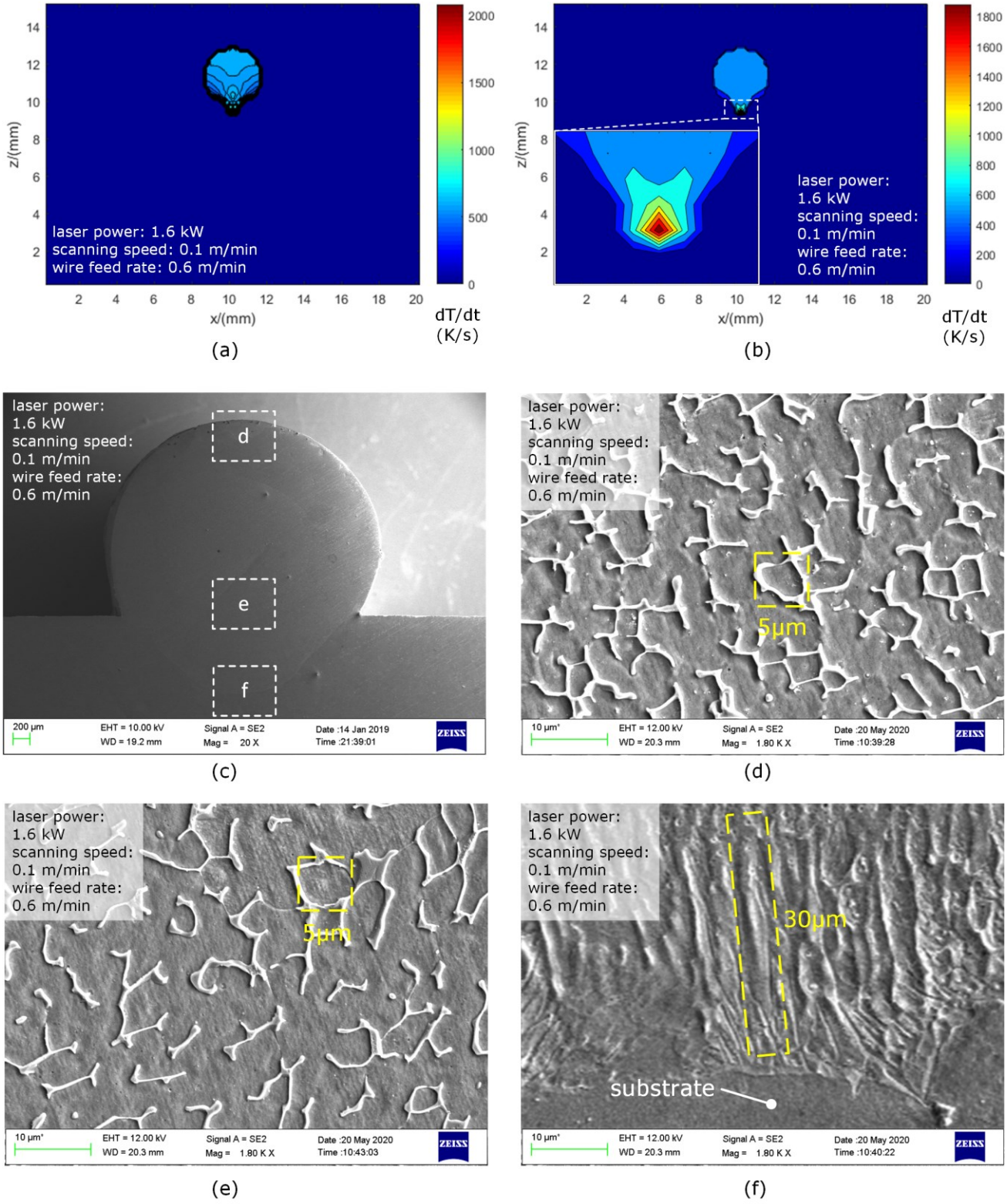

Figure 4.10 Solidification pattern: (a) overall cooling rate plot, (b) regions of cooling rate plot, (c) regions of observation, (d) region near the top surface, (e) region at the inner of bulge, and (f) region near the bottom surface.

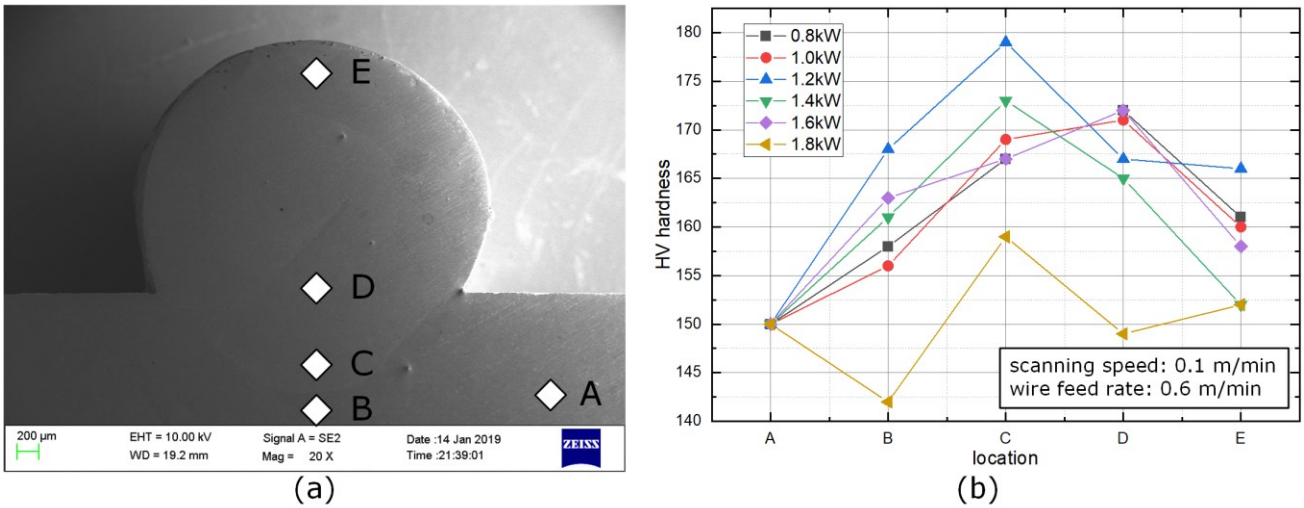

Figure 4.11 Hardness value at different targets under different laser power: (a) measurement points, and (b) HV hardness at the measurement points.

4.7 Model application cases

4.7.1 Prediction of defocus distance on dilution

The first application of the model is to predict the dilution by setting the defocus distance. A mathematical expression for dilution was developed in terms of clad geometric elements [165]. Contrast to welding [166] and sub-surface defects repairing [167], deep penetration of melt pool into substrate is not ideal in laser cladding [168]. To have shallow melt pool, a plausible option is to increase the defocus distance d_o (decreasing the laser power P may be one option [169] but the energy to melt wire material is the concern). By increasing the defocus distance d_o from 0mm to 40mm linearly (see Figure 4.12a), the dilution D decreases from 70% to 20% abruptly (see Figure 4.12b). But when the defocus distance d_o keeps increasing to 50mm, the dilution D drops to 0, meaning the additive material does not have proper bonding to the substrate. Increasing the

defocus distance d_o also leads to the transition of the bulge centre z_o (meaning stronger growth in vertical direction) and contact angle θ (meaning the body of bulge wider than the root of the bulge) (see Figure 4.12c and d). Without the model, this detailed description of process change can not be fulfilled and one can only obtain limited information by cutting cross sections through multiple material preparation procedures. This proposed model is superior to the one based on energy balance approach using regression analysis [170].

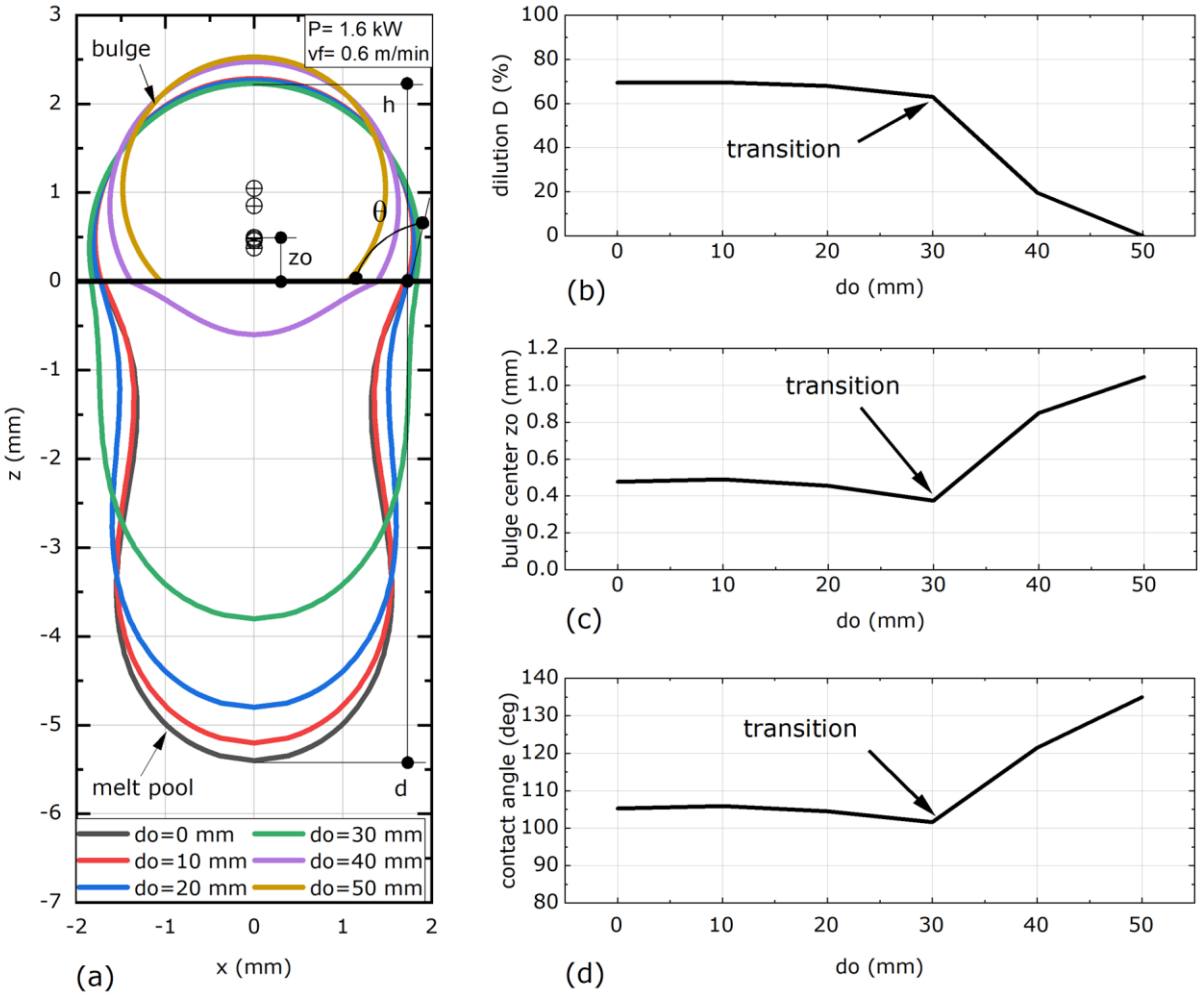

Figure 4.12 Profile at different defocus distance: (a) full profile of bulge and melt pool, (b) depth of melt pool, (c) vertical position of bulge centre, (d) contact angle.

4.7.2 Prediction of heat flow inside cladded track

The second application of the model is to predict the heat flow by calculating the temperature gradient. While the heat flow inside the material is impossible to detect in experiments, the proposed model is capable to provide detailed temperature on each cell (see Figure 4.13a and b) and heat flow direction (see Figure 4.13c).

Based on the heat flow direction and isotherm density inside the region enclosed by the melting isotherm (see Figure 4.13b), the melting region at the top of track dispersed heat outwards slower than the region at the wetting corner. As a result, the melted track has enough time to smoothen (driven by surface tension) any unsteadiness (e.g. the movement of wire feeding in) of the surface before the wetting region solidified. With the boiling region (enclosed by boiling isotherm) existing, the fluid inside the region must expand and move upwards until it reaches the top and is restrained by surface tension. The rising up fluid must escape backwards (towards the cladded track) because there is more space (than towards the wetting corner) for the movement. This movement will bring more heat backwards, further delaying the solidification.

After the thermodynamic condition is known, the thermostatics can also be deducted. Figure 4.13c shows the thermostatics inside the cladding zone based

on the calculation of the model. Obviously, it does not contain any fluid dynamics which will bring in the modelling complexity and time-consuming calculation. From the thermostatic condition, the bulge and melt pool profiles in the proposed model are calculated based on the average temperature in the melt liquid, any change of processing parameters (i.e. laser power, scanning speed and wire feed rate) will lead to the temperature change and reflect as the profiles change of bulge and melt pool. Besides, the melting isotherm marks the melt pool depth no matter it is shallow or deep. Traditionally, the deep melt pool is not acceptable because the dilution is large and the superior of the cladded surface is mitigated. However, the deep melt pool is able to directly repair any defects (e.g. cracks, if any existing) below the substrate surface.

In summary, this diagram supports the following items:

- The model is able to track solidification rate at each location.
- The model is able to correlate track profile to any processing parameter.
- The model is able to avoid the modelling complexity and time-consuming calculation of fluid dynamics.
- The model is able to predict melt pool depth which can be used for repairing.

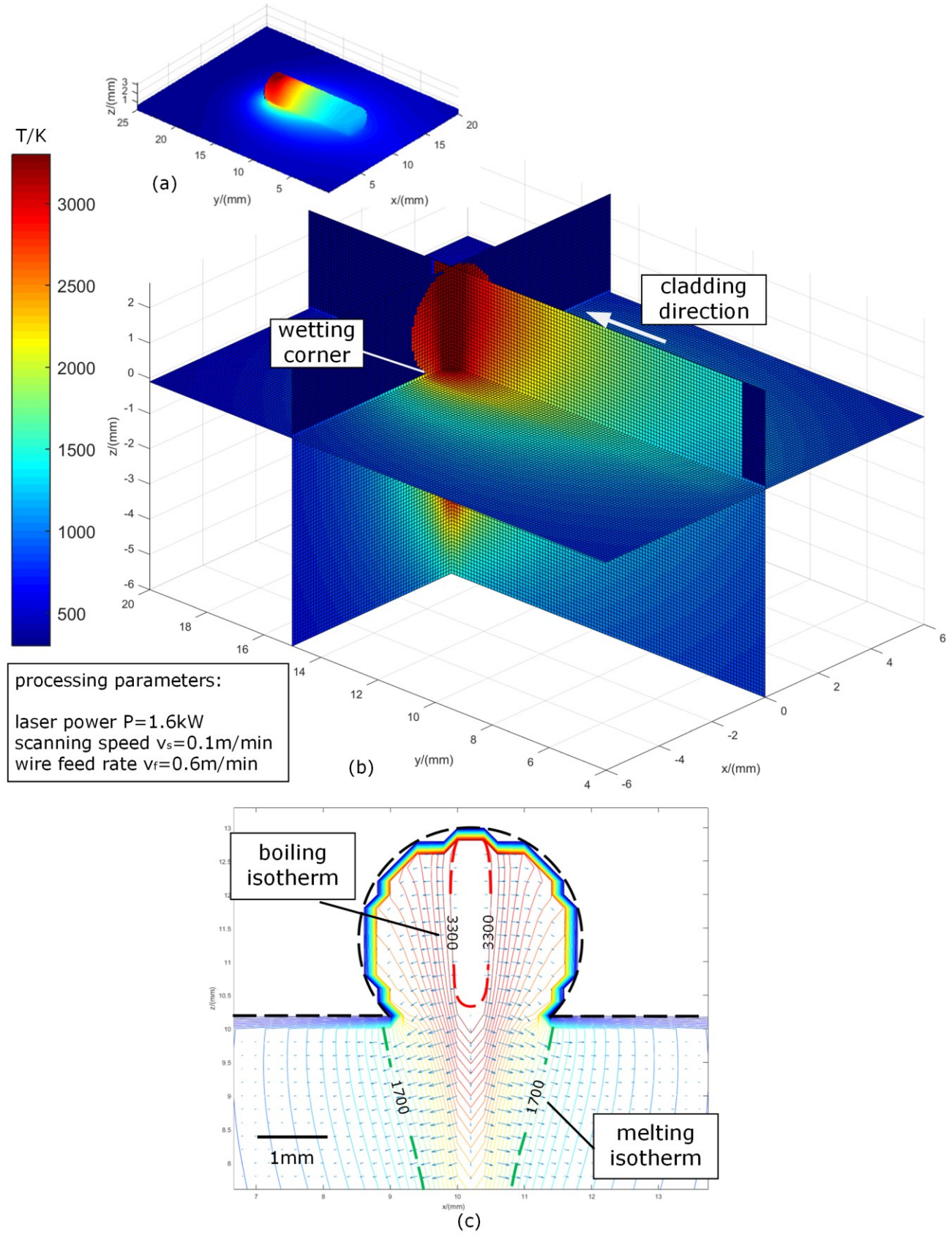

Figure 4.13 Calculation results of temperature field and heat flow in (a) isometric view, (b) slice view, and (c) cross sectional view.

4.7.3 Control strategy of single-track profiles with the change of scanning speed

The final aim of the proposed model is to facilitate the WLC process by an automated system (e.g. manipulator/machine tool) which offers the advantage of varying scanning speed with high accuracy and thus, enabling easy implementation of control strategies. Therefore, in this part, the outcomes of changing scanning speed during WLC process are presented as a way forward to use the models for process control. This means that the shape of the bulge and the melt pool will be dynamically controlled by only varying the scanning speed.

To prove this, the scanning speed is varied in a range (between 0.05m/min - 0.2m/min) that ensures track continuity (see Figure 4.14a and b) while the laser power and wire feed rate are kept constant at 1.6kW and 0.6m/min respectively; these process parameters are expected to yield stable process outputs (e.g. continuous and geometrically well-defined clads). After started, the scanning speed keeps constant at 0.1m/min at the first section (see y1-y2 in Figure 4.14a) to ensure cladding process under a relatively steady heat balance. Subsequently, the scanning speed decreases to 0.05m/min (see y2-y3 in Figure 4.14a) and then increases to 0.2m/min till the end (see y3-y5 in Figure 4.14a).

Under the continuous change of scanning speed, the cladding affected area is changing also continuously and smoothly in accordance with the dependencies highlighted by the previously presented models. Figure 4.14a shows that in general the calculated bulge height and melt pool depth are close to the experimental ones when the scanning speed is changed, where the maximum relative error is 30% at the bulge (see y2-y3 in Figure 4.14a). Both the calculated

and experimental results indicate the same tendency, i.e. when the scanning speed changes linearly, the bulge height follows the tendency of cross section area in Equation (4.17).

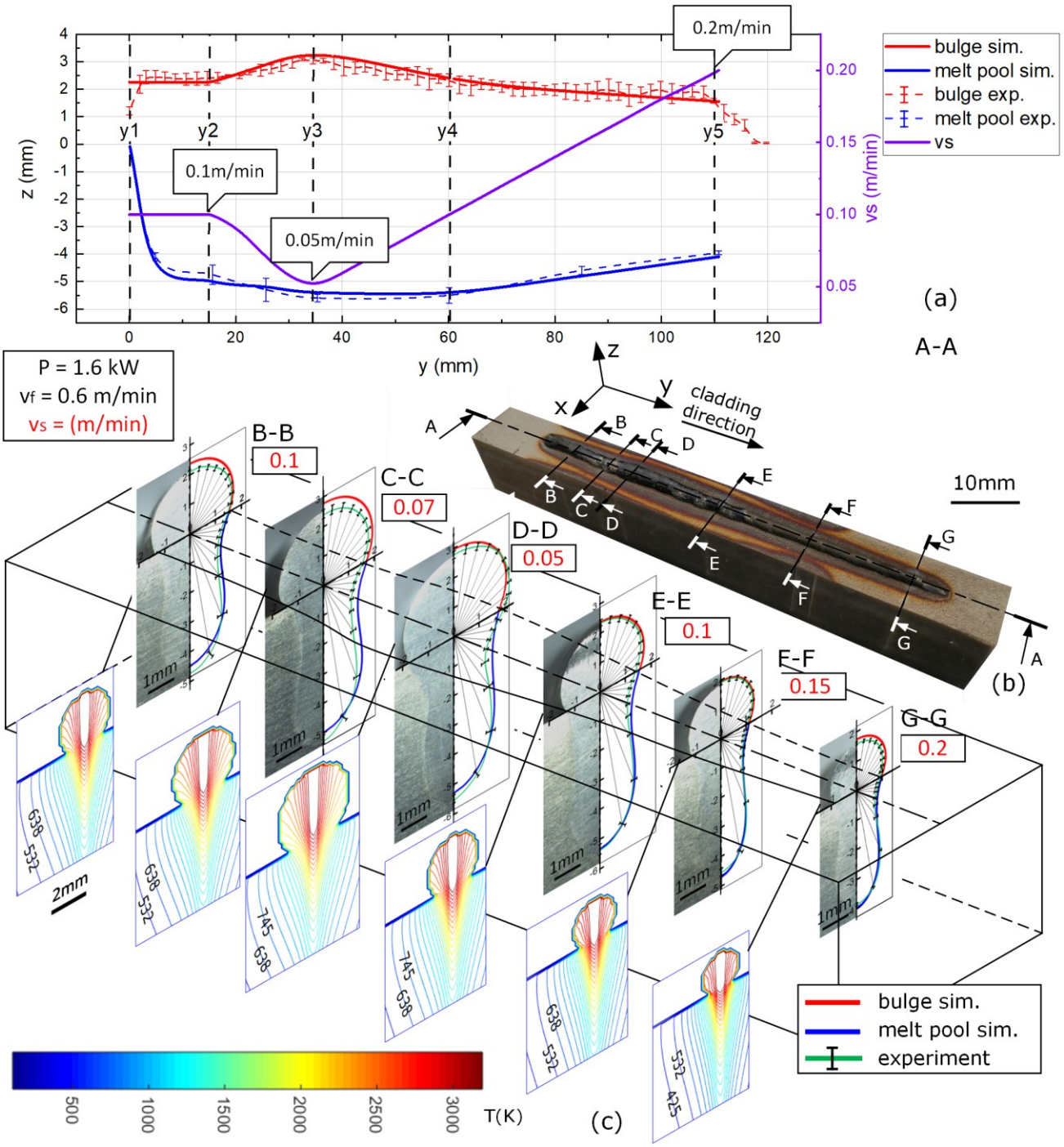

Figure 4.14 Control strategy of varied scanning speed, (a) bulge height in longitudinal direction obtained under CMM and melt pool depth in longitudinal

direction obtained by measuring cross sections, (b) cladding sample and (c) bulge and melt pool profiles at different cross sections under varied scanning speed.

The melt pool depth does not strictly follow the variation of scanning speed. This is caused by two aspects: i) On one hand, it takes time for a cross section to reach heat balance under one specific scanning speed. When the scanning speed changes continuously, the melt pool does not have time to reach the expected depth; ii) On the other hand, the variation of scanning speed leads to the material volume change in the same time. For example, when scanning speed decreases, the heat fluence increases. Yet in the same time, the bulge size increases, and the extra heat fluence is distributed by the extra material. As a result, the variation of melt pool depth does not have an obvious variation tendency.

Up to now, no generation varying clad surfaces by continuously altering the scanning speed has been reported. However, based on the proposed models this is now possible. Figure 4.14c shows that in general the calculated cross-section profiles (from B-B to G-G) are close to the experimental ones when the scanning speed is changed continuously, where the maximum relative error is 30% at the bulge (see Figure 4.14c C-C). If the proposed model is used to predict the temperature (see diagrams in Figure 4.14c), the bulge and the melt pool at any scanning speed continuously, it is likely there is some discontinuity when changing the scanning speed. While the model calculates all the bulges and melt pools continuously, although the movement of laser is continuous, the phenomenon occurring at one scanning speed is very likely affected by another

one (i.e. the steady-state conditions are not reached). For example, the abnormal section (see Figure 4.14c C-C) occurs probably because the scanning speed changes too fast which causes the mass of current section is pulled by the previous section due to surface tension. This phenomenon occurs when scanning speed change (either increase or decrease) above a certain rate that is dependent on the material properties and flux of input energy. The determinant factor is the change rate; less is the change rate, lower error occurs. To generate precise clad surface, the change rate of scanning speed needs to be considered, and in the present conditions, it should not be bigger than the rate at section y3-y4 because surface tension is happening. These observations are based on the proposed models (firstly employed to generate clads at constant parameters) but they enable making informed judgements on the sensitivity of the models when conducting the WLC in a dynamic mode (i.e. varying scanning speed).

The model, developed from principle, deduction, to validation, is complete in explanation. To conclude the process, the model is transformed into the GUI with input parameters and output results on the control panel to simulate the industrial application (see Figure 4.15). The necessary inputs should be only processing parameters, e.g. laser power, scanning speed, and wire feed rate, for the user convenience. Laser configuration and material type that contain a set of properties are imported while they can also be selected after storage in database (see Figure 4.16). Output results show the temperature field and geometrical profile in different views, giving operators the chance to evaluate the cladding

process and adjust the input parameters. This simplistic version of GUI demonstrates the purpose of the model while it can be further designed based on requirement.

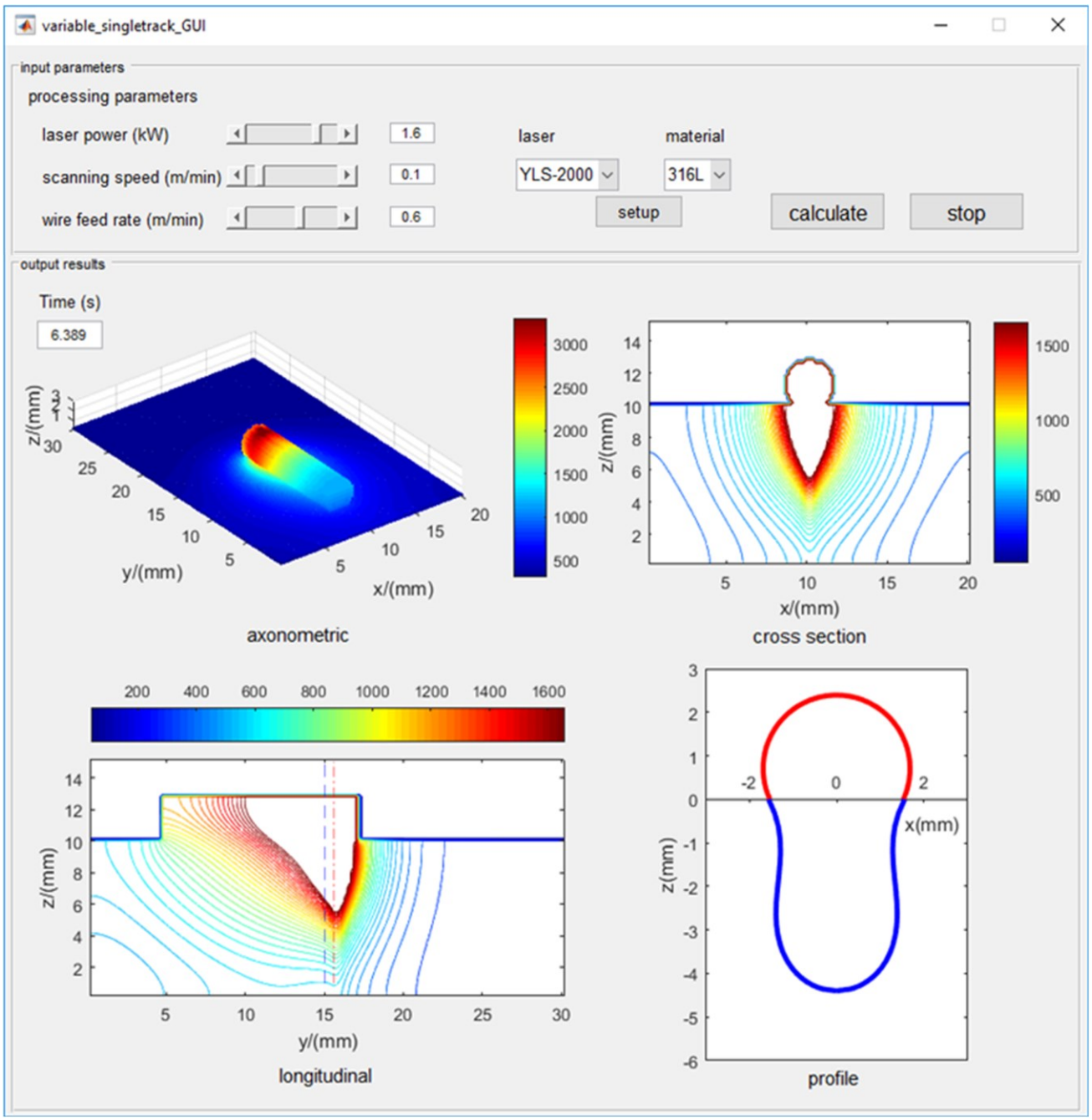

Figure 4.15 GUI control panel with built in model.

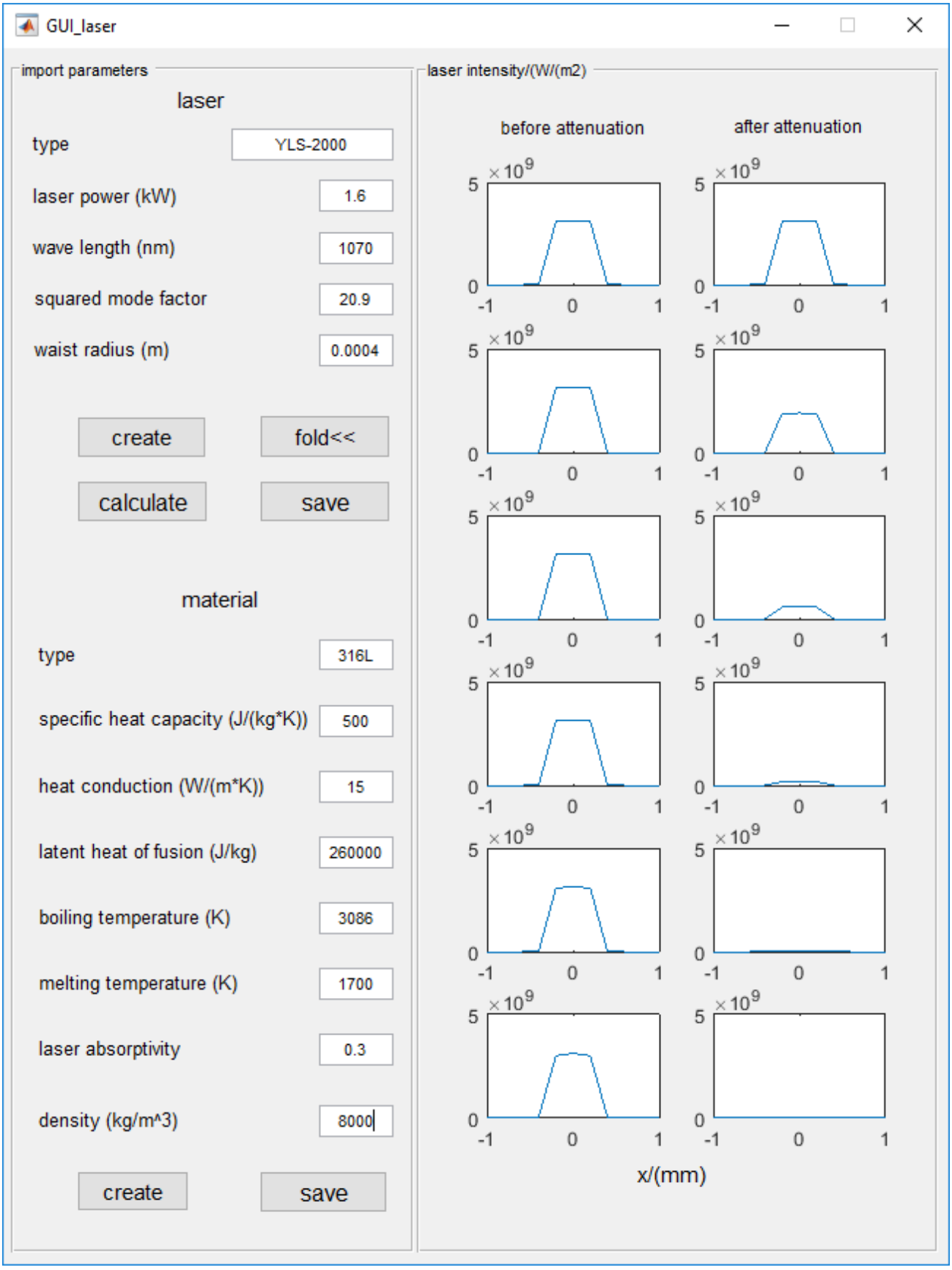

Figure 4.16 GUI of laser and material.

4.8 Summary

In this chapter, an analytical modelling approach is proposed for predicting the shape of the cladding affected area, i.e. deposited bulge and melt pool) in wire laser cladding (WLC). Firstly, the temperature field is constructed based on the laser intensity distribution. Then, the temperature-dependent interfacial tension is used to form the profile of bulge and melt pool. Finally, the direct relation between input processing parameters and output profiles of bulge and melt pool is built in the model. The model, validated at the geometrical and the physical aspects, distinguishes itself through the following key findings:

- The profiles of the bulge and the melt pool are calculated analytically with the proposed model under various processing parameters. As a result, the errors are 20% in average including bulges and melt pools. Moreover, predictions in high laser power, high scanning speed and low wire feed rate exhibit high accuracy (with maximum error as low as 14% at the bulge).
- The model reveals the underlying physics on track profile and correlates the thermal and geometrical parameters in the cladding process, giving the opportunity to analyse and understand the effect of varying processing parameters. As a result, it enables the engineers in industry to identify the window of processing parameters rather than to adopt a trial-and-error approach [171].
- The model avoids the calculation of fluid dynamics during cladding process and provides fast prediction of the cladding geometry. As a result, the model provides the tool for the efficient control of process when implemented on modern CNC manufacturing cells.

- By predicting the shape pool, the proposed model could turn a traditional approach that this is undesirable process outcome into, potentially, useful outcome. This refers to the possibility that a known shape of the melt pool could be useful when cracks under substrate surface existed prior the cladding process and, thus, these could be repaired.

In conclusion, the proposed model has been proven capable of predicting at an acceptable level of accuracy the temperature-dependent shape of the cladding affected area through the inclusion of capillary effect in the form of an interfacial tension function. Further, it is expected to provide the basis for overlap laser cladding modelling in the parts repairing and complex components additive manufacturing.

Chapter 5 Modelling of overlap wire-fed laser cladding on horizonal surface

5.1 Introduction

The modelling approach of WLC is presented in the previous chapter. It is proven applicable on the profile prediction of single track on horizontal surface. However, single track is usually limited in application, which brings the necessity of overlap cladding with multiple tracks. Stable overlap structure includes a layer (with tracks side by side) and a pad (with layer on layer).

The structure brings complexities on the model in terms of geometry, temperature, and metallurgy. Material remelting and bonding behaviour are involved in the integrity of cladding layer. The operating window of the track spacing was considered to avoid a lack of bonding between the tracks and substrate surface as well as protrusions between two tracks [76]. To study the overlap ratio, a recursive model was developed for predicting the profile of the coating layer formed via track overlap [172]. An ideal overlapping model was proposed based on which the optimal processing parameters were obtained and proved by the orthogonal experiments with 316 stainless steel powder [173]. A multi-bead tangent overlapping model was proposed with the concept of the critical valley for the stable overlapping process based on wire and arc additive manufacturing observations [174]. A geometrical model of the optimal overlap ratio was derived based on which reduced surface fluctuation in multi-track

claddings was obtained [175]. The thermal accumulation effect through the layers in multi-layer deposition led to a discrepancy between the height increment and the growth rate [50]. To study this height discrepancy, a model of multi-layer powder-fed laser cladding was developed based on which the process heating/cooling rates, and 3D clad geometry can be efficiently predicted [176]. Strategies were also proposed for the deposition quality control. The deficiency in the layer height was compensated by adjusting the wire feed rate on the next deposition layer [177] while cooling rates were increased on Ti-6Al-4V wire cladding buildups by increasing scanning speed [178].

The structure of this chapter is: (i) the full overlap shape of the material deposition on horizontal surface is analytically modelled, (ii) validation by experiments for various process parameters followed by the appropriate measurements under optical microscope of the cross sections cutups, (iii) further discussions about the model, e.g. useful information from the model compared with microstructure observations, and (iv) application cases with the model based on the encountered situations in repair.

5.2 Process background

In WLC process, a laser beam radiates on a feeding wire and static substrate while the laser beam and the wire move along the cladding direction (see Figure 5.1a). The wire material absorbs the energy, melts, and forms a track of deposited material on the substrate. When cladding the ith layer, the subsequent

*j*th tracks are cladded aside with the previous tracks with overlapping areas. Thus, the following aspects should be considered in the modelling:

- The remelting and bonding between horizonal overlap tracks. The subsequent track brings heat to the previous track by conduction through overlap area. The remelting of material raises the problems including material deposition location of subsequent track, metallurgy, and mechanical properties [179]. The bonding at the overlap area raises the problem of layer integrity [180]. These problems are expected to be predicted in the model.
- The valid thickness measured at the valleys of horizontal cladded layer. On horizontal surface, the overlap ratio between tracks significantly affects the surface flatness of a layer [181, 182]. When overlap ratio is low, the distance between peak and valley is obvious which impairs the flatness. When overlap ratio is high, the bulge height accumulates which leads to a variant thickness of layer.
- The real-time, theoretically predictable layer thickness control. For industrial application, the adaptive, time-variant layer thickness control will not depend on the feedback from on-site monitoring [183] which is an additional system that is not incorporated into the cladding system. Thus, the theoretically predictable layer thickness will release the burden of adding monitoring system.

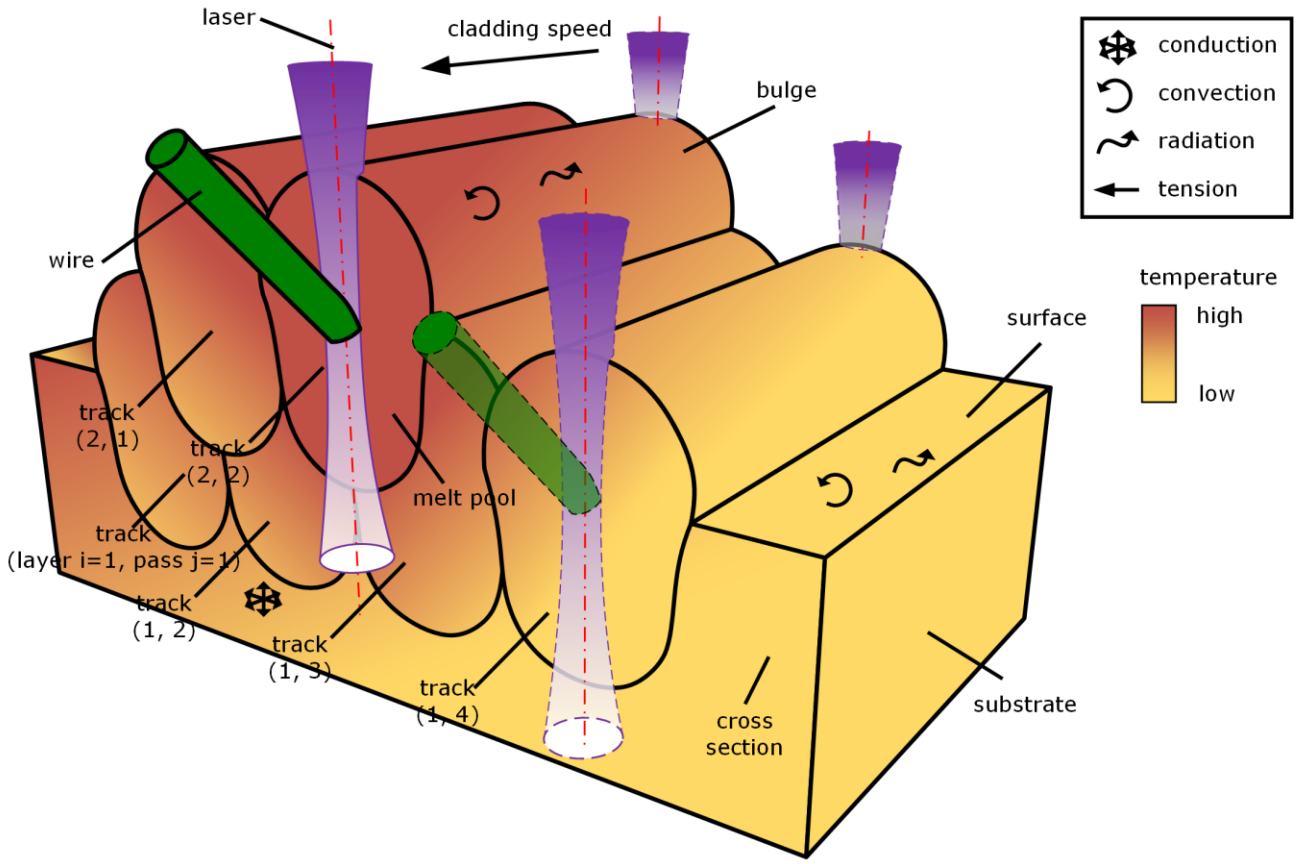

Figure 5.1 Schematics of WLC process: overlap on horizontal surface.

5.3 Model description

5.3.1 Modelling principle

The proposed model, in general, is based on the discretization of the full 3d computation domain into cubic unit cells. The computation domain (see Figure 5.2a) includes the substrate part and the deposition zone with dimensions. For modelling, the computation domain is sliced into pieces (see Figure 5.2b). The model inherits the single-track model that is in a circle shape governed by interfacial tension (see Figure 5.2c). The subsequent tracks will also be circle shapes that contain the overlap area.

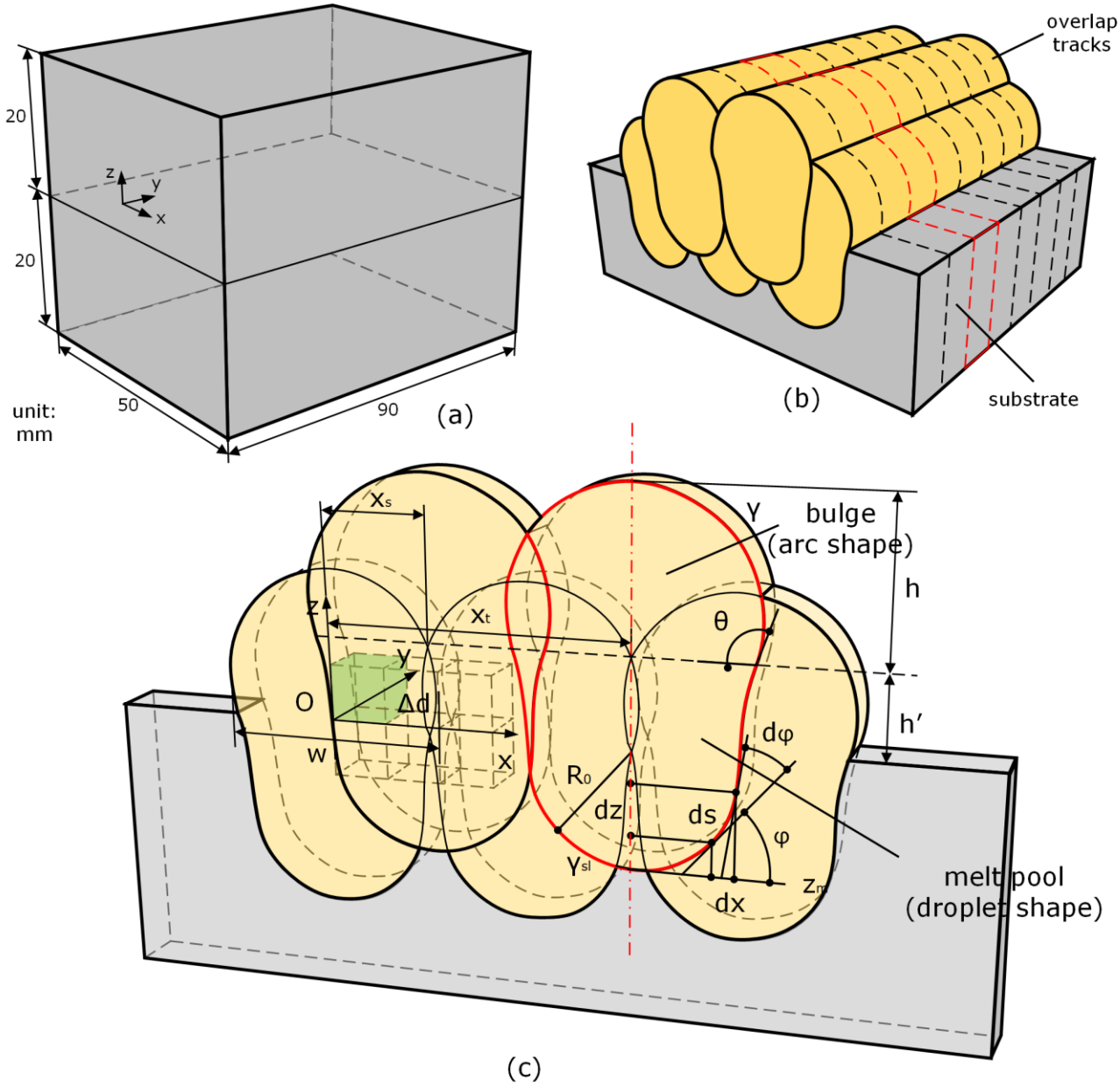

Figure 5.2 Schematic of tracks overlap modelling:(a) computation domain, (b) slices of the computation domain, and (c) the parameters in the modelling steps.

5.3.2 Calculation of temperature field in the tracks and substrate

The temperature field is calculated to estimate the shapes of the bulge and melt pool. To obtain the full temperature field in the WLC, the calculation domain is divided into cubic cells with the edge length Δd. Each cell position is defined as (x, y, z) in the coordinate system (see Figure 5.2c) and has a varied temperature

owing to both the laser heating and the heat transfer. The detailed modeling process is presented in Chapter 4.

5.3.3 Calculation of bulges profile on horizontal surface

Based on the observations of trial of two horizontal bulges overlap, the as-clad bulge and newly cladded bulge are both in circle shapes. Therefore, we can assume the newly cladded bulge evolves from the as-clad bulge into a bigger bulge with the centre line aligned with its own position (see Figure 5.2a), written as

$$(x - x_t)^2 + \left(z - h' + \frac{hcos\theta}{1 - cos\theta}\right)^2 = \left(\frac{h}{1 - cos\theta}\right)^2. \tag{5.1}$$

where x_t is the horizontal position, h' is the vertical position, θ is the bulge contact angle and h the bulge height.

The bulge height h is deduced by geometrical relation with cross section area of an arc written as

$$h = \sqrt{\frac{S(1 - cos\theta)^2}{\theta - \frac{1}{2}sin2\theta}}. \tag{5.2}$$

To calculate the area of the evolved bulge, we first assume the contact angle θ is constant. The newly added area is calculated by iteration until it equals to the mass input

$$S - S_{(i,j)\cap(i-1,j-1)} - S_{(i,j)\cap(i-1,j)} - S_{(i,j)\cap(i-1,j+1)} - S_{(i,j)\cap(i,j-1)} = \frac{\pi R_w^2 v_f}{v_s}, \tag{5.3}$$

where v_s is the scanning speed, v_f is the wire feed rate and R_w is the radius of wire.

The horizontal position of the current bulge x_t in Equation (5.1) is calculated from overlap rates and widths by

$$x_t = x_s + w(j-1)(1-\eta), \tag{5.4}$$

where w is the width of first bulge at the first layer, j denotes the jth bulge of the layer, η is the overlap ratio, and x_s is the stagger distance starting from second layer written as

$$x_s = w\delta(i-1)(1-\eta), \tag{5.5}$$

where δ is the stagger ratio and i denotes the ith layer.

The vertical distance h' in Equation (5.1) is the platform which is calculated by iteration from initial z_t to steady $h'_{i,j}$ (see Figure 5.3), written as

$$h' = \begin{cases} z_t \ , & initial \\ h'_{i,j} \ , & steady \end{cases}. \tag{5.6}$$

Figure 5.3 shows the track evolution that includes initial material drop, remelt and combination with the as-clad tracks. The final profile is the calculated result that rests on its calculated platform. There are occasions with predictable behaviours: (i) at the first layer and (ii) at the second layer, as follows.

(i) At the first layer (see Figure 5.3a), the melted track only interacts with the previous track and the platform is on the substrate surface.

(ii) At the second layer and when the first track is laid close to the edge (see Figure 5.3b), the melted track remelts the entire lower track and the platform is

still on the substrate surface. When the second track is laid (see Figure 5.3c), the melted track remelts the adjacent tracks and the platform is on the lower layer with the rest point that depends on the material balance.

When the first track is laid far enough away the edge (see Figure 5.3d), the melted track remelts the adjacent tracks and the platform is on the lower layer with the rest point that depends on the material balance. When the second track is laid (see Figure 5.3e), the melted track rests on the lower layer with the point that depends on the material balance.

Please note that the principle shown in Figure 5.3 is based on the determination of the one side that rests on a lower point than the other side. It covers the occasion that the track is laid at the edge of the lower layer, or other occasions such as the to-be-clad layers are inside a cavity, i.e. the groove after material being machined, in which the track at the edge leans on the cavity wall.

Profile sections that overlap with the as-clad profile are imaginary, bulge and melt pool, as assumed in the model which do not necessarily represent the actual melting line. It is still justified by the reasons that the outline of the as-clad layers fulfils the filler material needs as can be predicted by the model and the interior material enclosed by the outline merges as an entity.

The contact angle of each track is assumed not dependant on the curve surface based on the fact that the melted platform is horizontal and flat. The contact angle, therefore, can be assumed as the usual concept of intrinsic angle [184] that is correspond to gravitational horizontal plane regardless of the solid geography [185, 186].

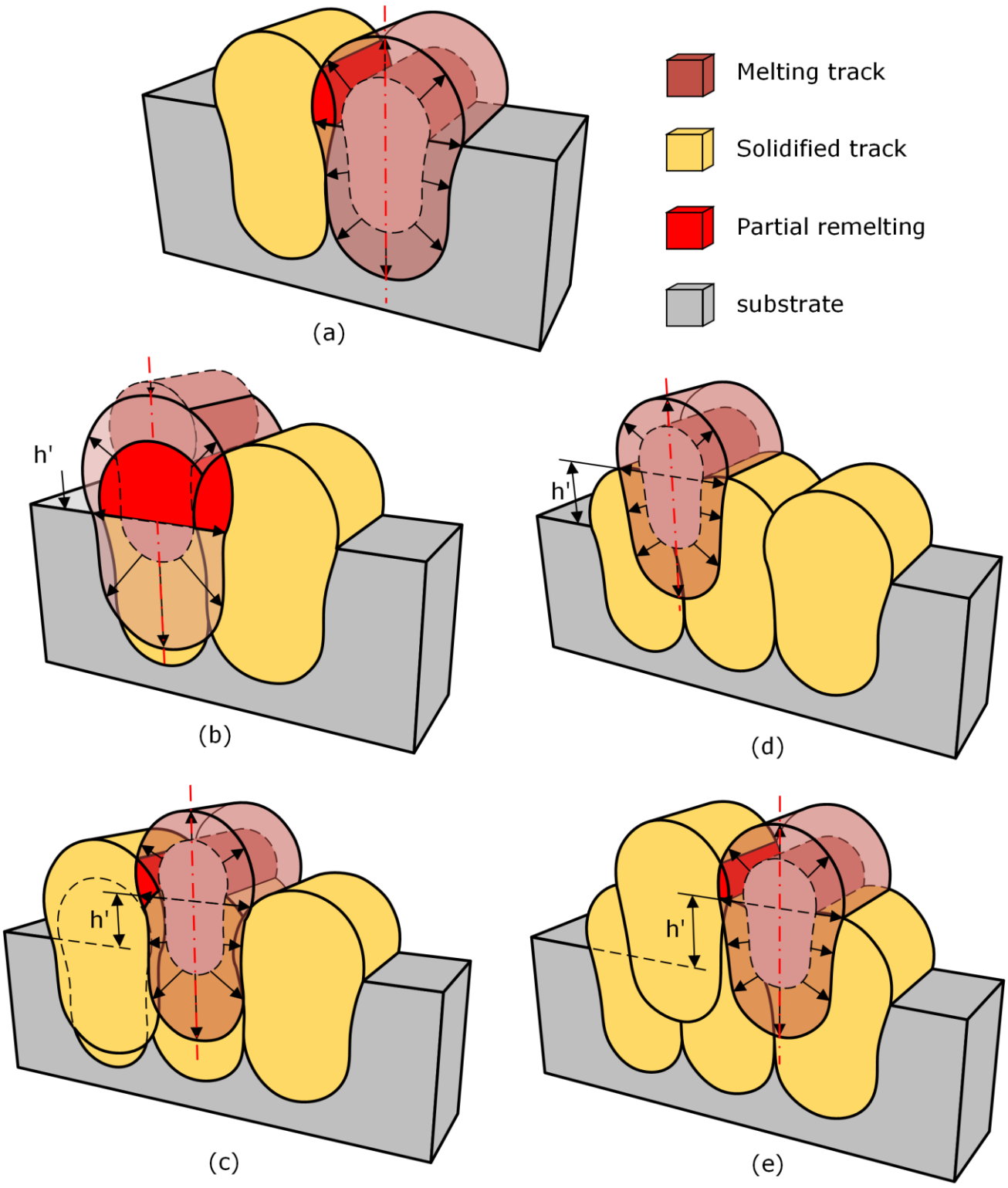

Figure 5.3 Schematic of platform height evolution: (a) platform of the first layer on the substrate, (b) platform of the first track when stagger ratio is low, (c) platform of the subsequent tracks when stagger ratio is low, (d) platform of the first track when stagger ratio is high, and (e) platform of the subsequent tracks when stagger ratio is high.

5.3.4 Calculation of melt pools profile below horizontal surface

The calculation method of melt pools profile is the same as described in Chapter 4, which is modelled analytically as [159]

$$\frac{d\varphi}{ds} = \frac{\rho g c_m (z_m - z)}{\gamma_{sl}} - \frac{sin\varphi}{x} + \frac{2}{R_0}, \tag{5.7}$$

$$\frac{dx}{ds} = cos\varphi, \tag{5.8}$$

$$\frac{dz}{ds} = sin\varphi, \tag{5.9}$$

$$\varphi(0) = 0, \qquad x(0) = x_t, \qquad z(0) = z_m, \tag{5.10}$$

where the only difference is the starting point $x(0) = x_t$.

Please note that there is an assumption, that the melt pool profile coincides with the bulge profile at the calculated platform while they usually do not coincide at the platform because the bulge profile usually does not extend to the platform. In this research, it is assumed acceptable because the melt pool profile is still inside the predicted deposition layer profiles while the outer boundary profile is the main focus.

5.3.5 Flowchart of modelling

The work fulfils the calculation loops from track, layer to pad under the input of processing parameters with the geometrical horizontal overlap profiles output (see Figure 5.4). The mathematical model is realized by putting codes on the MATLAB calculation platform.

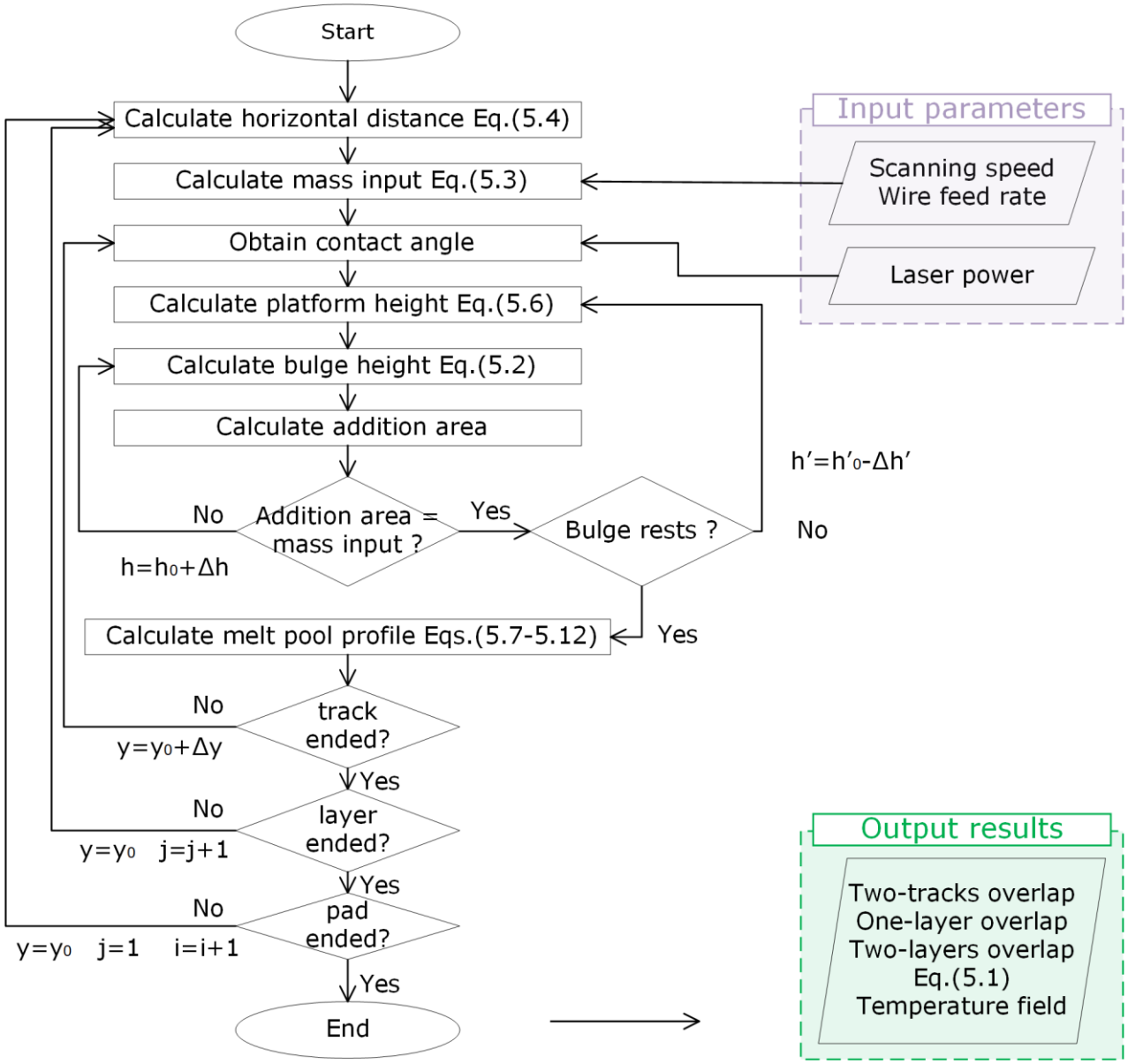

Figure 5.4 Flowchart of theoretical modelling from inputting processing parameters to outputting horizontal overlap profiles.

5.4 Experimental setup

To validate the proposed model that predicts cladding affected area, a set of experiments were performed.

The employed parameters for cladding experiments (see Table 5.1) were based on single-variable principle as it enabled robust evaluation of the model in relation

to the described physics of the process (described in Section 5.3). To obtain steady smooth tracks and sufficient bonding, laser power was set 1.6kW, scanning speed 0.1m/min and wire feed rate 0.6m/min at the fed in angle of 45 degrees. Under the same processing parameters, three trials were arranged. Trial 1 was designed to explore the two bulges overlap behaviours at overlap ratios of 10%, 30%, 50%, 70% (set up as Figure 5.5b). Trial 2 was designed to explore the layer effect at overlap ratios of 10% and 50% (set up as Figure 5.5c). Trial 3 was designed to explore the layers effect at overlap ratio of 10% and stagger ratios of 0%, 25%, 50%, and 75% (set up as Figure 5.5d, with the distance of 25mm at the second layer from the threshold to avoid the stagnation). Each track was cladded 70mm in length to ensure reaching stable thermal status and for the statistical sampling for analysis. N_2 protection gas kept feeding onto the cladding surface steadily. Two neighboring tracks had a time interval of 30 min so that heat effect on the next track can be reduced.

Table 5.1 Parameters for WLC experiments of overlap on horizontal surface

	Aims	Parameters	Values
Trial 1	Two overlap bulges	Overlap ratio	10%, 30%, 50%, 70%
Trial 2	One layer	Overlap ratio	10%, 50%
Trial 3	Two layers	Overlap ratio	10%
		Stagger ratio	0%, 25%, 50%, 75%

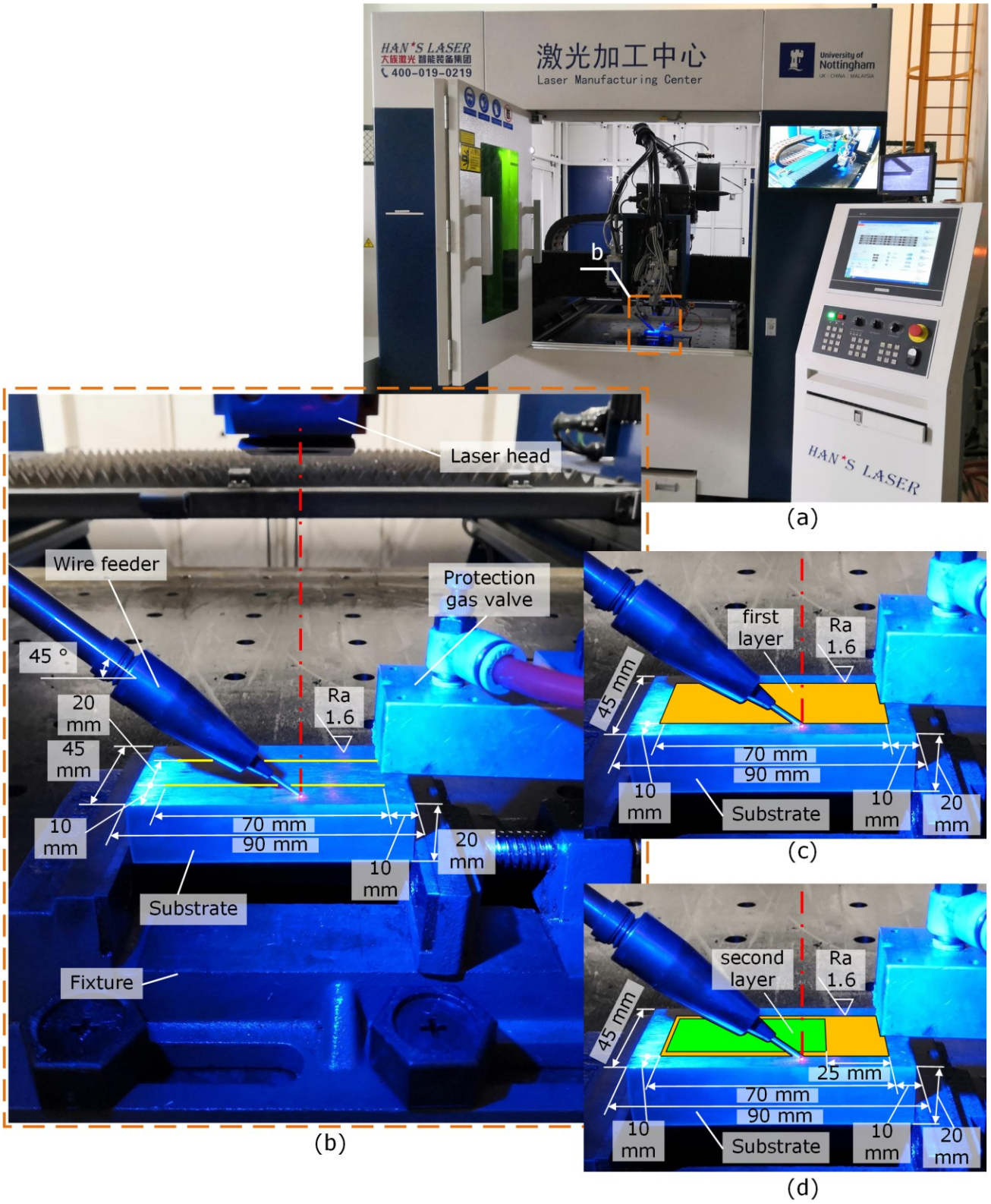

Figure 5.5 Illustration of experiment: (a) laser manufacturing centre and (b) two-tracks cladding setup for Trial 1, (c) one-layer cladding setup for Trial 2, and (d) two-layers cladding setup for Trial 3.

5.5 Model validation

The new estimation method of the geometrical profile is introduced first. The sections are divided into: (i) error estimation, (ii) two bulges overlap, (iii) one layer on horizontal surface, and (iv) two layers on horizontal surface.

5.5.1 Error estimation

A new method of error estimation is firstly proposed (see Figure 5.6). The estimation for one track requires the error at the sampling points on the profile, while it is not highly necessary and operable on the multiple tracks overlap profile. The profiles that come from the multiple cross sections of experiment are put together and only one of the cross sections is considered the valid experiment area. The profile that comes from the calculation are align with the experiment at the original point. Therefore, the error can be estimated according to the ratio of discrepancy area (the unit of experiment and calculation minus the intersection of the experiment and calculation) to experiment area, written as

$$\epsilon = \frac{S_{exp} \cup S_{cal} - S_{exp} \cap S_{cal}}{S_{exp}}, \tag{5.11}$$

where S_{exp} is the set of elements inside experiment profile and S_{cal} is the set of elements inside calculation profile.

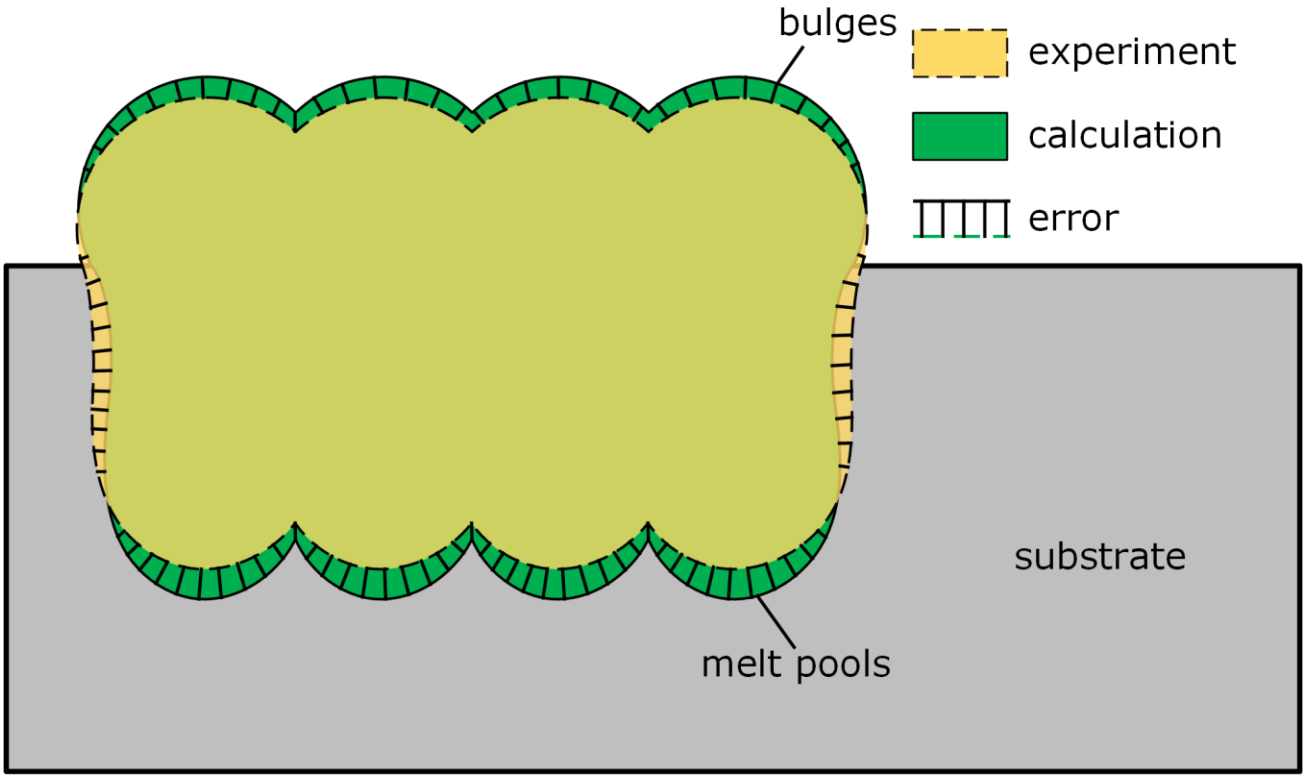

Figure 5.6 Schematic of error estimation according to the ratio of discrepancy area to experiment area.

5.5.2 Two bulges overlap on horizontal surface

Figure 5.7 shows that, in general, the calculated full track profiles on horizontal surface is close to the experimental ones when the overlap ratio is changed, where the maximum relative error is 21.3%.

The first issue is to verify whether the second bulge still stays at the position align with the laser, e.g. its cladding position. The laser positions are marked on the figure (3.42mm at 10%, 2.66mm at 30%, 1.9mm at 50%, and 1.14mm at 70%) which are measured and input on the laser automation system. The laser position is held in the accuracy of 0.001mm. Judged by the position of melt pool apex, we can determine that the centre of track is aligned with laser.

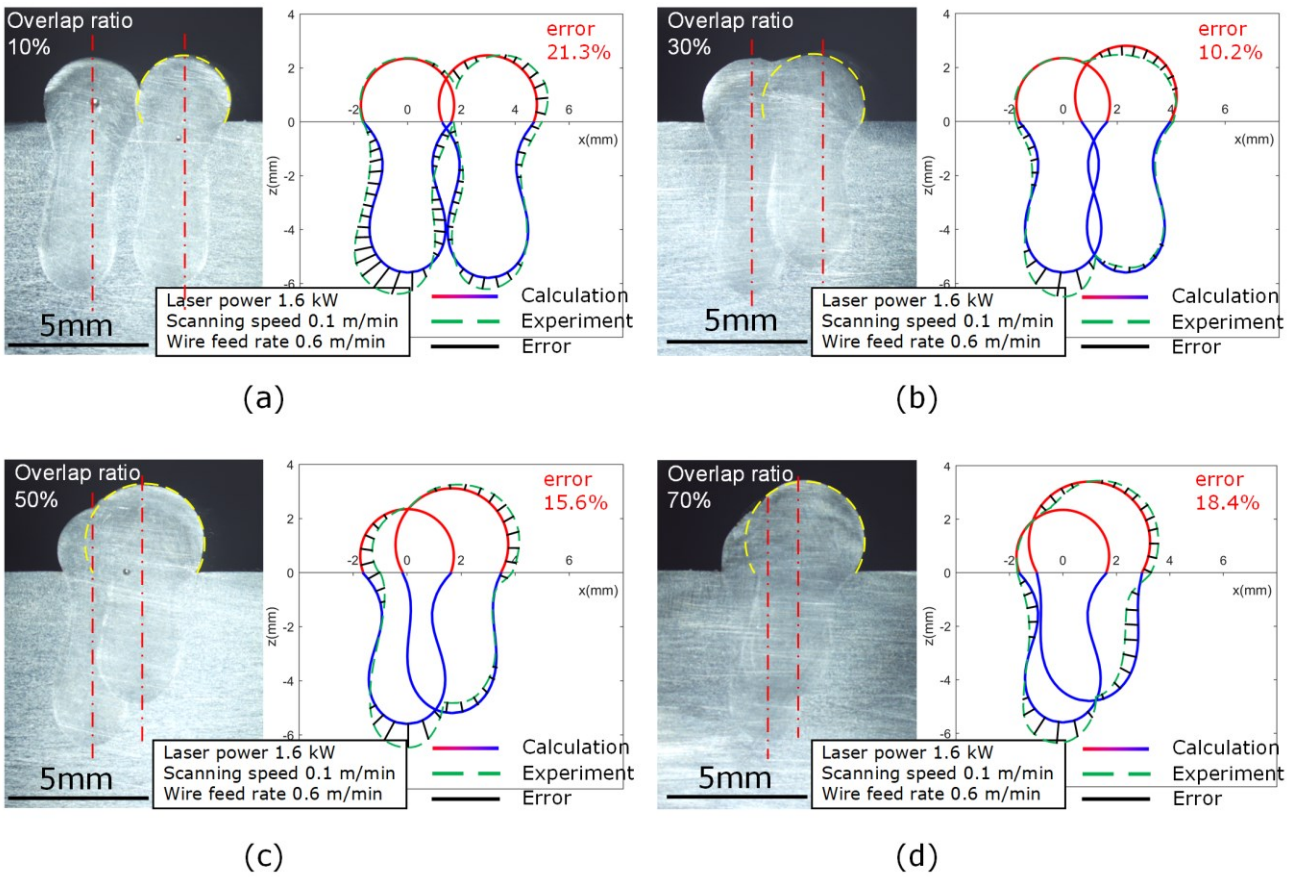

Figure 5.7 Observations of two horizontal bulges overlap at ratios of (a)10%, (b)30%, (c)50%, and (d)70% at constant (P =1.6kW, v_s =0.1m/min and v_f=0.6m/min).

While the first bulge is in a circle shape, the second bulge also remains a circle shape bigger than the previous one. It validates the assumption of mimicking circles for each bulge which is the basis of the model. The model is also able to predict the contact angle of the bulges.

This result vividly shows the evolution of overlap. As overlap ratio increases, the second bulge is approaching, climbing on the first bulge, and trying to melt partial material of the first bulge. There are rare chances that gaps occur between two bulges because the cladding wire is pointed at the substrate surface where melt material starts accumulations. It is not like the occasion of the drop-on-demand

metal droplet printing where melt droplet drops on the previous drop but solidifies instantly without filling the gaps [187, 188]. Therefore, the laser cladding is a superior method that can avoid gaps as long as overlap ratio is properly chosen (better above 10%).

The next step is to validate the model capability of predicting a horizontally cladded layer.

5.5.3 One layer on horizontal surface

Figure 5.8 shows that, in general, the calculated full track profiles on horizontal surface is close to the experimental ones when the overlap ratio is changed, where the maximum relative error is 20.9%.

The height of each track in overlap ratio of 10% does not deviate a lot. Each bulge is the mimic of the first bulge with around the same size. It is the convenient case when the layer thickness requires strict control. If the model prediction is accurate, the valid height at the valleys between bulges can also be predicted accurately. The machining afterwards can be conducted to remove the caps above the valid height. In the mechanical properties point of view, the bonding force at the overlap region at cladding layer of overlap ratio 10% should be tested before it can be relied on. If there is more than one layer, the valley between each track in a lower overlap ratio contributes to the balance of the upper layer and the bonding force problem will be improved. The melt pool depth in the experiment remains the relative same level while in the calculation it keeps increasing although the cooling time has been considered in the model.

The height of each track in overlap ratio of 50% keeps increasing. If the caps above the valleys are removed horizontally, much of the material is wasted. The overlap ratio should be kept less to ensure valid height and no gaps at the same time. The high overlap ratio can also be utilized to obtain the inclined feature when slicing horizontal to the valleys. If the model accuracy is ensured, the valley height can be accurately predicted, thus the accurate inclined slope. It should be noted that the height will gradually reach balance as track number increases.

Since the layer height at overlap ratio of 10% is steady, it is selected to stack another on top of the first layer at the next step.

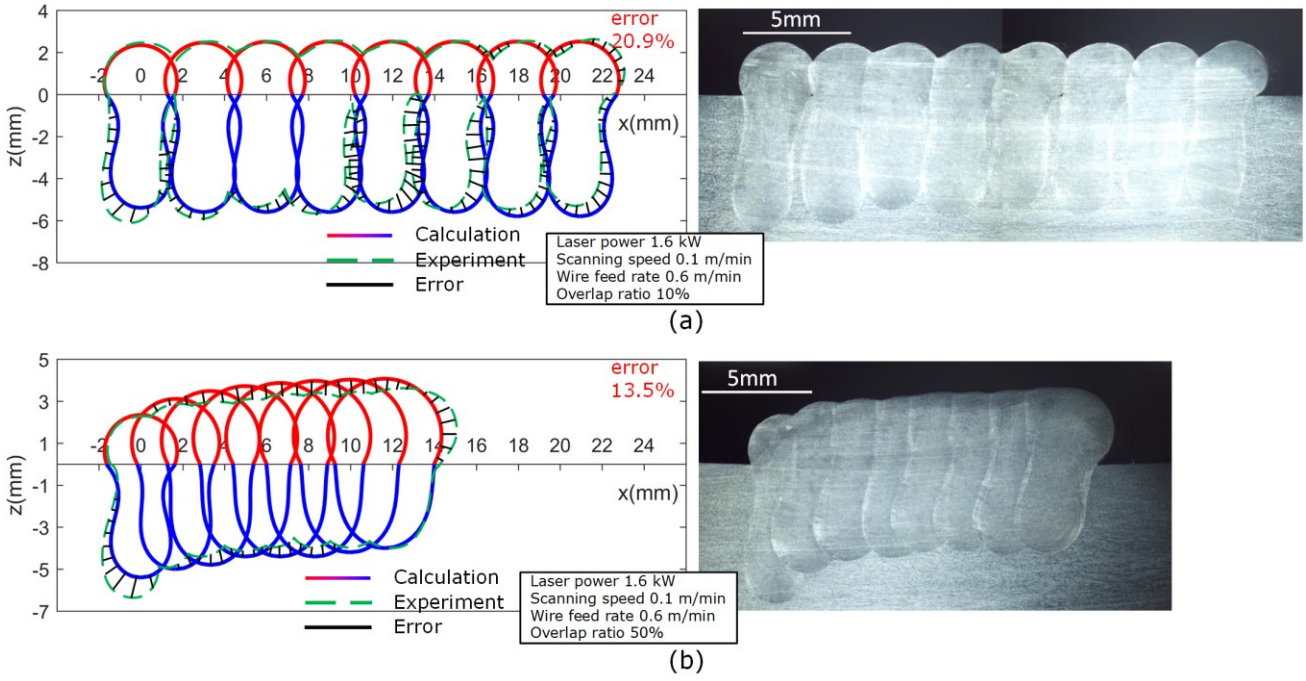

Figure 5.8 Cross sections of the cladding affected area for varying overlap ratio: (a) 10% and (b) 50% at constant (P=1.6kW, v_s=0.1m/min and v_f=0.6m/min).

5.5.4 Two layers on horizontal surface

Figure 5.9 shows that in general the calculated full tracks profile is close to the experimental ones when the stagger ratio is changed, where the maximum

relative error is 16.8% at the stagger ratio of 25%. The error mainly comes from the first track of the second layer when the remelting condition at the first layer is predicted inaccurately. Pores were also observed due to bubbles [189].

The selection of stagger ratio depends on the repair requirement. The collapse of the first track at the second layer due to the remelting leads to the delay of gaining average height of the second layer. The decrease valid height at the beginning edge of the layer may be avoided by increasing the stagger ratio or shifting the position forwards away from the high strength requirement zone when low stagger ratio is selected. The model is responsible for predicting both of the occasions. Other than increasing stagger ratio, the track collapsing can also be eliminated by reducing material input [190].

The melt pool profiles above the first layer may not be required in the geometrical predictions but are still presented in the results. It is only required in the metallurgical prediction of microstructure that goes through different stages of remelting and solidification, and in the mechanical properties prediction of overlap region that generates internal forces at the interface. These topics are not the focus of this thesis but are listed as one of the items at the chapter of future works.

After investigating the beginning edge of the cladded layer closely, the layers that reach flat are investigated next since the flat layers are actually needed in the application.

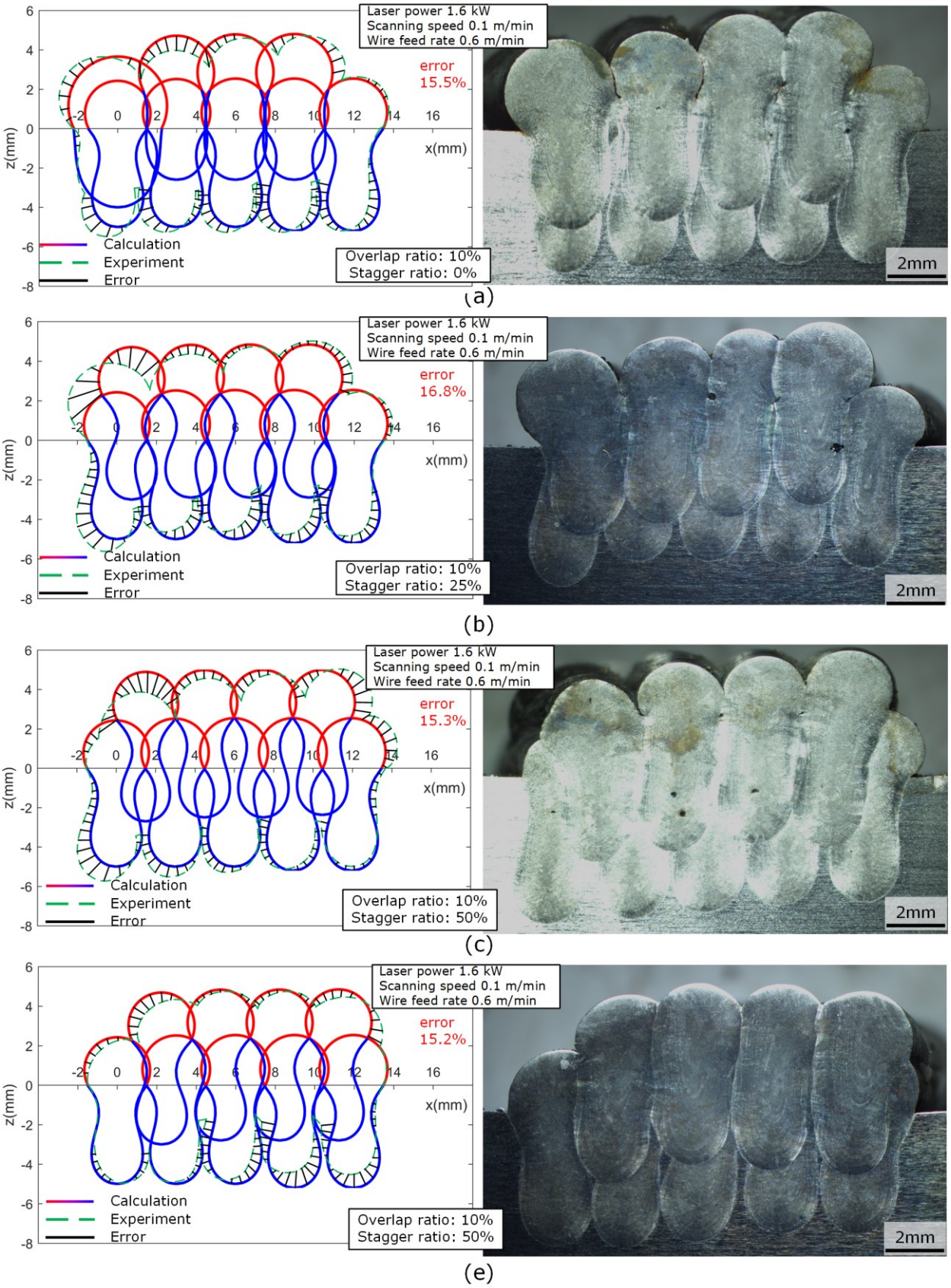

Figure 5.9 Cross sections of the cladding affected area at the beginning edge for varying stagger ratio: (a) 0%, (b) 25%, (c) 50%, and (d) 75% at constant (P=1.6kW, v_s=0.1m/min, v_f=0.6m/min and overlap ratio 10%).

Figure 5.10 shows that in general the calculated full tracks profile is close to the experimental ones when the stagger ratio is changed, where the maximum relative error is 18.5% at the first layer.

At the second layer, there is a preparation range at the beginning where bulges climb up until they reach steady height. As stagger ratio increases, this preparation range decreases. Although the first layer with overlap ratio of 10% seems flat, the second layer still shows obvious climbing characteristics. It is one guess that the new cladded bulge melts the previous bulge partially and absorbs the extra material. It can be observed that the extra material may not come from the previous bulge at the same layer because there is some lack of fusion between two horizontal bulges. Then the extra material should come from the previous layer. Therefore, the stagger ratio is chosen from 50% to 75% where the preparation range is short.

Another problem is that the number of tracks in one layer decreases one as layer level increases. Eventually, only the trapezoid pad, or even the triangle pad, is obtained. It has the limitation on the geometry although it is not a problem in V- or U-grooves filling [191]. One solution is to make complementary track on the sunken track. It requires the model to predict the sunken ratio accurately. Based on the observation, the complementary solution is better conducted at overlap ratio of 50% because the complementary track will fill the sunken height and stagger width at the beginning and end tracks. Possible additional adjustment may be conducted from one of the processing parameters, e.g. laser power, scanning speed, and wire feed rate. Laser power determines the sunken ratio.

Scanning speed and wire feed rate determine the complementary width and height.

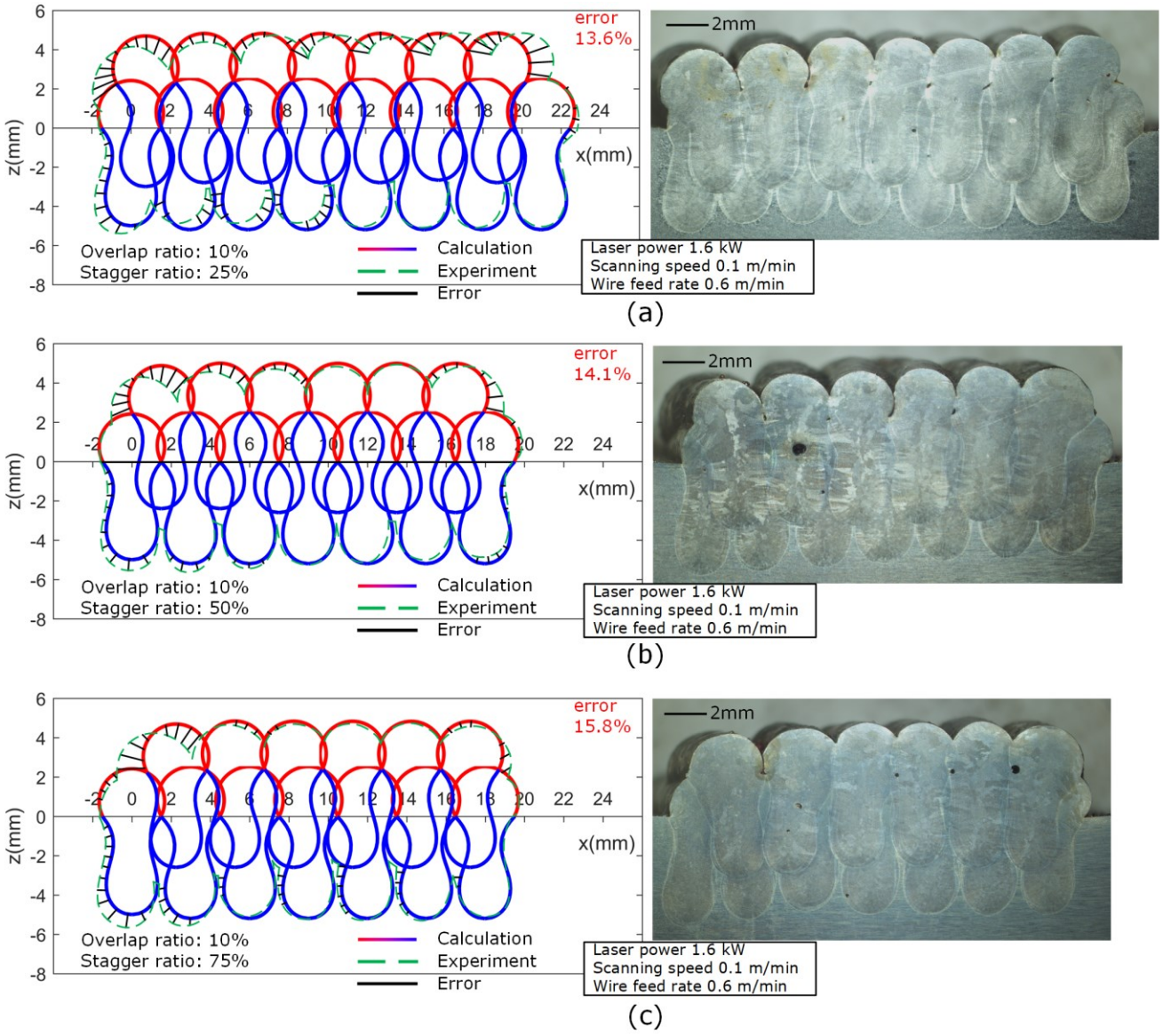

Figure 5.10 Cross sections of the cladding affected area for varying stagger ratio: (a) 25%, (b) 50%, and (c) 75% at constant (P =1.6kW, v_s =0.1m/min, v_f=0.6m/min and overlap ratio 10%).

5.6 Further discussions based on the model

Metallurgical observations around the two bulges overlap are discussed based on the model (see Figure 5.11a).

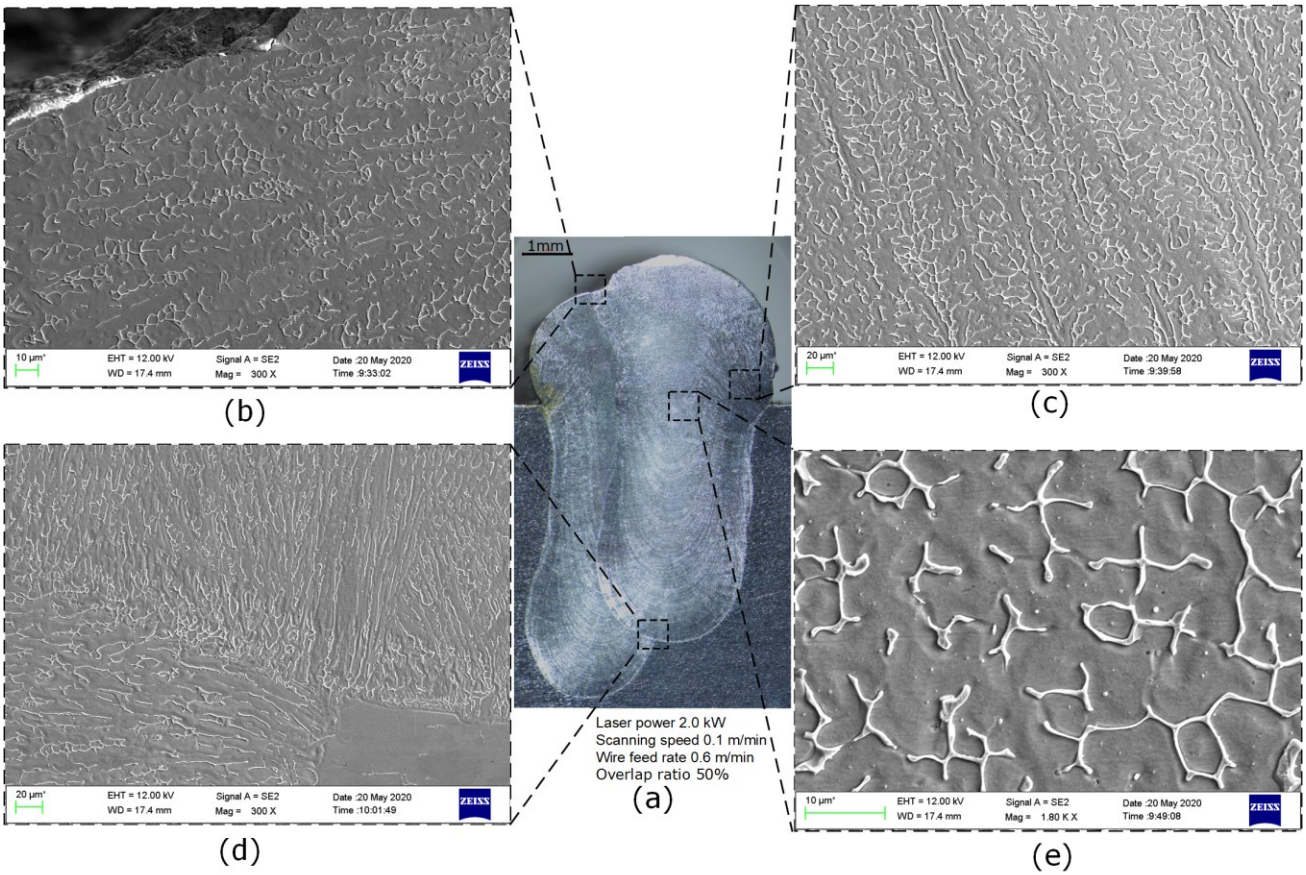

Figure 5.11 The metallurgy inside the core of two tracks: (a) picture under optical microscope with 8X, (b) upper overlap corner picture under SEM with 300X, (c) contact corner picture under SEM with 300X, (d) bottom overlap corner picture under SEM with 300X, and (e) interior picture under SEM with 1.8kX.

The overall microstructure distribution of two bulges overlap trace is revealed where the second bulge penetrates into the substrate and intrudes into the first bulge at the same time (see Figure 5.11a). There is no obvious divide line of microstructure, meaning no abrupt temperature variation (see Figure 5.11b). It indicates that there is enough time for the bulge to form shape under the control of surface tension. It meets the assumption of the model that the second will mimic the circle shape. Dendritic grains are distributed at the temperature gradient direction normal to the melt pool-substrate boundary (see Figure 5.11c). It should be noted that the temperature gradient is the sign of rapid solidification

at the contact corner which lock the contact angle at a rapid speed once the laser moves past the present cross section. Dendritic grains distribute at the temperature gradient direction normal to the melt pool-substrate boundary (see Figure 5.11d). It profoundly changes the grain direction of the first track melt pool. The behaviour brings out the necessity of predicting the melt pool profile for the mechanical behaviour model. Grains at the core of bulge point at the direction of feeding, e.g. normal into screen (see Figure 5.11e). If the mechanical behaviour model is to be developed, the direction of this grain is another significant factor to be considered. It should determine the force direction and the breakage behaviour, i.e. the fatigue crack path development or the force distribution when the track being pulled up.

5.7 Model application cases

5.7.1 Control strategy of temperature on tracks and substrate

The first application of the model is to control the temperature on the tracks and substrate. The analytical model provides the transient temperature calculations of overlap WLC on horizontal surface (see Figure 5.12). The heat focuses on the laser leading area while the periphery extends to the neighbouring tracks. The extension of heat periphery leads to the partial remelting of the previous one or two tracks. The base temperature is also increasing (colour is more and more bright) as the tracks are subsequently laid out on the surface. The interval time between two tracks is the factor to set so that the periodic base temperature can be maneuvered, lower or higher than a value, as the need of metallurgy after the periodic tempering [192, 193]. Strategies can also be made to fabricate thin-wall

part that was sensitive to temperature [194, 195]. Without the model, this detailed description of process change can not be fulfilled.

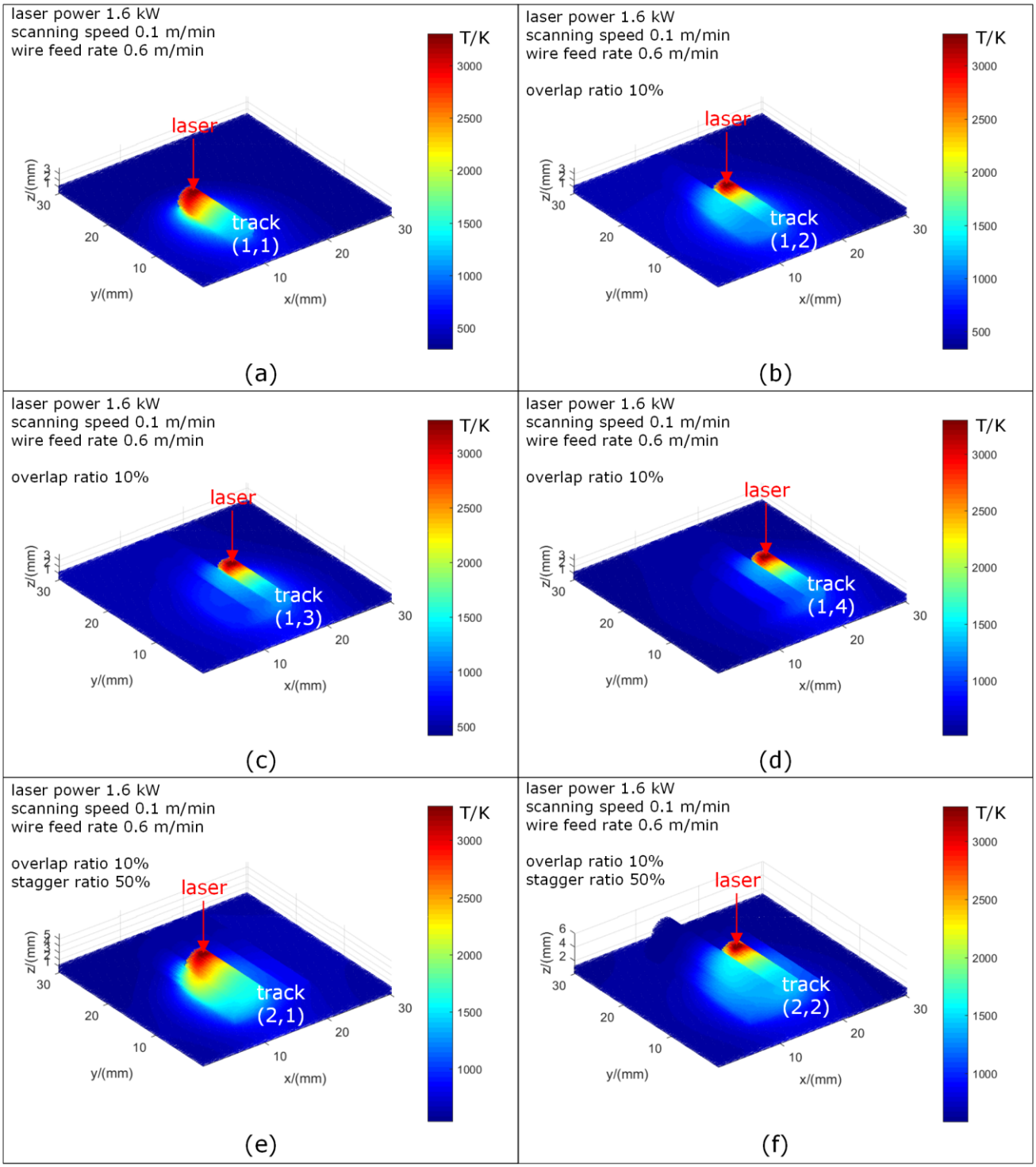

Figure 5.12 Temperature field calculation results of overlap WLC on horizontal surface: (a) track (1,1), (b) track (1,2), (c) track (1,3), (d) track (1,4), (e) track (2,1), and (f) track (2,2).

The overall transient dimensional temperature information can be further used for other occasions. Therefore, the analytical model developed in this study is a potential part of another bigger model based on the application requirements with further combinations, i.e. the microstructure simulation [196, 197].

5.7.2 Control strategy of gear tooth rebuild

The second application of the model is to control the gear tooth rebuild. Gear is the motion and torque transmission part in mechanical equipment. The manufacturing process of a gear involves special procedures: initializing (i.e. casting, forging, extrusion, and blanking), forming (i.e. milling, shaping, and hobbing), enhancing (i.e. heat treatment, carburization, and shot blasting), and finishing (i.e. formed grinding), which makes it the high value component. A gear ended by the failure, which includes breaking, wearing, pitting, and sticking, is expected to repair. To demonstrate the application of the proposed model in the repair process, the gear with a broken tooth is prepared to repair with the additive process, e.g. WLC in this case (see Figure 5.13a).

The parameters of the gear tooth, especially the modulus, can be calculated by measuring the diameter of the gear and counting the tooth number (see Figure 5.13b). The pressure angle can be measured by the protractor. The thickness is measured with ruler. The whole broken tooth is machined, leaving the horizontal flat surface. The surface is polished to Ra 1.6μm to remove contaminations (see Figure 5.13c). With the modulus, tooth number, and pressure angle, the profile of the gear tooth can be generated with gear profile tool (see Figure 5.13d). The model is used to calculate the bugles distribution on each layer that fill the tooth

profile while the material collapse at the edge is considered and the interference with the next tooth is avoided.

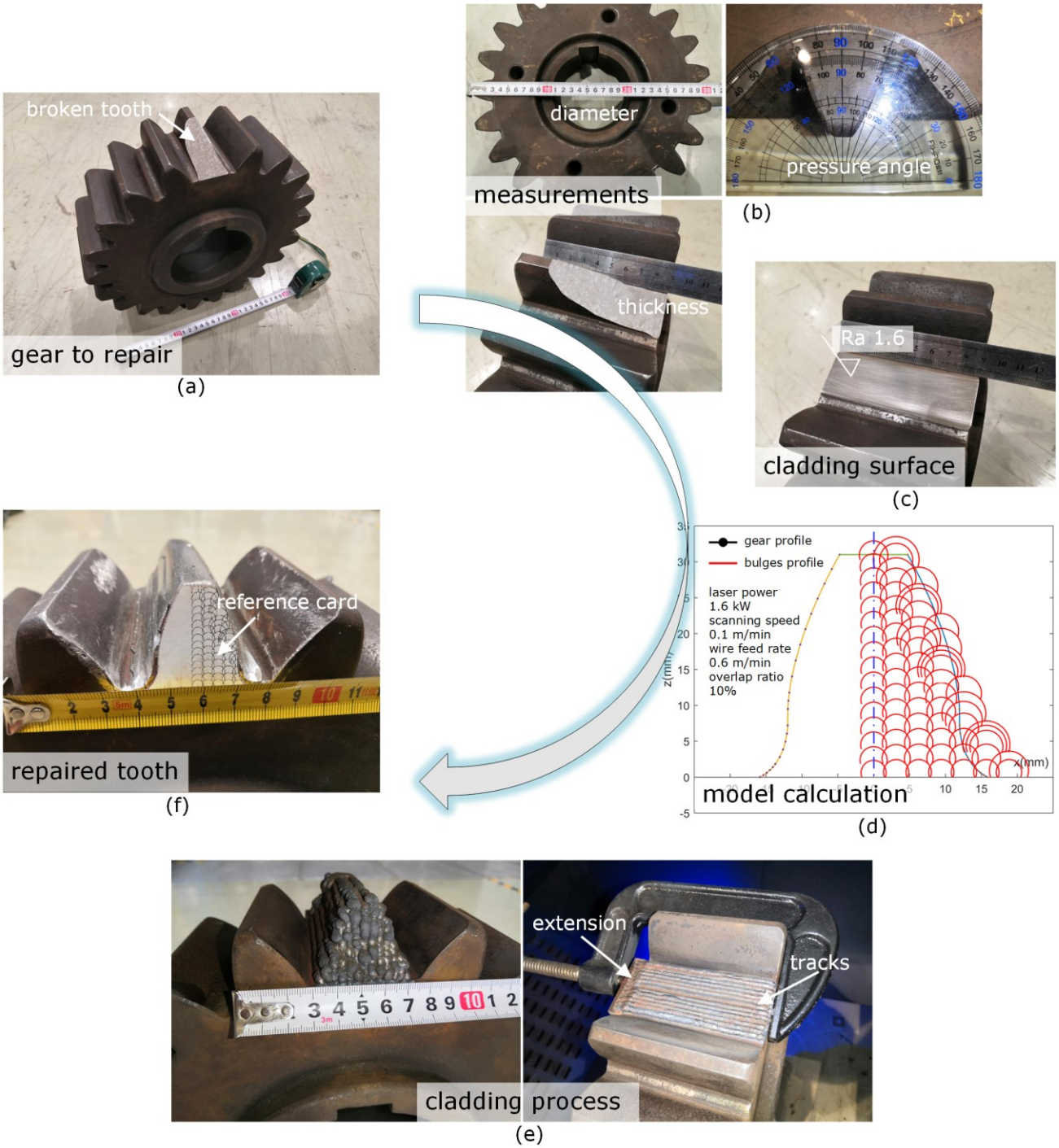

Figure 5.13 The additive repair process of gear: (a) gear with one broken tooth, (b) measurements, (c) cladding surface preparation, (d) model calculation, (e) cladding process, and (f) final view of repaired gear.

During cladding, processing parameters include laser power 1.6kW, scanning speed 0.1m/min, and wire feed rate 0.6m/min which enable the smooth tracks. For each layer, the track at the symmetry line is cladded first, then the tracks at both sides are cladded. After one layer is completed, the upper layer begins (see Figure 5.13e). Please note that an extension section at the end of track is added to delay the defective ending. The completed cladding is finalized by formed milling to obtain the final tooth shape, with the accuracy marked by the reference card (see Figure 5.13f). This application case proves the capability of the model on the overlap behavior prediction and the suggestion of bulges distribution within each layer to fill the designed profile.

The model, developed from the single track to horizontal overlap, is complete in explanation. The GUI transformation of model demonstrated in Chapter 4 is still applicable on horizontal surface cladding. In this chapter, there are additional parameters, e.g. layers, tracks, overlap ratio, and stagger ratio, that require inputs by operators on the GUI control panel (see Figure 5.14). The laser configuration and material type are already explained in Chapter 4. Another new characteristic of cladding on horizontal surface is the prejudgement of the filler layers to cover the designated area and thickness by determining layers, tracks, overlap ratio and stagger ratio. It is also helpful to judge on the melt pools at the bottom layer to ensure the subsurface defects are covered, based on the profile prediction on the repair requirements. The calculation capability of the workstation, or server, should be powerful enough to enable the multiple adjustments of input parameters until the output results reach the repair requirements.

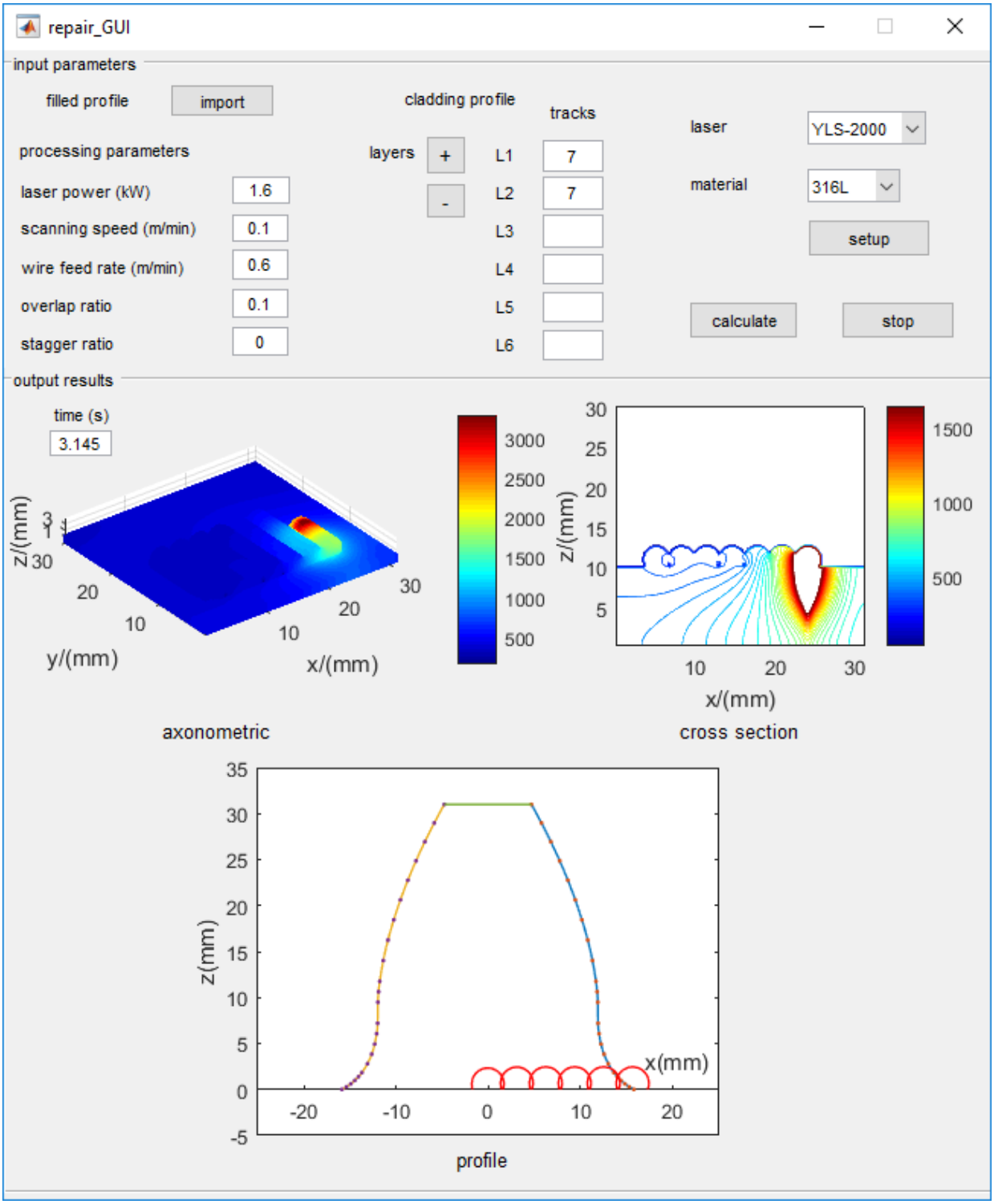

Figure 5.14 GUI control panel with built in model.

5.8 Summary

In this chapter, an analytical modelling approach is proposed for predicting the shape of the cladding affected area, i.e. deposited overlap tracks, in wire laser

cladding (WLC). Firstly, the overlap profile on horizonal surface is constructed based on the principle that the secondary track partially melts the previous track and takes the material to form a larger track with the same cross section profile, namely an arc. The model, validated at the geometrical and the physical aspects, distinguishes itself through the following key findings:

- The model successfully incorporates the remelting and bonding between newly-clad and as-clad tracks, especially the material deposition on the as-clad layers. It enables the geometrical solve of profile prediction based on the as-clad single track complete profiles and process accumulations.
- The profiles of the horizontal overlap cladding are calculated analytically with the proposed model under various overlap ratio and stagger ratio. As a result, the errors are in range of 10%-20%.
- The model reveals the underlying physics on overlap track profile and correlates the thermal and geometrical parameters in the cladding process, giving the opportunity to analyse and understand the effect of varying overlap ratio and stagger ratio. As a result, it enables the engineers in industry to identify the distribution of tracks and layers on the designated area on the to-be-repaired parts.

In conclusion, the proposed model has been proven capable of predicting at an acceptable level of accuracy for the temperature-dependent shape of the overlap cladding on horizontal surface.

Chapter 6 Modelling of overlap wire-fed laser cladding on inclined surface

6.1 Introduction

The model has been through the previous chapters 4 and 5 and developed with the prediction capability of a layer cladded on the horizonal surface. However, the industry applications require more from the model, i.e. the prediction of cladding on the inclined surface. The need for WLC on inclined, or even non-horizontal, surfaces is largely driven by the vast repairing market of high-valued parts such as molds and dies [198], aerostructures [199], and power units [200]. The geometrical complexity of these components are: (i) molds and dies contain cavity walls that are frequently the combinations of drafts, fillets, notches, pads, steps, and round corners; (ii) aerostructures, i.e. turbine blade tip, contain aerodynamically optimized features that are frequently the combinations of varied profile cross sections, forward sweep, and twist; (iii) power units, i.e. bearing girder, contain rotational features that are frequently the combinations of concave and convex surfaces. The non-horizontal surfaces or features on these components lead to substantial unique physical phenomena in WLC on inclined surfaces [201] (such as downward migration owing to gravity [202-204]) in comparison with the one on flat surfaces. This uniqueness challenges the stable

formation (e.g. Marangoni convection instability [205]) of self-retained tracks and requires frequent manual intervention.

The structure of this chapter is: (i) the full shape of the material deposition on inclined surface is analytically modelled, (ii) validation by experiments for various process parameters followed by the appropriate measurements, e.g. on coordinate measurement machine of deposition layer and under optical microscope of the cross sections cutups, (iii) further discussions about the model, e.g. useful information from the model compared with microstructure observations, and (iv) application cases with the model based on the encountered situations in repair.

6.2 Process background

In the WLC process, a high-intensity focused laser beam radiates on a feeding wire and fixed substrate, while the wire follows the laser beam moving along the designated direction (see Figure 6.1a). The wire material absorbs the radiative energy, melts and forms liquid tracks, and a marked sequence with (layer i, pass j) of the deposited material on the substrate. The laser radiates through the liquid track and brings heat to the bulge and melt pool. Heat transfers, including conduction, convection, and radiation, are involved inside the track from the periphery of the bulge and melt pool to the substrate and environment.

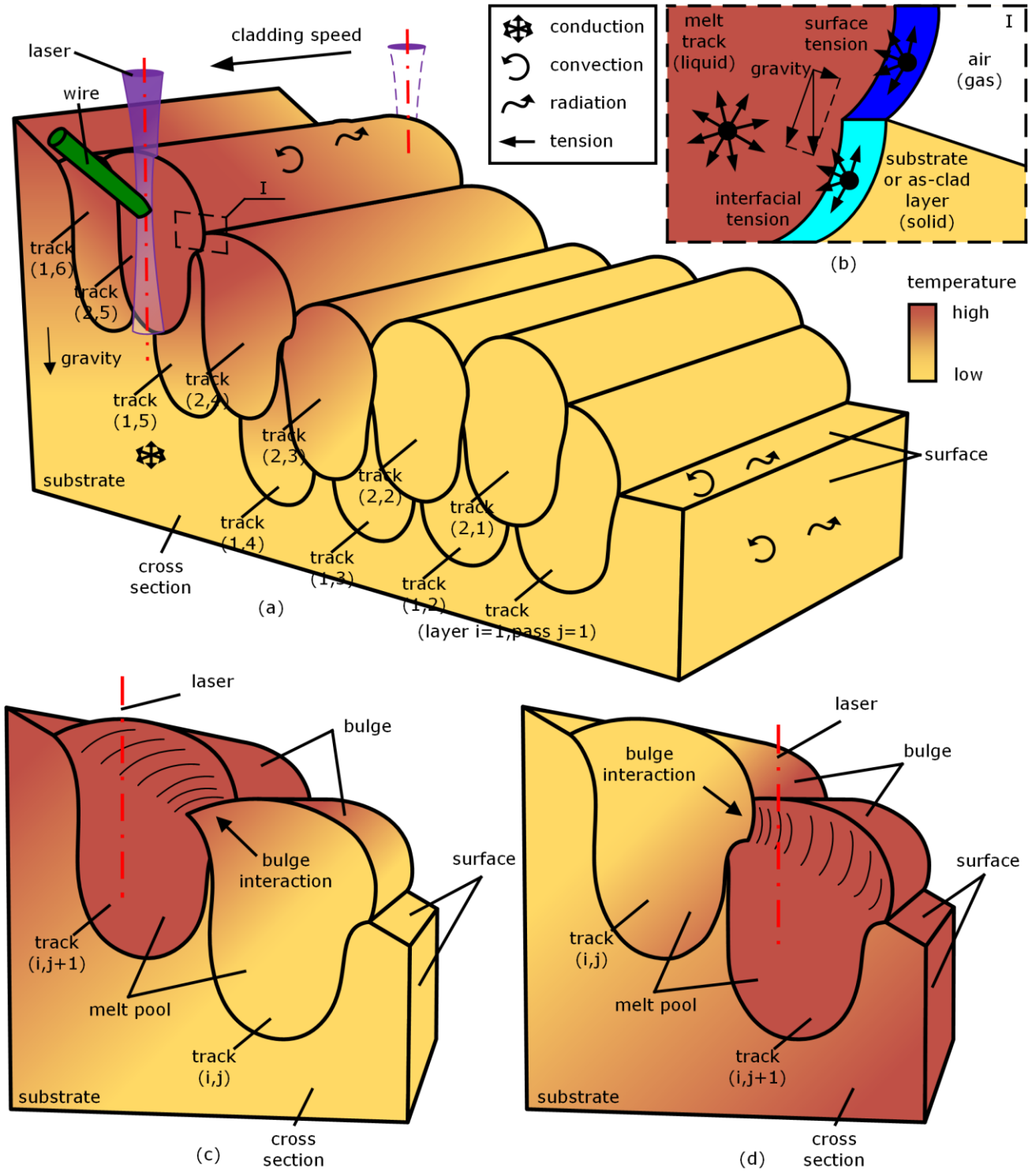

Figure 6.1 Schematics of WLC process: (a) cladding on horizontal surface and inclined surface, (b) tensions on the interface that forms the track geometry, (c) cladding in the climbing-up direction, and (d) cladding in the step-down direction.

Thus, the following aspects should be considered in the modeling:

- The balance between the interfacial tension and gravity is the dominant factor in track profile modeling (see Figure 6.1b). The profiles of the liquid bulge and melt pool are governed by the temperature-dependent interfacial tension. For horizontal surface cladding, gravity can be ignored, and each track remains an arc cross-section owing to the surface tension. However, for the inclined surface cladding, gravity intervenes in the interfacial tension and forces the bulge and melt pool to migrate and deform. Eventually, the heat transfer mechanism finishes the heat balance, when the liquid bulge and melt pool cease from evolving and solidify on the substrate.
- Climbing and step-down characteristics of overlap on inclined surfaces are the two different conditions that need specific considerations. On climbing, the position of the tracks follows the rise of height, accompanied by the deformation and shifting of tracks (see Figure 6.1c). The climbing situation is in contrast to the step-down situation, where the second bulge is pushed downward the incline and causes the collapse of the bulge (see Figure 6.1d). It enables the focus on the climbing situation while exploring the step-down situation by mitigating the inclined angle.

6.3 Model description

6.3.1 Model principle

The concept of surface tension is widely used to account for the shape of a droplet pending on a surface. However, it is usually not sufficient to explain the

interaction force between particles from a microscopic point of view and not strong when the condition is slightly altered, i.e., from a horizontal to an inclined surface (see Figure 6.2). Therefore, as a priority, the fundamental principle of droplet forming shape should be supported by the following theory:

The cladding track can be viewed as a string of droplets pending on the substrate surface. When it is on the horizontal surface (see Figure 6.2a), the geometry of the track can be illustrated in the cross-section from the middle A-A and from the bottom B-B. When viewed from plane A-A (see Figure 6.2b), the internal microscopic structure of the droplet can be simplified as a system of springs that are actually the van der Waals force. The van der Waals force holds a constant distance between the two particles. The van der Waals force (tension or compression) between two particles should be equal so that the entire system is in a balanced state. Under such circumstances, the curvature should be constant. Otherwise, imagine that there is one particle deviated from the system, the unbalanced tension force must pull it back to the system and the whole system reaches a new balance state. Viewed from plane B-B (see Figure 6.2c), the internal microscopic structure of the droplet, e.g., the system of springs, holds the bottom curvature constant.

When on the inclined surface (see Figure 6.2d), the geometry of the track can be illustrated in the cross-section from the middle C-C and from the bottom D-D.

When viewed from the plane C-C (see Figure 6.2e), the spring system is still the internal microscopic structure that holds the shape of the track, except the material shifts downward and exhibits two parts. As there can only be one state of the spring, either tension or compression, the part that is constructed by the compressed springs exhibits one curvature, while the other part constructed by the tension springs exhibits another curvature. When viewed from planes D-D (see Figure 6.2f), owing to the downward-shifting material, the geometry also exhibits two parts. The part constructed by the compressed springs is compressed from the circle into one ellipse, while the other part constructed by the tension springs is pulled from the circle into another ellipse. Please note that this spring system is proposed only to illustrate the balance state while spring parameters, e.g. elastic coefficient, are not involved in the discussions.

Based on the above discussion, the track geometry governed by surface tension is strongly supported by the theory of the internal microscopic spring system. The spring system ascertains the constant curvature of the track at the cross-section and bottom on the horizontal surface, the two curved parts of the track on the inclined surface, and the two elliptical parts of the track bottom profile on the inclined surface. Therefore, the modeling process can proceed based on the above theory.

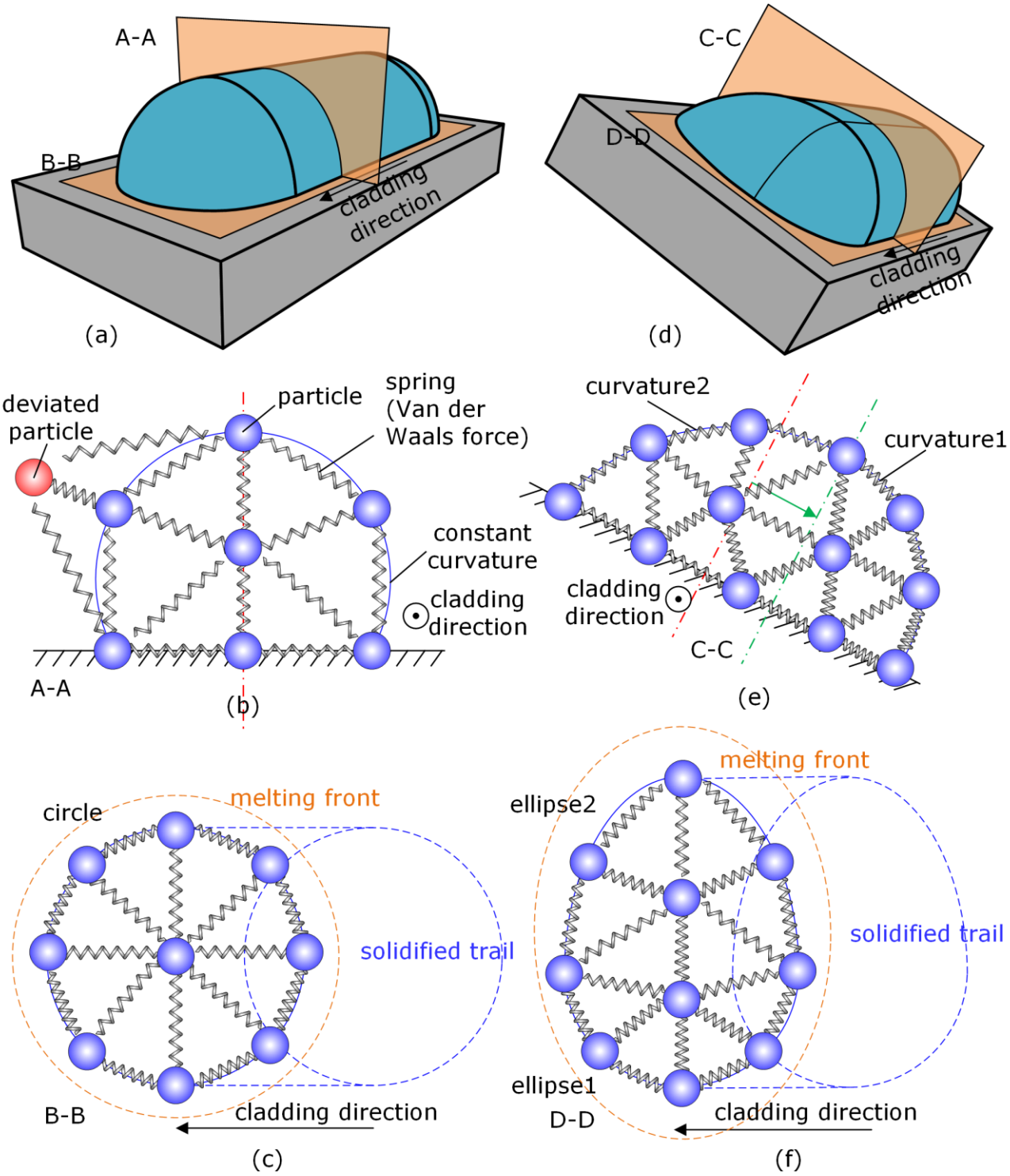

Figure 6.2 The schematics of (a) the track on the horizontal surface, (b) the spring system inside the cross-section plane A-A, (c) the spring system inside the longitudinal plane B-B, (d) the track on the inclined surface, (e) the spring system inside the cross-section plane C-C, and (f) the spring system inside the longitudinal plane D-D.

In general, the proposed model is based on the segmentation of the full 3D computation domain into cubic unit cells. The computation domain (see Figure 6.3a) includes the substrate and deposition zones with dimensions. For modeling, the computation domain was sliced into pieces (see Figure 6.3b). To obtain the 3D temperature field in the WLC, the calculation domain is segmented into cubic cells with the edge length Δd. Each cell position is marked as (x, y, z) in the predefined coordinate system (see Figure 6.3c) and a transient-spacial temperature owing to both the laser heating and the heat transfer.

The model begins with the calculation of laser energy absorption and heat transfer and determines the complete profiles of the deposited material when varying the inclined angles with the same processing parameters (e.g., laser power, scanning speed, and wire feed rate). As the tracks are cladded on the inclined surface, the deformation pulled by gravity is considered in the model. Therefore, the modeling process is divided into: (i) the calculation of the temperature field based on absorptivity and heat transfer (see Section 6.3.2), (ii) the bulge profile on the inclined surface (see Section 6.3.3), and (iii) the melt pool profile under an inclined surface (see Section 6.3.4).

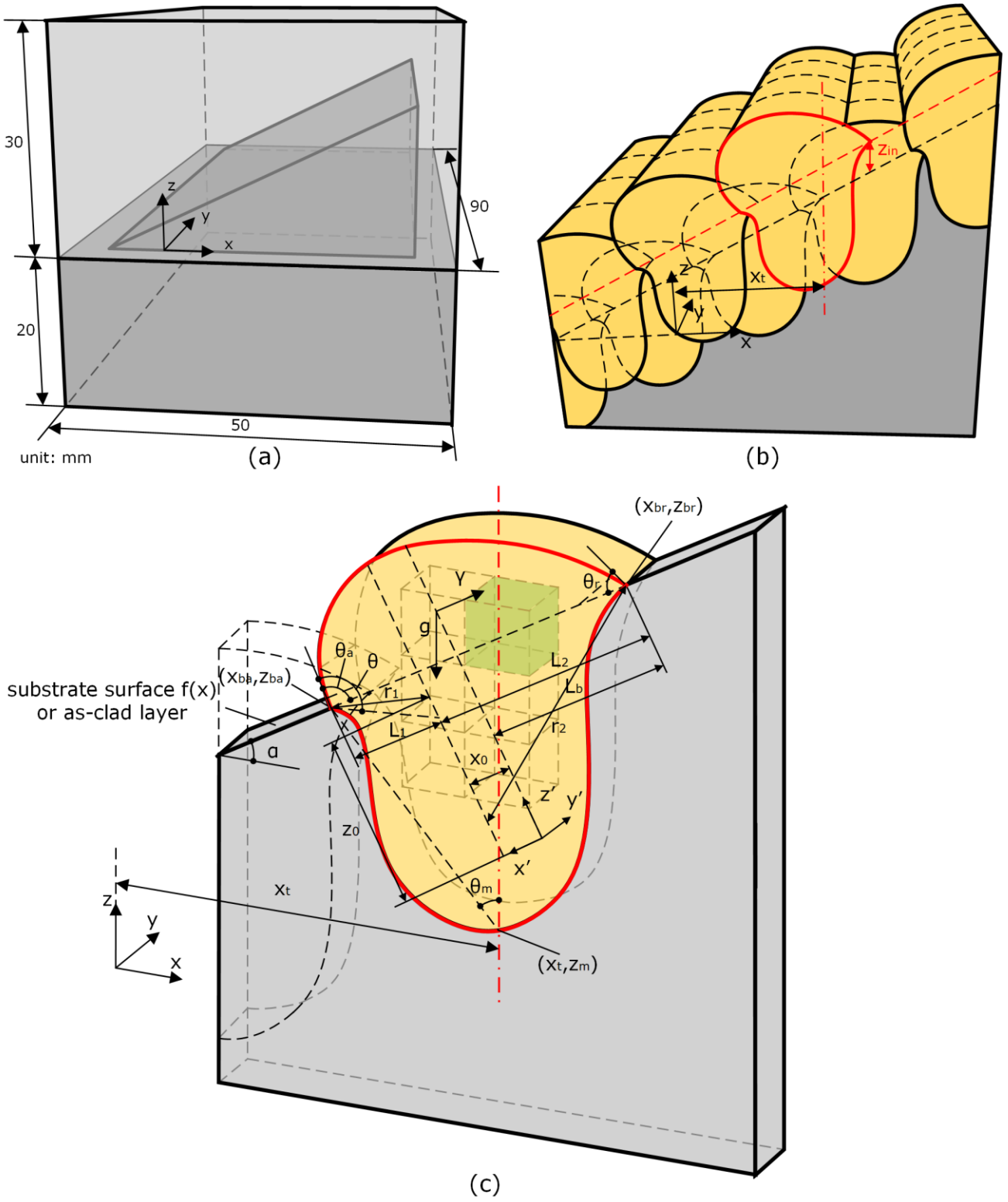

Figure 6.3 Schematics of theoretical modelling on inclined surface: (a) computation domain, (b) slices of computation domain, and (c) modelling parameters.

6.3.2 Calculation of temperature field in the tracks and substrate

Our temperature field calculation is based on laser absorptivity and heat transfer. Heat transfer means that the heat is transferred from the periphery of bulge to the environment by convection and radiation, while at the periphery of melt pool, the heat is transferred to the substrate by conduction and eventually to the environment by convection and radiation. The detailed modeling and time-dependent calculation process is the same as the one has been published in our previous study [206]. Here only the difference on the consideration of absorptivity is explained.

The absorptivity of material β describes the absorption of laser intensity I by the material and will vary due to the evolution of the melt pool written as follows [207]

$$\beta = 1 - \sigma^{\frac{\pi}{4\theta_m}+1}, \tag{6.1}$$

where $\sigma = 0.65$ is the Fresnel reflection of stainless steel [152] under the laser wavelength of $1\,\mu m$ [67], θ_m is the estimated angle to measure the extension of the melt pool (see Figure 6.3c), and it calculates the ratio of entrapped laser caused by multiple reflections inside the melt pool.

6.3.3 Calculation of bulges profile on inclined surface

Based on the experimental observations [208, 209], the cross-sectional retention profile of a bulge on an inclined surface can be approximated by two sections of arc (see Figure 6.3c), written as

$$(x - x_a)^2 + (z - z_a)^2 = r_1^2, \tag{6.2}$$

$$(x - x_r)^2 + (z - z_r)^2 = r_2^2, \tag{6.3}$$

where the position (x_a, z_a), (x_r, z_r), and radii r_1 and r_2 are calculated as follows:

The positions (x_a, z_a) and (x_r, z_r) are at the global coordinate and are transferred from the relative coordinates for deduction easiness, written as

$$\begin{bmatrix} x_a & z_a & 1 \\ x_r & z_r & 1 \end{bmatrix}$$

$$= \begin{bmatrix} x_0 & z_0 & 1 \\ x_0 & 0 & 1 \end{bmatrix} \begin{bmatrix} -\cos\alpha & -\sin\alpha & 0 \\ -\sin\alpha & \cos\alpha & 0 \\ (r_2 cos\theta_r)\sin\alpha - dx\cos\alpha + x_t & f(x_t) - (r_2 cos\theta_r)\cos\alpha - dx\sin\alpha & 1 \end{bmatrix}, \tag{6.4}$$

where $f(x)$ is the function of the inclined surface, and z_{in} is the height at the intersection point of the two bulges at the lower layer (see Figure 6.3c).

The horizontal position of the current bulge, x_t in Equations (6.2) and (6.3) is calculated from the overlap rates and widths by

$$x_t = w(1 - \eta_{OR})\big((j-1) + \eta_{SR}(i-1)\big), \tag{6.5}$$

where w is the width of the first bulge in the first layer, η_{OR} is the overlap ratio, and η_{SR} is the stagger ratio, i denotes the ith layer, and j denotes the jth bulge of the layer.

The horizontal position x_0 is calculated based on the drop height reaching a maximum, which is deduced as follows:

$$x_0 = \frac{-c_3 + \sqrt{c_3^2 - 2c_1c_2}}{c_1}, \tag{6.6}$$

$$c_1 = \frac{(\rho_l - \rho_a) g sin\alpha}{\gamma}, \tag{6.7}$$

$$c_2 = \frac{1}{2}\left(\sin\theta_a - \sin\theta_r - \frac{(\rho_l - \rho_a) g L_b^2 sin\alpha}{\gamma}\right), \tag{6.8}$$

$$c_3 = \frac{\sin\theta_a + \sin\theta_r}{2L_b}, \tag{6.9}$$

where θ_a and θ_r are the advancing and receding angles, respectively, ρ_l and ρ_a are the densities of the metal liquid and air, γ is the surface tension, g is the gravity acceleration, α is the inclined angle, and L_b is the half-length of the retention drop.

The vertical position z_0 is calculated based on two circles having a common tangent at the maximum value of the z-coordinate, which is deduced as follows:

$$z_0 = \frac{L_2}{\sin\theta_r} - \frac{L_1}{\sin\theta_a}, \tag{6.10}$$

$$L_1 = \frac{2L_b L_f}{1 + L_f}, \tag{6.11}$$

$$L_2 = \frac{2L_b}{1 + L_f}, \tag{6.12}$$

$$L_f = \frac{\sin\theta_a\,(1 - \cos\theta_r)}{\sin\theta_r\,(1 - \cos\theta_a)}. \tag{6.13}$$

The radius r_1 and r_2 are calculated as

$$r_1 = \frac{L_b - x_0}{\sin\theta_a}, \tag{6.14}$$

$$r_2 = \frac{L_b + x_0}{\sin\theta_r}. \tag{6.15}$$

The above position (x_0, z_0) and radii r_1 and r_2 are related to the corresponding advancing and receding angles θ_a and θ_r. The advancing angle θ_a can be calculated based on the intrinsic angle θ [184], written as follows:

$$\theta_a = \theta - \alpha. \tag{6.16}$$

The receding angle θ_r can be calculated based on the force balance [210] between gravity in x component F_{gx} [211] and surface tension γ (see Figure 6.*4*), written as

$$\theta_r = \cos^{-1}\left(\frac{F_{gx}}{\gamma l} + \cos\theta_a\right), \tag{6.17}$$

$$F_{gx} = \frac{\pi R_w^2 v_f}{v_s} l\left(\rho_l - \rho_g\right) g \sin\alpha, \tag{6.18}$$

where $\frac{\pi R_w^2 v_f}{v_s}$ denotes the area calculated from the wire material addition, and the half-length of the retention drop L_b is limited by the cross-sectional area, which can be deduced based on the geometrical relation as an implicit function of the advancing and receding angles θ_a and θ_r, written as

$$(L_b - x_0)^2\left(\frac{\theta_a - sin\theta_a cos\theta_a}{sin^2\theta_a}\right) + (L_b + x_0)^2\left(\frac{\theta_r - sin\theta_r cos\theta_r}{sin^2\theta_r}\right) = 2\left(\frac{\pi R_w^2 v_f}{v_s} + S_{overlap}\right). \tag{6.19}$$

where $S_{overlap}$ is the overlap area with the previous bulge calculated by a grid.

The above discussions are with regard to the profile geometry, yet the position of the profile has shifted down the inclined surface (see Figure 6.4). As the drop profile from the normal top view can be fitted by a circle at the drop front and an ellipse at the drop tail, as explained in Section 6.3.1 [208], the shifted distance dx can be calculated by subtracting the ellipse focus c by the transition position

x_0. The ellipse focus c, by definition, is calculated by multiplying the eccentricity e (regarded as $sin\alpha$) of the ellipse with the semi-major axis L_2, written as

$$dx = L_2 sin\alpha - x_0. \tag{6.20}$$

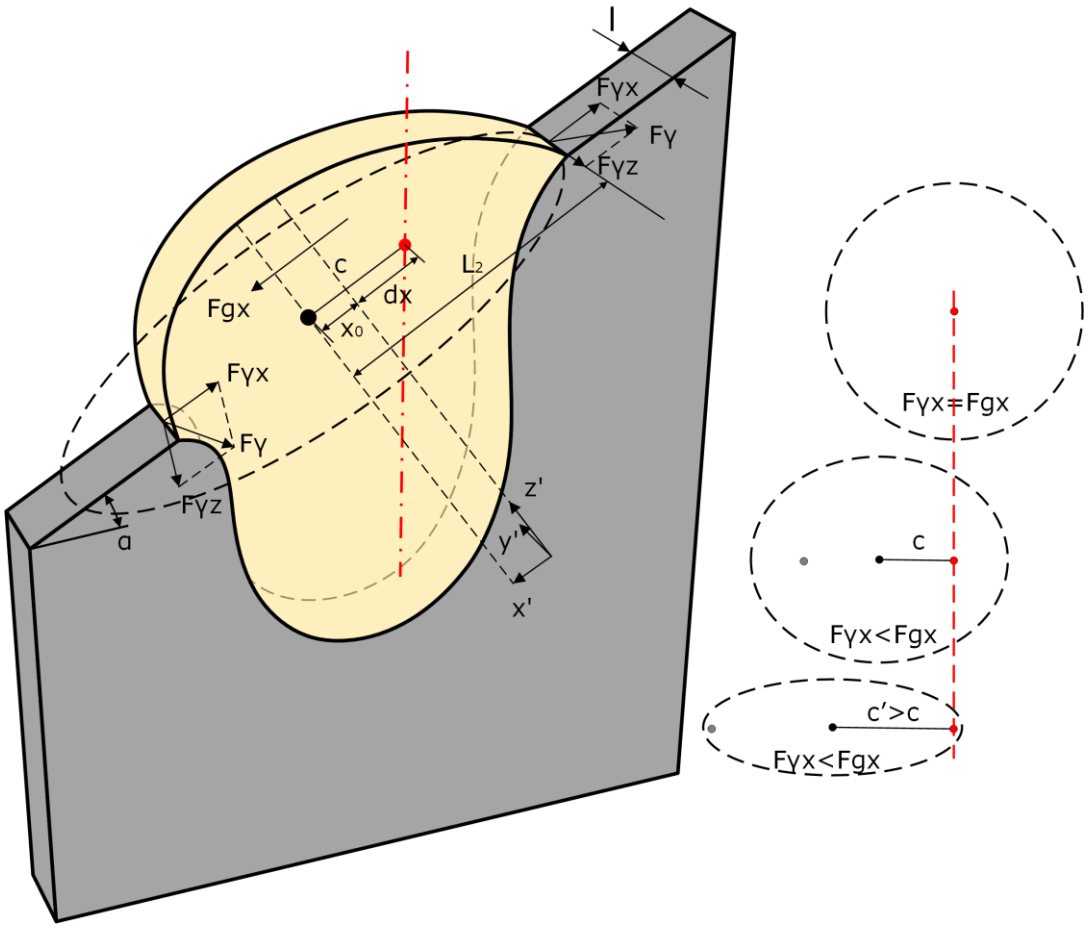

Figure 6.4 Schematic of forces on the droplet on inclined surface and the determination of shifted distance.

6.3.4 Calculation of melt pools profile below inclined surface

As the material of the bulge shifted downward from the inclined surface, the profile of the melt pool had to be adapted to the bulge profile. Based on the experimental observations, the melt pool profiles are different as the inclined angle varies and can be modeled based on the extension of the melt pool: (i) penetration mode and (ii) conduction mode.

(i) Penetration mode

The melt pool learns the behavior of the pendant droplet on an inclined surface. Simultaneously, based on the experimental observations of the melt pool profile, the bottom of the melt pool aligns with the laser location. The melt pool profile is separated into two sections, i.e., the advancing and receding sides, because there are different calculation methods for them, although the principle is based on the same interfacial tension of the pendant droplet.

For the advancing side, the melt pool boundary profile is modeled by the traditional pendant droplet with analytical solution $z = f(x)$ of the interfacial tension [159] connecting the points (x_t, z_m) and (x_{ba}, z_{ba}), written as

$$\frac{d\varphi}{ds} = \frac{\rho g c_m (z_m - z)}{\gamma_{sl}} - \frac{sin\varphi}{x} + \frac{2}{R_0}, \tag{6.21}$$

$$\frac{dx}{ds} = cos\varphi, \tag{6.22}$$

$$\frac{dz}{ds} = sin\varphi, \tag{6.23}$$

$$R_0 = \delta_a (x_t - x_{ba}) \tag{6.24}$$

$$\varphi(0) = 0, \qquad x(0) = \mathrm{x}_t, \qquad z(0) = z_m, \tag{6.25}$$

where z_m is the lowest point of the melt pool obtained from the temperature field, and coefficient c_m is the modification factor that ensures that the curve constructed by Equations (6.21)-(6.25) aligns with the curve of the bulge, γ_{sl} is the interfacial tension, and R_0 is the curvature radius at the bottom of the melt pool.

For the receding side, the melt pool boundary profile is modeled by the traditional pendant droplet with analytical solution $z = f(x)$ of the interfacial tension, hanging below the middle point of bulge $(0.5(x_{ba} + x_{br}), z_m)$ and later aligning back to the laser location connecting the points (x_t, z_m) and (x_{br}, z_{br}), written as

$$\frac{d\varphi}{ds} = \frac{\rho g c_m (z_m - z)}{\gamma_{sl}} - \frac{sin\varphi}{x'} + \frac{2}{R_0}, \tag{6.26}$$

$$\frac{dx'}{ds} = cos\varphi, \tag{6.27}$$

$$\frac{dz}{ds} = sin\varphi, \tag{6.28}$$

$$R_0 = \delta_r (x_{br} - x_{ba})/2 \tag{6.29}$$

$$\varphi(0) = 0, \qquad x'^{(0)} = 0.5(x_{ba} + x_{br}), \qquad z(0) = z_m, \tag{6.30}$$

$$x = x' + \frac{x_t - x'^{(0)}}{(z_m - z_{br})}(z_m - z). \tag{6.31}$$

In Equations (6.21)–(6.31), the interfacial tension γ_{sl} is correlated to the reference temperature, e.g. the average temperature in the melt liquid [206]; and the coefficients δ_a and δ_r affect the melt pool profile and are related to the wire and substrate material type which can be determined by a calibration procedure (see Section 6.4).

The melt pool profile constructed by Equations (6.21)–(6.31) is assumed as a liquid-fluid system due to the existence of a sticky mushy layer, another phase of fluid, between the melt liquid and substrate solid [158].

Please note, $\rho g(z_m - z)$ in Equation (6.21) and (6.26) is the hydrostatic pressure difference from the melt pool bottom to the calculated point. As the WLC is

conducted on an inclined surface, the static pressure contribution to balance the surface tension force takes the inclined angle into consideration by the height difference $(z_m - z)$.

(ii) Conduction mode

If the advancing side of the melt pool (x_{ba}, z_{ba}) is lower than the melt pool bottom (x_t, z_m), the melt pool wall profile is modeled by the parabola [212] with analytical solution $z = f(x)$, hanging between the two retention points of bulge (x_{ba}, z_{ba}), (x_{br}, z_{br}) and the melt pool bottom (x_t, z_m), written as

$$z = [x^2 \quad x \quad 1] \begin{bmatrix} x_{ba}^2 & x_{ba} & 1 \\ x_{br}^2 & x_{br} & 1 \\ x_t^2 & x_t & 1 \end{bmatrix}^{-1} \begin{bmatrix} z_{ba} \\ z_{br} \\ z_m \end{bmatrix}. \tag{6.32}$$

In summary, the melt pool profile is obtained using Eqs. (6.21)–(6.32).

All the related parameters in the model are concluded (see Table 6.1). Most of the parameters in the equations are referred to the existing research, which are applied in the same conditions. Only the melt pool profile coefficients δ_a and δ_r need calibration.

Table 6.1 Parameters in the proposed model

Properties	Values	Units	Applied conditions
g	9.8	m/s^2	near earth surface
σ	0.65 [152]		wavelength 1.070 μm, stainless steel
δ_a and δ_r	see Section 6.4		calibration
ρ_l	7130 [213]	kg/m^3	Liquid 316L
ρ_a	1.225 [214]	kg/m^3	At sea level and 15 $°C$

6.3.5 Flowchart of modelling

A flowchart of the complete profile calculation is presented in Figure 6.5 to conclude the modeling steps. All above-mentioned equations were transferred into codes in MATLAB.

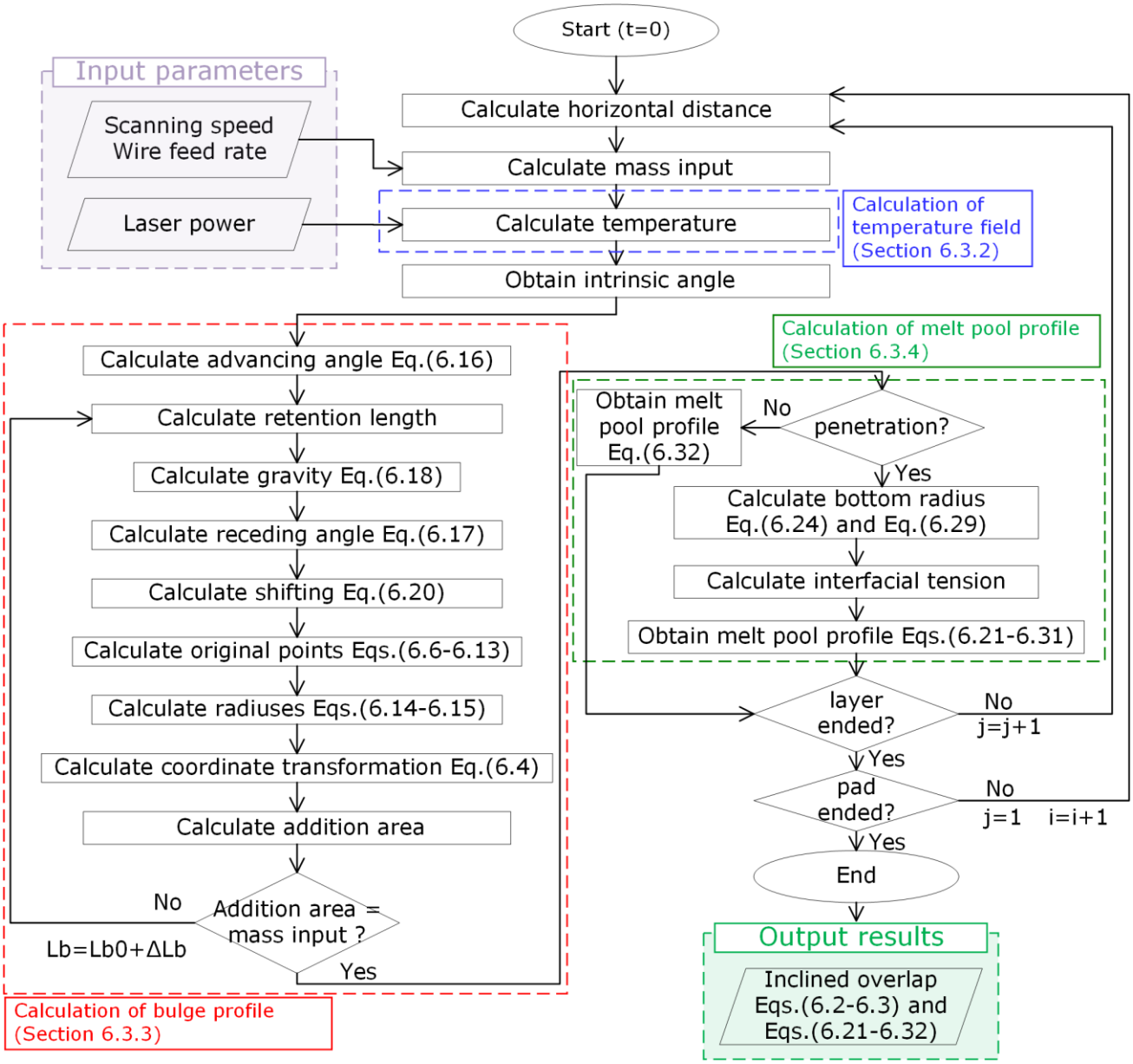

Figure 6.5 Flowchart of theoretical modelling to calculate horizontal overlap and inclined retention profile by inputting processing parameters including laser power, scanning speed and wire feed rate.

6.4 Experimental setup

To validate the proposed model that predicts the cladding-affected area, a set of experiments was performed. During cladding, the employed parameters for cladding experiments (see Table 6.2) were divided into the common processing parameters—Trial 1 for the single track on an inclined surface, and Trial 2 for the overlap on the inclined surface—as it enabled robust evaluation of the model in relation to the described physics of the process (mentioned in Section 6.3).

Table 6.2 Track parameters for WLC experiments

No.	Aims	Parameters	Values
Trial 1	Single track on inclined surface	Inclined angle	10°, 30°, 45°
Trial 2	Overlapped track on inclined surface	Overlap ratio	10%
		Stagger ratio	50%
		Inclined angle	30°

To obtain a steady and smooth track, the laser power was set to 1.6 kW, scanning speed to 0.1 m/min, and wire feed rate to 0.6 m/min at the feed in and inclined angle of 45°. Each track was kept 60 mm in length to ensure a stable thermal status and for the convenience of selecting the smooth section to cut samples for analysis (see Figure 6.6b). Trial 1 was set up at inclined angles of 10°, 30°, and 45° (see Figure 6.6c to e). Trial 2 was set up at an inclined angle of 30° with an overlap ratio of 10% and a stage ratio of 50% (margins can be referred to Figure 6.6b with an overlap layer filling the area). N_2 protection gas was steadily fed onto the cladding surface. Two neighboring tracks had a time interval of 30 mins so that heat effect on the next track can be reduced (see Figure 6.7).

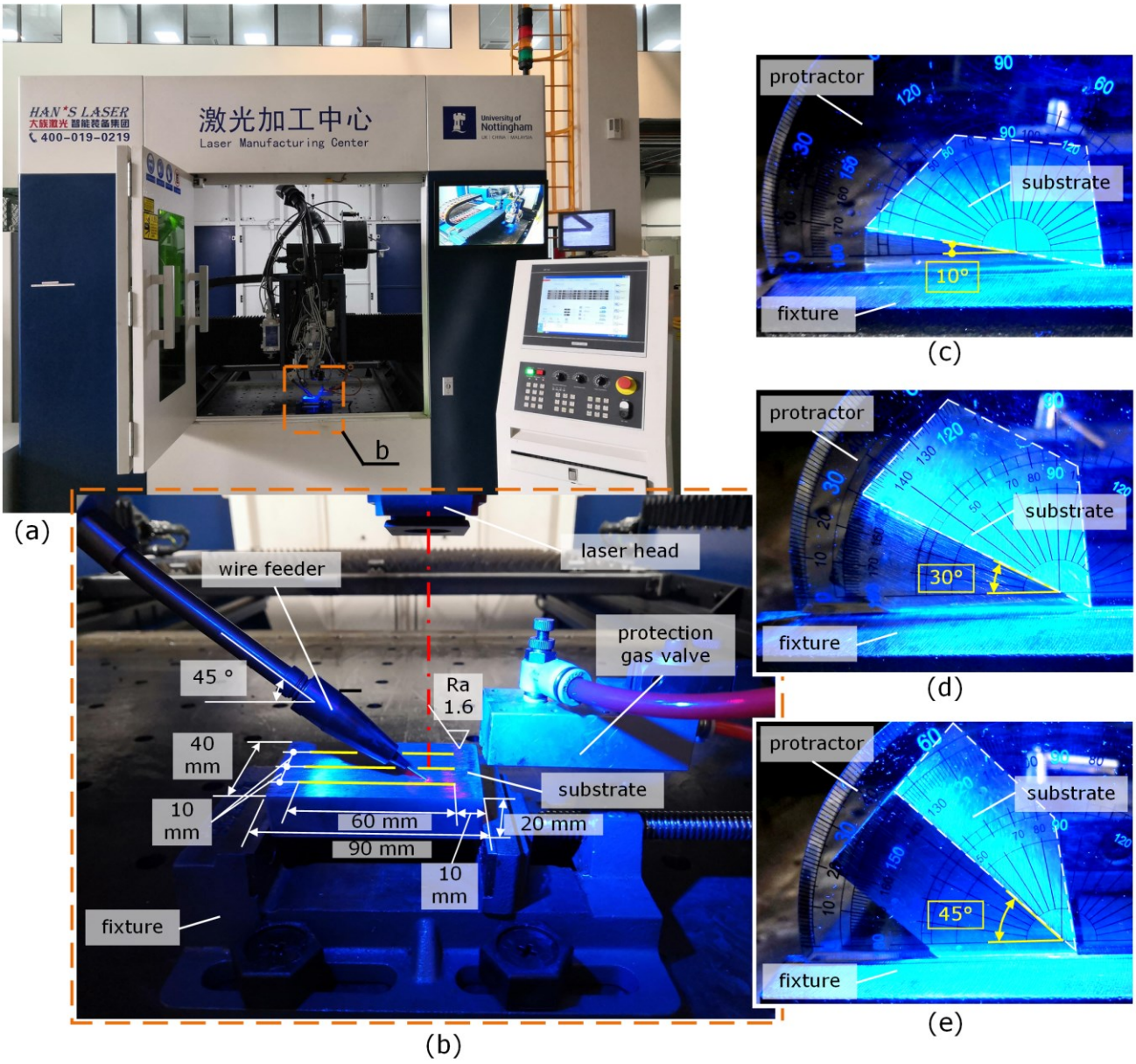

Figure 6.6 Illustration of experiment: (a) laser manufacturing centre, (b) cladding setup, (c) 10° inclined setting, (d) 30° inclined setting, and (e) 45° inclined setting.

The calibration of the coefficients δ_a and δ_r (mentioned in Section 6.3.4) included three steps: (i) one cladding trial on an inclined substrate with 30° was performed firstly (the angle was enough to show incline effect while tracks were in stable states as Figure 6.8a); (ii) the melt pool profile was then measured and compared with the profiles calculated by different coefficients δ_a and δ_r(see Figure 6.8b);

and (iii) the coefficients δ_a and δ_r were determined when the experimental and calculated profiles matched the most. δ_a=0.6 and δ_r=0.9 were determined in this paper (see Figure 6.8b).

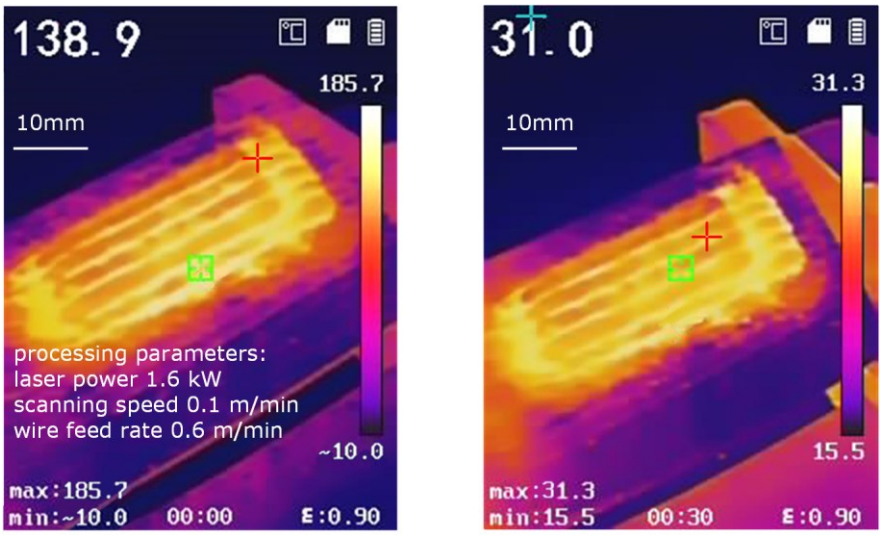

(a) (b)

Figure 6.7 Temperature domain: (a) after cladding and (b) after 30 mins.

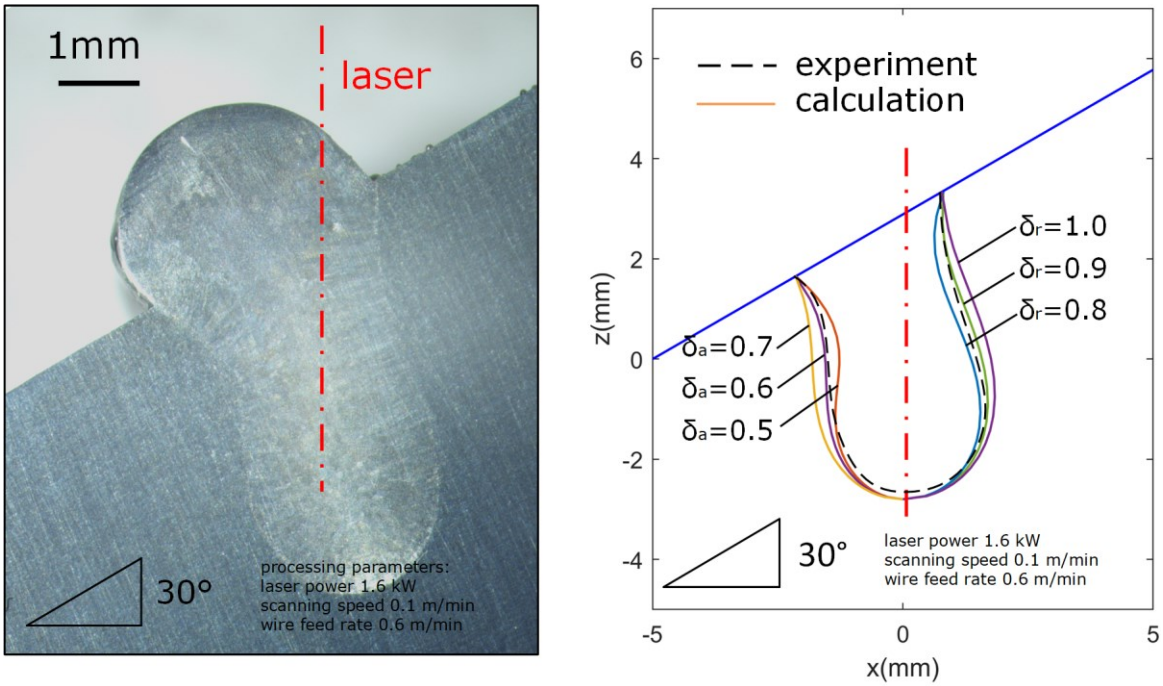

(a) (b)

Figure 6.8 The calibration of the coefficients δ_a and δ_r: (a) experimental trial on an inclined substrate with 30° and (b) comparisons between experimental and calculated profiles.

6.5 Model validation

The model validation includes: (i) one track on the inclined surface, and (ii) one layer on the inclined surface, and (iii) two layers on the inclined surface.

6.5.1 Single track on the inclined surface

Figure 6.9 shows that, in general, the calculated full track profile on the inclined surface is close to the experimental profile when the inclined angle is changed, where the maximum relative error is 25% at the melt pool of 45° inclined angle. The calculations rightly simulate the retention of one bulge in the deformation and shifting aspects when the inclined angle is changed. The melt material was deposited onto the inclined surface, while melting was always accompanied by material migration. The complex fluid dynamics are bypassed by focusing on the boundary where surface tension exists. The force acting on the interface is a convenient factor for determining the advancing and receding angles, and therefore, to determine the entire geometry of the bulge.

The advancing angle is calculated using the inclined angle and intrinsic angle. The accuracy of predicting the intrinsic angle is relatively unreliable and may be a source of error. It is usually affected by the surface roughness of the substrate surface and the probable outcomes of discontinuous migration. However, it does not profoundly affect the geometry profile. The material shift is an internal factor of the boundary deformation but not an independent move of deposition. This is

calculated separately owing to the need for a mathematical model. The relationship to the inclined angle seems accurate based on the results.

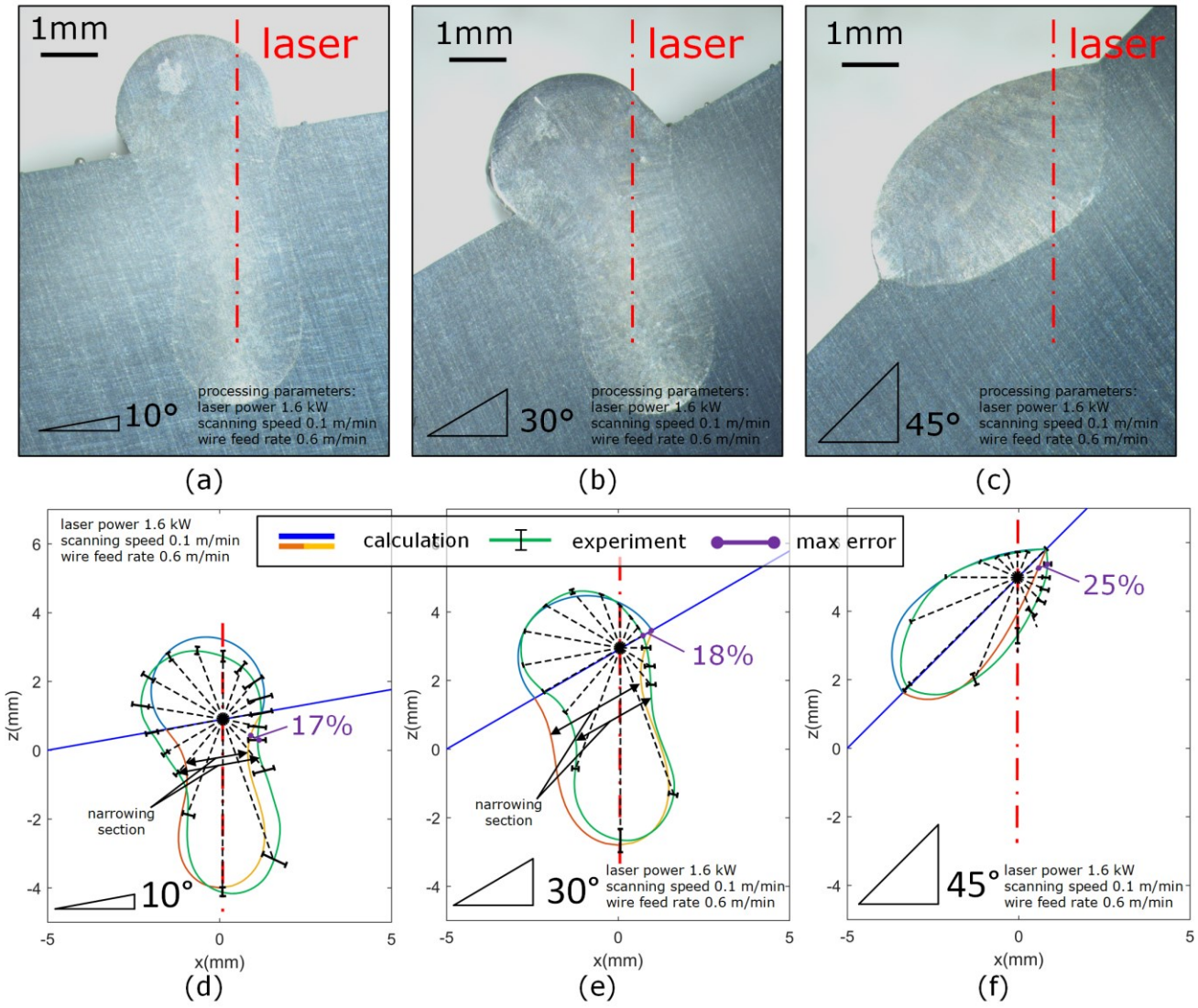

Figure 6.9 Cross-sections of the cladding-affected area for varying inclined angle: (a) exp. 10° (b) exp. 30° (c) exp. 45° (d) exp. and cal. 10° (e) exp. and cal. 30°, and (f) exp. and cal. 45° (P = 1.6 kW, v_s = 0.1 m/min, v_f = 0.6 m/min).

The melt pool interface profile is constructed with two sections: the advancing side and the receding side. The near surface end of the advancing side evolves downward the inclined surface owing to the bulge migration at the advancing contact corner. This is the cause of the obvious narrowing section on the profile,

as can be seen in the results, and it raises the requirement for the model to predict it. However, migration does not affect the melt pool bottom. The near surface end of the receding side also follows the bulge migration at the receding contact corner, and there is also an obvious narrowing section on the profile, except for the 45° inclined angle.

The detailed estimation of the profile error validates the model in the single-track aspect, while the overlap profiles are also required of the model and are introduced next.

6.5.2 One layer on the inclined surface

Figure 6.10 shows that the calculated one-layer profile on the inclined surface is close to the experimental one, with an error of 15.1%, mainly at the melt pool. The error is estimated as the ratio of the discrepancy area to the experimental area. Under such an estimation method, any discrepancy in the profile reflects the error value, thereby making it reasonable and convenient to quantify the accuracy of the overlap track profile.

Please note the cap thickness is defined by a line fitted with the valley points B to H in Figure 6.11 based on least square method (except the ones at both ends A and I which are usually unstable).

There are gaps between tracks that indicate unmelted regions, which means there will be discontinuous spots on the surface when the caps are machined. As the gaps are regular and visible, repairing it with another laser pass to remelt the overlapping regions is convenient. The gaps and porosities are normal

phenomena occurring in additive manufacturing, especially the scheme involving powder, i.e., powder bed fusion, powder-fed laser cladding where defects usually occur irregularly [215] or invisible [216]. One case is concerned about the repair of porosities and cracks on laser-sintered tools with WLC [217].

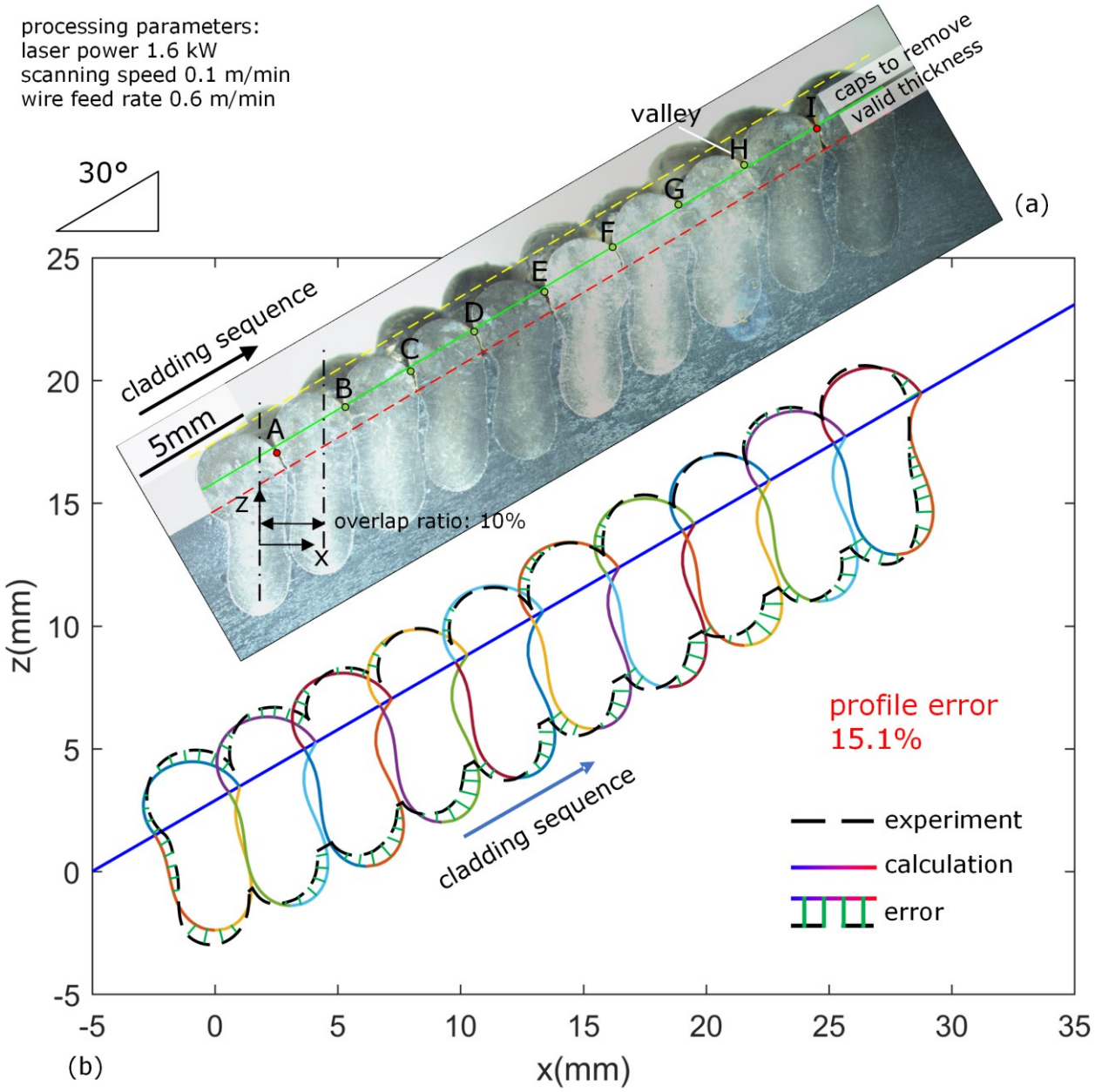

Figure 6.10 Cross-sections of the one-layer cladding-affected area on 30° inclined surface: (a) experimental cutups and (b) validation results, at constant (P = 1.6 kW, v_s = 0.1 m/min, v_f = 0.6 m/min, and overlap ratio = 10%).

One-layer cladding is usually applied when the thickness is highly restricted or when only one layer can be conducted. Under such conditions, the thickness control method is operable by tilting the substrate at the calculated angle, achieving a valid thickness. There are three advantages to conducting such a scheme: (i) to eliminate the caps that need to be machined, which increases material utilization; (ii) to expand the cover area in one pass under the optimized processing parameters (for a stable track); and (iii) to reduce dilution (ratio of melt pool depth to total height), which reserves the add-in material properties in the cladding of dissimilar materials.

While the cladding on an inclined flat surface can be stable, the cladding on an as-clad layer on an inclined surface may be a challenge, which is discussed next.

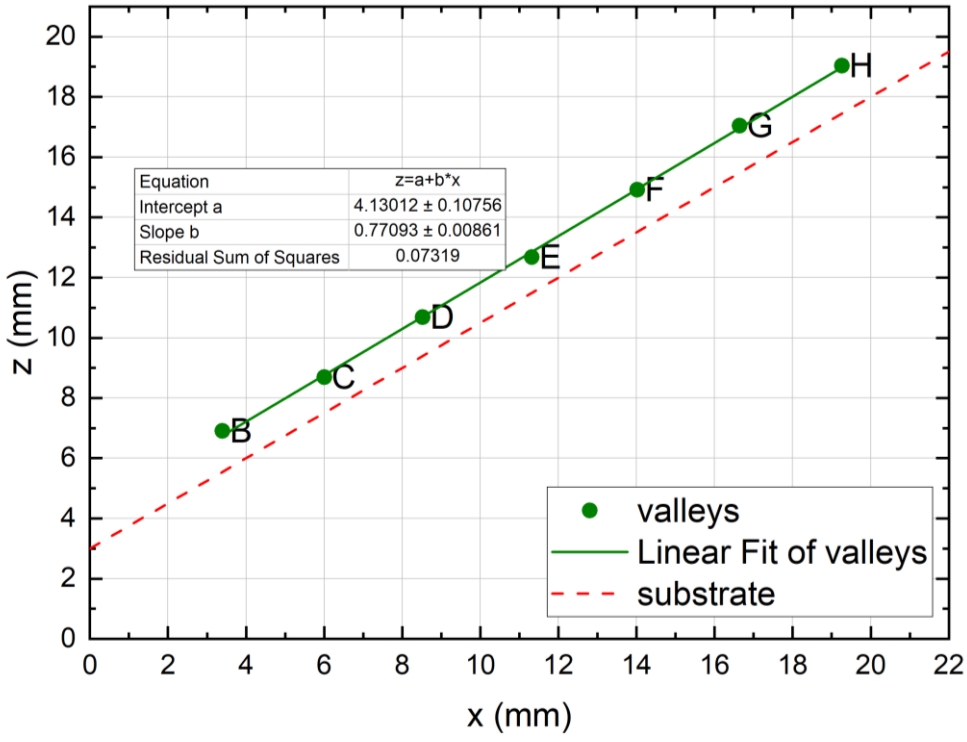

Figure 6.11 The measurement of cap thickness based on least square method.

6.5.3 Two layers on the inclined surface

Figure 6.12 shows that the calculated two-layer profile on inclined surface is close to the experimental ones with the error of 13.2%. The second layer is able to rest on the inclined wavy surface of the first layer. Although there are gaps between tracks that indicate unmelt regions, they are eliminated when the second layer is cladded (see Figure 6.12a). It is reasonable to consider the pad (more than one layer) as a unit and only estimate the error of the pad outline for application purpose (see Figure 6.12b). For example, the detachment of the cladded pad can be analyzed when the workpiece sustains mechanical loads, i.e. tension, compression, bending, or torsion. Alternative noncontact procedures were proposed for measuring mechanical properties of laser cladded parts by using femtosecond laser ultrasonics [218]. The behavior must be highly related to the profile. The melt pool profiles above the first layer in the calculation may not be required in the geometrical predictions but are still presented in the results (see Figure 6.12b). It may be required in the metallurgical prediction of microstructures that go through different stages of remelting and solidification, as well as in the prediction of the mechanical properties of the overlap region that generates internal forces at the interface. External forces, encountered with the characteristic crystallographic orientation, were also required for machinability assessment of any alloy manufactured by laser cladding [219].

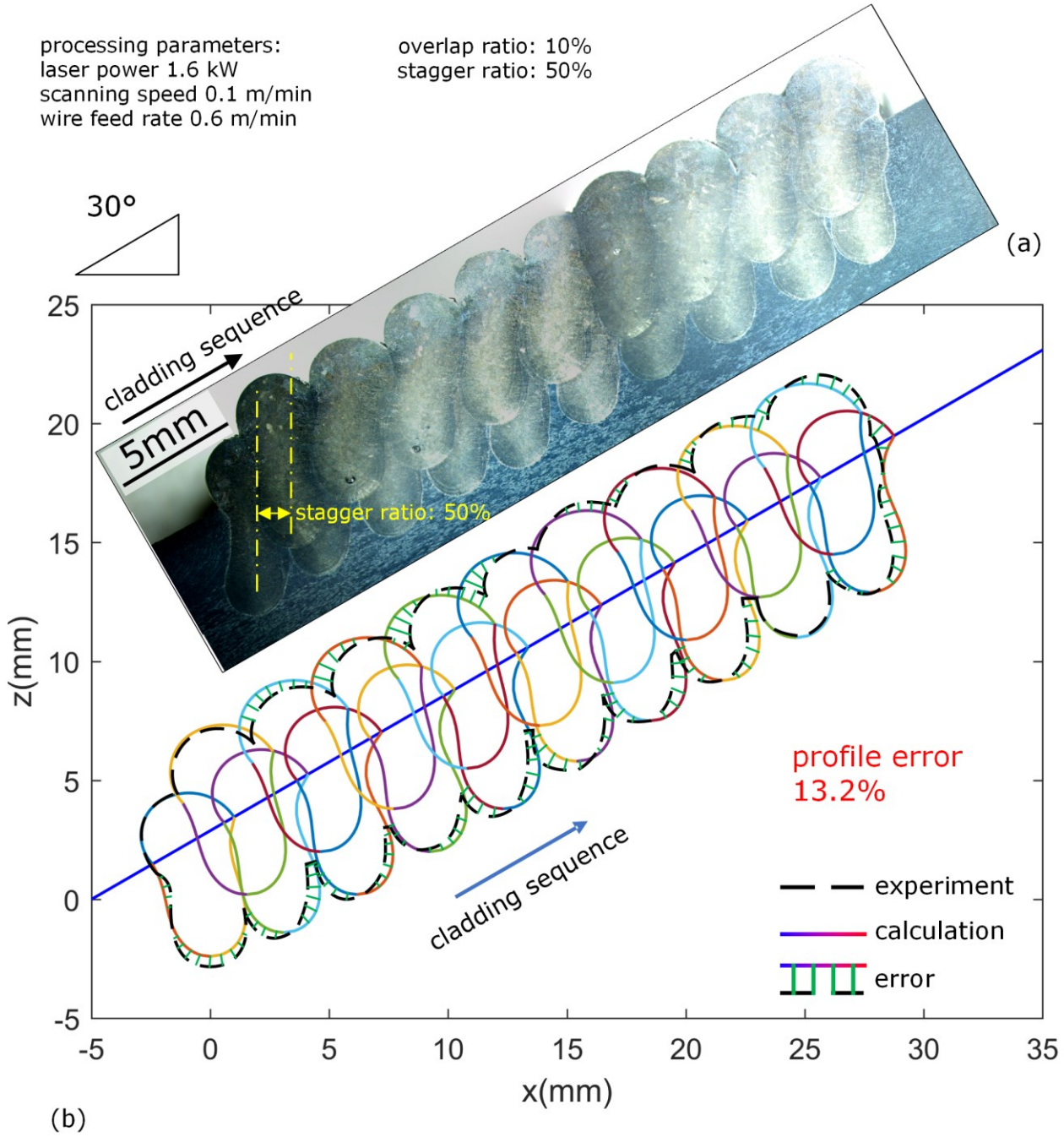

Figure 6.12 Cross-sections of the two-layer-cladding-affected area on 30° inclined surface: (a) experimental cutups and (b) validation results, at constant (P = 1.6 kW, v_s = 0.1 m/min, v_f = 0.6 m/min, overlap ratio = 10%, and stagger ratio = 50%).

Please note that the inter-layer temperature is naturally considered in the model because our model is calculated based on time. Figure 6.13 is an example that

shows the capability of predicting the fixed point temperature at the inter-layer where the point temperature is time dependent and it will also influence the melt pool shape of the second layer. The inclusion of dwell times between individual layers to allow for additional cooling during the deposition process brought decreased distortion and residual stress levels in a Inconel 625 laser cladding [220].

The model is validated by comparing the profiles of experiments and model calculations in a single track, one layer, and two layers on an inclined surface. An application case regarding the model is discussed next to reveal the characteristics of the CNC machine.

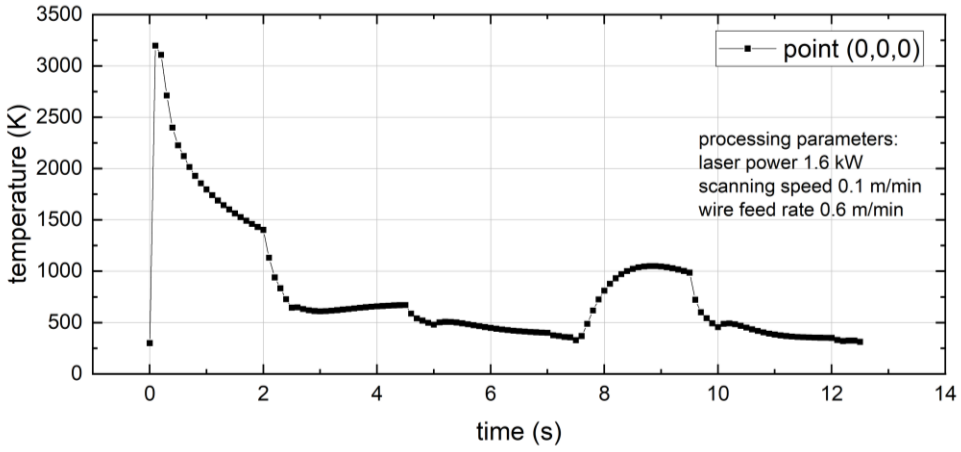

Figure 6.13 The temperature of a fixed point at the inter-layer predicted by the model.

6.6 Further discussions on the model

Metallurgical observations abound the track on inclined surface are discussed based on the model. The bulge shifts down along the surface compared to the laser position and the melt pool follows the change, (see Figure 6.14a). The small

equiaxed grains at the core of bulge point at the direction of feeding, e.g. normal into screen (Figure 6.14b). It indicates that the slow cooling rate during solidification. The dendritic grains distribute at the temperature gradient direction normal to the melt pool-substrate boundary (Figure 6.14c). It should be noted that the temperature gradient is the sign of rapid solidification at the contact corner which lock the contact angle at a rapid speed once the laser moves past the present cross section. The measurements of the diffusivity for both inter- and intralayer transport placed an upper bound on the Ehrlich-Schwoebel barrier for downhill interlayer diffusion [221].

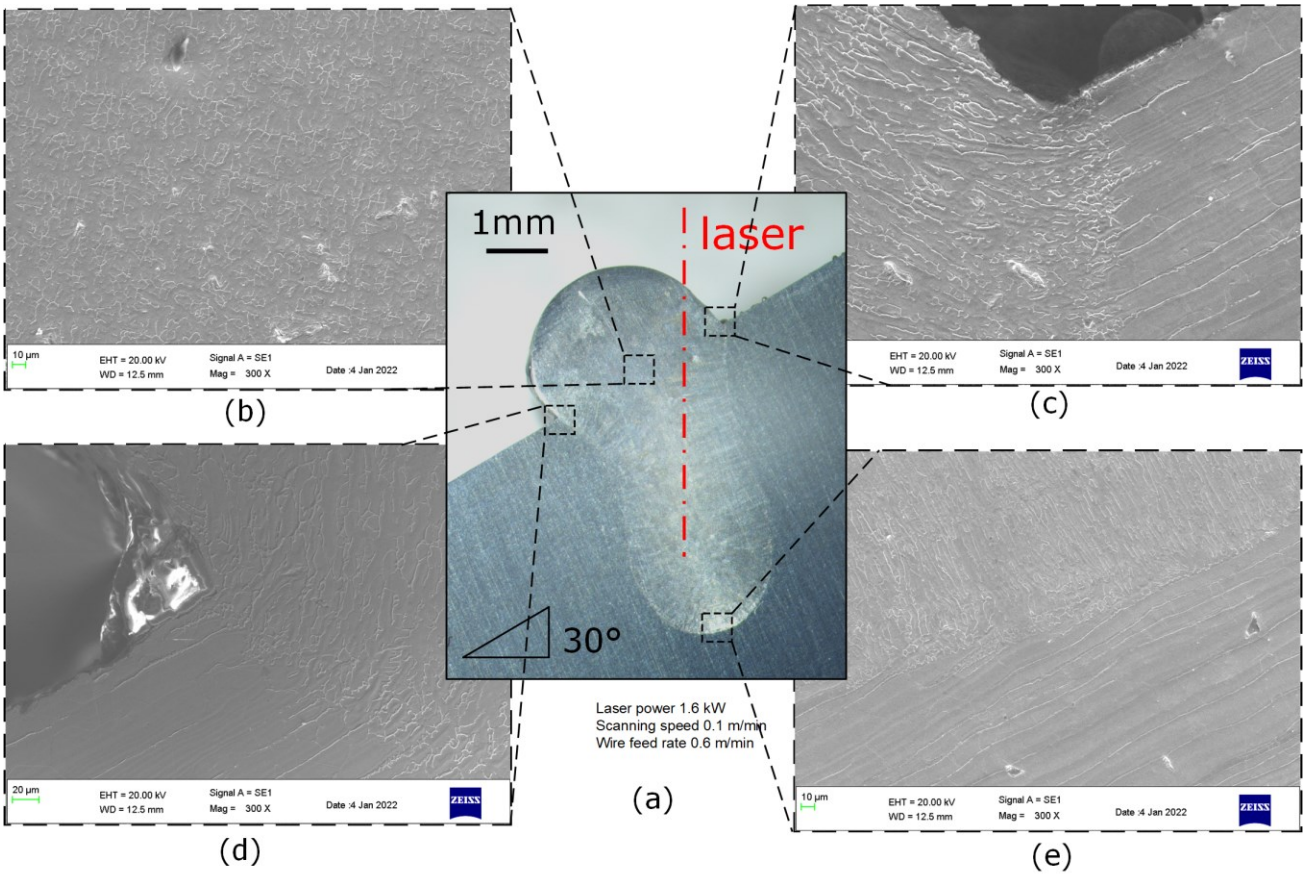

Figure 6.14 Microstructure observations of single track WLC on inclined surface: (a) track overview, (b) inside bulge, (c) receding side, (d) advancing side, and (e) melt pool bottom.

6.7 Model application cases

6.7.1 Control strategy of temperature on track and substrate

The first application of the model is to control the temperature on the track and substrate. The analytical model provides the transient temperature calculations of WLC on inclined surface (see Figure 6.15).

The heat focuses on the laser leading area while the periphery extends to the neighbouring tracks. The extension of heat periphery leads to the partial remelting of the previous one or two tracks, which is calculated by the model.

The base temperature is also increasing (colour is more and more bright) as the tracks are subsequently laid out on the surface which is calculated by the model. The interval time between two tracks is the factor to set so that the periodic base temperature can be maneuvered lower or higher than a value, as the need of metallurgy after the periodic tempering.

Without the model, these detailed descriptions of process change can not be fulfilled.

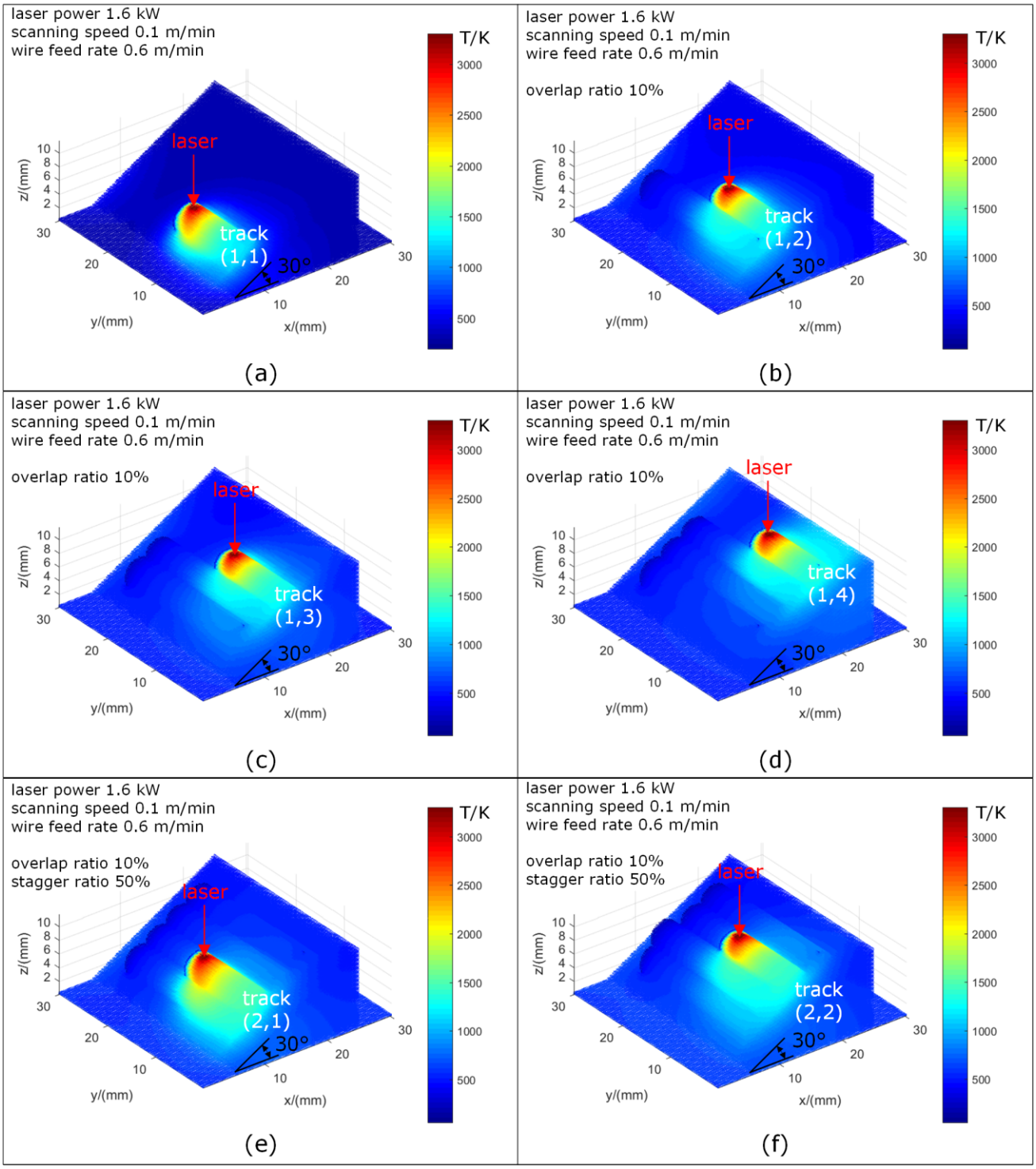

Figure 6.15 Temperature field calculation results of WLC on inclined surface: (a) track (1,1), (b) track (1,2), (c) track (1,3), (d) track (1,4), (e) track (2,1), and (f) track (2,2).

6.7.1 Control strategy of mould surface cladding

The second application of the model is to control the cladding layer thickness on the mould surfaces. The mould usually contains inclined surfaces and the cladding may be following the height variation [222], or perpendicular to height variation in this application case. One of the potentials of the developed model is to ensure that the cladding layer has a constant thickness. The valid thickness of the layer is the thickness at the valleys between the two bulges, while the caps above the valleys are machined. The model is expected to predict the valley thicknesses and provide an adjustment plan for one of the processing parameters, i.e., laser power, scanning speed, and wire feed rate, to maintain the thickness variations within an acceptable range. In this case, the scanning speed is varied because it is convenient and accurate for the automation system.

To prove this, the scanning speed is calculated by the model (0.102 m/min at 5° step-down, 0.075° m/min at 40°, 0.085 m/min at 30°, and 0.105 m/min at 10°) that ensures valleys between tracks in constant thickness in reference to the horizontal cladding section (see Figure 6.16a) while the laser power and wire feed rate are kept constant at 1.6 kW and 0.6 m/min, respectively; these process parameters are expected to yield stable process outputs (e.g. continuous and geometrically well-defined clads).

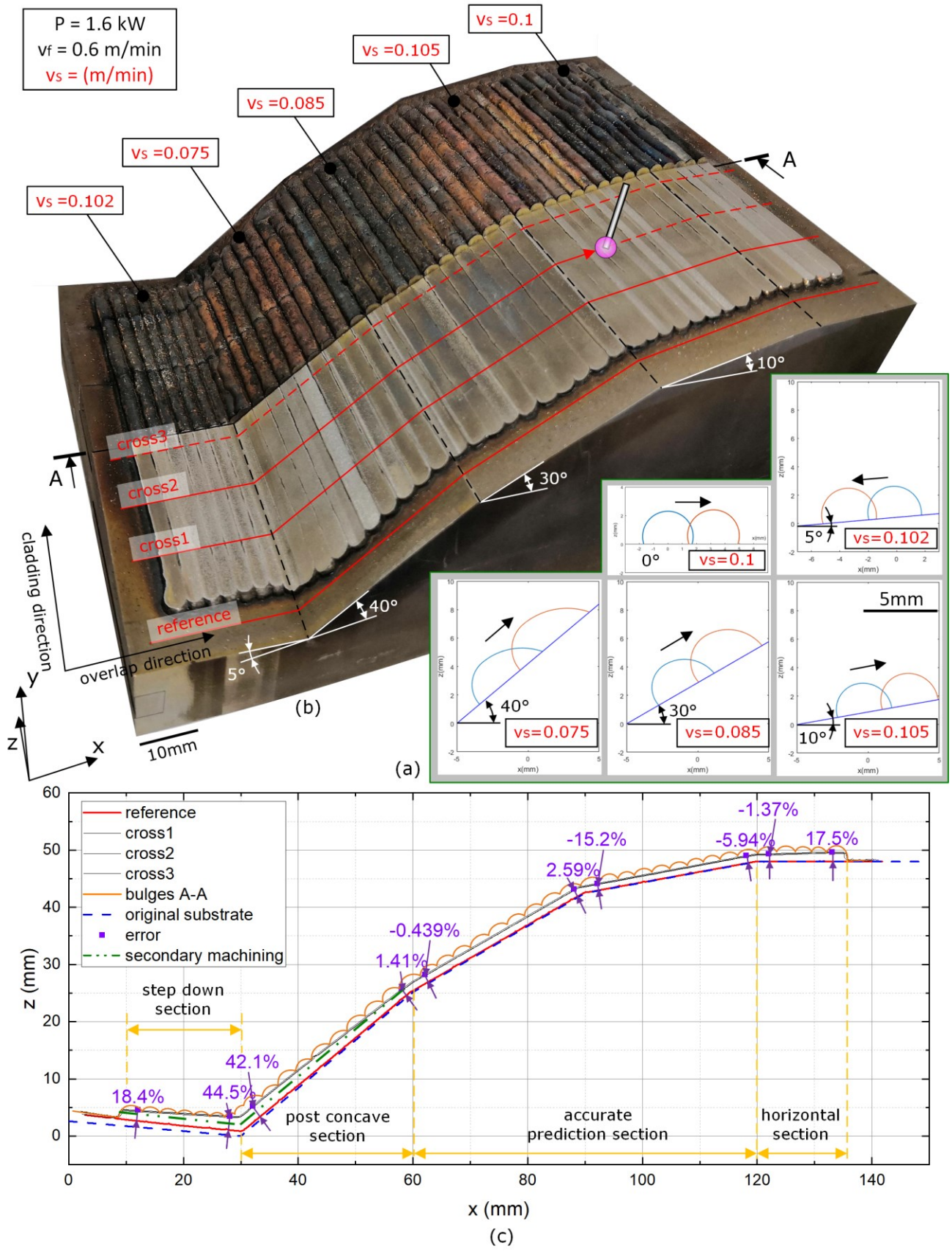

Figure 6.16 Trial results of cladding on continuous inclined surface with constant layer thickness parameters adjustments: (a) valleys thickness vs varied scanning

speed on inclined surface; (b) cladding experiment blocks with designed inclined angle; and (c) layer thickness before and after machining.

Before the cladding, the substrate with continuous inclined surfaces was machined into a shape (see Figure 6.16b) from the raw 316 L stainless steel block by electrical discharge machining. The surface roughness was within Ra3.2.

The cladding starts from the slow 5° step-down section with a track length of 100 mm. The interval distance was maintained when the cladding was pushed forward onto the inclined surfaces. Two neighboring tracks had a gap of 30 min to avoid the heat accumulation effect. The N_2 protection gas continues to feed on the cladding surface steadily.

Half of the track length was machined to remove the caps, for example, the part above the valley line. The flat machined surface was profiled using a coordinate measurement machine with a probe of diameter 2 mm. The other half was placed under an optical microscope to obtain the profile. As a result, the layer thickness with removed caps is revealed with positive and negative errors in reference to the calculated horizontal valley thickness (see Figure 6.16c). The profile can be divided into four sections: step-down section, post-concave section, accurate prediction section, and horizontal section. The step-down section is thicker because the laser tends to radiate on the previous track more closely and melts its material, thereby increasing the valley thickness. Each section gains thickness, which is a normal phenomenon due to the overlap accumulation, except for the post-concave section. The post-concave section is affected by the piles up of the

bulges owing to the concave corner. The secondary machining plan is also proposed in both sections at the concave corner because it is the usual procedure to remove excessive thickness by milling [223] or grinding [224], and probably the surface finish as a last step [225].

Overall, the idea of model application on constant layer thickness control by adjusting the processing parameters is validated by the experiment on continuous inclined angle change surfaces. The main problem of the model calculation is the thickness of the valleys, which depend sensitively on the geometries of the bulges. The accuracy of the model was critically tested in the trial. The thickness is approximately 1.5 mm under the processing parameters. There are many methods to increase the thickness if necessary: (i) addition of a layer over the as-clad or machined layer; (ii) decreasing the scanning speed or increasing the wire feed rate (laser power must be increased simultaneously for either adjustment); and (iii) increasing the overlap ratio, for example, decreasing the distance between bulges. All above-mentioned methods can be based on the same model for convenient calculations. The convenience depends on the only necessary calculation of the first two bulges for each inclined angle surface because the valley thickness after the first two bulges will increase. Therefore, the model also meets the requirements of efficiency in repair procedures. The model can also be applied on freeform surface which is partitioned into separate inclined cladding surfaces [226]. Additional attentions are paid to the tracks at the sharp edge [227], the effect of contact line pinning to the contact angle [228].

In this chapter, the additional parameter that requires inputs from operator on the GUI control panel is the inclined angle (see Figure 6.17). The inclined surface may be in varied angle gradients, i.e. the substrate in the previous application case. The possible increasing complexity of the substrate geometry will require a new graphic model design module or external CAD imported model.

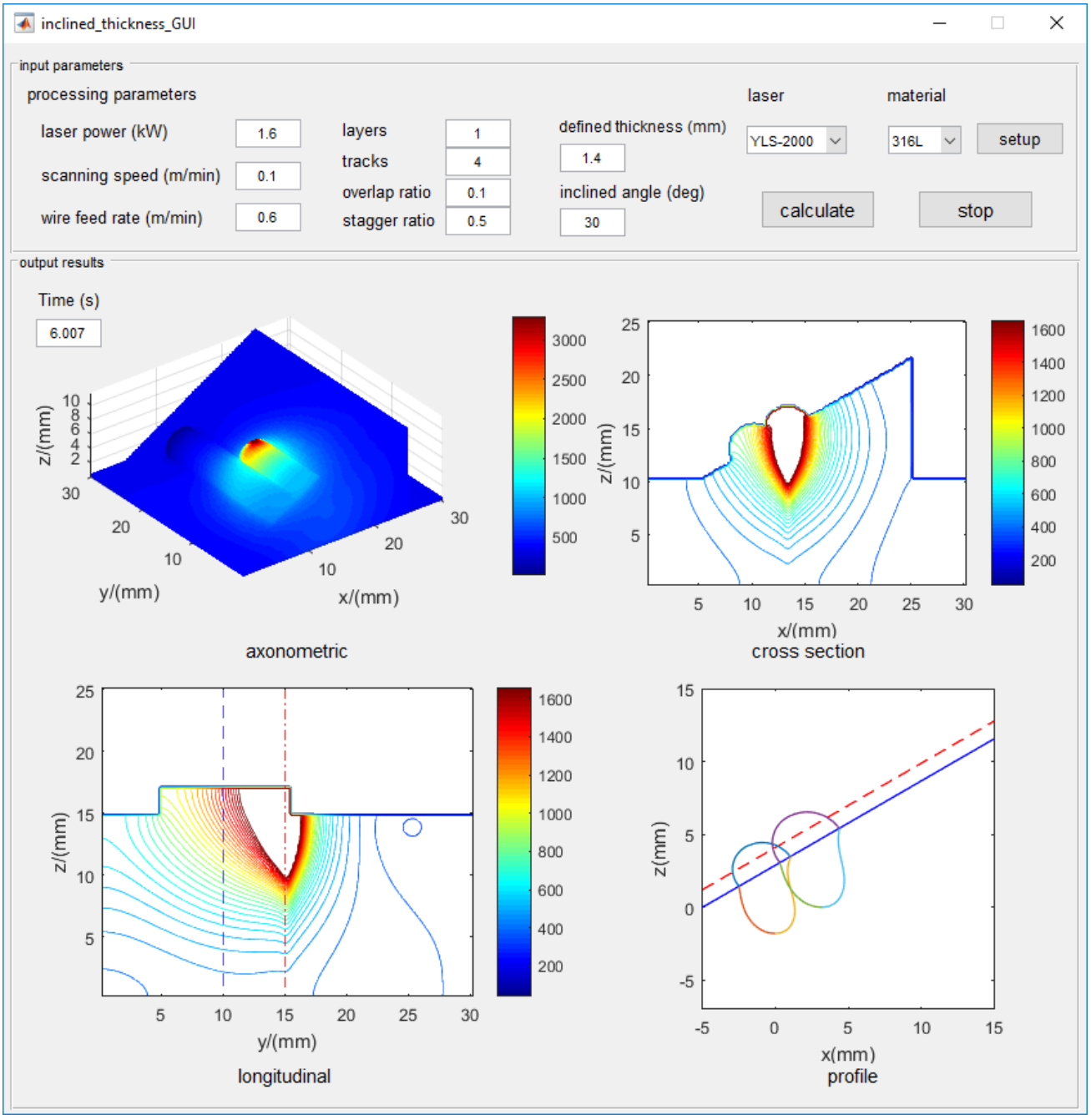

Figure 6.17 GUI control panel with built in model.

6.8 Summary

This chapter investigated the overlapped WLC on inclined surfaces by not only proposing and validating an analytical model but also providing a model application. The possible new findings can include:

- By considering the balance between gravity and surface tension, the analytical model is proposed to predict the deposition shapes on a surface with various inclined angles. The model is experimentally validated, where the two-dimensional profile errors are within an acceptable range.
- The gravity effect on shape deformations and overlap cladding situations (including climb-up and step-down behaviors) are obviously observed in the experimental trials, proving the importance of the proposed model.
- To show the model ability, the deposited bulge shapes on various inclined surfaces are accurately controlled by calculating the scanning speed according to the proposed model. The generated layer thickness error is within an acceptable range.

Based on above, the proposed model can predict temperature-dependent shape of the overlapped cladding-affected area on an inclined surface with an acceptable accuracy, and therefore can be considered promising in repairing of high-valued parts including molds and dies, aerostructures, and power units.

Chapter 7 Conclusions

The overall research works are completely presented by the previous chapters. This chapter aims to summarize the research, discuss the findings, contributions to knowledge, and suggest some possible future works.

7.1 Research work summaries

This thesis begins with the evaluation of the trend, possibility and development of the part repair industry and laser cladding in application. At the same time, it reveals some general limitations of the current technology, thus proposing academic research under the motivation of solving obstacles (Chapter 1). Literatures are reviewed to follow the current research states (including WLC physics, outputs, and modellings) and the research gaps are identified in these aspects (Chapter 2). In order to fill the research gaps, this research work is started on the basis of previewing the overall method including material selection, experimental procedures, and analytical modelling process (Chapter 3). The detailed modelling processes are unfolded regarding single track (Chapter 4), overlap (Chapter 5), and retention behaviours (Chapter 6) during WLC process.

7.2 Research findings and outcomes

The model, validated at the geometrical and the thermal aspects, distinguishes itself through the following key findings and outcomes:

- The model reveals the underlying physics on track profile and correlates the thermal and geometrical parameters in the cladding process, giving the

opportunity to analyse and understand the effect of varying processing parameters. As a result, the errors are 20% in average including bulges and melt pools. Moreover, predictions in high laser power, high scanning speed and low wire feed rate exhibit high accuracy (with maximum error as low as 14% at the bulge).

- The model successfully incorporates the remelting and bonding between newly-clad and as-clad tracks, especially the material deposition on the as-clad layers. It enables the geometrical solve of profile prediction based on the as-clad single track complete profiles and process accumulations. As a result, the profiles of the horizontal overlap cladding are calculated analytically with the proposed model under various overlap ratio and stagger ratio with the errors in range of 10%-20%.
- The model considers the effects of gravity and surface tension so that it can predict the shape of a bulge deposited on a surface with various angles/slope gradients, which has been validated on a flat (initially machined) surface. As a result, the two-dimensional profile errors can be within 17%. The model can also predict the interaction between tracks deposited on an inclined surface so that the resultant surface can be predicted after successive deposited layers, and the two-dimensional profile error can be within 13%.

The model is developed within the acceptable accuracy.

7.3 Contributions to knowledge

The development of the model provides the following contributions to the knowledge of laser cladding:

- Cease the argument of the basic shape. The basic shape of cladding has been a continuous argument due to the lack of physics justification and application condition. This is ceased by the consideration of surface tension within the capillary length in WLC.
- Lift the overlapping restriction. The overlapping has been a concerning situation due to the lack of proper material interaction prediction. This restriction is lifted by the model that is able to predict the interaction between tracks and layers.
- Allow the external force incorporation. The external force is an inevitable condition in laser cladding. The model enables the incorporation of the external force by the proposed spring system theory.

The proposed model extends the understanding of WLC.

7.4 Future works

This research thesis has presented an analytical modelling of WLC. The model works fine at the single track, overlap, and retention behaviours. However, the following works are not proceeded due to the limit of the project period but worth of bringing up for future works.

- Theoretical modelling of overlap on freeform surface. This project stops at the theoretical modelling of overlap on inclined surface and does not reach the overlap on freeform surface with the laser head following a three-dimensional path [229], probably with laser incidence angle changing [230] or adjusting [231]. Although the freeform surface can be discretized into separate inclined

surface, this theory is not really validated especially the distortion of substrate in reality [232, 233]. The bigger problem is that the stepping down cladding one steep angle cannot be done because overlap bulges are not steady and will collapse as it has been observed in the exploratory trials. If the tilted worktable is not an option and all of the freeform surface is only cladded in climbing up method, the path planning of arranging areas is the topic to discuss [234].

- Longitudinal cladding profile modelling. While the cross section cladding profile is the focus of this thesis, the longitudinal profile has never been discussed. Bulges collapse at the edge while they also do at the front and tail (referred to the repair case of gear in Chapter 5). Another problem in the longitudinal direction is that the height variation [235-241] from the previous tracks and the dynamic melt pool [242, 243] may lead to the discontinuous track of upper layer if the capillary bridge cannot compensate the height variation [244, 245]. The integration of capillary bridge into the model is necessary based on the current research regarding stabilization [246], dynamic contact angle hysteresis [247], geometrical modelling [248], and non-isothermal dynamic response [249].
- Dissimilar cladding material in the model. The materials used in the research is the same for wire and substrate. However, the dissimilar material cladded is not validated whether the model can still adapt to the prediction [250].
- Detachment model based on the melt pool profile. One significant meaning of predicting the model pool profile in the above model is that the melt pool profile can be further used to analyse the detachment when the track is

exerted external force, i.e. vertical force (like pulling up a tooth) or horizontal force (like pushing the building on a foundation) or bending force (like popping out a nut) [251]. The profile of melt pool will act in certain pattern under such force conditions. The detachment model, based on the melt pool profile, will be useful for the predictions of breaking behaviours such as tension, compression, bend, torsion, vibration, and especially fatigue.

(This page is left blank)

Appendices

Appendix A MATLAB code of Main, Parameters, and Initialization

```
%%%%%%%%%%%%%%%%%%%%%%%%%%%%%%%%%%%%%%% main %%%%%%%%%%%%%%%%%%%%%%%%%%%%%%%%%%%%%%%%%%%

%%%%%%%%%%%%%%%%%%%%%% parameters %%%%%%%%%%%%%%%%%%%%%%%%%%%%%%%

parameters;

%%%%%%%%%%%%%%%%%%%%%%%% initialization %%%%%%%%%%%%%%%%%%%%%%%%%%%

initialization;

for zi=1:zn %vertical

if zi>1

buildup;

iniverclad;

end

for xi=1:xn %horizontal

if xi>1

xt=x0+(xi-1)*l;

xpi(zi,xi)=xt;

layer;

inihoriclad;

end

for ti=0:dt:6

yt=v*ti+y0;

%%%%%%%%%%%%%%%%%%%%%%% clad %%%%%%%%%%%%%%%%%%%%%%%%%%%%%%%

clad;

%%%%%%%%%%%%%%%%%%%%%%% heating %%%%%%%%%%%%%%%%%%%%%%%%

heating;

%%%%%%%%%%%%%%%%%%% conduction %%%%%%%%%%%%%%%%%%%%%%%%%

heat_transfer;

%%%%%%%%%%%%%%%%%%%%%% temperature field %%%%%%%%%%%%%%%%%%%%%%%%%%

Temperature_field;

end

%%%%%%%%%%%%%%%%%%%%%% cooling %%%%%%%%%%%%%%%%%%%%%%%%%%%%%%%%%

for ti=6+dt:dt:10-dt %ti=6+dt:dt:10-dt
```

```
    heat_transfer;

end

if zi==zn && xi==xn-1 && zn>1
    break;
end

end

%%%%%%%%%%%%%%%%%%%% relocation %%%%%%%%%%%%%%%%%%%%%%

xi=1;

x0=x0+0.5*l; %stagger

xt=x0;

end

final;
```

```
%%%%%%%%%%%%%%%%%%%%%%%%%%%%%%%%%%%% Parameters %%%%%%%%%%%%%%%%%%%%%%%%%%%%%%%%%%%%%%%%%%%%

%calibration from Hans
cin=0.85;

%processing
P=1.6*1000*cin; %laser power (kW)
v=0.1/(60); %scanning speed (m/min)
F=0.6/(60); %wire feed rate (m/min)

%dimension
Hc=0.01; %height of clad (m)
Hs=0.01; %height of substrate (m)
H=Hs+Hc; %height (m) (substrate+clad)
Wl=0.005;%computation left width (m)
Wr=0.03;%computation right width (m)
W=Wl+Wr; %computation width (m) %0.04
L=0.03; %length (m)

%material
Tb=3300; %boiling point of material (K)
T0=300; %ambient temperature T0 (K)
em=0.59; %emissivity of material
Tm=1700; %melting temperature of material (K)
Lf=260*1000; %latent heat of fusion (kJ/kg) 260*1000 140
Cp0=450; %specific heat capacity (J/(kg*K)) 450 300
Cp=Lf/(Tm-T0)+Cp0; %modify Cp
ab=2.5*10^2; %absorption coefficient (m^(-1))
beta=0.03; %absorptivity 0.5 0.6
g=9.8; %gravity (m/s^2)
rho=8000; %density (kg/m^3)
k=20; %thermal conductivity (W/m*K)
alpha=k/(rho*Cp); %thermal diffusivity
V=7.09/(100000); %molar volume (mL/mol)
Tc=8500; %critical temperature (K)
kc=2.1*10^(-7); %contant for Eotvos rule (J/(K*mol^(2/3)))
R=0.6/(1000); %radius of wire (mm)
kb=1.38*10^(-23); %Boltzmann constant (J/K)
Ratom=0.126*10^(-9); %radius of atom (nm)
om=(4/3)*pi*Ratom^3; %atomic volume (m^3)


%laser
```

```
lambda=1.06*10^(-6); %wave length (m)
Msq=20.9; %mode factor squared
rw=0.4/1000; %radius of waist (mm)
zR=pi*rw^2/(lambda*Msq); %Rayleigh range (m)

%time
ti=0; %transient time (s)
x0=0; %starting x (m)
xt=x0; %transient x (m)
y0=0.005; %starting y (m)
yt=y0; %transient y (m)
z0=0; %starting z (m)
zt=z0; %transient z (m)
seg=5; %segments in one mm %5
dt=10/10000; %time increment (s) %10/10000
Fo=alpha*dt/(1/seg/1000)^2; %time factor
tclad=0; %time to creat clad (s)
j=0; %sequence to save image
zn=2;%number of layer
xn=8;%number of bulge
eta=0.1;%horizontal overlap ratio
```

```
%%%%%%%%%%%%%%%%%%%%%%%%%%%%%%%%%%%% initialization %%%%%%%%%%%%%%%%%%%%%%%%%%%%%%%%%%%%%%%%

%record geometry
the=0*ones(zn,xn);
h=0*ones(zn,xn);
the0=0*ones(zn,xn); %initial contact angle
h0=0*ones(zn,xn); %initial height
hpi=0*ones(zn,xn); %height of platform
xpi=0*ones(zn,xn); %position of bulge
s=0*ones(zn,xn); %melt pool depth
ga2=0*ones(zn,xn); %melt pool tension
theq=the;
hq=h;
hpiq=hpi;
% xpiq=xpi;
sq=s;
ga2q=ga2;

%bulge geometry
ga=kc*(Tc-(Tm+450))/(V^(2/3)); %initialize surface tension
A=pi*R^2*F/v; %cross section area
the(1,1)=acos(2.299-3.606*ga); %theta
h(1,1)=sqrt(A*(1-cos(the(1,1)))^2/(the(1,1)-0.5*sin(2*the(1,1)))); %height
rp=h(1,1)/(1-cos(the(1,1))); %radius
b=rp*cos(the(1,1)-pi/2); %half width
hpi(1,1)=0;
xpi(1,1)=xt;
w=2*rp;%bulge width
l=w*(1-eta);%distance of two bulges

%melt pool
% ga2=0.54*kb*Tm/(om^(2/3)); %liquid-solid interfacial tension
s(1,1)=0; %record melt pool bottom
cm=4; %coefficient to modify melt pool boundary
er=0.00001; %error to modify melt pool boundary width

%domain
T=0*ones(round(L*1000*seg)+1,round(W*1000*seg)+1,round(H*1000*seg)+1);
S=T;
[X,Y,Z]=meshgrid(-Wl:1/seg/1000:Wr,0:1/seg/1000:L,-Hs:1/seg/1000:Hc);
```

```
Th=squeeze(T(1,:,:)); %to plot heat map
Sh=Th; %mark temperature below melting point

%laser
rl=rw*sqrt(1+((Z-zt)/zR).^2); %radius of laser beam (m)
ks=0.022^2/7*8./(0.022^2/7+(Z-zt).^2); %power of super Gaussian
% laserbeam; %show laser beam

%substrate
T(1:end,1:end,1:Hs*1000*seg)=T0;
S(1:end,1:end,1:Hs*1000*seg)=1;

%clad
x=-Wl;
z=0;

for u=Hs*1000*seg+1:1:H*1000*seg+1
    for f=1:1:W*1000*seg+1
        if x^2<=(h(1,1)/(1-cos(the(1,1))))^2-(z+h(1,1)*cos(the(1,1))/(1-
cos(the(1,1))))^2


            T(y0*1000*seg+7,f,u)=T0;
            S(y0*1000*seg+7,f,u)=1;
            T(y0*1000*seg+6,f,u)=T0;
            S(y0*1000*seg+6,f,u)=1;
            T(y0*1000*seg+5,f,u)=T0;
            S(y0*1000*seg+5,f,u)=1;
            T(y0*1000*seg+4,f,u)=T0;
            S(y0*1000*seg+4,f,u)=1;
            T(y0*1000*seg+3,f,u)=T0;
            S(y0*1000*seg+3,f,u)=1;
            T(y0*1000*seg+2,f,u)=T0;
            S(y0*1000*seg+2,f,u)=1;
            T(y0*1000*seg+1,f,u)=T0;
            S(y0*1000*seg+1,f,u)=1;
            T(y0*1000*seg,f,u)=T0;
            S(y0*1000*seg,f,u)=1;
            T(y0*1000*seg-1,f,u)=T0;
            S(y0*1000*seg-1,f,u)=1;

        end
            x=x+1/seg/1000;
    end
    x=-Wl;
    z=z+1/seg/1000;
end
```

Appendix B MATLAB code of Add step, track, and layer

```
%%%%%%%%%%%%%%%%%%%%%%%%%%%%%%%%%%%%% add step %%%%%%%%%%%%%%%%%%%%%%%%%%%%%%%%%%%%%%%%%

if floor(yt*1000*seg)+1-v*tclad*1000*seg>0 || ti==0

    tclad=ti;
    S(floor(yt*1000*seg)+8,:,Hs*1000*seg+1:end)=S(y0*1000*seg,:,Hs*1000*seg+1:end);

T(floor(yt*1000*seg)+8,:,Hs*1000*seg+1:end)=T(floor(yt*1000*seg)+8,:,Hs*1000*seg+1:end)-
T0;
    T(T<0)=0;

T(floor(yt*1000*seg)+8,:,Hs*1000*seg+1:end)=T(floor(yt*1000*seg)+8,:,Hs*1000*seg+1:end)+
T0*S(floor(yt*1000*seg)+8,:,Hs*1000*seg+1:end);

end
```

```
%%%%%%%%%%%%%%%%%%%%%%%%%%%%%%%%%% add track %%%%%%%%%%%%%%%%%%%%%%%%%%%%%%%%%%%%%%%%%%%%

%%%%%%%%%%%%%%%%%%%%%% calculate track in one layer %%%%%%%%%%%%%%%%%%%%%%%%%%%%%%%%

%cal platform height based on melt pool bottom and laser height

if zi>1
    if x0~=0 %stagger
    if xt>xpi(zi-1,xi) && xt<xpi(zi-1,xi+1)-h0(zi-1,xi+1)/(1-cos(the0(zi-1,xi+1))) %left
        zt=sqrt((h0(zi-1,xi)/(1-cos(the0(zi-1,xi))))^2-(xt-xpi(zi-1,xi))^2)+hpi(zi-
1,xi)-h0(zi-1,xi)*cos(the0(zi-1,xi))/(1-cos(the0(zi-1,xi)))+hpi(zi-1,xi);
    elseif xt<xpi(zi-1,xi+1) && xt>xpi(zi-1,xi)+h0(zi-1,xi)/(1-cos(the0(zi-1,xi)))
%right
        zt=sqrt((h0(zi-1,xi+1)/(1-cos(the0(zi-1,xi+1))))^2-(xt-xpi(zi-
1,xi+1))^2)+hpi(zi-1,xi+1)-h0(zi-1,xi+1)*cos(the0(zi-1,xi+1))/(1-cos(the0(zi-
1,xi+1)))+hpi(zi-1,xi+1);
    elseif sqrt((h0(zi-1,xi)/(1-cos(the0(zi-1,xi))))^2-(xt-xpi(zi-1,xi))^2)+hpi(zi-
1,xi)-h0(zi-1,xi)*cos(the0(zi-1,xi))/(1-cos(the0(zi-1,xi))) ...
            >= sqrt((h0(zi-1,xi+1)/(1-cos(the0(zi-1,xi+1))))^2-(xt-xpi(zi-
1,xi+1))^2)+hpi(zi-1,xi+1)-h0(zi-1,xi+1)*cos(the0(zi-1,xi+1))/(1-cos(the0(zi-1,xi+1)))
%middle-left
        zt=sqrt((h0(zi-1,xi)/(1-cos(the0(zi-1,xi))))^2-(xt-xpi(zi-1,xi))^2)+hpi(zi-
1,xi)-h0(zi-1,xi)*cos(the0(zi-1,xi))/(1-cos(the0(zi-1,xi)))+hpi(zi-1,xi);
    else %middle-right
        zt=sqrt((h0(zi-1,xi+1)/(1-cos(the0(zi-1,xi+1))))^2-(xt-xpi(zi-
1,xi+1))^2)+hpi(zi-1,xi+1)-h0(zi-1,xi+1)*cos(the0(zi-1,xi+1))/(1-cos(the0(zi-
1,xi+1)))+hpi(zi-1,xi+1);
    end
    else %array
        zt=sqrt((h0(zi-1,xi)/(1-cos(the0(zi-1,xi))))^2-(xt-xpi(zi-1,xi))^2)+hpi(zi-
1,xi)-h0(zi-1,xi)*cos(the0(zi-1,xi))/(1-cos(the0(zi-1,xi)))+hpi(zi-1,xi);
    end
    hpi(zi,xi)=zt;
end

ga=kc*(Tc-Tcon)/(V^(2/3)); %initialize surface tension

the(zi,xi)=acos(2.299-3.606*ga); %theta

A=pi*R^2*F/v; %cross section area

h(zi,xi)=sqrt(A*(1-cos(the(zi,xi)))^2/(the(zi,xi)-0.5*sin(2*the(zi,xi)))); %height

Aiter=0; %cross section area iteration
hiter=h(zi,xi); %height iteration
x=-Wl;
z=0;
while Aiter<A
    Aiter=0;
    for u=Hs*1000*seg*10+1:1:H*1000*seg*10+1
        for f=1:1:W*1000*seg*10+1
            if zi==1 %base layer
                if (x-xpi(zi,xi))^2<=(hiter/(1-cos(the(zi,xi))))^2-(z-
hpi(zi,xi)+hiter*cos(the(zi,xi))/(1-cos(the(zi,xi))))^2 ... %self
                        && (x-xpi(zi,xi-1))^2>(h0(zi,xi-1)/(1-cos(the0(zi,xi-1))))^2-(z-
hpi(zi,xi-1)+h0(zi,xi-1)*cos(the0(zi,xi-1))/(1-cos(the0(zi,xi-1))))^2 %left
                    Aiter=Aiter+(1/(seg*10)/1000)^2;
                end
            else %top layer
                if (x-xpi(zi,xi))^2<=(hiter/(1-cos(the(zi,xi))))^2-(z-
hpi(zi,xi)+hiter*cos(the(zi,xi))/(1-cos(the(zi,xi))))^2 ... %self
                        && (x-xpi(zi,xi-1))^2>(h0(zi,xi-1)/(1-cos(the0(zi,xi-1))))^2-(z-
hpi(zi,xi-1)+h0(zi,xi-1)*cos(the0(zi,xi-1))/(1-cos(the0(zi,xi-1))))^2 ... %left
```

```
                        && (x-xpi(zi-1,xi))^2>(h0(zi-1,xi)/(1-cos(the0(zi-1,xi))))^2-(z-
hpi(zi-1,xi)+h0(zi-1,xi)*cos(the0(zi-1,xi))/(1-cos(the0(zi-1,xi))))^2 ... %down
                        && (x-xpi(zi-1,xi+1))^2>(h0(zi-1,xi+1)/(1-cos(the0(zi-
1,xi+1))))^2-(z-hpi(zi-1,xi+1)+h0(zi-1,xi+1)*cos(the0(zi-1,xi+1))/(1-cos(the0(zi-
1,xi+1))))^2 %down-right
                    Aiter=Aiter+(1/(seg*10)/1000)^2;
                end
            end
            x=x+1/(seg*10)/1000;
        end
        x=-Wl;
        z=z+1/(seg*10)/1000;
    end
    hiter=hiter+1/(seg*10)/1000;
    z=0;
end

h(zi,xi)=hiter;


%%%%%%%%%%%%%%%%%% initialize horizontal clad %%%%%%%%%%%%%%%%%%%%%%%%%

%clad
x=-Wl;
z=0;

if zi==1

for u=Hs*1000*seg+1:1:H*1000*seg+1
    for f=1:1:W*1000*seg+1
        if (x-xt)^2<=(h(zi,xi)/(1-cos(the(zi,xi))))^2-(z+h(zi,xi)*cos(the(zi,xi))/(1-
cos(the(zi,xi))))^2 ...
                && (x-xpi(zi,xi-1))^2>(h0(zi,xi-1)/(1-cos(the0(zi,xi-1))))^2-
(z+h0(zi,xi-1)*cos(the0(zi,xi-1))/(1-cos(the0(zi,xi-1))))^2

            T(y0*1000*seg+7,f,u)=T0;
            S(y0*1000*seg+7,f,u)=1;
            T(y0*1000*seg+6,f,u)=T0;
            S(y0*1000*seg+6,f,u)=1;
            T(y0*1000*seg+5,f,u)=T0;
            S(y0*1000*seg+5,f,u)=1;
            T(y0*1000*seg+4,f,u)=T0;
            S(y0*1000*seg+4,f,u)=1;
            T(y0*1000*seg+3,f,u)=T0;
            S(y0*1000*seg+3,f,u)=1;
            T(y0*1000*seg+2,f,u)=T0;
            S(y0*1000*seg+2,f,u)=1;
            T(y0*1000*seg+1,f,u)=T0;
            S(y0*1000*seg+1,f,u)=1;
            T(y0*1000*seg,f,u)=T0;
            S(y0*1000*seg,f,u)=1;
            T(y0*1000*seg-1,f,u)=T0;
            S(y0*1000*seg-1,f,u)=1;


        end
            x=x+1/seg/1000;
    end
    x=-Wl;
    z=z+1/seg/1000;
end

else

for u=Hs*1000*seg+1:1:H*1000*seg+1
    for f=1:1:W*1000*seg+1
        if (x-xt)^2<=(h(zi,xi)/(1-cos(the(zi,xi))))^2-(z-
hpi(zi,xi)+h(zi,xi)*cos(the(zi,xi))/(1-cos(the(zi,xi))))^2 ... % self
```

```
                && (x-xpi(zi,xi-1))^2>(h0(zi,xi-1)/(1-cos(the0(zi,xi-1))))^2-(z-
hpi(zi,xi-1)+h0(zi,xi-1)*cos(the0(zi,xi-1))/(1-cos(the0(zi,xi-1))))^2 ... % left
                && (x-xpi(zi-1,xi))^2>(h0(zi-1,xi)/(1-cos(the0(zi-1,xi))))^2-(z-hpi(zi-
1,xi)+h0(zi-1,xi)*cos(the0(zi-1,xi))/(1-cos(the0(zi-1,xi))))^2 % down

            T(y0*1000*seg+7,f,u)=T0;
            S(y0*1000*seg+7,f,u)=1;
            T(y0*1000*seg+6,f,u)=T0;
            S(y0*1000*seg+6,f,u)=1;
            T(y0*1000*seg+5,f,u)=T0;
            S(y0*1000*seg+5,f,u)=1;
            T(y0*1000*seg+4,f,u)=T0;
            S(y0*1000*seg+4,f,u)=1;
            T(y0*1000*seg+3,f,u)=T0;
            S(y0*1000*seg+3,f,u)=1;
            T(y0*1000*seg+2,f,u)=T0;
            S(y0*1000*seg+2,f,u)=1;
            T(y0*1000*seg+1,f,u)=T0;
            S(y0*1000*seg+1,f,u)=1;
            T(y0*1000*seg,f,u)=T0;
            S(y0*1000*seg,f,u)=1;
            T(y0*1000*seg-1,f,u)=T0;
            S(y0*1000*seg-1,f,u)=1;


        end
            x=x+1/seg/1000;
    end
    x=-Wl;
    z=z+1/seg/1000;
end

end
```

```
%%%%%%%%%%%%%%%%%%%%%%%%%%%%%%%%%%%% add layer %%%%%%%%%%%%%%%%%%%%%%%%%%%%%%%%%%%%%%%%%%%%

%%%%%%%%%%%%%%%%%%%% calculate buildup structure %%%%%%%%%%%%%%%%%%%%%%%%%

xpi(zi,xi)=xt;

%cal platform height based on melt pool bottom and laser height

if xt>=xpi(zi-1,xi) && xt<xpi(zi-1,xi+1)-h(zi-1,xi+1)/(1-cos(the(zi-1,xi+1))) %left
%     hpi(zi,xi)=sqrt((h(zi-1,xi)/(1-cos(the(zi-1,xi))))^2-(xt-xpi(zi-1,xi))^2)+hpi(zi-
1,xi)-h(zi-1,xi)*cos(the(zi-1,xi))/(1-cos(the(zi-1,xi)))+(hpi(zi-1,xi)+s(zi-1,xi))/2;
    zt=sqrt((h(zi-1,xi)/(1-cos(the(zi-1,xi))))^2-(xt-xpi(zi-1,xi))^2)+hpi(zi-1,xi)-h(zi-
1,xi)*cos(the(zi-1,xi))/(1-cos(the(zi-1,xi)))+hpi(zi-1,xi);
elseif xt<xpi(zi-1,xi+1) && xt>xpi(zi-1,xi)+h(zi-1,xi)/(1-cos(the(zi-1,xi))) %right
%     hpi(zi,xi)=sqrt((h(zi-1,xi+1)/(1-cos(the(zi-1,xi+1))))^2-(xt-xpi(zi-
1,xi+1))^2)+hpi(zi-1,xi+1)-h(zi-1,xi+1)*cos(the(zi-1,xi+1))/(1-cos(the(zi-
1,xi+1)))+(hpi(zi-1,xi)+s(zi-1,xi+1))/2;
    zt=sqrt((h(zi-1,xi+1)/(1-cos(the(zi-1,xi+1))))^2-(xt-xpi(zi-1,xi+1))^2)+hpi(zi-
1,xi+1)-h(zi-1,xi+1)*cos(the(zi-1,xi+1))/(1-cos(the(zi-1,xi+1)))+hpi(zi-1,xi+1);
elseif sqrt((h(zi-1,xi)/(1-cos(the(zi-1,xi))))^2-(xt-xpi(zi-1,xi))^2)+hpi(zi-1,xi)-h(zi-
1,xi)*cos(the(zi-1,xi))/(1-cos(the(zi-1,xi))) …
        >= sqrt((h(zi-1,xi+1)/(1-cos(the(zi-1,xi+1))))^2-(xt-xpi(zi-1,xi+1))^2)+hpi(zi-
1,xi+1)-h(zi-1,xi+1)*cos(the(zi-1,xi+1))/(1-cos(the(zi-1,xi+1))) %middle-left
%     hpi(zi,xi)=sqrt((h(zi-1,xi)/(1-cos(the(zi-1,xi))))^2-(xt-xpi(zi-1,xi))^2)+hpi(zi-
1,xi)-h(zi-1,xi)*cos(the(zi-1,xi))/(1-cos(the(zi-1,xi)))+(hpi(zi-1,xi)+s(zi-1,xi))/2;
    zt=sqrt((h(zi-1,xi)/(1-cos(the(zi-1,xi))))^2-(xt-xpi(zi-1,xi))^2)+hpi(zi-1,xi)-h(zi-
1,xi)*cos(the(zi-1,xi))/(1-cos(the(zi-1,xi)))+hpi(zi-1,xi);
else %middle-right
%     hpi(zi,xi)=sqrt((h(zi-1,xi+1)/(1-cos(the(zi-1,xi+1))))^2-(xt-xpi(zi-
1,xi+1))^2)+hpi(zi-1,xi+1)-h(zi-1,xi+1)*cos(the(zi-1,xi+1))/(1-cos(the(zi-
1,xi+1)))+(hpi(zi-1,xi)+s(zi-1,xi+1))/2;
```

```
    zt=sqrt((h(zi-1,xi+1)/(1-cos(the(zi-1,xi+1))))^2-(xt-xpi(zi-1,xi+1))^2)+hpi(zi-
1,xi+1)-h(zi-1,xi+1)*cos(the(zi-1,xi+1))/(1-cos(the(zi-1,xi+1)))+hpi(zi-1,xi+1);
end

hpi(zi,xi)=zt;

ga=kc*(Tc-Tcon)/(V^(2/3)); %initialize surface tension

the(zi,xi)=acos(2.299-3.606*ga); %theta %2.299-3.606*ga 5.305-7.212*ga

A=pi*R^2*F/v; %cross section area

h(zi,xi)=sqrt(A*(1-cos(the(zi,xi)))^2/(the(zi,xi)-0.5*sin(2*the(zi,xi)))); %height

Aiter=0; %cross section area iteration
hiter=h(zi,xi); %height iteration
x=-Wl;
z=0;
while Aiter<A
    Aiter=0;
    for u=Hs*1000*seg*10+1:1:H*1000*seg*10+1
        for f=1:1:W*1000*seg*10+1
            if (x-xpi(zi,xi))^2<=(hiter/(1-cos(the(zi,xi))))^2-(z-
hpi(zi,xi)+hiter*cos(the(zi,xi))/(1-cos(the(zi,xi))))^2 … %self
                    && (x-xpi(zi-1,xi))^2>(h0(zi-1,xi)/(1-cos(the0(zi-1,xi))))^2-(z-
hpi(zi-1,xi)+h0(zi-1,xi)*cos(the0(zi-1,xi))/(1-cos(the0(zi-1,xi))))^2 … %down
                    && (x-xpi(zi-1,xi+1))^2>(h0(zi-1,xi+1)/(1-cos(the0(zi-1,xi+1))))^2-
(z-hpi(zi-1,xi+1)+h0(zi-1,xi+1)*cos(the0(zi-1,xi+1))/(1-cos(the0(zi-1,xi+1))))^2 %down-
right
                    Aiter=Aiter+(1/(seg*10)/1000)^2;
            end
            x=x+1/(seg*10)/1000;
        end
        x=-Wl;
        z=z+1/(seg*10)/1000;
    end
    hiter=hiter+1/(seg*10)/1000;
    z=0;
end

h(zi,xi)=hiter;

%%%%%%%%%%%%%%%%%% initialize clad %%%%%%%%%%%%%%%%%%%%%%%%%

%clad
x=-Wl;
z=0;

for u=Hs*1000*seg+1:1:H*1000*seg+1
    for f=1:1:W*1000*seg+1
        if (x-xt)^2<=(h(zi,xi)/(1-cos(the(zi,xi))))^2-(z-
hpi(zi,xi)+h(zi,xi)*cos(the(zi,xi))/(1-cos(the(zi,xi))))^2 ... %self
                && (x-xpi(zi-1,xi))^2>(h0(zi-1,xi)/(1-cos(the0(zi-1,xi))))^2-(z-hpi(zi-
1,xi)+h0(zi-1,xi)*cos(the0(zi-1,xi))/(1-cos(the0(zi-1,xi))))^2 %down

            T(y0*1000*seg+7,f,u)=T0;
            S(y0*1000*seg+7,f,u)=1;
            T(y0*1000*seg+6,f,u)=T0;
            S(y0*1000*seg+6,f,u)=1;
            T(y0*1000*seg+5,f,u)=T0;
            S(y0*1000*seg+5,f,u)=1;
            T(y0*1000*seg+4,f,u)=T0;
            S(y0*1000*seg+4,f,u)=1;
            T(y0*1000*seg+3,f,u)=T0;
            S(y0*1000*seg+3,f,u)=1;
            T(y0*1000*seg+2,f,u)=T0;
            S(y0*1000*seg+2,f,u)=1;
            T(y0*1000*seg+1,f,u)=T0;
```

```
            S(y0*1000*seg+1,f,u)=1;
            T(y0*1000*seg,f,u)=T0;
            S(y0*1000*seg,f,u)=1;
            T(y0*1000*seg-1,f,u)=T0;
            S(y0*1000*seg-1,f,u)=1;
%
        end
            x=x+1/seg/1000;
    end
    x=-Wl;
    z=z+1/seg/1000;
end
```

Appendix C MATLAB code of Heating and Heat transfer

```
%%%%%%%%%%%%%%%%%%%%%%%%%%%%%%%%%%% laser heating %%%%%%%%%%%%%%%%%%%%%%%%%%%%%%%%%%%%%%

ab1=ab; %save absorption coefficient

Tx=T(floor(yt*seg*1000)+1,:,:);
Tx=squeeze(Tx);
Tmx=Tx';
[row,col]=find(Tmx>=Tm);

s0=s; %record original melt pool bottom

if length(row)>=1
    s=-Hs+min(row)/seg/1000;
    if s<0 && abs(s)>b
        ab=ab1-0.7*10^2; %penetration mode
    else
        ab=ab1; %conduction mode
    end
end

Ixy=2.^(1./ks).*ks*P./(pi*rl.^2.*gamma(1./ks)).*exp(-2*(((X-xt).^2+(Y-
yt).^2)./rl.^2).^ks); %laser intensity (J/(m^2*s))
Ha=h-Z; %attenuation layer;
Ha(:,:,ceil((h+Hs)*1000*seg):end)=0; %confine attenuation
I=exp(-ab*Ha).*Ixy; %attenuation (J/(m^2*s))
Ql=(1/seg/1000)^2*dt*I; %laser enregy (J)
T=T+beta*S.*Ql/(rho*(1/seg/1000)^3*Cp);

ab=ab1; %based on conduction mode
```

```
%%%%%%%%%%%%%%%%%%%%%%%%%%%%%%%%%%% heat transfer %%%%%%%%%%%%%%%%%%%%%%%%%%%%%%%%%%%%%%

%convection & radiation
hc=24.1*10^(-4)*em*T.^(1.61); %combined coefficient
hc(:,:,Hs*seg*1000:end)=hc(:,:,Hs*seg*1000:end)+1000; %forced convection surface
Bi=hc*(1/seg/1000)/k; %Biot number

%interior
Tnew=Fo*S.*(circshift(T,[0 0 -1])+circshift(T,[0 -1 0])+circshift(T,[0 0
1])+circshift(T,[0 1 0])+circshift(T,[1 0 0])+circshift(T,[-1 0 0])-6*T)+T;

%face
Tex=T(1:2,:,1:Hs*seg*1000); %front
Biex=Bi(1:2,:,1:Hs*seg*1000);
Tex=Fo*(2*circshift(Tex,[-1,0,0])+circshift(Tex,[0,1,0])+circshift(Tex,[0,-
1,0])+circshift(Tex,[0,0,-1])+circshift(Tex,[0,0,1])-6*Tex+2*Biex.*(T0-Tex))+Tex;
Tnew(1,2:W*seg*1000,2:Hs*seg*1000-1)=Tex(1,2:W*seg*1000,2:Hs*seg*1000-1);
```

```
Tex=T(L*1000*seg:end,:,1:Hs*seg*1000); %back
Biex=Bi(L*1000*seg:end,:,1:Hs*seg*1000);
Tex=Fo*(2*circshift(Tex,[1,0,0])+circshift(Tex,[0,1,0])+circshift(Tex,[0,-
1,0])+circshift(Tex,[0,0,-1])+circshift(Tex,[0,0,1])-6*Tex+2*Biex.*(T0-Tex))+Tex;
Tnew(end,2:W*seg*1000,2:Hs*seg*1000-1)=Tex(2,2:W*seg*1000,2:Hs*seg*1000-1);

Tex=T(:,:,1:2); %bottom
Biex=Bi(:,:,1:2);
Tex=Fo*(2*circshift(Tex,[0,0,-1])+circshift(Tex,[0,1,0])+circshift(Tex,[0,-
1,0])+circshift(Tex,[-1,0,0])+circshift(Tex,[1,0,0])-6*Tex+2*Biex.*(T0-Tex))+Tex;
Tnew(2:L*1000*seg,2:W*seg*1000,1)=Tex(2:L*1000*seg,2:W*seg*1000,1);

Tex=T(:,1:2,1:Hs*seg*1000); %left
Biex=Bi(:,1:2,1:Hs*seg*1000);
Tex=Fo*(2*circshift(Tex,[0,-1,0])+circshift(Tex,[0,0,1])+circshift(Tex,[0,0,-
1])+circshift(Tex,[-1,0,0])+circshift(Tex,[1,0,0])-6*Tex+2*Biex.*(T0-Tex))+Tex;
Tnew(2:L*1000*seg,1,2:Hs*seg*1000-1)=Tex(2:L*1000*seg,1,2:Hs*seg*1000-1);

Tex=T(:,W*seg*1000:end,1:Hs*seg*1000); %right
Biex=Bi(:,W*seg*1000:end,1:Hs*seg*1000);
Tex=Fo*(2*circshift(Tex,[0,1,0])+circshift(Tex,[0,0,1])+circshift(Tex,[0,0,-
1])+circshift(Tex,[-1,0,0])+circshift(Tex,[1,0,0])-6*Tex+2*Biex.*(T0-Tex))+Tex;
Tnew(2:L*1000*seg,end,2:Hs*seg*1000-1)=Tex(2:L*1000*seg,2,2:Hs*seg*1000-1);

%edge
Tex=T(:,1:2,1:2); %left-bottom
Biex=Bi(:,1:2,1:2);
Tex=2*Fo*(circshift(Tex,[0,-1,0])+circshift(Tex,[1,0,0])+circshift(Tex,[-
1,0,0])+circshift(Tex,[0,0,-1])-4*Tex+2*Biex.*(T0-Tex))+Tex;
Tnew(2:L*1000*seg,1,1)=Tex(2:L*1000*seg,1,1);

Tex=T(:,W*seg*1000:end,1:2); %right-bottom
Biex=Bi(:,W*seg*1000:end,1:2);
Tex=2*Fo*(circshift(Tex,[0,1,0])+circshift(Tex,[1,0,0])+circshift(Tex,[-
1,0,0])+circshift(Tex,[0,0,-1])-4*Tex+2*Biex.*(T0-Tex))+Tex;
Tnew(2:L*1000*seg,end,1)=Tex(2:L*1000*seg,2,1);

Tex=T(:,1:2,Hs*seg*1000-1:Hs*seg*1000); %left-up
Biex=Bi(:,1:2,Hs*seg*1000-1:Hs*seg*1000);
Tex=2*Fo*(circshift(Tex,[0,-1,0])+circshift(Tex,[1,0,0])+circshift(Tex,[-
1,0,0])+circshift(Tex,[0,0,1])-4*Tex+2*Biex.*(T0-Tex))+Tex;
Tnew(2:L*1000*seg,1,Hs*seg*1000)=Tex(2:L*1000*seg,1,2);

Tex=T(:,W*seg*1000:end,Hs*seg*1000-1:Hs*seg*1000); %right-up
Biex=Bi(:,W*seg*1000:end,Hs*seg*1000-1:Hs*seg*1000);
Tex=2*Fo*(circshift(Tex,[0,1,0])+circshift(Tex,[1,0,0])+circshift(Tex,[-
1,0,0])+circshift(Tex,[0,0,1])-4*Tex+2*Biex.*(T0-Tex))+Tex;
Tnew(2:L*1000*seg,end,Hs*seg*1000)=Tex(2:L*1000*seg,end,2);

Tex=T(1:2,:,1:2); %front-bottom
Biex=Bi(1:2,:,1:2);
Tex=2*Fo*(circshift(Tex,[0,1,0])+circshift(Tex,[0,-1,0])+circshift(Tex,[-
1,0,0])+circshift(Tex,[0,0,-1])-4*Tex+2*Biex.*(T0-Tex))+Tex;
Tnew(1,2:W*seg*1000,1)=Tex(1,2:W*seg*1000,1);

Tex=T(1:2,:,Hs*seg*1000-1:Hs*seg*1000); %front-up
Biex=Bi(1:2,:,Hs*seg*1000-1:Hs*seg*1000);
Tex=2*Fo*(circshift(Tex,[0,1,0])+circshift(Tex,[0,-1,0])+circshift(Tex,[-
1,0,0])+circshift(Tex,[0,0,1])-4*Tex+2*Biex.*(T0-Tex))+Tex;
Tnew(1,2:W*seg*1000,Hs*seg*1000)=Tex(1,2:W*seg*1000,2);

Tex=T(L*1000*seg:end,:,1:2); %back-bottom
Biex=Bi(L*1000*seg:end,:,1:2);
Tex=2*Fo*(circshift(Tex,[0,1,0])+circshift(Tex,[0,-
1,0])+circshift(Tex,[1,0,0])+circshift(Tex,[0,0,-1])-4*Tex+2*Biex.*(T0-Tex))+Tex;
Tnew(end,2:W*seg*1000,1)=Tex(end,2:W*seg*1000,1);
```

```
Tex=T(L*1000*seg:end,:,Hs*seg*1000-1:Hs*seg*1000); %back-up
Biex=Bi(L*1000*seg:end,:,Hs*seg*1000-1:Hs*seg*1000);
Tex=2*Fo*(circshift(Tex,[0,1,0])+circshift(Tex,[0,-
1,0])+circshift(Tex,[1,0,0])+circshift(Tex,[0,0,1])-4*Tex+2*Biex.*(T0-Tex))+Tex;
Tnew(end,2:W*seg*1000,Hs*seg*1000)=Tex(end,2:W*seg*1000,2);

Tex=T(1:2,1:2,1:Hs*seg*1000); %front-left
Biex=Bi(1:2,1:2,1:Hs*seg*1000);
Tex=2*Fo*(circshift(Tex,[-1,0,0])+circshift(Tex,[0,-
1,0])+circshift(Tex,[0,0,1])+circshift(Tex,[0,0,-1])-4*Tex+2*Biex.*(T0-Tex))+Tex;
Tnew(1,1,2:Hs*seg*1000-1)=Tex(1,1,2:Hs*seg*1000-1);

Tex=T(1:2,W*seg*1000:end,1:Hs*seg*1000); %front-right
Biex=Bi(1:2,W*seg*1000:end,1:Hs*seg*1000);
Tex=2*Fo*(circshift(Tex,[-
1,0,0])+circshift(Tex,[0,1,0])+circshift(Tex,[0,0,1])+circshift(Tex,[0,0,-1])-
4*Tex+2*Biex.*(T0-Tex))+Tex;
Tnew(1,end,2:Hs*seg*1000-1)=Tex(1,end,2:Hs*seg*1000-1);

Tex=T(L*1000*seg:end,1:2,1:Hs*seg*1000); %back-left
Biex=Bi(L*1000*seg:end,1:2,1:Hs*seg*1000);
Tex=2*Fo*(circshift(Tex,[1,0,0])+circshift(Tex,[0,-
1,0])+circshift(Tex,[0,0,1])+circshift(Tex,[0,0,-1])-4*Tex+2*Biex.*(T0-Tex))+Tex;
Tnew(end,1,2:Hs*seg*1000-1)=Tex(end,1,2:Hs*seg*1000-1);

Tex=T(L*1000*seg:end,W*seg*1000:end,1:Hs*seg*1000); %back-right
Biex=Bi(L*1000*seg:end,W*seg*1000:end,1:Hs*seg*1000);
Tex=2*Fo*(circshift(Tex,[1,0,0])+circshift(Tex,[0,1,0])+circshift(Tex,[0,0,1])+circshift
(Tex,[0,0,-1])-4*Tex+2*Biex.*(T0-Tex))+Tex;
Tnew(end,end,2:Hs*seg*1000-1)=Tex(end,end,2:Hs*seg*1000-1);

%corner
%front-left-bottom
Tnew(1,1,1)=2*Fo*(T(1,2,1)+T(1,1,2)+T(2,1,1)-3*T(1,1,1)+2*Bi(1,1,1)*(T0-
T(1,1,1)))+T(1,1,1);

%front-right-bottom
Tnew(1,end,1)=2*Fo*(T(1,W*seg*1000,1)+T(1,end,2)+T(2,end,1)-
3*T(1,end,1)+2*Bi(1,end,1)*(T0-T(1,end,1)))+T(1,end,1);

%front-left-up
Tnew(1,1,Hs*seg*1000)=2*Fo*(T(1,2,Hs*seg*1000)+T(1,1,Hs*seg*1000-1)+T(2,1,Hs*seg*1000)-
3*T(1,1,Hs*seg*1000)+2*Bi(1,1,Hs*seg*1000)*(T0-T(1,1,Hs*seg*1000)))+T(1,1,Hs*seg*1000);

%front-right-up
Tnew(1,end,Hs*seg*1000)=2*Fo*(T(1,W*seg*1000,Hs*seg*1000)+T(1,end,Hs*seg*1000-
1)+T(2,end,Hs*seg*1000)-3*T(1,end,Hs*seg*1000)+2*Bi(1,end,Hs*seg*1000)*(T0-
T(1,end,Hs*seg*1000)))+T(1,end,Hs*seg*1000);

%back-left-bottom
Tnew(end,1,1)=2*Fo*(T(end,2,1)+T(end,1,2)+T(L*1000*seg,1,1)-
3*T(end,1,1)+2*Bi(end,1,1)*(T0-T(end,1,1)))+T(end,1,1);

%back-right-bottom
Tnew(end,end,1)=2*Fo*(T(end,W*seg*1000,1)+T(end,end,2)+T(L*1000*seg,end,1)-
3*T(end,end,1)+2*Bi(end,end,1)*(T0-T(end,end,1)))+T(end,end,1);

%back-left-up
Tnew(end,1,Hs*seg*1000)=2*Fo*(T(end,2,Hs*seg*1000)+T(end,1,Hs*seg*1000-
1)+T(L*1000*seg,1,Hs*seg*1000)-3*T(end,1,Hs*seg*1000)+2*Bi(end,1,Hs*seg*1000)*(T0-
T(end,1,Hs*seg*1000)))+T(end,1,Hs*seg*1000);

%back-right-up
Tnew(end,end,Hs*seg*1000)=2*Fo*(T(end,W*seg*1000,Hs*seg*1000)+T(end,end,Hs*seg*1000-
1)+T(L*1000*seg,end,Hs*seg*1000)-3*T(end,end,Hs*seg*1000)+2*Bi(end,end,Hs*seg*1000)*(T0-
T(end,end,Hs*seg*1000)))+T(end,end,Hs*seg*1000);
```

```
for u=1:1:H*1000*seg+1
    for d=1:1:L*1000*seg+1
    for f=1:1:W*1000*seg+1
        if T(d,f,u)~=0
            if u==Hs*seg*1000 && f~=1 && f~=W*seg*1000+1 && d~=1 && d~=L*1000*seg+1 &&
T(d,f,u+1)==0
            Tnew(d,f,u)=Fo*(2*T(d,f,u-1)+T(d,f-1,u)+T(d,f+1,u)+T(d-1,f,u)+T(d+1,f,u)-
6*T(d,f,u)+2*Bi(d,f,u)*(T0-T(d,f,u)))+T(d,f,u); %up
            end
            if d>1 && d<L*1000*seg+1 && f>1 && f<W*seg*1000+1 && u>Hs*seg*1000 &&
u<H*seg*1000+1
                if u==Hs*seg*1000 && T(d,f-1,u+1)==0 && T(d,f,u+1)~=0 && d==y0*1000*seg-
1
                    Tnew(d,f,u)=(4/3)*Fo*(Bi(d,f,u)*(T0-T(d,f,u))+T(d,f+1,u)+(T(d,f-
1,u)+T(d+1,f,u)+T(d-1,f,u)+T(d,f,u-1)+T(d,f,u+1))-6*T(d,f,u))+T(d,f,u); %front-left-
contact corner
                elseif u==Hs*seg*1000 && T(d,f+1,u+1)==0 && T(d,f-1,u+1)~=0 &&
d==y0*1000*seg-1
                    Tnew(d,f,u)=(4/3)*Fo*(Bi(d,f,u)*(T0-T(d,f,u))+T(d,f+1,u)+(T(d,f-
1,u)+T(d+1,f,u)+T(d-1,f,u)+T(d,f,u-1)+T(d,f,u+1))-6*T(d,f,u))+T(d,f,u); %front-right-
contact corner
                elseif u==Hs*seg*1000 && T(d,f-1,u+1)==0 && T(d,f,u+1)~=0 &&
d==floor(yt*1000*seg)+7
                    Tnew(d,f,u)=(4/3)*Fo*(Bi(d,f,u)*(T0-T(d,f,u))+T(d,f+1,u)+(T(d,f-
1,u)+T(d+1,f,u)+T(d-1,f,u)+T(d,f,u-1)+T(d,f,u+1))-6*T(d,f,u))+T(d,f,u); %back-left-
contact corner
                elseif u==Hs*seg*1000 && T(d,f+1,u+1)==0 && T(d,f-1,u+1)~=0 &&
d==floor(yt*1000*seg)+7
                    Tnew(d,f,u)=(4/3)*Fo*(Bi(d,f,u)*(T0-T(d,f,u))+T(d,f+1,u)+(T(d,f-
1,u)+T(d+1,f,u)+T(d-1,f,u)+T(d,f,u-1)+T(d,f,u+1))-6*T(d,f,u))+T(d,f,u); %back-right-
contact corner
                elseif u==Hs*seg*1000 && T(d,f-1,u+1)==0 && T(d,f,u+1)~=0 &&
d~=y0*1000*seg-1 && d~=floor(yt*1000*seg)+7
                    Tnew(d,f,u)=(4/3)*Fo*(Bi(d,f,u)*(T0-T(d,f,u))+T(d,f+1,u)+T(d,f-
1,u)+T(d-1,f,u)+T(d+1,f,u)+T(d,f,u-1)+T(d,f,u+1)-6*T(d,f,u))+T(d,f,u); %left-contact
edge
                elseif u==Hs*seg*1000 && T(d,f+1,u+1)==0 && T(d,f,u+1)~=0 &&
d~=y0*1000*seg-1 && d~=floor(yt*1000*seg)+7
                    Tnew(d,f,u)=(4/3)*Fo*(Bi(d,f,u)*(T0-T(d,f,u))+T(d,f-
1,u)+T(d,f+1,u)+T(d-1,f,u)+T(d+1,f,u)+T(d,f,u-1)+T(d,f,u+1)-6*T(d,f,u))+T(d,f,u);
%right-contact edge
                elseif T(d,f-1,u)==0 && T(d,f+1,u)~=0 && d==y0*1000*seg-1
                    Tnew(d,f,u)=2*Fo*(T(d,f+1,u)+T(d+1,f,u)-2*T(d,f,u)+2*Bi(d,f,u)*(T0-
T(d,f,u)))+T(d,f,u); %track front-left curve
                elseif T(d,f+1,u)==0 && T(d,f-1,u)~=0 && d==y0*1000*seg-1
                    Tnew(d,f,u)=2*Fo*(T(d,f-1,u)+T(d+1,f,u)-2*T(d,f,u)+2*Bi(d,f,u)*(T0-
T(d,f,u)))+T(d,f,u); %track front-right curve
                elseif T(d,f,u+1)==0 && T(d,f-1,u)~=0 && T(d,f+1,u)~=0 &&
d==y0*1000*seg-1
                    Tnew(d,f,u)=2*Fo*(T(d,f-1,u)+T(d,f+1,u)+T(d+1,f,u)+T(d,f,u-1)-
4*T(d,f,u)+2*Bi(d,f,u)*(T0-T(d,f,u)))+T(d,f,u); %missing points
                elseif T(d,f-1,u)==0 && T(d,f+1,u)~=0 && d==floor(yt*1000*seg)+7
                    Tnew(d,f,u)=2*Fo*(T(d,f+1,u)+T(d-1,f,u)-2*T(d,f,u)+2*Bi(d,f,u)*(T0-
T(d,f,u)))+T(d,f,u); %track back-left curve
                elseif T(d,f+1,u)==0 && T(d,f-1,u)~=0 && d==floor(yt*1000*seg)+7
                    Tnew(d,f,u)=2*Fo*(T(d,f-1,u)+T(d-1,f,u)-2*T(d,f,u)+2*Bi(d,f,u)*(T0-
T(d,f,u)))+T(d,f,u); %track back-right curve
                elseif T(d,f,u+1)==0 && T(d,f-1,u)~=0 && T(d,f+1,u)~=0 &&
d==floor(yt*1000*seg)+7
                    Tnew(d,f,u)=2*Fo*(T(d,f-1,u)+T(d,f+1,u)+T(d-1,f,u)+T(d,f,u-1)-
4*T(d,f,u)+2*Bi(d,f,u)*(T0-T(d,f,u)))+T(d,f,u); %missing points
                elseif d==y0*1000*seg-1 && T(d,f-1,u)~=0 && T(d,f+1,u)~=0 && T(d,f,u-
1)~=0 && T(d,f,u+1)~=0
                    Tnew(d,f,u)=Fo*(2*T(d+1,f,u)+T(d,f-
1,u)+T(d,f+1,u)+T(d,f,u+1)+T(d,f,u-1)-6*T(d,f,u)+2*Bi(d,f,u)*(T0-T(d,f,u)))+T(d,f,u);
%track front
```

```
                elseif d==floor(yt*1000*seg)+7 && T(d,f-1,u)~=0 && T(d,f+1,u)~=0 &&
T(d,f,u-1)~=0 && T(d,f,u+1)~=0
                    Tnew(d,f,u)=Fo*(2*T(d-1,f,u)+T(d,f-
1,u)+T(d,f+1,u)+T(d,f,u+1)+T(d,f,u-1)-6*T(d,f,u)+2*Bi(d,f,u)*(T0-T(d,f,u)))+T(d,f,u);
%track back
                elseif T(d,f-1,u)==0 && T(d,f+1,u)==0 && d~=y0*1000*seg-1 &&
d~=floor(yt*1000*seg)+7
                    Tnew(d,f,u)=Fo*(T(d-1,f,u)+T(d+1,f,u)-4*T(d,f,u)+2*T(d,f,u-
1)+2*Bi(d,f,u)*(T0-T(d,f,u)))+T(d,f,u); %track top type one
                elseif T(d,f,u+1)==0 && T(d,f+1,u)~=0 && T(d,f-1,u)~=0 &&
d~=y0*1000*seg-1 && d~=floor(yt*1000*seg)+7
                    Tnew(d,f,u)=Fo*(2*T(d,f,u-1)+T(d,f-1,u)+T(d,f+1,u)+T(d-
1,f,u)+T(d+1,f,u)-6*T(d,f,u)+2*Bi(d,f,u)*(T0-T(d,f,u)))+T(d,f,u); %track top type two
                elseif T(d,f-1,u)==0 && T(d,f+1,u)~=0 && d~=y0*1000*seg-1 &&
d~=floor(yt*1000*seg)+7
                    Tnew(d,f,u)=Fo*(T(d-1,f,u)+T(d+1,f,u)+2*T(d,f+1,u)-
4*T(d,f,u)+2*Bi(d,f,u)*(T0-T(d,f,u)))+T(d,f,u); %track left
                elseif T(d,f+1,u)==0 && T(d,f-1,u)~=0 && d~=y0*1000*seg-1 &&
d~=floor(yt*1000*seg)+7
                    Tnew(d,f,u)=Fo*(T(d-1,f,u)+T(d+1,f,u)+2*T(d,f-1,u)-
4*T(d,f,u)+2*Bi(d,f,u)*(T0-T(d,f,u)))+T(d,f,u); %track right
                end
            end
        end
    end
    end
end

Tnew(Tnew>Tb)=Tb; %evaporation


T=Tnew;
```

Appendix D MATLAB code of Temperature field output

```
%%%%%%%%%%%%%%%%%%%%%%%%%%%% temperature field output %%%%%%%%%%%%%%%%%%%%%%%%%%%%%%%%

%%%%%%%%%%%%%% axonometric view %%%%%%%%%%%%%%

EX=T(1:end,1:end,Hs*1000*seg:end); %temperature data array

Tshow=EX(EX~=0); %extract nonzero temperature data

Yshow=rem(rem((find(EX)-1),(L*1000*seg+1)*(W*1000*seg+1)),L*1000*seg+1)+1;
%Y index

Xshow=fix(rem((find(EX)-1),(L*1000*seg+1)*(W*1000*seg+1))/(L*1000*seg+1))+1;
%X index

Zshow=fix((find(EX)-1)/((L*1000*seg+1)*(W*1000*seg+1)))+1; %Z index

figure(1) scatter3(Xshow/seg,Yshow/seg,Zshow/seg,1,Tshow,'.'); axis equal
xlabel('x/(mm)'); ylabel('y/(mm)'); zlabel('z/(mm)'); colormap jet;
colorbar('location','EastOutside');

%%%%%%%%%%%%%% fixed crosssection %%%%%%%%%%%%%%
dis=0.01; %distance of plane
Tx=T(dis*seg*1000,:,:);
Tx=squeeze(Tx);
Tx(Tx>Tm)=Tm; %mark melt pool
figure(2)
contour((1:W*1000*seg+1)/seg,(1:H*1000*seg+1)/seg,Tx',40);axis equal
xlabel('x/(mm)');
ylabel('z/(mm)');
colormap jet;
```

```
colorbar('location','EastOutside');

%%%%%%%%%%%%%% cross section following laser %%%%%%%%%%%%%%
Tx=T(floor(yt*seg*1000)+1,:,:);
Tx=squeeze(Tx);

Tcon=mean(Tx(Tx>=Tm));

%update geometry
if ti==6 || ti==0
updategeo;
end

Tx(Tx>Tm)=Tm; %mark melt pool
figure(3)
contour((1:round(W*1000*seg)+1)/seg,(1:H*1000*seg+1)/seg,Tx',40);axis equal
xlabel('x/(mm)');
ylabel('z/(mm)');
colormap jet;
colorbar('location','EastOutside');

%%%%%%%%%%%%%% longitudinal cross section %%%%%%%%%%%%%%
Tx=T(:,W/2*1000*seg+1,:);
Tx=squeeze(Tx);
Tx(Tx>Tm)=Tm; %mark melt pool
figure(4)
contour((1:L*1000*seg+1)/seg,(1:H*1000*seg+1)/seg,Tx',40);axis equal
hold on;
plot([yt*1000,yt*1000],[1,H*1000],'-.','color','r');
plot([dis*1000,dis*1000],[1,H*1000],'--','color','b');
hold off;
xlabel('y/(mm)');
ylabel('z/(mm)');
colormap jet;
colorbar('location','EastOutside');
```

Appendix E MATLAB code of Geometry profile output

E.1 On horizontal surface

```
%%%%%%%%%%%%%%%%%%%%%%%%%%%%%%%%%% geometry profile %%%%%%%%%%%%%%%%%%%%%%%%%%%%%%%%%%

%%%%%%%%%%%%%%%%% on horizontal surface %%%%%%%%%%%%%%%%
for q=1:zn
    for p=1:xn

%bulge
angle=0:pi/10000:2*theq(q,p);
rp=hq(q,p)/(1-cos(theq(q,p)));
x=xpi(q,p)+rp*cos(angle-(theq(q,p)-pi/2));
z=hpiq(q,p)+rp*sin(angle-(theq(q,p)-pi/2))+rp*sin(theq(q,p)-pi/2);

%melt pool

b=rp*cos(theq(q,p)-pi/2); %half width of track

for sqDel=hpiq(q,p)+(sq(q,p)-hpiq(q,p))/10:(sq(q,p)-hpiq(q,p))/10:sq(q,p)

if abs(hpiq(q,p)-sqDel)<b
    cm=4;
end

if (-sqDel/b)>2.5
    er=0.00002; %modify tolerance for deep melt pool
```

```
end

if -sqDel>=0.0038
    er=0.00003;
end


meltpool;

%modify melt pool boundary
while abs(b-xp(end))>er && ((hpiq(q,p)-sqDel)/b)>0.3

    if b<xp(end)
        cm=cm-1.01/exp(((hpiq(q,p)-sqDel)/b)^2); %2
        meltpool;
    else
        cm=cm+1/exp(((hpiq(q,p)-sqDel)/b)^2);
        meltpool;
    end

end

end


figure(6)

plot(x*1000,z*1000,'r',(xpi(q,p)+xp)*1000,zp'*1000,'b',(xpi(q,p)-
xp)*1000,zp'*1000,'b','LineWidth',3); %plot bulge & melt pool


hold on;

if q==zn && p==xn-1 && zn>1 %stagger
    break;
end

    end

end
hold off;
axis equal
set(gca,'XAxisLocation','origin');
xlim([-5 20]);
ylim([-5 10]);
xlabel('x(mm)');
ylabel('z(mm)');
```

E.1.1 Melt pool boundary

```
%%%%%%%%%%%%%%%%%%%%%%%%%%%%%%%%%% geometry profile %%%%%%%%%%%%%%%%%%%%%%%%%%%%%%%%%%

%%%%%%%%%%%%%%% melt pool boundary %%%%%%%%%%%%%%%%%%

%solve melt pool boundary 1
tspan=[0 2*(zmp-sqDel+b)];
xm0=[0 eps sqDel];
[tm,xm]=ode45(@(tm,xm) interface(tm,xm,rho,g,ga2(zi,xi),cm,sqDel,R0),tspan,xm0);

for zpik=1:length(xm(:,3))
    if xm(zpik,3)>zmp
        break;
    end
end

%fit melt pool boundary
[zData,xData]=prepareCurveData(xm(1:zpik-1,3),xm(1:zpik-1,2));
```

```
ft='linearinterp';
[fitresult,gof]=fit(zData,xData,ft,'Normalize','on');
zp=linspace(sqDel,zmp);
xp=feval(fitresult,zp);
```

E.1.2 Melt pool interface

```
%%%%%%%%%%%%%%%%%%%%%%%%%%%%%%%% geometry profile %%%%%%%%%%%%%%%%%%%%%%%%%%%%%%%%

%%%%%%%%%%%%%%%%%% melt pool interface %%%%%%%%%%%%%%%%%%

function dxdy=interface(t,y,rho,g,ga,cm,s,R0) %y(1) to the, y(2) to x, y(3) to z

f=(rho*g*(s-y(3))*cm)/ga-sin(y(1))/y(2)+2/R0; %force balance f=(rho*g*(h-y(3))*cm)/ga-
sin(y(1))/y(2); 0.8*b

k=cos(y(1));

q=sin(y(1));

dxdy=[f;k;q];

end
```

E.2 On inclined surface

```
%%%%%%%%%%%%%%%%%%%%%%%%%%%%%%%% geometry profile %%%%%%%%%%%%%%%%%%%%%%%%%%%%%%%%

%%%%%%%%%%%%%%%%%%% on inclined surface %%%%%%%%%%%%%%%%%%

%%%%%%%%%%%%% bulge %%%%%%%%%%%%%%

if Tcon>Tm && Tcon<=Tb

ga=kc*(Tc-Tcon)/(V^(2/3)); %surface tension

ga2(zi,xi)=kb*Tm/(om^(2/3))*(0.228+0.3135*Tcon/Tm); %liquid-solid interfacial tension

end

the(zi,xi)=acos(2.299-3.606*ga);

if xi==1 && zi==1

    A=pi*R^2*F/v; %cross section area

    Aiter2=0;

    Lb(zi,xi)=rp/2; %initial half length

    retention; %first bulge geometry

    lr=(X5(end)-X5(1))*(1-eta);%distance of two retention

    l=lr; %update to temperature field

else

A=pi*R^2*F/v; %cross section area

Lb(zi,xi)=rp; %initial half length

Aiter2=0; %overlap area iteration

retention;
```

```
Aiter=0; %cross section area iteration

% x=-Wl;
% z=0;
while Aiter-Aiter2<=A
    retention;
    Aiter2=0;
    x=-Wl;
    z=0;
    for u=Hs*1000*seg*50+1:1:H*1000*seg*50+1
        for f=1:1:W*1000*seg*50+1
            if zi==1 %base layer
                if (x-xpia(zi,xi))^2<=(r1(zi,xi))^2-(z-zpia(zi,xi))^2 ... %self
                        && (x-xpir(zi,xi-1))^2<=(r2(zi,xi-1))^2-(z-zpir(zi,xi-1))^2 ...
%left
                        && z>=freeform(x) %inclined surface
                    Aiter2=Aiter2+(1/(seg*50)/1000)^2;
                end
            else %top layer
                if xi==1 %first bulge
                    if (((x-xpia(zi,xi))^2<=(r1(zi,xi))^2-(z-zpia(zi,xi))^2 &&
z<=zpia(zi,xi)+tan(pi/2-alp*pi/180)*(xpia(zi,xi)-x)) || ((x-
xpir(zi,xi))^2<=(r2(zi,xi))^2-(z-zpir(zi,xi))^2 && z>=zpia(zi,xi)+tan(pi/2-
alp*pi/180)*(xpia(zi,xi)-x))) ... %self
                            && (((x-xpir(zi-1,xi))^2<=(r2(zi-1,xi))^2-(z-zpir(zi-
1,xi))^2) ... %down
                            || ((x-xpia(zi-1,xi+1))^2<=(r1(zi-1,xi+1))^2-(z-zpia(zi-
1,xi+1))^2 && z<=zpia(zi-1,xi+1)+tan(pi/2-alp*pi/180)*(xpia(zi-1,xi+1)-x)) || ((x-
xpir(zi-1,xi+1))^2<=(r2(zi-1,xi+1))^2-(z-zpir(zi-1,xi+1))^2 && z>=zpia(zi-
1,xi+1)+tan(pi/2-alp*pi/180)*(xpia(zi-1,xi+1)-x))) ... %down-right
                            && z>=freeform(x)+hinter
                        Aiter2=Aiter2+(1/(seg*50)/1000)^2;
                    end
                else
                    if (((x-xpia(zi,xi))^2<=(r1(zi,xi))^2-(z-zpia(zi,xi))^2 &&
z<=zpia(zi,xi)+tan(pi/2-alp*pi/180)*(xpia(zi,xi)-x)) || ((x-
xpir(zi,xi))^2<=(r2(zi,xi))^2-(z-zpir(zi,xi))^2 && z>=zpia(zi,xi)+tan(pi/2-
alp*pi/180)*(xpia(zi,xi)-x))) ... %self
                            && (((x-xpir(zi,xi-1))^2<=(r2(zi,xi-1))^2-(z-zpir(zi,xi-
1))^2) ... %left
                            || ((x-xpir(zi-1,xi))^2<=(r2(zi-1,xi))^2-(z-zpir(zi-
1,xi))^2) ... %down
                            || ((x-xpia(zi-1,xi+1))^2<=(r1(zi-1,xi+1))^2-(z-zpia(zi-
1,xi+1))^2 && z<=zpia(zi-1,xi+1)+tan(pi/2-alp*pi/180)*(xpia(zi-1,xi+1)-x)) || ((x-
xpir(zi-1,xi+1))^2<=(r2(zi-1,xi+1))^2-(z-zpir(zi-1,xi+1))^2 && z>=zpia(zi-
1,xi+1)+tan(pi/2-alp*pi/180)*(xpia(zi-1,xi+1)-x))) ... %down-right
                            && z>=freeform(x)+hinter
                        Aiter2=Aiter2+(1/(seg*50)/1000)^2;
                    end
                end
            end
            x=x+1/(seg*50)/1000;
        end
        x=-Wl;
        z=z+1/(seg*50)/1000;
    end
    z=0;
end

end

%%%%%%%%%%%%%%%% melt pool %%%%%%%%%%%%%%%%%%%

if sq(zi,xi)<Y5(1) && ((Y5(1)-sq(zi,xi))/abs(X5(1)-xt))>0

%left side

b=abs(X5(1)-xt); %half width of track 0.5*abs(X5(1)-X5(end));
```

```
R0=0.6*b; %radius of melt pool bottom 0.6

zmp=Y5(1); %obtain melt pool top

meltpool;

Xm1=xt-xp;

Zm1=zp';

%right side

b=0.5*abs(X5(1)-X5(end)); %half width of track

R0=0.9*b;

zmp=Y5(end); %obtain melt pool top

meltpool;

Xm2=(X5(1)+X5(end))/2+xp;

Zm2=zp';

Xm2=Xm2+abs((Xm2(1)-xt)./(Zm2(1)-Zm2(end)))*(Zm2(end)-Zm2);

else

    Xm1=(X5(1):(X5(end)-X5(1))/20:X5(end))';
    Zm1=[Xm1.^2 Xm1 Xm1./Xm1]*inv([(X5(1))^2 X5(1) 1;(X5(end))^2 X5(end) 1;(xt)^2 xt
1])*[Y5(1);Y5(end);sq(zi,xi)];


end

%%%%%%%%%%%%%%%%%%%%%%%%% output %%%%%%%%%%%%%%%%%%%%%%%%%

figure(10);

if zi==1 && xi==1

xf=-0.005:0.0001:0.045;

plot(xf*1000,freeform(xf)*1000,'b','LineWidth',1); %plot substrate

end

hold on;

if sq(zi,xi)<Y5(1) && ((Y5(1)-sq(zi,xi))/abs(X5(1)-xt))>0
    plot(X5*1000,Y5*1000,Xm1*1000,Zm1*1000,Xm2*1000,Zm2*1000,'LineWidth',1); %plot track
else
    plot(X5*1000,Y5*1000,Xm1*1000,Zm1*1000,'LineWidth',1);
end

axis equal
xlim([-5 5]);
ylim([-5 7]);
xlabel('x(mm)');
ylabel('z(mm)');

if zn==1 && xn==1
    hold off;
end
```

E.2.1 Retention

```
%%%%%%%%%%%%%%%%%%%%%%%%%%%%%%%%%% geometry profile %%%%%%%%%%%%%%%%%%%%%%%%%%%%%%%%%%%%

%%%%%%%%%%%%%%%%%%%%%%% on inclined surface %%%%%%%%%%%%%%%%%%%%%%%%

%%%%%%%%%%%%%%%%%%%%% retention %%%%%%%%%%%%%%%%%%%%%%%%

%geometry

thea(zi,xi)=the(zi,xi)-alp; %advancing angle


Aiter=0; %cross section area iteration

Fgr=pi*R^2*F/v*rho*g*sin(alp);


while Aiter-Aiter2<=A

    ther(zi,xi)=acos(Fgr/ga-cos(pi-thea(zi,xi)));

    c1=rho*g*sin(alp)/ga;

    c3=0.5*(sin(thea(zi,xi))-sin(ther(zi,xi))-rho*g*Lb(zi,xi)^2*sin(alp)/ga);

    c5=(sin(thea(zi,xi))+sin(ther(zi,xi)))/(2*Lb(zi,xi));

    X0=(-c5+sqrt(c5^2-2*c1*c3))/c1;

    Lf=sin(thea(zi,xi))*(1-cos(ther(zi,xi)))/(sin(ther(zi,xi))*(1-cos(thea(zi,xi))));

    L1=2*Lb(zi,xi)*Lf/(1+Lf);

    L2=2*Lb(zi,xi)/(1+Lf);

    r1(zi,xi)=L1/sin(thea(zi,xi));

    r2(zi,xi)=L2/sin(ther(zi,xi));

    Aiter=0.5*((r1(zi,xi))^2*thea(zi,xi)+(r2(zi,xi))^2*ther(zi,xi)-
(r1(zi,xi))^2*sin(thea(zi,xi))*cos(thea(zi,xi))-
(r2(zi,xi))^2*sin(ther(zi,xi))*cos(ther(zi,xi)));

    Lb(zi,xi)=Lb(zi,xi)+0.0000001;

end

Y0=L2/sin(ther(zi,xi))-L1/sin(thea(zi,xi));

angle=pi/2-thea(zi,xi):pi/10000:pi/2;

x1=r1(zi,xi)*cos(angle)+X0;

y1=r1(zi,xi)*sin(angle)+Y0;

angle=pi/2:pi/10000:pi/2+ther(zi,xi);

x2=r2(zi,xi)*cos(angle)+X0;

y2=r2(zi,xi)*sin(angle);

X1=[x1,x2];

X1=-X1; %horizontal flip

Y1=[y1,y2];

%position
```

```
dx=r2(zi,xi)*sin(ther(zi,xi))*sin(alp)-X0;

X2=X1-dx; %shift

Y2=Y1;

dy=r2(zi,xi)*cos(ther(zi,xi));

X3=X2; %put on original point

Y3=Y2-dy;

X4=X3*cos(alp)-Y3*sin(alp); %rotation

Y4=X3*sin(alp)+Y3*cos(alp);

X5=X4+0.5*lr*(zi-1)+lr*(xi-1); %put on inclined surface

if zi==1
    Y5=Y4+freeform(0.5*lr*(zi-1)+lr*(xi-1));
else
    Y5=Y4+freeform(0.5*lr*(zi-1)+lr*(xi-1))+hinter;
end

xpia(zi,xi)=-X0*cos(alp)-Y0*sin(alp)-dx*cos(alp)+dy*sin(alp)+0.5*lr*(zi-1)+lr*(xi-1);

if zi==1
    zpia(zi,xi)=-X0*sin(alp)+Y0*cos(alp)+freeform(0.5*lr*(zi-1)+lr*(xi-1))-dy*cos(alp)-
dx*sin(alp);
else
zpia(zi,xi)=-X0*sin(alp)+Y0*cos(alp)+freeform(0.5*lr*(zi-1)+lr*(xi-1))+hinter-
dy*cos(alp)-dx*sin(alp);
end

xpir(zi,xi)=-X0*cos(alp)-dx*cos(alp)+dy*sin(alp)+0.5*lr*(zi-1)+lr*(xi-1);

if zi==1
    zpir(zi,xi)=-X0*sin(alp)+freeform(0.5*lr*(zi-1)+lr*(xi-1))-dy*cos(alp)-dx*sin(alp);
else
zpir(zi,xi)=-X0*sin(alp)+freeform(0.5*lr*(zi-1)+lr*(xi-1))+hinter-dy*cos(alp)-
dx*sin(alp);
end
```

E.2.2 Substrate incline angle

```
%%%%%%%%%%%%%%%%%%%%%%%%%%%%%%%%%% geometry profile %%%%%%%%%%%%%%%%%%%%%%%%%%%%%%%%%%

%%%%%%%%%%%%%%%%%%%%%%%% on inclined surface %%%%%%%%%%%%%%%%%%%%%%


%%%%%%%%%%%%%%%%%%%%%%%% substrate incline angle %%%%%%%%%%%%%%%%%%%%%%%

function dxdy=freeform(xt) %y(1) to the, y(2) to x, y(3) to z


dxdy=tan(30*pi/180)*(xt+0.005); %tan(30*pi/180)*(xt+0.005);

end
```

Appendix F MATLAB code of GUI application cases

F.1 Variable single-track profile

```
%%%%%%%%%%%%%%%%%%%%%%%%%%%% activate calculation process %%%%%%%%%%%%%%%%%%%%%%%%%%%%%%%%
function calculate_Callback(hObject, eventdata, handles)
main;

%%%%%%%%%%%%%%%%%%%% input parameters %%%%%%%%%%%%%%%%%%%%
function slider1_Callback(hObject, eventdata, handles)
P=get(handles.slider1,'value');%obtain current laser power
set(handles.edit21,'string',num2str(P));%display current laser power

function slider2_Callback(hObject, eventdata, handles)
v=get(handles.slider2,'value');%obtain current scanning speed
set(handles.edit22,'string',num2str(v));%display current scanning speed

function slider3_Callback(hObject, eventdata, handles)
F=get(handles.slider3,'value');%obtain current wire feed rate
set(handles.edit23,'string',num2str(F));%display current wire feed rate

%%%%%%%%%%%%%%%%%% output results %%%%%%%%%%%%%%%%%%%%

axes(handles.axonometric)
scatter3(Xshow/seg,Yshow/seg,Zshow/seg,1,Tshow,'.'); axis equal

axes(handles.followlaser)
contour((1:round(W*1000*seg)+1)/seg,(1:round(H*1000*seg)+1)/seg,Tx',40);axis equal

axes(handles.longitudinal)
contour((1:L*1000*seg+1)/seg,(1:H*1000*seg+1)/seg,Tx',40);axis equal

axes(handles.profile)

if s>=0
    plot(x*1000,z*1000,'r','LineWidth',3); %plot bulge & melt pool
else
    plot(x*1000,z*1000,'r',xp*1000,zp'*1000,'b',-xp*1000,zp'*1000,'b','LineWidth',3);
%plot bulge & melt pool
end
```

F.2 Gear tooth repairing profile

```
%%%%%%%%%%%%%%%%%%%%%%%%%%%%%%%%%%%% input parameters %%%%%%%%%%%%%%%%%%%%%%%%%%%%%%%%%%%%
function edit26_Callback(hObject, eventdata, handles)
ovlap =get(handles.edit26,'value');%obtain overlap ratio

function edit27_Callback(hObject, eventdata, handles)
stag=get(handles.edit27,'value');%obtain stagger ratio

function edit28_Callback(hObject, eventdata, handles)
xn=get(handles.edit28,'value');%obtain tracks in a layer

%%%%%%%%%%%%%%%%%%%%%%%%%%%%%%%%%%%% output results %%%%%%%%%%%%%%%%%%%%%%%%%%%%%%%%%%%%
%gear tooth
xs=[15.854 15.357 14.886 14.453 14.05 13.689 13.076 12.616 12.289 12.079 11.971 11.941
11.87 11.742 11.362 10.846 10.219 9.496 8.686 7.799 6.841 5.817 4.73];
zs=[0 0.284 0.608 0.981 1.387 1.831 2.795 3.842 4.937 6.062 7.2 9.487 10.628 11.765
14.02 16.249 18.448 20.619 22.758 24.867 26.944 28.989 31.002];
ts=1:23;
tss=1:0.01:23;
axes(handles.axes3)
plot(spline(ts,xs,tss),spline(ts,zs,tss),xs,zs,'.','LineWidth',1);
hold on
plot(spline(ts,-xs,tss),spline(ts,zs,tss),-xs,zs,'.','LineWidth',1);
plot([xs(end),-xs(end)],[zs(end),zs(end)],'LineWidth',1);
axis equal
set(gca,'XAxisLocation','origin');
xlim([-25 25]);
ylim([-5 35]);
```

```
xlabel('x(mm)');
ylabel('z(mm)');


%deposition

for q=1:zn
    for p=1:xn

%bulge
angle=0:pi/10000:2*theq(q,p);
rp=hq(q,p)/(1-cos(theq(q,p)));
x=xpi(q,p)+rp*cos(angle-(theq(q,p)-pi/2));
z=hpiq(q,p)+rp*sin(angle-(theq(q,p)-pi/2))+rp*sin(theq(q,p)-pi/2);

axes(handles.axes3)


plot(x*1000,z*1000,'r','LineWidth',1); %plot bulge & melt pool

    end

end
hold off;
```

F.3 Mould surface repairing profile

```
%%%%%%%%%%%%%%%%%%%%%%%%%%%%%%%%% input parameters %%%%%%%%%%%%%%%%%%%%%%%%%%%%%%%%%%%%
function edit26_Callback(hObject, eventdata, handles)
dth=get(handles.edit26,'value');%obtain defined thickness

function edit27_Callback(hObject, eventdata, handles)
ang=get(handles.edit27,'value');%obtain inclined angle


%%%%%%%%%%%%%%%%%%%%%%%%%%%%%%%%% output results %%%%%%%%%%%%%%%%%%%%%%%%%%%%%%%%%%%%
axes(handles.profile)

if zi==1 && xi==1

xf=-0.005:0.0001:0.045;

plot(xf*1000,freeform(xf)*1000,'b','LineWidth',1); %plot substrate

hold on;

plot(xf*1000,freeform(xf)*1000+1.4*cos(30*pi/180),'--r','LineWidth',1); %plot defined
thickness

end

hold on;

plot(X5*1000,Y5*1000,Xm1*1000,Zm1*1000,Xm2*1000,Zm2*1000,'LineWidth',1); %plot track
axis equal
xlim([-5 15]);
ylim([-7 15]);
xlabel('x(mm)');
ylabel('z(mm)');
```

Bibliographies

[1] Z. Liu, Q. Jiang, T. Li, S. Dong, S. Yan, H. Zhang, B. Xu, Environmental benefits of remanufacturing: A case study of cylinder heads remanufactured through laser cladding, Journal of Cleaner Production 133 (2016) 1027-1033.
[2] Blade Maintenance and Repair. https://www.ropepartner.com/wind-energy-services/wind-turbine-blade-repair. (Accessed 11/1 2022).
[3] REFURBISHING AND REPAIR. https://marmeninc.com/en/services/refurbishing-and-repair. (Accessed 11/1 2022).
[4] Air Compressor Parts & Service. https://acecompressorservices.com/. (Accessed 11/1 2022).
[5] Pump Repairs. https://www.junkmail.co.za/services/maintenance-and-construction-services/gauteng/johannesburg/east-rand/pump-repairs/25b72ee935ef4ed194b17c4907cee975. (Accessed 11/1 2022).
[6] VALVE REPAIR & OVERHAUL SERVICES. https://www.unicomechanical.com/valve-repair-and-overhaul.html. (Accessed 11/1 2022).
[7] INDUSTRIAL HEAT EXCHANGER SERVICE AND REPAIR. https://heatexchangegroup.co.uk/services/industrial-heat-exchanger-service-and-repair/. (Accessed 11/1 2022).
[8] Industrial Crankshaft Repair Houston. https://www.fusionhouston.com/industrial-crankshaft-repair-houston/. (Accessed 11/1 2022).
[9] Quality Tool & Die Repair Services. http://www.trwelding.com/quality-tool-die-repair-services_1.html. (Accessed 11/1 2022).
[10] Production: Most modern machines AND manual work. https://www.neumeisterhydraulik.de/en/home/company/about-us. (Accessed 11/1 2022).
[11] Gearbox Repair Process (Step By Step). https://mygearboxrepair.com/gearbox-repair-process-step-step. (Accessed 11/1 2022).
[12] Railroad Track Repair And Maintenance. https://railroadrails.com/knowlege/railroad-track-repair/. (Accessed 11/1 2022).
[13] Custom Manufacturing & Heavy Equipment Repairs. http://www.riversedgewelding.ca/services.html. (Accessed 11/1 2022).
[14] P.m. research, Global Market Study on Rotating Equipment Repair: Applications in Oil & Gas and Power Generation to Witness an Upsurge, 2019. https://www.persistencemarketresearch.com/market-research/rotating-equipment-repair-market.asp. (Accessed 11/1 2022).
[15] D. Parker, K. Riley, S. Robinson, H. Symington, J. Tewson, K. Jansson, S. Ramkumar, D. Peck, Remanufacturing market study, European remanufacturing network, 2015.
[16] M.o.I.a.I.T.o.t.P.s.R.o. China, Welding repairing technical requirements for marine diesel engine parts, 2013.
[17] I.a.Q.o.t.P.s.R.o.C. General Administration of Quality Supervision, C.N.S.M. Committee, Laser repairing general specification, 2013.
[18] ASME, Repair of Pressure Equipment and Piping, ASME, 2018.
[19] BSI, Specification for mechanical fittings for use in the repair, connection and renovation of pressurized water supply pipelines, BSI, 2013.
[20] N.A. Aziz, N.A.A. Adnan, D.A. Wahab, A.H. Azman, Component design optimisation based on artificial intelligence in support of additive manufacturing repair and restoration: Current status and future outlook for remanufacturing, Journal of Cleaner Production 296 (2021) 126401-126420.
[21] Pedro Vilaça, J.o. Gandra, C. Vidal, Linear Friction Based Processing Technologies for Aluminum Alloys: Surfacing, Stir Welding and Stir Channeling, 2012. https://www.intechopen.com/books/aluminium-alloys-new-trends-in-fabrication-and-applications/linear-friction-based-processing-technologies-for-aluminum-alloys-surfacing-stir-welding-and-stir-ch. (Accessed 11/1 2022).

[22] L. Carolo, The 7 Main Types of Additive Manufacturing, 2020. https://all3dp.com/2/main-types-additive-manufacturing/. (Accessed 11/1 2022).
[23] H. Brodin, SIEMENS processes for advanced components and prototypes. https://3dp.se/wp-content/uploads/2014/12/hakan-brodin-siemens.pdf. (Accessed 11/1 2022).
[24] V. Champagne, D. Helfritch, Critical Assessment 11: Structural repairs by cold spray, Materials Science and Technology 31(6) (2015) 627-634.
[25] A. Clare, O. Oyelola, J. Folkes, P. Farayibi, Laser cladding for railway repair and preventative maintenance, Journal of Laser Applications 24(3) (2012) 032004-032014.
[26] M. Brandt, The role of lasers in additive manufacturing, Laser Additive Manufacturing, Woodhead Publishing, Sawston Cambridge, 2017.
[27] Laser Cladding Equipment Market by Power, End-user, and Geography - Forecast and Analysis 2020-2024, 2020. https://www.technavio.com/report/laser-cladding-equipment-market-industry-analysis. (Accessed 11/1 2022).
[28] Global Laser Cladding Material Market Growth 2019-2024, 2019. https://www.fiormarkets.com/report/global-laser-cladding-material-market-growth-2019-2024-379807.html. (Accessed 11/1 2022).
[29] Laser Cladding Service Market Size By Product, By Application, By Geographic Scope And Forecast, 2019. https://www.verifiedmarketresearch.com/product/laser-cladding-service-market/. (Accessed 11/1 2022).
[30] S.M. Thompson, L. Bian, N. Shamsaei, A. Yadollahi, An overview of Direct Laser Deposition for additive manufacturing; Part I: Transport phenomena, modeling and diagnostics, Additive Manufacturing 8 (2015) 36-62.
[31] PTA, Laser and One step fusible powders. http://www.plasmatransferredarcpowder.com/. (Accessed 11/1 2022).
[32] CMC flux cored wire series. http://www.mould-mending.com/sm_product_detail.asp?Fkindno=F002472&Skindno=S004377&Itemno=&Pidno=201403310001. (Accessed 11/1 2022).
[33] E. Capello, B. Previtali, The influence of operator skills, process parameters and materials on clad shape in repair using laser cladding by wire, Journal of Materials Processing Technology 174(1-3) (2006) 223-232.
[34] S. Zhou, T. Xu, C. Hu, H. Wu, H. Liu, X. Ma, Effect of different topologies on microstructure and mechanical properties of multilayer coatings deposited by laser cladding with Inconel 625 wire, Surface and Coatings Technology 421 (2021) 127299-127312.
[35] CO2 Lasers: The Industrial Workhorse. https://www.photonics.com/Articles/COSUB2_SUB_Lasers_The_Industrial_Workhorse/a25155. (Accessed 11/1 2022).
[36] Nd:YAG laser. http://www.physics-and-radio-electronics.com/physics/laser/ndyaglaser.html. (Accessed 11/1 2022).
[37] J. Du, Y. Yu, X. An, J. Shang, J. Lei, J. Jiang, L. Jiang, W. Lv, G. Fan, Q. Gao, 60 mm-aperture high average output power Nd:YAG composite ceramic disk laser, Optik 172 (2018) 197-202.
[38] F. Boiocchi, Direct diode lasers: how technology evolution is opening new markets, 2019. https://www.metalworkingworldmagazine.com/direct-diode-lasers-how-technology-evolution-is-opening-new-markets/. (Accessed 11/1 2022).
[39] Y. Liu, G. Yang, Z. Wang, T. Li, S. Tang, Y. Zhao, Y. Lan, A. Demir, High-power operation and lateral divergence angle reduction of broad-area laser diodes at 976 nm, Optics & Laser Technology 141 (2021).
[40] https://www.laserfocusworld.com/articles/print/volume-48/issue-04/features/the-state-of-the-art.html. (Accessed 11/1 2022).
[41] P. Shukla, J. Lawrence, Y. Zhang, Understanding laser beam brightness: A review and new prospective in material processing, Optics & Laser Technology 75 (2015) 40-51.
[42] M.N. Zervas, C.A. Codemard, High Power Fiber Lasers: A Review, IEEE Journal of Selected Topics in Quantum Electronics 20(5) (2014) 219-241.

[43] J.W. Dawson, M.N. Zervas, F. Ghiringhelli, M.K. Durkin, I. Crowe, Distribution of photodarkening-induced loss in Yb-doped fiber amplifiers, Fiber Lasers VIII: Technology, Systems, and Applications 7914 (2011) 79140L1-79140L8.
[44] J.W. Dawson, C. Jauregui, J. Limpert, A. Tünnermann, On the Raman threshold of passive large mode area fibers, Fiber Lasers VIII: Technology, Systems, and Applications 7914 (2011) 7914081-7914086.
[45] R. Tao, R. Su, P. Ma, X. Wang, P. Zhou, Suppressing mode instabilities by optimizing the fiber coiling methods, Laser Physics Letters 14(2) (2017) 025101-025108.
[46] A.V. Kudryashov, O. Homburg, A.H. Paxton, T. Mitra, V.S. Ilchenko, Gaussian-to-top-hat beam shaping: an overview of parameters, methods, and applications, Proceedings of SPIE 8236 (2012) 82360A1-82360A9.
[47] N. Goffin, J.R. Tyrer, L.C.R. Jones, R.L. Higginson, Simulated and experimental analysis of laser beam energy profiles to improve efficiency in wire-fed laser deposition, The International Journal of Advanced Manufacturing Technology 114(9-10) (2021) 3021-3036.
[48] J.Z. Wu, H.Y. Wei, F.B. Yuan, P.H. Zhao, Y. Zhang, Effect of beam profile on heat and mass transfer in filler powder laser welding, Journal of Materials Processing Technology 258 (2018) 47-57.
[49] C. Brecher, F. Klocke, T. Breitbach, D. Do-Khac, D. Heinen, A. Karlberger, C.-J. Rosen, A hybrid machining center for enabling new die manufacturing and repair concepts, Production Engineering 5(4) (2011) 405-413.
[50] M. Motta, A.G. Demir, B. Previtali, High-speed imaging and process characterization of coaxial laser metal wire deposition, Additive Manufacturing 22 (2018) 497-507.
[51] S. Ji, F. Liu, T. Shi, G. Fu, S. Shi, Effects of Defocus Distance on Three-Beam Laser Internal Coaxial Wire Cladding, Chinese Journal of Mechanical Engineering 34(1) (2021) 34-45.
[52] S.H. Mok, G. Bi, J. Folkes, I. Pashby, Deposition of Ti–6Al–4V using a high power diode laser and wire, Part I: Investigation on the process characteristics, Surface and Coatings Technology 202(16) (2008) 3933-3939.
[53] F. Moures, E. Cicală, P. Sallamand, D. Grevey, B. Vannes, S. Ignat, Optimisation of refractory coatings realised with cored wire addition using a high-power diode laser, Surface and Coatings Technology 200(7) (2005) 2283-2292.
[54] F. Silze, M. Schnick, I. Sizova, M. Bambach, Laser Metal Deposition of Ti-6Al-4V with a Direct Diode Laser Set-up and Coaxial Material Feed, Procedia Manufacturing 47 (2020) 1154-1158.
[55] M. Bambach, I. Sizova, F. Kies, C. Haase, Directed energy deposition of Inconel 718 powder, cold and hot wire using a six-beam direct diode laser set-up, Additive Manufacturing 47 (2021) 102269-102280.
[56] N.J. Goffin, R.L. Higginson, J.R. Tyrer, The use of holographic optical elements (HOE's) to investigate the use of a flat irradiance profile in the control of heat absorption in wire-fed laser cladding, Journal of Materials Processing Technology 220 (2015) 191-201.
[57] M. Kotar, M. Fujishima, G.N. Levy, E. Govekar, Advances in the understanding of the annular laser beam wire cladding process, Journal of Materials Processing Technology 294 (2021) 117105-117116.
[58] M. Kotar, E. Govekar, The influence of the workpiece illumination proportion in annular laser beam wire deposition process, Proc Cirp 74 (2018) 228-232.
[59] H. Siva Prasad, J. Frostevarg, A.F.H. Kaplan, The stability of laser welding with an off-axis wire feed, Journal of Materials Processing Technology 264 (2019) 84-90.
[60] X. Xu, G. Mi, Y. Luo, P. Jiang, X. Shao, C. Wang, Morphologies, microstructures, and mechanical properties of samples produced using laser metal deposition with 316 L stainless steel wire, Optics and Lasers in Engineering 94 (2017) 1-11.
[61] T.E. Abioye, J. Folkes, A.T. Clare, A parametric study of Inconel 625 wire laser deposition, Journal of Materials Processing Technology 213(12) (2013) 2145-2151.
[62] S. Zhao, L. Yang, Y. Huang, S. Xu, A novel method to fabricate Ni/WC composite coatings by laser wire deposition: Processing characteristics, microstructural evolution and mechanical properties under different wire transfer modes, Additive Manufacturing 38 (2021) 101738-101752.
[63] E. Brandl, V. Michailov, B. Viehweger, C. Leyens, Deposition of Ti–6Al–4V using laser and wire, part I: Microstructural properties of single beads, Surface and Coatings Technology 206(6) (2011) 1120-1129.
[64] W. Huang, J. Xiao, S. Chen, X. Jiang, Control of wire melting behavior during laser hot wire deposition of aluminum alloy, Optics & Laser Technology 150 (2022) 107978-107986.

[65] M. Akbari, R. Kovacevic, An investigation on mechanical and microstructural properties of 316LSi parts fabricated by a robotized laser/wire direct metal deposition system, Additive Manufacturing 23 (2018) 487-497.
[66] J.L. Zou, Y. He, S.K. Wu, T. Huang, R.S. Xiao, Experimental and theoretical characterization of deep penetration welding threshold induced by 1-μm laser, Applied Surface Science 357 (2015) 1522-1527.
[67] A.F.H. Kaplan, Fresnel absorption of 1μm- and 10μm-laser beams at the keyhole wall during laser beam welding: Comparison between smooth and wavy surfaces, Applied Surface Science 258(8) (2012) 3354-3363.
[68] M. Froend, S. Riekehr, N. Kashaev, B. Klusemann, J. Enz, Process development for wire-based laser metal deposition of 5087 aluminium alloy by using fibre laser, Journal of Manufacturing Processes 34 (2018) 721-732.
[69] C. Kästner, M. Neugebauer, K. Schricker, J.P. Bergmann, Strategies for Increasing the Productivity of Pulsed Laser Cladding of Hot-Crack Susceptible Nickel-Base Superalloy Inconel 738 LC, Journal of Manufacturing and Materials Processing 4(3) (2020) 84-106.
[70] M. Froend, V. Ventzke, N. Kashaev, B. Klusemann, J. Enz, Thermal analysis of wire-based direct energy deposition of Al-Mg using different laser irradiances, Additive Manufacturing 29 (2019) 100800-100811.
[71] X.P. Ding, H.M. Li, J.Q. Zhu, G.Y. Wang, H.Z. Cao, Q. Zhang, H.L. Ma, Application of infrared thermography for laser metal-wire additive manufacturing in vacuum, Infrared Physics & Technology 81 (2017) 166-169.
[72] Z. Nie, G. Wang, J.D. McGuffin-Cawley, B. Narayanan, S. Zhang, D. Schwam, M. Kottman, Y. Rong, Experimental study and modeling of H13 steel deposition using laser hot-wire additive manufacturing, Journal of Materials Processing Technology 235 (2016) 171-186.
[73] T. Bergs, S. Kammann, G. Fraga, J. Riepe, K. Arntz, Experimental investigations on the influence of temperature for Laser Metal Deposition with lateral Inconel 718 wire feeding, Procedia CIRP 94 (2020) 29-34.
[74] Y.-X. Sang, M.-Z. Xiao, Z.-J. Zhang, Q.-Y. Fu, Effect of auxiliary heating process on low power pulsed laser wire feeding deposition, Materials & Design 218 (2022) 110666-110680.
[75] B. Korojy, Volume change effects during solidification of alloys, Materials Science and Engineering, Royal Institute of Technology, Stockhom, Sweden, 2009.
[76] X. Cao, M. Jahazi, J. Fournier, M. Alain, Optimization of bead spacing during laser cladding of ZE41A-T5 magnesium alloy castings, Journal of Materials Processing Technology 205(1-3) (2008) 322-331.
[77] J.C. Heigel, M.F. Gouge, P. Michaleris, T.A. Palmer, Selection of powder or wire feedstock material for the laser cladding of Inconel® 625, Journal of Materials Processing Technology 231 (2016) 357-365.
[78] Y. Fu, N. Guo, C. Zhou, G. Wang, J. Feng, Investigation on in-situ laser cladding coating of the 304 stainless steel in water environment, Journal of Materials Processing Technology 289 (2021) 116949-116958.
[79] Y.N. Zhang, X. Cao, P. Wanjara, Microstructure and hardness of fiber laser deposited Inconel 718 using filler wire, The International Journal of Advanced Manufacturing Technology 69(9-12) (2013) 2569-2581.
[80] J. Fu, L. Gong, Y. Zhang, Q. Wu, X. Shi, J. Chang, J. Lu, Microstructure and Mechanical Properties of Ti-6Al-4V Fabricated by Vertical Wire Feeding with Axisymmetric Multi-Laser Source, Applied Sciences 7(3) (2017) 227-237.
[81] H. Ye, K. Ye, B.-g. Guo, F.-b. Le, C. Wei, X. Sun, G.-y. Wang, Y. Liu, Effects of combining ultrasonic micro-forging treatment with laser metal wire deposition on microstructural and mechanical properties in Ti–6Al–4V alloy, Materials Characterization 162 (2020) 110187-110199.
[82] J.C. Lippold, D.J. Kotecki, Welding metallurgy and weldability of stainless steels, John Wiley & Sons, Hoboken, New Jersey, 2005.
[83] J.N. Dupont, J.C. Lippold, S.D. Kiser, Welding metallurgy and weldability of nickel-base alloys, 2009.
[84] P. Wen, Z. Feng, S. Zheng, Formation quality optimization of laser hot wire cladding for repairing martensite precipitation hardening stainless steel, Optics & Laser Technology 65 (2015) 180-188.
[85] X. Xu, G.Y. Mi, L. Chen, L.D. Xiong, P. Jiang, X.Y. Shao, C.M. Wang, Research on microstructures and properties of Inconel 625 coatings obtained by laser cladding with wire, Journal of Alloys and Compounds 715 (2017) 362-373.

[86] F.T. Cheng, K.H. Lo, H.C. Man, A preliminary study of laser cladding of AISI 316 stainless steel using preplaced NiTi wire, Materials Science and Engineering: A 380(1-2) (2004) 20-29.
[87] X. Xu, G. Mi, L. Xiong, P. Jiang, X. Shao, C. Wang, Morphologies, microstructures and properties of TiC particle reinforced Inconel 625 coatings obtained by laser cladding with wire, Journal of Alloys and Compounds 740 (2018) 16-27.
[88] S. Zhou, T. Xu, C. Hu, H. Wu, H. Liu, X. Ma, A comparative study of tungsten carbide and carbon nanotubes reinforced Inconel 625 composite coatings fabricated by laser cladding, Optics & Laser Technology 140 (2021) 106967-106977.
[89] Y.-N. Zhang, X. Cao, P. Wanjara, M. Medraj, Tensile properties of laser additive manufactured Inconel 718 using filler wire, Journal of Materials Research 29(17) (2014) 2006-2020.
[90] F. Caiazzo, Additive manufacturing by means of laser-aided directed metal deposition of titanium wire, The International Journal of Advanced Manufacturing Technology 96(5-8) (2018) 2699-2707.
[91] E. Brandl, B. Baufeld, C. Leyens, R. Gault, Additive manufactured Ti-6Al-4V using welding wire: comparison of laser and arc beam deposition and evaluation with respect to aerospace material specifications, Physics Procedia 5 (2010) 595-606.
[92] Q. Cheng, N. Guo, Y. Fu, D. Zhang, G. Wang, M. Yu, Underwater wire-feed laser deposition of thin - Walled tubular structure of aluminum alloy, Journal of Manufacturing Processes 67 (2021) 56-62.
[93] K. Li, D. Li, D. Liu, G. Pei, L. Sun, Microstructure evolution and mechanical properties of multiple-layer laser cladding coating of 308L stainless steel, Applied Surface Science 340 (2015) 143-150.
[94] T.E. Abioye, D.G. McCartney, A.T. Clare, Laser cladding of Inconel 625 wire for corrosion protection, Journal of Materials Processing Technology 217 (2015) 232-240.
[95] Q. Cheng, N. Guo, Y. Fu, G. Wang, M. Yu, J. He, Investigation on in-situ laser cladding 5356 aluminum alloy coating on 5052 aluminum alloy substrate in water environment, Journal of Materials Research and Technology 15 (2021) 4343-4352.
[96] W. Huang, S. Chen, J. Xiao, X. Jiang, Y. Jia, Laser wire-feed metal additive manufacturing of the Al alloy, Optics & Laser Technology 134 (2021) 106627-106635.
[97] W. Peng, S. Jiguo, Z. Shiqing, W. Gang, Control of wire transfer behaviors in hot wire laser welding, The International Journal of Advanced Manufacturing Technology 83(9-12) (2015) 2091-2100.
[98] S.P. Wei, G. Wang, Y.C. Shin, Y.M. Rong, Comprehensive modeling of transport phenomena in laser hot-wire deposition process, International Journal of Heat and Mass Transfer 125 (2018) 1356-1368.
[99] L. Jiao, Z. Wang, R. Chen, X. Zhu, Q. Liao, D. Ye, B. Zhang, W. Li, D. Li, Simulation on the Marangoni flow and heat transfer in a laser-heated suspended droplet, Chemical Engineering Science 209 (2019) 115202-115211.
[100] Z. Gan, G. Yu, X. He, S. Li, Surface-active element transport and its effect on liquid metal flow in laser-assisted additive manufacturing, International Communications in Heat and Mass Transfer 86 (2017) 206-214.
[101] Y. Zhao, C.Y. Zhao, Z.G. Xu, Numerical study of solid-liquid phase change by phase field method, Computers & Fluids 164 (2018) 94-101.
[102] T. Mukherjee, W. Zhang, T. DebRoy, An improved prediction of residual stresses and distortion in additive manufacturing, Computational Materials Science 126 (2017) 360-372.
[103] J. Yan, W. Yan, S. Lin, G.J. Wagner, A fully coupled finite element formulation for liquid–solid–gas thermo-fluid flow with melting and solidification, Computer Methods in Applied Mechanics and Engineering 336 (2018) 444-470.
[104] X. Li, Q. Guo, L. Chen, W. Tan, Quantitative investigation of gas flow, powder-gas interaction, and powder behavior under different ambient pressure levels in laser powder bed fusion, International Journal of Machine Tools and Manufacture 170 (2021) 103797-103806.
[105] S.M.H. Hojjatzadeh, N.D. Parab, Q. Guo, M. Qu, L. Xiong, C. Zhao, L.I. Escano, K. Fezzaa, W. Everhart, T. Sun, L. Chen, Direct observation of pore formation mechanisms during LPBF additive manufacturing process and high energy density laser welding, International Journal of Machine Tools and Manufacture 153 (2020) 103555-103562.

[106] R. Sun, Y. Shi, X. Wang, Y. Guo, X. Zhou, Understanding the thermal process during laser assisted ultra-high frequency induction deposition with wire feeding, International Journal of Heat and Mass Transfer 153 (2020) 119536-119556.
[107] R. Sun, Y. Shi, X. Wang, Y. Guo, X. Zhou, Investigation of laser assisted ultra-high frequency induction deposition method: Processes, fluid flow, and microstructure characteristic, Journal of Materials Research and Technology 9(3) (2020) 2773-2792.
[108] R. Sun, Y. Shi, Z. Bing, Q. Li, R. Wang, Metal transfer and thermal characteristics in drop-on-demand deposition using ultra-high frequency induction heating technology, Applied Thermal Engineering 149 (2019) 731-744.
[109] H. Gu, L. Li, Computational fluid dynamic simulation of gravity and pressure effects in laser metal deposition for potential additive manufacturing in space, International Journal of Heat and Mass Transfer 140 (2019) 51-65.
[110] F.E. Bock, J. Herrnring, M. Froend, J. Enz, N. Kashaev, B. Klusemann, Experimental and numerical thermo-mechanical analysis of wire-based laser metal deposition of Al-Mg alloys, Journal of Manufacturing Processes 64 (2021) 982-995.
[111] L. Du, D. Gu, D. Dai, Q. Shi, C. Ma, M. Xia, Relation of thermal behavior and microstructure evolution during multi-track laser melting deposition of Ni-based material, Optics & Laser Technology 108 (2018) 207-217.
[112] P. Farahmand, R. Kovacevic, An experimental–numerical investigation of heat distribution and stress field in single- and multi-track laser cladding by a high-power direct diode laser, Optics & Laser Technology 63 (2014) 154-168.
[113] J.J. Shi, P. Zhu, G.Y. Fu, S.H. Shi, Geometry characteristics modeling and process optimization in coaxial laser inside wire cladding, Optics and Laser Technology 101 (2018) 341-348.
[114] J. Xiong, G. Zhang, H. Gao, L. Wu, Modeling of bead section profile and overlapping beads with experimental validation for robotic GMAW-based rapid manufacturing, Robotics and Computer-Integrated Manufacturing 29(2) (2013) 417-423.
[115] K. Chongbunwatana, Simulation of vapour keyhole and weld pool dynamics during laser beam welding, Production Engineering 8(4) (2014) 499-511.
[116] W. Liu, J.N. DuPont, Effects of melt-pool geometry on crystal growth and microstructure development in laser surface-melted superalloy single crystals: Mathematical modeling of single-crystal growth in a melt pool (part I), Acta Materialia 52(16) (2004) 4833-4847.
[117] W. Liu, J.N. DuPont, Effects of substrate crystallographic orientations on crystal growth and microstructure development in laser surface-melted superalloy single crystals. Mathematical modeling of single-crystal growth in a melt pool (Part II), Acta Materialia 53(5) (2005) 1545-1558.
[118] F. Liu, S.J. Song, F. Sommer, E.J. Mittemeijer, Evaluation of the maximum transformation rate for analyzing solid-state phase transformation kinetics, Acta Materialia 57(20) (2009) 6176-6190.
[119] Q. Yu, M. Nosonovsky, S.K. Esche, Monte Carlo simulation of grain growth of single-phase systems with anisotropic boundary energies, International Journal of Mechanical Sciences 51(6) (2009) 434-442.
[120] J. Svoboda, E. Gamsjäger, F.D. Fischer, Y. Liu, E. Kozeschnik, Diffusion processes in a migrating interface: The thick-interface model, Acta Materialia 59(12) (2011) 4775-4786.
[121] H. Wang, F. Liu, Y. Tan, Modeling grain refinement for undercooled single-phase solid-solution alloys, Acta Materialia 59(12) (2011) 4787-4797.
[122] Y.H. Jiang, F. Liu, S.J. Song, An extended analytical model for solid-state phase transformation upon continuous heating and cooling processes: Application in γ/α transformation, Acta Materialia 60(9) (2012) 3815-3829.
[123] P. Peng, General model on position of the solid/liquid interface during preparation of a directionally solidified peritectic alloy containing intermetallic compound phases, Materials Chemistry and Physics 223 (2019) 641-647.
[124] P. Peng, Migration of liquid particle from mushy zone interface in temperature gradient, International Journal of Heat and Mass Transfer 142 (2019) 118467-118470.

[125] M.S. Uddin, R.C. Gosh, G.M. Bhuiyan, Investigation of surface tension, viscosity and diffusion coefficients for liquid simple metals, Journal of Non-Crystalline Solids 499 (2018) 426-433.
[126] M.-W. Chen, Y. Wang, H. Guo, The effect of anisotropic surface tension on interfacial evolution of a particle in the binary alloy melt, Journal of Crystal Growth 510 (2019) 32-39.
[127] M. Lappa, An alternative theoretical approach for the derivation of analytic and numerical solutions to thermal Marangoni flows, International Journal of Heat and Mass Transfer 114 (2017) 407-418.
[128] P. Solana, J.L. Ocana, A mathematical model for penetration laser welding as a free-boundary problem, J Phys D Appl Phys 30(9) (1997) 1300-1313.
[129] C. Huh, R.L. Reed, A Method for Estimating Interfacial-Tensions and Contact Angles from Sessile and Pendant Drop Shapes, J Colloid Interf Sci 91(2) (1983) 472-484.
[130] M.G. Cabezas, A. Bateni, J.M. Montanero, A.W. Neumann, Determination of surface tension and contact angle from the shapes of axisymmetric fluid interfaces without use of apex coordinates, Langmuir 22(24) (2006) 169-183.
[131] Thyssenkrupp, Stainless Steel 316L 1.4404, 2020. https://www.thyssenkrupp-materials.co.uk/stainless-steel-316l-14404.html. (Accessed 11/1 2022).
[132] Y. Zhang, J. Zhang, Modeling of solidification microstructure evolution in laser powder bed fusion fabricated 316L stainless steel using combined computational fluid dynamics and cellular automata, Additive Manufacturing 28 (2019) 750-765.
[133] X.-H. Yang, J. Liu, A novel method for determining the melting point, fusion latent heat, specific heat capacity and thermal conductivity of phase change materials, International Journal of Heat and Mass Transfer 127 (2018) 457-468.
[134] M.J.K. Lodhi, K.M. Deen, W. Haider, Corrosion behavior of additively manufactured 316L stainless steel in acidic media, Materialia 2 (2018) 111-121.
[135] P.S. Korinko, S.H. Malene, Considerations for the weldability of types 304L and 316L stainless steel, Practical Failure Analysis 1(4) (2001) 61-68.
[136] X. Chen, J. Li, X. Cheng, B. He, H. Wang, Z. Huang, Microstructure and mechanical properties of the austenitic stainless steel 316L fabricated by gas metal arc additive manufacturing, Materials Science and Engineering: A 703 (2017) 567-577.
[137] G. Ma, T. Di, C. Song, F. Niu, J. Lu, D. Wu, Phase transformation mechanism and mechanical properties of Ti-45Al-8Nb alloy prepared by directed laser deposition, Materials Characterization 193 (2022) 112256-112264.
[138] S. Pratheesh Kumar, S. Elangovan, R. Mohanraj, V. Sathya Narayanan, Significance of continuous wave and pulsed wave laser in direct metal deposition, Materials Today: Proceedings 46 (2021) 8086-8096.
[139] H. El Cheikh, B. Courant, J.Y. Hascoët, R. Guillén, Prediction and analytical description of the single laser track geometry in direct laser fabrication from process parameters and energy balance reasoning, Journal of Materials Processing Technology 212(9) (2012) 1832-1839.
[140] F. Wirth, K. Wegener, A physical modeling and predictive simulation of the laser cladding process, Additive Manufacturing 22 (2018) 307-319.
[141] S.H. Nikam, N.K. Jain, S. Jhavar, Thermal modeling of geometry of single-track deposition in micro-plasma transferred arc deposition process, Journal of Materials Processing Technology 230 (2016) 121-130.
[142] D. Cha, D. Axinte, J. Billingham, Geometrical modelling of pulsed laser ablation of high performance metallic alloys, International Journal of Machine Tools and Manufacture 141 (2019) 78-88.
[143] I. Sanchez, D. Axinte, R. Smith, Modelling of rotational multiple plain water jets for controlled removal of multi-material coatings, CIRP Annals - Manufacturing Technology 101 (2020) 1-4.
[144] Z. Shang, Z. Liao, J.A. Sarasua, J. Billingham, D. Axinte, On modelling of laser assisted machining: Forward and inverse problems for heat placement control, International Journal of Machine Tools and Manufacture 138 (2019) 36-50.
[145] D. Axinte, J. Billingham, Time-dependent manufacturing processes lead to a new class of inverse problems, Proc Natl Acad Sci U S A 116(12) (2019) 5341-5343.

[146] E.A. Hochmann, I. Salehinia, How convection on the substrate affects the thermal history of the build in direct laser deposition—finite element analysis, The International Journal of Advanced Manufacturing Technology 96(9-12) (2018) 3471-3480.
[147] J.F. Li, L. Li, F.H. Stott, Comparison of volumetric and surface heating sources in the modeling of laser melting of ceramic materials, International Journal of Heat and Mass Transfer 47(6) (2004) 1159-1174.
[148] D. Halliday, R. Resnick, J. Walker, F. Edwards, J.J. Merrill, Fundamentals of Physics, John Wiley & Sons, Inc., New York, 2018.
[149] M. Alimardani, E. Toyserkani, J.P. Huissoon, Three-dimensional numerical approach for geometrical prediction of multilayer laser solid freeform fabrication process, Journal of Laser Applications 19(1) (2007) 14-25.
[150] J.P. Holman, Heat transfer, McGraw-Hill, New York, 2010.
[151] C.S. Baird, Absorption of electromagnetic radiation, McGraw-Hill Education, New York, 2019.
[152] J.F. Ready, Handbook of Laser Materials Processing, Laser Institute of America, Orlando, 2001.
[153] M. Abramowitz, I.A. Stegun, Handbook of Mathematical Functions: with Formulas, Graphs, and Mathematical Tables, Dover Publications, New York, 2012.
[154] P.-G.d. Gennes, F. Brochard-Wyart, D. Quere, Capillarity and Wetting Phenomena - Drops, Bubbles, Pearls, Waves, Springer - Verlag, New York, 2003.
[155] A.W. Adamson, A.P. Gast, Physical Chemistry of Surfaces, 6th edn. ed., John Wiley and Sons, New York, 1997.
[156] N.K. Adam, The Physics and Chemistry of Surfaces, Oxford University Press, London, 1941.
[157] S. Lu, H. Fujii, K. Nogi, Marangoni convection and weld shape variations in He–CO2 shielded gas tungsten arc welding on SUS304 stainless steel, Journal of Materials Science 43(13) (2008) 4583-4591.
[158] B. Chen, L. Song, K. Gao, F. Liu, Two zone model for mushy region of solid–liquid phase change based on Lattice Boltzmann method, International Communications in Heat and Mass Transfer 98 (2018) 1-12.
[159] A. Gajewski, A couple new ways of surface tension determination, International Journal of Heat and Mass Transfer 115 (2017) 909-917.
[160] R.M. Digilov, Solid–liquid interfacial tension in metals: correlation with the melting point, Physica B: Condensed Matter 352(1-4) (2004) 53-60.
[161] J. Yang, J. Han, H. Yu, J. Yin, M. Gao, Z. Wang, X. Zeng, Role of molten pool mode on formability, microstructure and mechanical properties of selective laser melted Ti-6Al-4V alloy, Materials & Design 110 (2016) 558-570.
[162] M. Khorasani, A. Ghasemi, M. Leary, E. Sharabian, L. Cordova, I. Gibson, D. Downing, S. Bateman, M. Brandt, B. Rolfe, The effect of absorption ratio on meltpool features in laser-based powder bed fusion of IN718, Optics & Laser Technology 153 (2022) 108263-108276.
[163] L. Chen, Y. Zhao, B. Song, T. Yu, Z. Liu, Modeling and simulation of 3D geometry prediction and dynamic solidification behavior of Fe-based coatings by laser cladding, Optics & Laser Technology 139 (2021) 107009-107022.
[164] M.O. Sklyar, G.A. Turichin, O.G. Klimova, O.G. Zotov, I.K. Topalov, Microstructure of 316L stainless steel components produced by direct laser deposition, Steel in Translation 46(12) (2017) 883-887.
[165] A.K. Singh, K.S. Bal, D. Dey, A.K. Das, A.R. Pal, D.K. Pratihar, A. Roy Choudhury, Experimental investigation and parametric optimization for minimization of dilution during direct laser metal deposition of tungsten carbide and cobalt powder mixture on SS304 substrate, Powder Technology 390 (2021) 339-353.
[166] F. Farrokhi, B. Endelt, M. Kristiansen, A numerical model for full and partial penetration hybrid laser welding of thick-section steels, Optics & Laser Technology 111 (2019) 671-686.
[167] Y. Li, Q. Han, I. Horváth, G. Zhang, Repairing surface defects of metal parts by groove machining and wire + arc based filling, Journal of Materials Processing Technology 274 (2019) 116268-116279.
[168] G. Zhao, C. Cho, J.-D. Kim, Application of 3-D finite element method using Lagrangian formulation to dilution control in laser cladding process, International Journal of Mechanical Sciences 45(5) (2003) 777-796.
[169] S. Liao, S. Webster, D. Huang, R. Council, K. Ehmann, J. Cao, Simulation-guided variable laser power design for melt pool depth control in directed energy deposition, Additive Manufacturing 56 (2022) 102912-102923.

[170] S.S. Chakraborty, S. Dutta, Estimation of dilution in laser cladding based on energy balance approach using regression analysis, Sādhanā 44(6) (2019) 1-6.
[171] M. Mazzarisi, S.L. Campanelli, A. Angelastro, M. Dassisti, Phenomenological modelling of direct laser metal deposition for single tracks, The International Journal of Advanced Manufacturing Technology 111(7-8) (2020) 1955-1970.
[172] V. Ocelik, O. Nenadl, A. Palavra, J.T.M. De Hosson, On the geometry of coating layers formed by overlap, Surf Coat Tech 242 (2014) 54-61.
[173] K. Zhang, S.J. Wang, W.J. Liu, X.F. Shang, Characterization of stainless steel parts by Laser Metal Deposition Shaping, Materials & Design 55 (2014) 104-119.
[174] D. Ding, Z. Pan, D. Cuiuri, H. Li, A multi-bead overlapping model for robotic wire and arc additive manufacturing (WAAM), Robotics and Computer-Integrated Manufacturing 31 (2015) 101-110.
[175] C. Chen, G. Lian, J. Jiang, Q. Wang, Simplification and experimental investigation of geometrical surface smoothness model for multi-track laser cladding processes, Journal of Manufacturing Processes 36 (2018) 621-628.
[176] Y. Huang, M.B. Khamesee, E. Toyserkani, A new physics-based model for laser directed energy deposition (powder-fed additive manufacturing): From single-track to multi-track and multi-layer, Optics & Laser Technology 109 (2019) 584-599.
[177] A. Heralić, A.-K. Christiansson, B. Lennartson, Height control of laser metal-wire deposition based on iterative learning control and 3D scanning, Optics and Lasers in Engineering 50(9) (2012) 1230-1241.
[178] N. Chekir, Y. Tian, R. Gauvin, N. Brodusch, J.J. Sixsmith, M. Brochu, Effect of travel speed and stress relief on thin Ti-6Al-4V laser wire deposits, Materials Science and Engineering: A 724 (2018) 335-347.
[179] S.C. Bozeman, O.B. Isgor, J.D. Tucker, Effects of processing conditions on the solidification and heat-affected zone of 309L stainless steel claddings on carbon steel using wire-directed energy deposition, Surface and Coatings Technology 444 (2022) 128698-128708.
[180] L.E. dos Santos Paes, H.S. Ferreira, M. Pereira, F.A. Xavier, W.L. Weingaertner, L.O. Vilarinho, Modeling layer geometry in directed energy deposition with laser for additive manufacturing, Surface and Coatings Technology 409 (2021) 126897-126905.
[181] D. Tyralla, H. Köhler, T. Seefeld, C. Thomy, R. Narita, A multi-parameter control of track geometry and melt pool size for laser metal deposition, Procedia CIRP 94 (2020) 430-435.
[182] P. Kumar, N.K. Jain, M.S. Sawant, Development of theoretical models for dimensions of single-layer multi-track and multi-layer multi-track depositions by μ-PTA additive manufacturing process, Journal of Materials Research and Technology 17 (2022) 95-110.
[183] S. Takushima, D. Morita, N. Shinohara, H. Kawano, Y. Mizutani, Y. Takaya, Optical in-process height measurement system for process control of laser metal-wire deposition, Precision Engineering 62 (2020) 23-29.
[184] A. Marmur, Contact angle equilibrium: the intrinsic contact angle, Journal of Adhesion Science and Technology 6(6) (1992) 689-701.
[185] W.J. Jasper, N. Anand, A generalized variational approach for predicting contact angles of sessile nano-droplets on both flat and curved surfaces, Journal of Molecular Liquids 281 (2019) 196-203.
[186] Y. Ding, L. Jia, Q. Peng, J. Guo, Thermodynamic analysis of steady wetting state of droplet on single microstructure surface, Colloids and Surfaces A: Physicochemical and Engineering Aspects 597 (2020) 124797-124808.
[187] H. Yi, L. Qi, J. Luo, N. Li, Hole-defects in soluble core assisted aluminum droplet printing: Metallurgical mechanisms and elimination methods, Applied Thermal Engineering 148 (2019) 1183-1193.
[188] H. Yi, L. Qi, J. Luo, D. Zhang, H. Li, X. Hou, Effect of the surface morphology of solidified droplet on remelting between neighboring aluminum droplets, International Journal of Machine Tools and Manufacture 130-131 (2018) 1-11.
[189] K. Tanaka, T. Yamaguchi, Direct observation of bubble generation processes inside a molten pool during laser cladding, Surf Coat Tech 447 (2022) 128831-128837.

[190] G. Luo, D. Wu, Y. Zhou, Y. Hu, Z. Yao, Laser printing of large-scale metal micro/nanoparticle array: Deposition behavior and microstructure, International Journal of Machine Tools and Manufacture 173 (2022) 103845-103851.
[191] B. Graf, A. Gumenyuk, M. Rethmeier, Laser Metal Deposition as Repair Technology for Stainless Steel and Titanium Alloys, Physics Procedia 39 (2012) 376-381.
[192] T. Amine, J.W. Newkirk, F. Liou, An investigation of the effect of laser deposition parameters on characteristics of multilayered 316 L deposits, The International Journal of Advanced Manufacturing Technology 73(9-12) (2014) 1739-1749.
[193] T. Amine, J.W. Newkirk, F. Liou, Methodology for Studying Effect of Cooling Rate During Laser Deposition on Microstructure, Journal of Materials Engineering and Performance 24(8) (2015) 3129-3136.
[194] X. Wang, D. Deng, M. Qi, H. Zhang, Influences of deposition strategies and oblique angle on properties of AISI316L stainless steel oblique thin-walled part by direct laser fabrication, Optics & Laser Technology 80 (2016) 138-144.
[195] P. Sreeramagiri, A. Bhagavatam, H. Alrehaili, G. Dinda, Direct laser metal deposition of René 108 single crystal superalloy, Journal of Alloys and Compounds 838 (2020) 155634-155642.
[196] C. Körner, M. Markl, J.A. Koepf, Modeling and Simulation of Microstructure Evolution for Additive Manufacturing of Metals: A Critical Review, Metallurgical and Materials Transactions A 51(10) (2020) 4970-4983.
[197] D. Verdi, M.A. Garrido, C.J. Múnez, P. Poza, Microscale evaluation of laser cladded Inconel 625 exposed at high temperature in air, Materials & Design 114 (2017) 326-338.
[198] S. Jhavar, C.P. Paul, N.K. Jain, Causes of failure and repairing options for dies and molds: A review, Engineering Failure Analysis 34 (2013) 519-535.
[199] T. Ünal-Saewe, L. Gahn, J. Kittel, A. Gasser, J.H. Schleifenbaum, Process Development for Tip Repair of Complex Shaped Turbine Blades with IN718, Procedia Manufacturing 47 (2020) 1050-1057.
[200] V. Grubišić, N. Vulić, S. Sönnichsen, Structural durability validation of bearing girders in marine Diesel engines, Engineering Failure Analysis 15(4) (2008) 247-260.
[201] J. Hao, Q. Meng, C. Li, Z. Li, D. Wu, Effects of tilt angle between laser nozzle and substrate on bead morphology in multi-axis laser cladding, Journal of Manufacturing Processes 43 (2019) 311-322.
[202] C.P. Paul, S.K. Mishra, A. Kumar, L.M. Kukreja, Laser rapid manufacturing on vertical surfaces: Analytical and experimental studies, Surf Coat Tech 224 (2013) 18-28.
[203] X. Li, T. Li, B. Shi, D. Wang, M. Adnan, H. Lu, The influence of substrate tilt angle on the morphology of laser cladding layer, Surface and Coatings Technology 391 (2020) 125706-125716.
[204] Q. Chai, Z. Wang, C. Fang, Y. Xing, X. Qiu, Z. Zhou, Numerical and experimental study on the profile of metal alloys formed on the inclined substrate by laser cladding, Surface and Coatings Technology 422 (2021) 127494-127502.
[205] T.-S. Wang, L. Feng, W.-Y. Shi, Marangoni convection instability inside an evaporating droplet on an inclined substrate, International Journal of Heat and Mass Transfer 183 (2022) 122050-122060.
[206] J. Li, H.N. Li, Z. Liao, D. Axinte, Analytical modelling of full single-track profile in wire-fed laser cladding, Journal of Materials Processing Technology 290 (2021) 116978-116991.
[207] A. Kaplan, A model of deep penetration laser welding based on calculation of the keyhole profile, Journal of Physics D: Applied Physics 27 (1994) 1805-1814.
[208] A.I. ElSherbini, A.M. Jacobi, Liquid drops on vertical and inclined surfaces; I. An experimental study of drop geometry, J Colloid Interface Sci 273(2) (2004) 556–565.
[209] A.I. ElSherbini, A.M. Jacobi, Liquid drops on vertical and inclined surfaces; II. A method for approximating drop shapes, J Colloid Interface Sci 273(2) (2004) 566–575.
[210] G. Ahmed, M. Sellier, M. Jermy, M. Taylor, Modeling the effects of contact angle hysteresis on the sliding of droplets down inclined surfaces, European Journal of Mechanics - B/Fluids 48 (2014) 218-230.
[211] J. Xie, J. Xu, W. Shang, K. Zhang, Mode selection between sliding and rolling for droplet on inclined surface: Effect of surface wettability, International Journal of Heat and Mass Transfer 122 (2018) 45-58.
[212] N. Chatterjee, B.G. Nita, The hanging cable problem for practical applications, Journal of Mathematics 4(1) (2010) 70-77.

[213] F.L. Serafini, M. Peruzzo, I. Krindges, M.F.C. Ordoñez, D. Rodrigues, R.M. Souza, M.C.M. Farias, Microstructure and mechanical behavior of 316L liquid phase sintered stainless steel with boron addition, Materials Characterization 152 (2019) 253-264.
[214] A.M. Helmenstine, What Is the Density of Air at STP?, 2020. https://www.thoughtco.com/density-of-air-at-stp-607546. (Accessed 11/1 2022).
[215] C. Tan, Y. Chew, F. Weng, S. Sui, F.L. Ng, T. Liu, G. Bi, Laser aided additive manufacturing of spatially heterostructured steels, International Journal of Machine Tools and Manufacture 172 (2022) 103817-103830.
[216] S.J. Wolff, H. Wang, B. Gould, N. Parab, Z. Wu, C. Zhao, A. Greco, T. Sun, In situ X-ray imaging of pore formation mechanisms and dynamics in laser powder-blown directed energy deposition additive manufacturing, International Journal of Machine Tools and Manufacture 166 (2021) 103743-103756.
[217] E. Capello, D. Colombo, B. Previtali, Repairing of sintered tools using laser cladding by wire, Journal of Materials Processing Technology 164-165 (2005) 990-1000.
[218] S.-H. Park, P. Liu, K. Yi, G. Choi, K.-Y. Jhang, H. Sohn, Mechanical properties estimation of additively manufactured metal components using femtosecond laser ultrasonics and laser polishing, International Journal of Machine Tools and Manufacture 166 (2021) 103745-103756.
[219] A. Malakizadi, T. Hajali, F. Schulz, S. Cedergren, J. Ålgårdh, R. M'Saoubi, E. Hryha, P. Krajnik, The role of microstructural characteristics of additively manufactured Alloy 718 on tool wear in machining, International Journal of Machine Tools and Manufacture 171 (2021) 103814-103831.
[220] E.R. Denlinger, J.C. Heigel, P. Michaleris, T.A. Palmer, Effect of inter-layer dwell time on distortion and residual stress in additive manufacturing of titanium and nickel alloys, Journal of Materials Processing Technology 215 (2015) 123-131.
[221] J.D. Ferguson, G. Arikan, D.S. Dale, A.R. Woll, J.D. Brock, Measurements of surface diffusivity and coarsening during pulsed laser deposition, Phys Rev Lett 103(25) (2009) 256103-256106.
[222] K. Biester, L. Budde, A. Barroi, M. Lammers, J. Hermsdorf, L. Overmeyer, Investigation of deposition welding in vertical and horizontal position with a coaxial laser wire welding head, The International Journal of Advanced Manufacturing Technology 120(7-8) (2022) 5399-5410.
[223] J.D. Pérez-Ruiz, L.N.L. de Lacalle, G. Urbikain, O. Pereira, S. Martínez, J. Bris, On the relationship between cutting forces and anisotropy features in the milling of LPBF Inconel 718 for near net shape parts, International Journal of Machine Tools and Manufacture 170 (2021) 103801-103827.
[224] J. Chaves-Jacob, A. Beaucamp, W. Zhu, D. Kono, J.-M. Linares, Towards an understanding of surface finishing with compliant tools using a fast and accurate simulation method, International Journal of Machine Tools and Manufacture 163 (2021) 103704-103722.
[225] W.-L. Zhu, A. Beaucamp, Generic three-dimensional model of freeform surface polishing with non-Newtonian fluids, International Journal of Machine Tools and Manufacture 172 (2022) 103837-103856.
[226] A. Batal, A. Michalek, P. Penchev, A. Kupisiewicz, S. Dimov, Laser processing of freeform surfaces: A new approach based on an efficient workpiece partitioning strategy, International Journal of Machine Tools and Manufacture 156 (2020) 103593-103604.
[227] L. Qin, D. Zhao, W. Wang, G. Yang, Geometric defects identification and deviation compensation in laser deposition manufacturing, Optics & Laser Technology 155 (2022) 108374-108384.
[228] Z. Wang, K. Lin, Y.P. Zhao, The effect of sharp solid edges on the droplet wettability, J Colloid Interface Sci 552 (2019) 563-571.
[229] G. Lian, H. Zhang, Y. Zhang, C. Chen, X. Huang, J. Jiang, Control and prediction of forming quality in curved surface multi-track laser cladding with curve paths, The International Journal of Advanced Manufacturing Technology 106(9-10) (2020) 3669-3682.
[230] G. Zhang, W. Sun, D. Zhao, P. Fan, F. Guo, Y. Huang, P. Li, Effect of laser beam incidence angle on cladding morphology in laser cladding process, Journal of Mechanical Science and Technology 34(4) (2020) 1531-1537.
[231] A. Aprilia, N. Wu, W. Zhou, Repair and restoration of engineering components by laser directed energy deposition, Materials Today: Proceedings 101 (2022) 1-6.

[232] E.R. Denlinger, P. Michaleris, Effect of stress relaxation on distortion in additive manufacturing process modeling, Additive Manufacturing 12 (2016) 51-59.
[233] J. Yu, X. Lin, L. Ma, J. Wang, X. Fu, J. Chen, W. Huang, Influence of laser deposition patterns on part distortion, interior quality and mechanical properties by laser solid forming (LSF), Materials Science and Engineering: A 528(3) (2011) 1094-1104.
[234] X. Wang, W. Sun, Y. Chen, J. Zhang, Y. Huang, H. Huang, Research on trajectory planning of complex curved surface parts by laser cladding remanufacturing, The International Journal of Advanced Manufacturing Technology 96(5-8) (2018) 2397-2406.
[235] H.L. Wei, F.Q. Liu, W.H. Liao, T.T. Liu, Prediction of spatiotemporal variations of deposit profiles and inter-track voids during laser directed energy deposition, Additive Manufacturing 34 (2020) 101219-101229.
[236] S. Morville, M. Carin, P. Peyre, M. Gharbi, D. Carron, P. Le Masson, R. Fabbro, 2D longitudinal modeling of heat transfer and fluid flow during multilayered direct laser metal deposition process, Journal of Laser Applications 24(3) (2012) 032008-032017.
[237] M. Moradi, A. Ashoori, A. Hasani, Additive manufacturing of stellite 6 superalloy by direct laser metal deposition – Part 1: Effects of laser power and focal plane position, Optics & Laser Technology 131 (2020) 106328-106338.
[238] M. Moradi, A. Hasani, Z. Malekshahi Beiranvand, A. Ashoori, Additive manufacturing of stellite 6 superalloy by direct laser metal deposition – Part 2: Effects of scanning pattern and laser power reduction in differrent layers, Optics & Laser Technology 131 (2020) 106455-106465.
[239] M. Moradi, A. Hasani, Z. Pourmand, J. Lawrence, Direct laser metal deposition additive manufacturing of Inconel 718 superalloy: Statistical modelling and optimization by design of experiments, Optics & Laser Technology 144 (2021) 107380-107390.
[240] N.D. Jamnikar, S. Liu, C. Brice, X. Zhang, In situ microstructure property prediction by modeling molten pool-quality relations for wire-feed laser additive manufacturing, Journal of Manufacturing Processes 79 (2022) 803-814.
[241] N.G. Mbodj, M. Abuabiah, P. Plapper, M. El Kandaoui, S. Yaacoubi, Modeling and Control of Layer Height in Laser Wire Additive Manufacturing, Materials (Basel) 15(13) (2022) 4479-4496.
[242] Q. Guo, C. Zhao, M. Qu, L. Xiong, S.M.H. Hojjatzadeh, L.I. Escano, N.D. Parab, K. Fezzaa, T. Sun, L. Chen, In-situ full-field mapping of melt flow dynamics in laser metal additive manufacturing, Additive Manufacturing 31 (2020) 100939-100948.
[243] H. Gu, T. Väistö, L. Li, Numerical and experimental study on the molten pool dynamics and fusion zone formation in multi-pass narrow gap laser welding, Optics & Laser Technology 126 (2020) 106081-106094.
[244] C.-F. Zhao, N.P. Kruyt, O. Millet, Capillary bridges between unequal-sized spherical particles: Rupture distances and capillary forces, Powder Technology 346 (2019) 462-476.
[245] W. Tao, Z. Yang, Y. Chen, L. Li, Z. Jiang, Y. Zhang, Double-sided fiber laser beam welding process of T-joints for aluminum aircraft fuselage panels: Filler wire melting behavior, process stability, and their effects on porosity defects, Optics & Laser Technology 52 (2013) 1-9.
[246] M. Haynes, E.J. Vega, M.A. Herrada, E.S. Benilov, J.M. Montanero, Stabilization of axisymmetric liquid bridges through vibration-induced pressure fields, J Colloid Interface Sci 513 (2018) 409-417.
[247] Z. Shi, Y. Zhang, M. Liu, D.A.H. Hanaor, Y. Gan, Dynamic contact angle hysteresis in liquid bridges, Colloids and Surfaces A: Physicochemical and Engineering Aspects 555 (2018) 365-371.
[248] X. Sun, M. Sakai, A liquid bridge model for spherical particles applicable to asymmetric configurations, Chemical Engineering Science 182 (2018) 28-43.
[249] S. Yang, R. Liang, G. Wang, Y. Gao, R. Ma, Y. Xu, Y. Xia, The experimental investigation on dynamic response of free surface for non-isothermal liquid bridge with the varying shear airflow, Experimental Thermal and Fluid Science 98 (2018) 662-673.
[250] N. Tamanna, I.R. Kabir, S. Naher, Thermo-mechanical modelling to evaluate residual stress and material compatibility of laser cladding process depositing similar and dissimilar material on Ti6Al4V alloy, Therm Sci Eng Prog 31 (2022) 101283-101292.
[251] U. Zerbst, G. Bruno, J.Y. Buffiere, T. Wegener, T. Niendorf, T. Wu, X. Zhang, N. Kashaev, G. Meneghetti, N. Hrabe, M. Madia, T. Werner, K. Hilgenberg, M. Koukolikova, R. Prochazka, J. Dzugan, B. Moller, S. Beretta,

A. Evans, R. Wagener, K. Schnabel, Damage tolerant design of additively manufactured metallic components subjected to cyclic loading: State of the art and challenges, Prog Mater Sci 121 (2021) 100786-100858.